Inês Isabel Fortuna Neves Fernandes da Cunha

Mestre em Engenharia de Materiais

Printed and drawn flexible electronics based on cellulose nanocomposites

Dissertação para obtenção do Grau de Doutor em
Nanotecnologias e Nanociências

Orientador: Doutor Luís Miguel Nunes Pereira,
Professor Associado, Faculdade de Ciências e Tecnologia da Universidade Nova de Lisboa FCT-UNL

Co-orientador: Doutor Rodrigo Ferrão de Paiva Martins,
Professor Catedrático, Faculdade de Ciências e Tecnologia da Universidade Nova de Lisboa FCT-UNL

Júri:
Presidente: Prof. Doutora Elvira Maria Correia Fortunato
Arguentes: Doutora Maria Smolander
Prof. Doutora Verónica Cortés de Zea Bermudez
Vogais: Prof. Doutora Florinda Mendes da Costa
Prof. Doutor Rogério Manuel dos Santos Simões
Prof. Doutora Elvira Maria Correia Fortunato
Prof. Doutor Luís Miguel Nunes Pereira
Prof. Doutor Pedro Miguel Cândido Barquinha

FACULDADE DE
CIÊNCIAS E TECNOLOGIA
UNIVERSIDADE NOVA DE LISBOA

Junho 2021

Inês Isabel Fortuna Neves Fernandes da Cunha

Mestre em Engenharia de Materiais

Printed and drawn flexible electronics based on cellulose nanocomposites

Dissertação para obtenção do Grau de Doutor em
Nanotecnologias e Nanociências

Orientador: Doutor Luís Miguel Nunes Pereira,
Professor Associado, Faculdade de Ciências e Tecnologia da Universidade Nova de Lisboa FCT-UNL

Co-orientador: Doutor Rodrigo Ferrão de Paiva Martins,
Professor Catedrático, Faculdade de Ciências e Tecnologia da Universidade Nova de Lisboa FCT-UNL

Júri:
Presidente: Prof. Doutora Elvira Maria Correia Fortunato
Arguentes: Doutora Maria Smolander
Prof. Doutora Verónica Cortés de Zea Bermudez
Vogais: Prof. Doutora Florinda Mendes da Costa
Prof. Doutor Rogério Manuel dos Santos Simões
Prof. Doutora Elvira Maria Correia Fortunato
Prof. Doutor Luís Miguel Nunes Pereira
Prof. Doutor Pedro Miguel Cândido Barquinha

FACULDADE DE
CIÊNCIAS E TECNOLOGIA
UNIVERSIDADE NOVA DE LISBOA

Junho 2021

Printed and drawn flexible electronics based on cellulose nanocomposites

Acknowledgments

Permitam-me que este agradecimento se inicie por esta frase: *Everything starts with a tree*! Uma frase inocente de aparente contexto utópico, mas que releva precisamente a essência desta tese, a qual se enraizou, cresceu e fortaleceu num ambiente fértil no domínio do "engenho e arte", das pessoas e *know-how* envolvido, e que por fim sustentou este presente trabalho que envolve a *masterpiece* das árvores… a celulose.

A analogia de uma árvore ao crescimento pessoal é inevitável, o qual dependeu das pessoas envolvidas, seja pela sua mestria, paciência, companheirismo, ânimo, altruísmo, e carinho, que me proporcionaram uma data de experiências, seja a nível pessoal ou profissional, e que me moldaram enquanto pessoa e cientista. É a elas que dedico inteiramente este humilde capítulo, no entanto os meus agradecimentos excedem em tudo as presentes páginas, o que me dificulta esta nobre tarefa de vos agradecer apropriadamente, mas certamente que a vida se ocupará de o fazer.

Inevitável começar pelo começo…, mas isso é uma longa história, certamente mais curta que o *Bing Bang*. Avanço antes para o despertar desta saga científica que se iniciou com a mentoria da equipa liderada pela Prof. Elvira Fortunato e o Prof. Rodrigo Martins, que conseguiram deter a atenção do mundo ao conquistarem e marcarem o início de numa nova era na eletrónica sustentável, onde o papel é o protagonista. Graças a ambos, a História agora "escreve-se" de uma forma curiosamente diferente! Agradeço a vossa exigência temperada de uma incontestável perseverança e espírito indomável, bem como a vossa total e incansável devoção no rumo da inovação. A vossa dedicação garante o constante aprimoramento dos centros de investigação CENIMAT e CEMOP, tanto em termos de recursos, formação e parcerias dos quais pude usufruir, que asseguram a excelente qualidade das atividades ligadas à investigação avançada.

Não é de surpreender o enorme privilégio e admiração que sinto por ser orientada por dois elementos cruciais desta equipa, o Prof. Luís Pereira e o Prof. Rodrigo Martins, a quem dirijo uma palavra de enorme apreço e gratidão pelo suporte, acompanhamento, otimismo e confiança depositada no meu trabalho, que me permitiram evoluir de forma segura e firme, bem como alargar os horizontes. Acima de tudo agradeço o apoio incondicional e o constante incentivo a novos desafios, porque a entropia consegue ser uma perfeita aliada à ciência quando bem direcionada! Neste ponto, agradeço em especial ao meu orientador Prof. Luís Pereira, por me auxiliar a guiar o meu entusiamo e a direcionar os meus inúmeros e efusivos *brainstormings* na concretização deste trabalho, a quem dou o mérito da simplificação. A seu tempo e paradoxalmente, espero que este meu aparente "defeito" se tenha convertido numa "qualidade", pois isto é claramente uma consequência de uma equipa hospedada num ambiente propício para discutir ciência de uma forma livre, amigável e informal, onde o incentivo é mútuo e persistente.

Agradeço também à Fundação para a Ciência e Tecnologia pelo financiamento da minha bolsa de doutoramento SFRH/BD/126409/2016, bem como à Comissão Europeia no âmbito do projeto

NewFun (ERC-StG-2014, GA 640598). Este trabalho foi também apoiado pelos fundos FEDER através do Programa COMPETE 2020 e pelos Fundos Nacionais através da Fundação Portuguesa para a Ciência e Tecnologia no âmbito do Projeto n.º POCI-01-0145-FEDER-007688, Referência UID/CTM/50025, projeto CHIHC, referência PTDC/NAN-MAT/32558/2017 e projeto europeu SYNERGY, H2020-WIDESPREAD-2020-5, CSA, proposta nº 952169.

Segue-se uma lista infindável de pessoas a quem devo especial reconhecimento.

Começo por agradecer à Sónia Pereira (633 4ever!), por me ter facilitado a minha integração na equipa e pela sua tão intrínseca ternura que me suportou no arranque das minhas atividades no CENIMAT/CEMOP.

Agradeço seguidamente aos meus extraordinários “amigos da celulose”, Paul Grey, Cristina Gaspar, Diana Gaspar, José Tiago Carvalho, Raquel Barras, Joana Figueira, Susete Fernandes, não esquecendo os novos elementos, Alexandre Fonseca, e Guilherme Ferreira. É um prazer enorme a vossa companhia, e não dispenso os nossos animados debates sobre variados temas, um deles, o meu favorito, o conceito de “transparente”!

Um especial obrigado à Prof. Pydi Bahubalindruni e à paciência ilimitada do Jorzzze Martins, por toda a indispensável ajuda e mentoria que me deram na parte dos circuitos. Graças a vocês a eletrónica é ainda mais divertida! Este agradecimento também engloba a Sofia Ferreira pela sua ajuda preciosa na parte de produção de pós de óxido de zinco que se mostraram bastante promissores na demonstração de dispositivos dobráveis. Agradeço à Prof. Maria Paula Duarte pela valiosa contribuição no que respeita aos ensaios antibacterianos realizados nos materiais extraídos da cortiça.

Agradeço aos alunos de mestrado, João Rodrigues, Sabrina Rubin, António Além, Hélder Alves, Madalena Roque, João Azevedo, e alunos do Programa à Iniciação à Investigação Científica, Amanda Wscieklica, e Hugo Viana, pelos momentos divertidos de (des)orientação, e também na colaboração nos trabalhos envolvidos no meu doutoramento. Espero que tenha conseguido corresponder às vossas expectativas.

De longe menos importantes, agradeço a esta equipa fantástica e empática, que inclui a Alexandra Gonçalves, Joana Pinto, Joana Neto, Rita Branquinho, Pedro Barquinha, Asal Kiazadeh, Jonas Deuermier, Ana Pimentel, Daniela Gomes, Suman Nandy, Sumita Goswami, Manuel Mendes, Sirazul, Jenny Boane (Bicana), Deneb Menda, Guilherme Ribeiro, Emanuel Carlos (Manu), Maria João Oliveira, Ana Rovisco, Andreia dos Santos, Beatriz Coelho (Bia), Ana Santa, Tomás Calmeiro, Ana Carolina Marques, João Resende (Resi), Ricardo Ferreira, e Tiago Mateus. Acrescento ainda os aventureiros António Vicente e Bertrand Soulé, Pedro Alves, Pedro Freitas (Tchicky, o Monchicano), Adriana Costa (*always ready to squeeze my mind*!), Diogo Lima, Raquel Borda D’Agua, Daniela Salgueiro, e a minha dealer favorita de nanopartículas e açúcar Sofia Ferreira.

Torna-se fundamental incluir também as pessoas fantásticas que tive oportunidade de conhecer e partilhar alguns dos momentos mais hilariantes da minha vida, a oscilar entre ciência, turismo e cerveja artesanal (patrocinadas pela Birraria, Cerveteca e Canil). Falo do Rogério Morais,

Neusmar Cordeiro, e Pedro Ivo, não esquecendo a Craft Beer Team. É certo que a distância de milhares de quilómetros não importará, mesmo que seja da largura do Oceano Atlântico.

Agradeço também à nova geração de cientistas que vem enriquecer ainda mais a ciência: Sara Silvestre, João Coelho (*Bunny*), Tomás Pinheiro, Maria Pereira, Miguel Alexandre, Pedro Centeno, Gonçalo Narciso, Tomás Freire, Mariana Matias e Nuno Ferreira.

Seria de todo indispensável agradecer ao programa de empreendedorismo HiseedTech, desde coordenadores, mentores, alunos de gestão e os vários membros das equipas participantes, incluindo os membros da minha equipa (José Tiago Carvalho, Paul Grey, Prof. Luís Pereira, e Frederico Côrte-Real), que me desafiaram a sair da minha zona de conforto, e que me permitiram desenvolver novas capacidades na área competitiva e multifacetada do empreendedorismo.

Agradeço à Sara Oliveira, Sónia Soares e Luís Milhano por assegurarem o trabalho administrativo e por prestarem auxílio nas questões mais burocráticas. Este mesmo agradecimento estende-se à Valéria Gomes, Lúcia Mendes, Paulo Manteigas, Susana Mendes, Ana Vitorino (Iaaana), André Fonseca, por me terem proporcionado momentos bastante divertidos e únicos dos quais nunca me esquecerei, e ainda à minha querida Dona Antónia (Dama!) pelo seu lado maternal em sintonia com uma loucura sã que contagia qualquer pessoa.

Não poderia deixar de agradecer à equipa de Taekwondo do Clube do Pessoal da Siderurgia Nacional, onde pude libertar o meu excesso de energia ou mesmo extinguir alguma negatividade pontual. Obrigada pela "porrada" amigável e pelos momentos hilariantes, tanto nos treinos como nas competições, mas principalmente ao Mestre Nuno Soares, pela sua força de espírito, apoio e encorajamento, e à minha querida Luz, pela sua amabilidade, palavras acolhedoras, pacifismo e serenidade.

Dedico estas últimas palavras de gratidão aos amigos de uma vida, e também família, Miguel, Ivan, Monkey, Ana, Ribas, Bié, Monique, Iuri, Rio, Fábio, Flávia, Jovem, Carolina, Marta, Gui, Afonso, Gabi, Marcelo. Um especial obrigado à Carol, Mr. Pin, e Parra (*words are not needed*!). Vocês enchem-me o espírito de energia e boa disposição, fora o consolo e carinho que me dão quando é tão essencial. Sortuda por vos ter!

Por fim… a minha base, o meu tudo, a prova do amor incondicional! A minha Mãe, a minha Kéu, o meu Mano, o meu Cunhado, os meus queridos Sousas, o Charlie, a Mia e o Jôjô, e também os já não presentes, mas de longe distantes do meu pensamento e que para sempre habitarão no meu coração, no meu Eu. Ao meu amor, Miguel Pereira e à família e amigos que me acolheram de braços abertos! És puramente inexplicável!

Não consigo resistir a terminar com a célebre frase: Obrigada malta... Curti milhões!

Abstract

Sustainability, flexibility, and low-power consumption are key features to meet the growing requirements of simplicity and multifunctionality of low-cost, disposable/recyclable smart electronic systems in the emerging area of the "Internet-of-Things". Cellulose-based composites hold potential to fulfill such demands when explored as substrate and/or electrolyte-gate, or as active channel layer on printed transistors and integrated circuits based on ionic responses (iontronics). In this work, a new generation of reusable, healable and recyclable regenerated cellulose hydrogels with high ionic conductivity and conformability, capable of being provided in the form of stickers, are demonstrated. These hydrogels are obtained from a simple, fast, low-cost, and environmental-friendly aqueous alkali salt/urea dissolution method of native cellulose, combined with carboxymethyl cellulose (CMC) to improve the electrolyte's robustness, and subsequent regeneration and simultaneous ion incorporation with acetic acid. Their electrochemical properties can be also merged with the mechanical robustness, thermal resistance, transparency, and smoothness of micro/nanofibrillated cellulose nanopaper to yield an ionic conductive "paper-like" substrate.

Beyond gate dielectrics, a water-based screen-printable ink, composed of CMC binder and commercial zinc oxide (ZnO) semiconducting nanoparticles, was formulated. The ink enables the printing of relatively smooth and densely packed films on office paper with semiconducting functionality at room temperature. The rather use of porous ZnO nanoplates is beneficial to form percolative pathways at lower contents of functional material, at the cost of rougher surfaces.

The engineered cellulose composites are successfully integrated into flexible, recyclable, low-voltage (<3.5 V), printed electrolyte-gated transistors and "universal" logic gates fabricated on office paper or on the ionically modified nanopaper. Ubiquitous calligraphy accessories are used for easy and quick patterning of conductive/resistive tracks "on-the-fly" by merely drawing them out on the target substrate, where are already printed the devices. Such concept paves the way for a worldwide boom of creativity, where we can freely create personal electronic kits, while having fun at it and without generating waste.

Palavras-chave: cellulose; alkali salt/urea aqueous solvent system; electrolytes; oxide-based semiconductors; paper electronics; printed electronics; sustainability.

Resumo

Sustentabilidade, flexibilidade e baixo consumo energético são características chave para atender aos crescentes requisitos de simplicidade e multifuncionalidade de sistemas eletrónicos inteligentes de baixo custo, descartáveis/recicláveis na área emergente da “Internet-das-Coisas”. Compósitos à base de celulose têm potencial para atender a tais necessidades quando explorados como substrato e/ou porta-de-eletrólito ou como camada de canal ativo em transístores impressos e circuitos integrados baseados em respostas iónicas (*iontronics*).

Neste trabalho, é demonstrada uma nova geração de hidrogéis reutilizáveis, reparáveis e recicláveis baseados em celulose regenerada, que apresentam alta condução iónica e conformabilidade, podendo ser fornecidos na forma de adesivos. Estes hidrogéis são obtidos a partir de um método simples, rápido, barato e amigo do ambiente que permite a dissolução de celulose nativa em soluções aquosas com mistura de sal alcalino e ureia, combinado com carboximetil celulose (CMC) para melhorar a sua robustez, seguido da regeneração e simultâneo enriquecimento iónico com ácido acético. As suas propriedades eletroquímicas podem ser combinadas com a intrínseca robustez mecânica, resistência térmica, transparência e suavidade do “nanopapel” à base de celulose micro/nanofibrilada para obter um substrato eletrolítico semelhante a papel.

Para além de portas-dielétricas, foi formulada uma tinta aquosa compatível com serigrafia, composta por CMC como espessante e nanopartículas semicondutoras de ZnO. A tinta permite a impressão de filmes pouco rugosos e densamente percolados sobre papel de escritório, e com funcionalidade semicondutora à temperatura ambiente. O uso alternativo de nanoplacas porosas de ZnO é benéfico para criar caminhos percolativos com menores teores de material funcional, apesar de se obter filmes rugosos.

Os compósitos à base celulose foram integrados com sucesso em transístores e portas lógicas “universais”, flexíveis, recicláveis, com baixa tensão de funcionamento (<3.5 V), controladas por porta-eletrolítica, os quais foram impressos em papel de escritório ou no “nanopapel” ionicamente modificado. Acessórios de caligrafia permitem a fácil e rápida padronização de pistas condutoras/resistivas, desenhando-as no substrato alvo, onde estão impressos os dispositivos. Este conceito despoleta um mundo criativo, onde é possível criar livremente kits eletrónicos customizados de forma divertida e sem gerar resíduos.

Palavras-chave: celulose; sistema aquoso com sal alcalino e ureia, eletrólitos, óxidos semicondutores, eletrónica de papel, eletrónica impressa, sustentabilidade.

Contents

1. Designing a path for electronics to go “green” 1

1.1. Motivation 2

1.2. State-of-the-art 5

1.2.1. Cellulose as a sustainable natural source 5

1.2.1.1. Sources and hierarchical structure of cellulose 5

1.2.1.2. Isolation of nanocellulose and its properties 7

1.2.1.3. Regenerated cellulose materials from aqueous alkali hydroxide-based dissolution solvent systems 8

1.2.1.4. Cellulose-based hydrogels: the potential of self-healing property 10

1.2.2. Cellulose-based paper substrates for printed electronics 11

1.2.3. Printed electronics 12

1.2.3.1. The interest behind printed electronics 12

1.2.3.2. Printing “intelligence” on lifeless objects or surfaces 14

1.2.3.3. Challenges hampering printed electronics 19

1.2.4. Printing TMOS materials for flexible electronics 20

1.2.4.1. TMOSs vs. organic materials 20

1.2.4.2. Strategies to formulate printable TMOS-based inks 21

1.2.4.3. State-of-the-art of printed TMOS materials on transistors 22

1.2.5. Electrolyte-gated transistors 27

1.3. Outlined objectives 30

2. Materials and Methods 33

2.1. Screen-printable cellulose composite inks 34

2.1.1. Chemical synthesis and characterization of porous ZnO nanostructures 34

2.1.2. Preparation and characterization of cellulose composite semiconducting inks 35

2.1.3. Inks’ printability on office paper 36

2.2. Iontronic cellulose-based membranes 36

2.2.1. Preparation of self-healable cellulose iontronic stickers 36

2.2.2. Preparation of iontronic cellulose nanopaper composite 37

2.2.3. Characterization of the iontronic cellulose-based membranes 38

2.3. Oxide-based transistors and integrated circuits based on electrolyte-gating mechanism 38

2.3.1. Fabrication of CICH-gated IGZO transistors and inverters 38

2.3.2. Fabrication of ACICC-gated IGZO transistors 39

2.3.3. Fabrication of screen-printed ZnO EGTs and circuits on paper 39

2.3.4. Fabrication of ACICC-gated screen-printed ZnO transistors and logic gates 40

2.3.5. Electrical characterization of EGTs and integrated circuits 41

2.3.6. Electrical characterization of UV-responsive screen printed ZnO circuits 41

3. Cellulose composite semiconducting inks 43
3.1. Characterization of ZnO nanostructures 44
3.2. Characterization of office paper substrate 46
3.3. Formulation and screen-printing of cellulose composite inks 47
3.3.1. Formulation of cellulose composite inks 47
3.3.2. Printing trials on office paper 48
3.3.2.1. Influence of cellulose derivatives and ZnO content 48
3.3.2.2. Influence of drying conditions 51
3.3.2.3. Influence of ZnO nanostructures 53
4. Cellulose-based iontronic membranes 57
4.1. Development of self-healable cellulose iontronic hydrogels 58
4.1.1. Formulation using aqueous alkali hydroxide/urea dissolution system 58
4.1.1.1. Aqueous LiOH/urea solvent system 58
4.1.1.2. Aqueous mixed alkali salts/urea solvent system 60
4.1.2. Optical, structural, compositional, and morphological properties 61
4.1.3. Electrochemical properties 65
4.1.3.1. Influence of the addition of CMC 66
4.1.3.2. Influence of the alkali hydroxide 68
4.2. Development of iontronic cellulose nanopaper composites 70
4.2.1. Optical, structural, compositional, and morphological properties 70
4.2.2. Electrochemical properties 74
5. Ion-controlled IGZO transistors and circuits 77
5.1. CICH-gated IGZO transistors and logic gates 78
5.1.1. Design and architecture 78
5.1.2. Electrical performance of CICH-gated IGZO transistors 80
5.1.2.1. Li-CICHs as electrolyte-gate in IGZO EGTs on glass 80
5.1.2.2. Li-CICHs as electrolyte-gate in flexible IGZO EGTs 85
5.1.2.3. LN-CICHs and Na-CICHs as electrolyte-gate in flexible IGZO EGTs 90
5.1.3. Electrical performance of CICH-gated IGZO circuits on paper 95
5.2. “Interstrate” ACICC-gated IGZO transistors 97
6. Ion-controlled screen-printed ZnO transistors and circuits 101
6.1. Screen-printed ZnO EGTs and integrated circuits on paper 102
6.1.1. Design and architecture 102
6.1.1.1. Pencil-drawn resistive-load logic gates with screen-printed ZnO EGTs 102
6.1.1.2. Tunable optoelectrical resistor switch as load resistance for NOT logic gates 105
6.1.2. Electrical performance of screen-printed ZnO EGTs on office paper 106
6.1.2.1. Performance of as-printed devices 106
6.1.2.2. Air-stability overtime 108

6.1.2.3. Bending measurements ... 109

6.1.2.4. Environmental endurance: influence of temperature and humidity ... 111

6.1.2.5. Electrical stress: static and dynamic measurements ... 113

6.1.2.6. Optimization of EGTs' performance with porous ZnO nanoplates ... 114

6.1.3. Electrical performance of screen-printed ZnO circuits on office paper 116

6.1.3.1. Handwritten logic gates with screen-printed ZnO EGTs ... 116

6.1.3.2. UV-responsive inverters ... 118

6.2. Fully screen-printed ZnO nanopaper composite gated transistors and logic gates 122

6.2.1. Design and architecture 122

6.2.2. Electrical performance of fully screen-printed ZnO nanopaper composite gated transistors 124

6.2.2.1. Performance of as-printed devices ... 124

6.2.2.2. Air-stability overtime ... 126

6.2.2.3. Bending measurements ... 127

6.2.2.4. Electrical stress: static and dynamic measurements ... 130

6.2.3. Logic gate operations with fully printed ZnO nanopaper composite gated transistors 131

7. Environmental responsible strategies ... 133

7.1. Reuse, repair, and recyclability of cellulose iontronic stickers ... 135

7.2. Biodegradability and recyclability assessment of all-cellulose ionic conductive substrates ... 139

7.3. Adding value to cork wastes ... 144

8. General conclusions and new directions ... 151

8.1. Main achievements ... 152

8.1.1. Screen-printed ZnO semiconducting films with RT functionality 152

8.1.2. Cellulose-based ionic conductors: from stickers to substrates 153

8.1.3. Iontronic devices on paper or "paper-like" substrates 153

8.1.4. Sustainable end-of-life management 156

8.2. Future perspectives ... 157

8.2.1. Smoother cellulose-based (nano)paper substrates 157

8.2.2. Submicrometric channel lengths 158

8.2.3. Environmental stability 158

8.2.4. Low-temperature sintering of TMOS materials on paper 158

8.2.5. From personal fabrication to upscaling printed electronics based on cellulose materials 159

8.2.6. Printed cellulose-based ring oscillators with multi-responsiveness 160

8.2.7. Future prospects for suberinic-based composites 160

9. Outputs ... 163

9.1. Publications ... 164

9.2. Scientific conferences ... 165

9.3. Workshops and courses 166
9.4. Projects 166
9.5. Recognitions 166
10. References 167
Annex A. Supplementary figures 187
Annex B. Supplementary tables 195
Annex C. Supplementary equations 205

List of Figures

Figure 1.1. Design thinking of all the tasks needed to be fullfiled and unified, starting with a proper selection of raw materials and processes, to find the ideal conditions that combine efficiency, durability, stability, performance, and simplificity into the same materials and integrated devices, while boosting an enrironmental-conscious mentality through reusing, repairing, recycling or safer disposability (biodegradability). 3

Figure 1.2. Cellulose sources available in nature, from wood, plants, seed fibers, marine animals, and algae to bacteria. 5

Figure 1.3. Schematic of the hierarchical structure of tree wood, from macroscopic to molecular dimensions, also illustrating the chemical structure of cellulose and the establishment of the intra/intermolecular interactions within cellulose chains through hydrogen-bonding (H-bonding). Image adapted from references [63,66,70]. 6

Figure 1.4. Schematic of the dissolution process of cellulose in aqueous alkali hydroxide/urea solutions at low-temperature: **a)** cellulose bundle; **b)** swollen cellulose; **c)** formation of a stable IC (transparent solution). Image obtained from reference [87]. 9

Figure 1.5. Overview of current applications of printed electronics. Adapted from references [161–166]. 14

Figure 1.6. Schematic illustration of the most common printing techniques and typical functional materials used in inks' formulation. 16

Figure 1.7. Graphical summary of several literature reports related with the topic of printed TMOS transistors, showing typical device's performance for different kinds of TMOS materials using different printing techniques and thermal treatments. **a)** Variation of $I_{ON/OFF}$ and mobility. **b)** Influence of channel length in mobility. Influence of thermal treatment after printing in **c)** mobility and **d)** $I_{ON/OFF}$. A distinction between low-temperature (Low-T) and high-temperature (High-T) post-printing processes is presented in the graphs to correlate their potential compatibility with heat-sensitive substrates. SP, IJP, AJP, EHD, Gv, Flexo, DPF, QDs, NPs, NWs, NRs stand for screen-printing, inkjet-printing, aerosol-jet printing, electrohydrodynamic jet printing, gravure printing, flexographic printing, dual-phase film (metal salt precursor combined with TMOS nanostructures), quantum-dots, nanoparticles, nanowires, and nanorods, respectively. Data taken from references [52–54,57,58,132,178,187,189,190,203–242] 22

Figure 1.8. Overview of transistors configurations and gating mechanism. **a)** Schematic illustration of typical configurations of transistors: staggered top gate (STGT) or bottom gate (SBGT), coplanar top gate (CTGT) or bottom gate (CBGT) transistors. **b)** Cross-section of transistors depicting the semiconductor (n-type)/dielectric/gate electrode interfaces for different polarization mechanisms when using polymers dielectrics (dipole polarization), liquid electrolytes (ionic polarization), or solid polymer electrolytes (dipole and ionic polarizations). 28

Figure 3.1. Characterization of ZnO nanostructures. SEM images for different magnifications of **a)** commercial ZnO NPs, and **b)** synthesized ZnO PNPs. **c)** XRD diffractograms. **d)** FTIR spectra (inset: magnification of the absorption band at 600–530 cm^{-1}). 45

Figure 3.2. Morphological and structural characteristics of office paper substrate. **a)** SEM images of the surface of office paper for different magnifications (inset: XRD diffractogram of office paper). **b)** Cross-section image of office paper. **c)** 3D profilometry of office paper (area: 0.5 x 0.5 mm^2). 46

Figure 3.3. Inks' characteristics. a) Rheological behavior of CMC and EC binder solutions. **b)** Viscosity as function of the temperature for C3Z40 ink (Inset: photo of the cellulose composite semiconducting ink). 47

Figure 3.4. SEM images of the screen-printed cellulose/ZnO composite films on office paper. 48

Figure 3.5. Surface defects of the screen-printed ZnO films on office paper. SEM images for higher magnifications of screen-printed film on office paper using **a)** C3Z40 ink, and **b)** EC5Z40

ink. AFM images of the screen-printed films on office paper using **c)** C3Z40 ink and **d)** EC5Z40 ink. 49

Figure 3.6. Quality of the interface between the screen-printed films and office paper. Cross-section SEM images of the screen-printed films on office paper using **a)** C3Z40 ink, and **b)** EC5Z40 ink. 50

Figure 3.7. Printing resolution of the screen-printed films on office paper. Optical microscope image of screen-printed lines on office paper with different spacings (150 – 350 µm) for **a)** C3Z40 ink and **c)** EC5Z40 ink. Measured line width ($\text{width}_{\text{printed}}$) as a function of theoretical line width ($\text{width}_{\text{screen}}$) for **b)** C3Z40 ink and **d)** EC5Z40 ink, and respective lateral spreading ($\text{width}_{\text{printed}}/\text{width}_{\text{screen}}$). The values show the average and respective standard error of the mean obtained from ten measurements for each line. 51

Figure 3.8. Influence of the drying conditions. **a)** TGA curves of C3Z40 ink, EC5Z40 ink, and office paper, and respective derivatives. Normalized FTIR spectra of C3Z40 ink screen-printed on glass and dried at **b)** RT, and **e)** 120 ºC for different times. Magnifications of the normalized absorption bands at **c)** 600–525 cm^{-1}, and **d)** 3700–3000 cm^{-1} for C3Z40 ink screen-printed on glass and dried at RT for different times. Magnifications of the normalized absorption bands at **e)** 3700–3000 cm^{-1} for C3Z40 ink screen-printed on glass and dried at 120 ºC for different times.53

Figure 3.9. SEM images of screen-printed CMC/ZnO PNPs films on office paper. 54

Figure 3.10. Printing resolution of screen-printed CMC/ZnO PNPs films on office paper. **a)** Optical microscope image of screen-printed lines on office paper with different spacings (150 and 200 µm) for C3ZPN10 ink, C3ZPN20, and C3ZPN30 inks. Measured $\text{width}_{\text{printed}}$ as a function of the loading content of ZnO PNPs in the ink composition for a spacing of **b)** 150 and **c)** 200 µm, and respective lateral spreading ($\text{width}_{\text{printed}}/\text{width}_{\text{screen}}$). The values show the average and respective standard error of the mean obtained from ten measurements for each line. 55

Figure 4.1. Photography of different stage steps of the developed Li-ClCHs with different proportions of MCC:CMC**.** Photograph of the MCC:CMC solutions with different weight ratios of CMC (0, 2, and 4 wt.%) **a)** before and **b)** after regeneration. **c)** Resulting flexible, freestanding Li-ClCHs, referred to as MC0 (0 wt.% of CMC), M2C1 (2 wt.% of CMC), and M1C1 (4 wt.% of CMC). **d)** Demonstration of the high conformability and adhesion of the M1C1 hydrogel. 60

Figure 4.2. Photography of the different stage steps of the developed cellulose-based solutions with different proportions of LiOH and NaOH. The procedure starts with the dissolution of MCC powder in the aqueous alkali hydroxide/urea solvent system, followed by the addition of CMC and regeneration/ neutralization of the cellulosic solution with acetic acid. A freeze-thawing process is performed between each step in order to improve MCC dissolution. 61

Figure 4.3. Optical, structural, thermal, and mechanical properties of ClCHs. **a)** Photography of the developed highly conformable and sticky Na-ClCH, which was cut with the same shape of a leaf. Main properties of ClCH membranes: **b)** Total optical transmittance, **c)** XRD diffractograms, **d)** TGA curves and respective derivatives (dotted lines), **e)** FTIR spectra (MCC powder used as reference). 62

Figure 4.4. SEM micrographs of the different ClCHs for different magnifications. 64

Figure 4.5. Air-stability of the ClCHs. **a)** Photography of a slice of N100 hydrogel after one day of storage at ambient conditions. **b)** XRD diffractogram of N100 hydrogel after formation of urea dendrites. **c)** SEM images of L1N19 and N100 membranes obtained 28 hours after being cut and stick on the electrodes. 65

Figure 4.6. Schematic representation of the electrochemical cell assembly in a typical capacitor structure (metal/ClCH/metal) to perform the electrochemical characterization of the developed ClCHs. 66

Figure 4.7. Electrochemical characterization of Li-ClCHs with different proportions of MCC:CMC. **a)** Electrical equivalent circuit of the proposed impedance model, where C_b is the bulk capacitance, R_c and R_b are the electrical contact and bulk resistances, respectively, and CPE is the constant phase element. **b)** Capacitance and phase angle versus frequency plots for the developed Li-ClCHs (MC0, M2C1, and M1C1), and respective **c)** nyquist plots. The symbols and

the dashed lines denote the experimental and the fitted data, respectively. **d)** CV measurements of the Li-ClCHs from -2 to 2 V at different scan rates, whereas continuous and dashed lines correspond to 25 mV s^{-1} and 400 mV s^{-1}, respectively. 66

Figure 4.8. Electrochemical performance of the ClCHs. **a)** Capacitance and phase angle versus frequency plots of the developed ClCHs, and respective **b)** nyquist plots. The open symbols and the dashed lines denote the experimental and the fitted data, respectively. **c)** Representation of C_{DL} and σ_i as a function of LiOH:NaOH contents used for cellulose dissolution. The data points show the average and corresponding errors bars obtained from 4 samples. **d)** CV measurements of the ClCHs (the potential sweep was performed with a scanning rate of 50 mV s^{-1} in a potential range between -3 and 3 V). 69

Figure 4.9. Optical characterization of the engineered nanopapers. **a)** Photograph of the developed ACICC membrane, and **b)** its total transmittance compared with cellulose nanopaper. 70

Figure 4.10. Morphological characterization of the engineered nanopapers.SEM micrograph images of cellulose nanopaper and ACICC membrane on distinct surfaces (front, back surfaces, and cross-section). 71

Figure 4.11. AFM characterization of engineered nanopapers. Surface roughness of the front and back side of cellulose nanopaper and ACICC membrane. 72

Figure 4.12. Structural, chemical, and thermal characterization of the engineered nanopapers and comparison with the Li-ClCH membrane. a) XRD diffractograms. b) Normalized FTIR spectra. c) TGA curves and respective derivatives. 73

Figure 4.13. Electrochemical characterization of the engineered nanopapers. a) Design of the capacitor structure (carbon/membrane/carbon) with an active area of 1 mm^2. **b)** Nyquist plots for the engineered nanopapers, and respective. **c)** capacitance and **d)** phase angle as a function of frequency, where the ionic relaxation region is highlighted in blue and green for the cellulose nanopaper and ACICC membrane, respectively. The symbols and the dashed lines denote the experimental and the fitted data, respectively. 74

Figure 4.14. Electrochemical stability of the engineered nanopapers. **a)** CV curves of the cellulose nanopaper and ACICC membrane using carbon/membrane/carbon structure. **b)** Influence of the CMC/ZnO PNPs layer in the CV curve of the ACICC membrane (inset of the capacitor structure similar to the fabricated screen-printed ZnO PNPs NCGTs, including the semiconductor layer). All the curves were acquired for a scan rate of 0.2 V s^{-1} 76

Figure 5.1. Schematic illustration of two planar ClCH-gated IGZO EGTs fabricated on multilayer-coated paper integrated onto NOT gates with conductive/resistive tracks hand-drawn on office paper. Inset: SEM image of the smooth and impermeable surface of the multilayer-coated paper substrate used for fabrication of the EGTs. R_L, V_{DD}, V_{OUT}, and V_{IN}, stand for load resistance, supply voltage, output voltage and input voltage, respectively. 79

Figure 5.2. Electrical performance of IGZO transistors on glass gated by Li-ClCHs. **a)** Schematic illustration of two planar ClCH-gated IGZO EGTs fabricated on glass. Influence of V_{GS} scan rate on cyclic I_{DS}–V_{GS} curves of EGTs on glass gated by **b)** MC0, **c)** M2C1, and **d)** M1C1 for saturation regime (V_{DS} = 1.2 V), and respective I_{DS}–V_{DS} curves for a V_{GS} step of 0.25 V, from -0.5 to 2 V. Arrows represent the sweep direction, whereas continuous and dashed lines correspond to drain (I_{DS}) and leakage ($|I_{GS}|$) currents, respectively. 81

Figure 5.3. Comparison of electrical parameters obtained for the developed IGZO EGTs on glass gated by Li-ClCHs (MC0, M2C1, and M1C1) using distinct V_{GS} scan rates. 82

Figure 5.4. Electrochemical stability of IGZO/electrolyte interface. CV measurements of the developed Li-ClCHs combined with IGZO from -2 to 2 V at different scan rates, whereas continuous and dashed lines correspond to 25 and 400 mV s^{-1}, respectively (inset: schematic illustration of the electrochemical cell structure, including the IGZO layer). 83

Figure 5.5. Influence of V_{GS} scan rate on I_{DS} and $|I_{GS}|$ of IGZO EGTs on glass gated by Li-ClCHs, for saturation regime (V_{DS} = 1.2 V), on a narrow range of applied gate voltage from 0.5 to 2 V,

where it is visible a bump suggesting a redox reaction and consequently doping of the semiconductor. Arrows represent the sweep direction. 84

Figure 5.6. Electrical performance of IGZO EGTs on glass overtime. Cyclic I_{DS}–V_{GS} curves of EGTs gated by Li-ClCHs for saturation regime (V_{DS} = 1.2 V) at a fixed V_{GS} scan rate of 400 mV s^{-1}. Arrows represent the sweep direction, whereas continuous and dashed lines correspond to I_{DS} and $|I_{GS}|$, respectively. 85

Figure 5.7. Electrical performance of IGZO EGTs on multilayer-coated paper. **a)** Photography of the developed flexible IGZO EGT on multilayer-coated paper gated by M1C1 electrolyte. **b)** Cyclic I_{DS}–V_{GS} curves of the bendable device on its flat state at different V_{GS} scan rates for saturation regime (V_{DS} = 1.2 V) and respective I_{DS}–V_{DS} curves (the step for the V_{GS} was 0.25 V, from −0.5 up to 2 V). Arrows represent the sweep direction, whereas continuous and dashed lines correspond to I_{DS} and $|I_{GS}|$ currents, respectively. 86

Figure 5.8. Optical microscope images showing the IGZO and Ti/Au layers deposited on multilayer-coated paper, where are visible cracks on Ti/Au electrodes and a misalignment of the patterned IGZO with the source and drain contacts. 87

Figure 5.9. Electrical performance of IGZO EGTs on multilayer-coated paper under bending. **a)** Cyclic I_{DS}–V_{GS} curves of the IGZO EGT on paper gated by M1C1 electrolyte for saturation regime (V_{DS} = 1.2 V) at a fixed scan rate of 25 mV s^{-1} measured before bending, under inward (radius 5 mm) or outward (radius 5 mm) bending, and after removal of bending deformation (recovery to the flat state). Arrows represent the sweep direction, whereas continuous and dashed lines correspond to I_{DS} and $|I_{GS}|$, respectively. **b)** Comparison of electrical parameters before and after deformation for increasing bending radii. 87

Figure 5.10. Electrical performance stability of IGZO EGTs on paper gated by M1C1 electrolyte under electrical stress. Static measurements: **a)** cyclic I_{DS}–V_{GS} curves after 1 and 100 cycles (delay of 5 min between each cycle) for saturation regime (V_{DS} = 1.2 V) at a fixed scan rate of 25 mV s^{-1}. Arrows represent the sweep direction, whereas continuous and dashed lines correspond to I_{DS} and $|I_{GS}|$, respectively. **b)** Variation of V_{ON} and $I_{ON/OFF}$ after 100 cycles. Dynamic measurements: **c)** variation of $I_{ON/OFF}$ with increasing cycles for a square-wave gate signal between -0.6 until 2 V for a fixed V_{DS} of 1.2 V and at different frequencies; **d)** evolution of I_{ON} and I_{OFF} with frequency for the tenth cycle. 89

Figure 5.11. Electrical characteristics of the fabricated planar ClCH-gated IGZO EGTs on multilayer-coated paper. Cyclic I_{DS}–V_{GS} curves for saturation regime at V_{DS} = 1.2 V of IGZO EGTs gated by **a)** L100, **b)** L1N3, **c)** L1N19 or **d)** N100 membranes, and respective I_{DS}–V_{DS} curves obtained for a V_{GS} step of 0.25 V from -0.5 V until 2 V. For the transfer curves, arrows represent the sweep direction, whereas continuous and dashed lines correspond to I_{DS} and $|I_{GS}|$, respectively. All curves were acquired with a V_{GS} scan rate of 50 mV s^{-1}. 91

Figure 5.12. Statistical distribution of device metrics ($I_{ON/OFF}$, V_{ON}, μ_{Sat} and S_S) for flexible ClCH-gated IGZO EGTs on multilayer-coated paper substrate, represented as a function of LiOH and NaOH contents used for cellulose dissolution. The electrical parameters were calculated from transfer characteristic curves in the forward sweep direction and in the saturation regime at V_{DS} = 1.2 V for a V_{GS} scan rate = 50 mV s^{-1}. The data points show the average and corresponding errors bars obtained from five samples. 92

Figure 5.13. Electrical performance stability of the fabricated ClCH-gated IGZO transistors on multilayer-coated paper under static electrical stress. **a)** Cyclic I_{DS}–V_{GS} curves of the fabricated EGTs gated by L100, L1N3 or L1N19 membranes for saturation regime (V_{DS} = 1.2 V) at a fixed V_{GS} scan rate of 50 mV s^{-1} before and after 250 cycles (delay of 5 min between each cycle). Arrows represent the sweep direction. **b)** Variation of the electrical parameters ($I_{ON/OFF}$ and μ_{Sat}) after sucessive cycles. 93

Figure 5.14. Thermal behavior of multilayer-coated paper substrate. **a)** Photographs of the L1N3 membrane attached to the paper substrate after heating at different temperatures. **b)** TGA and respective derivative of the TGA curve. 94

Figure 5.15. Influence of temperature and humidity on the electrical performance of the fabricated L1N3 hydrogel-gated IGZO transistors on multilayer-coated paper. Variation of the electrical

parameters I_{ON} and I_{OFF} **a)** during heating directly on the probe station at different temperatures from RT to 120 ºC (20 min of stabilization at each temperature before measuring), and **b)** while cooling at ambient conditions a device previously heated at 80 ºC for 20 min. Variation of the electrical parameters I_{ON} and I_{OFF} **c)** under vacuum conditions, and **d)** during recovery at atmospheric pressure. All curves were acquired with a V_{GS} scan rate of 50 mV s^{-1} for saturation regime (V_{DS} = 1.2 V). Short dotted lines correspond to the original performance of the EGTs before heating or vacuum. 95

Figure 5.16. Electrical characterization of planar NOT gates on paper. **a)** Photograph of the fabricated flexible planar NOT-gates with IGZO transistors gated by N100 membrane and pencil-drawn resistive tracks (inset: circuit schematic). VTC curves for different load resistances along a pencil-drawn graphitic line (arrows represent the sweep direction): **b)** V_{OUT} vs. V_{IN}, and **c)** |gain| vs. V_{IN}. **d**) Variation of maximum V_{OUT} ($V_{OUT,\ Max.}$) with frequency for different resistances along a pencil-drawn graphitic line to an input square-wave pulse from V_{IN} = -0.5 V to 2.5 V and V_{DD} = 1 V after five cycles. Dynamic response of the flexible planar NOT gate with a pencil-drawn R_L of 36 kΩ to an input square-wave pulse from V_{IN} = -0.5 to 2.5 V and V_{DD} = 1 V for **e)** 0.1 Hz, **f)** 1 Hz, and **g)** 10 Hz. 96

Figure 5.17. Design and electrical characterization of the fabricated ACICC-gated IGZO transistors. **a)** Schematic illustration of the structure of the sputtered IGZO EGTs using the ACICC membrane as ionic conductive substrate. **b)** Optical micrograph image of a single device fabricated on the ACICC membrane, showing the source and drain contacts. I_{DS}–V_{GS} curves and respective I_{DS}–V_{DS} curves (the step for the V_{GS} was 0.25 V, starting from -0.5 up to 2 V), collected with a V_{DS} = 1.5 V and V_{GS} scan rate of 0.4 V s^{-1}: **c)** as-prepared, and **d)** after almost eleven months of storage under ambient conditions. Arrows represent the sweep direction, whereas continuous and dashed lines correspond to I_{DS} and $|I_{GS}|$, respectively. 98

Figure 5.18. Dynamic electrical characterization of the fabricated sputtered amorphous IGZO NCGTs. Evolution of I_{ON}, I_{OFF} and $I_{ON/OFF}$ with frequency for gate voltage pulses from -1 until 2 V (the data points show the average and corresponding errors bars obtained from five devices). 100

Figure 6.1. Schematic representation of the fabrication steps of handwritten logic gates with screen-printed ZnO EGTs on office paper gated by the Li-ClCH (inset: optical microscope image of a printed ZnO EGT on office paper). S, D, G, R_L, V_{DD}, V_{OUT}, GND, $V_{IN,A}$ and $V_{IN,B}$ are referred to source, drain, gate, load resistance, supply voltage, output voltage, ground, and input voltages for EGTs A and B, respectively. 103

Figure 6.2. Printability and electrical characteristics of screen-printed carbon electrodes on office paper. **a-c)** SEM images for different magnifications of screen-printed carbon films dried at 100 ºC for 30 min, and respective **d)** AFM image. **e)** Printing resolution of the carbon ink on office: $\text{width}_{\text{printed}}$ vs. $\text{width}_{\text{screen}}$, and respective $\text{width}_{\text{printed}}/\text{width}_{\text{screen}}$ ratio (inset: optical microscope image of screen-printed lines on office paper). The values show the average and respective standard error of the mean obtained from ten measurements for each line. 104

Figure 6.3. Schematic representation of the fabricated photoelectronic ZnO inverter on office paper, composed of a single screen-printed ZnO EGT gated by the Li-ClCH connected to a switchable opto-load resistance that is controlled by UV light (365 nm). 106

Figure 6.4. Electrical performance of screen-printed C3Z40 EGTs on office paper. Cyclic I_{DS}–V_{GS} curves of screen-printed C3Z40 EGTs for saturation regime (V_{DS} = 1.2 V) at a fixed V_{GS} scan rate of 50 mV s^{-1}, and respective I_{DS}–V_{DS} curves (the step for the V_{GS} was 0.25 V, from -0.5 up to 2.5 V). Arrows represent the sweep direction, whereas continuous and dashed lines correspond to I_{DS} and $|I_{GS}|$ currents, respectively. 106

Figure 6.5. Quality of the interfaces between the different layers that compose the printed EGTs, including the office paper substrate, screen-printed carbon electrode, screen-printed C3Z40 ink, and the electrolyte. **a)** Cross-section SEM image depicting the EGT's layers. EDS mapping of **b)** O, **c)** C, and **d)** Zn. 108

Figure 6.6. Electrical performance stability of screen-printed C3Z40 EGTs on standard office paper overtime under ambient conditions. I_{DS}–V_{GS} curves: **a)** obtained after storing a device up to

2 weeks under ambient conditions; b) obtained after storing separately the electrolyte and the office paper with the printed layers for nearly 3 years under ambient conditions (V_{DS} = 1.2 V, V_{GS} scan rate of 50 mV s^{-1}). Continuous and dashed lines correspond to I_{DS} and $|I_{GS}|$ currents, respectively. 108

Figure 6.7. Mechanical flexibility of screen-printed C3Z40 EGTs of office paper. Photos of the devices during **a)** inward and **b)** outward bending deformation. **c)** I_{DS}–V_{GS} curves of the devices obtained before bending (flat), during inward or outward bending, and after removal of bending deformation for V_{DS} = 1.2 V and V_{GS} scan rate = 50 mV s^{-1} (inset: photo of the flexible paper devices under outward bending). Respective electrical performance variation during **d)** inward, and **e)** outward bending stress. Comparison of the electrical parameters before bending (flat), during inward (bending radius of 15 mm) or outward bending (bending radii of 5 and 15 mm), and after removal of bending deformation: **f)** I_{OFF}, **g)** I_{ON}, **h)** μ_{Sat}. All the data points show the average and corresponding errors bars obtained from three devices for each bending condition. 110

Figure 6.8. Optical microscope images of the screen-printed layers on office paper before bending, and after extreme inward (-180° folding) and outward bending (180° folding). 111

Figure 6.9. Thermal response of screen-printed C3Z40 EGTs on office paper. **a)** I_{DS}-V_{GS} curves for different temperatures (V_{DS} = 1.2 V, V_{GS} scan rate = 50 mV s^{-1}), and **b)** respective variation of the electrical parameters with heating. **c)** I_{DS}-V_{GS} curves of a device during cooling at RT after being heated at 80 ºC for 20 min (V_{DS} = 1.2 V, V_{GS} scan rate = 50 mV s^{-1}), and **d)** respective variation of the electrical parameters (inset: optical microscope image of the CMC/ZnO layer after heating at 80 ºC for 20 min). 112

Figure 6.10. Humidity response of screen-printed C3Z40 EGTs on office paper. I_{DS}-V_{GS} curves **a)** under vaccum, and **b)** during recovery at atmospheric pressure (V_{DS} = 1.2 V, V_{GS} scan rate = 50 mV s^{-1}). Respective variation of the electrical parameters curves **b)** under vaccum, and **d)** during recovery at atmospheric pressure. Dotted horizontal lines correspond to the initial electrical performance of the device before depressurisation. 113

Figure 6.11. Static and dynamic electrical characterization of screen-printed CMC/ZnO EGTs on standard office paper. **a)** I_{DS}–V_{GS} curves after performing consecutive cycles (delay of 5 min between each cycle, V_{DS} = 1.2 V, V_{GS} scan rate of 50 mV s^{-1}). Arrows represent the sweep direction for each curve. **b)** Respective variation of the electrical parameters with increasing number of cycles. **c)** Dynamic response for different frequencies: 0.1, 1, and 10 Hz. **f)** Evolution of $I_{ON(VGS = 2.5 V)}$, $I_{OFF(VGS = -0.5 V)}$, and respective $I_{ON/OFF}$ with frequency for the tenth cycle of the square-shaped V_{GS} signal. 114

Figure 6.12. Electrical performance of screen-printed ZnO PNPs EGTs on office paper. Cyclic I_{DS}–V_{GS} curves of screen-printed ZnO PNPs EGTs with different contents of ZnO PNPs **a)** 20 wt.%, **b)** 30 wt.%, and **c)** 40 wt.%) for saturation regime (V_{DS} = 1.2 V) at a fixed V_{GS} scan rate of 50 mV s^{-1}, and respective I_{DS}–V_{DS} curves (the step for the V_{GS} was 0.25 V, from -0.5 up to 2.5 V). Arrows represent the sweep direction, whereas continuous and dashed lines correspond to I_{DS} and $|I_{GS}|$ currents, respectively. Respective electrical parameters obtained for screen-printed ZnO PNPs EGTs fabricated on office paper (the data points show the average and corresponding errors bars obtained from ten devices), and comparison with screen-printed commercial ZnO NPs (C3Z40 ink) EGTs (the data points show the average and corresponding errors bars obtained from twenty devices): **d)** I_{OFF} and I_{ON}, **e)** $|I_{GS}|$, **f)** $I_{ON/OFF}$, **g)** V_{ON}, **h)** S_S, and **i)** μ_{Sat}. 115

Figure 6.13. Electrical performance of planar pencil-drawn resistor-loaded logic gates with driving screen-printed C3Z40 EGTs on office paper. **a)** Photograph of the fabricated handritten/printed paper-based circuits. Schematic and VTC curves (V_{OUT} vs. V_{IN}) of the printed EGTs with a pencil-drawn resistance of 150 kΩ: **b)** NOT gate; **c)** NAND gate and **d)** NOR gate for a V_{DD} = 1.5 V and voltage scan rate of 50 mV s^{-1}. Arrows represent the sweep direction. Dynamic response (V_{OUT}, V_{IN} vs. time) of the logic gates with a pencil-drawn resistance of 50 kΩ for a V_{DD} = 1.5 V at 500 mHz: **e)** NOT, **f)** NAND, and **g)** NOR gates. 117

Figure 6.14. Dynamic response of the logic gates with a pencil-drawn resistance of 50 kΩ for a V_{DD} = 1.5 V at different frequencies (50 mHz, 100 mHz and 1 Hz). 118

Figure 6.15. Photoswitching characteristics of the screen-printed ZnO PNPs OERs on office paper under different UV light intensities: **a)** variation of the resistance overtime for a bias voltage of 1.5 V, during five consecutive ON/OFF cyles (LED ON: 150 s; LED OFF: 150 s), and **b)** respective dark resistance (R_{dark}), resistance under UV light (R_{light}), and OFF/ON ratio (R_{dark}/R_{light}) for the last ON/OFF cycle. The data points show the average and corresponding errors bars obtained from 4 samples. 118

Figure 6.16. Photoswitching characteristics of the fabricated planar OER-loaded opto-NOT gates under cyclic UV illumination. VTC curves acquired overtime during (**a, c, e**) and after (**b, d, f**) UV light exposure for a UV light intensity of 0.3, 2.0, and 8.7 mW cm^{-2}, respectively (LED ON: 3 min, LED OFF: 3 min, V_{DD} = 1.5 V, voltage scan rate = 400 mV s^{-1}). Grey arrows represent the sweep direction. 120

Figure 6.17. Electrical characterization of planar opto-NOT gates on office paper composed of screen-printed ZnO PNPs EGTs and OER as photoswitchable load resistance. Respective variation of the main figures of merit of the inverters during an ON/OFF cycle (3 min ON, and 3 min OFF) for increasing light intensities from 0.3 to 8.7 mW cm^{-2} (V_{DD} = 1.5 V, voltage scan rate = 400 mV s^{-1}): **a)** |gain|, **b)** output high level (V_{OH}), **c)** output low level (V_{OL}), **d)** maximum value of input interpreted by the inverter as a logic “0” (V_{IL}), and **e)** minimum value of input interpreted by the inverter as a logic “1” (V_{IH}). The data points show the average and corresponding errors bars obtained from 5 samples. **f)** Variation of V_{OUT} for successive ON/OFF UV illumination cycles (60 s ON, and 60 s OFF) at a fixed light intensity (0.3 or 8.7 mW cm^{-2}) and V_{IN} (0 or 3 V). 121

Figure 6.18. Schematic illustration of the fabrication process of the fully screen-printed ZnO NCGTs. 122

Figure 6.19. a-b) SEM images of the printed CMC/ZnO PNPs channel layer on ACICC membrane for different magnifications. 123

Figure 6.20. Schematics of the fabricated logic gates (from left to right – NOT, NAND, and NOR gates) with planar fully screen-printed NCGTs. 124

Figure 6.21. Electrical characterization of the fabricated fully screen-printed ZnO NCGTs. **a)** Photograph of the fabricated fully screen-printed “intertrates” EGTs on the ACICC membrane. **b)** Optical micrograph image of a single NCGT (S, G and D stand for source, gate and drain electrodes). **c)** Cyclic I_{DS}–V_{GS} curve, and respective I_{DS}–V_{DS} curve (the V_{GS} step was 0.25 V, starting from -0.5 up to 2.5 V) for saturation regime (V_{DS} = 1.2 V) at a fixed V_{GS} scan rate of 0.2 V s^{-1}. Arrows represent the sweep direction, whereas continuous and dashed lines correspond to I_{DS} and $|I_{GS}|$, respectively**.** Histograms of device metrics for 25 devices: **d)** V_{ON}, **e)** I_{OFF}, **f)** I_{ON}, **g)** $|I_{GS}|$, **h)** S_S, and **i)** μ_{Sat}. 125

Figure 6.22. Ageing effect of the fabricated fully screen-printed ZnO NCGTs. **a)** I_{DS}–V_{GS} curves obtained after three days, one week, and three weeks of storage under ambient conditions and comparison with the as-prepared devices (V_{DS} = 1.2 V, V_{GS} scan rate = 0.2 V s^{-1}). Arrows represent the sweep direction, whereas continuous and dashed lines correspond to I_{DS} and $|I_{GS}|$, respectively. Variation of electrical parameters overtime: **b)** I_{ON}, $|I_{GS}|$, I_{OFF}, **c)** V_{ON}, S_S, and μ_{Sat} (the data points show the average and corresponding errors bars obtained from six samples). 126

Figure 6.23. Electrical characterization of the fabricated fully screen-printed ZnO NCGTs before and after inducing a mechanical deformation. I_{DS}–V_{GS} curves obtained before and after performing **a)** inward or **b)** outward bending/folding (V_{GS} scan rate of 0.2 V s^{-1}). Arrows represent the sweep direction, whereas continuous and dashed lines correspond to I_{DS} and $|I_{GS}|$, respectively. 127

Figure 6.24. Electrical characterization of the fabricated fully screen-printed ZnO NCGTs before and after inducing mechanical deformation. Variation of the electrical parameters before and after performing **a)** inward or **d)** outward bending/folding (V_{DS} = 1.2 V, V_{GS} scan rate = 0.2 V s^{-1}). The data points show the average and corresponding errors bars obtained from five samples. SEM images of the devices in the flat state after performing **(b,c)** inward or **(e,f)** outward folding... 128

Figure 6.25. Mechanical electrical stress measurements of the fully screen-printed ZnO NCGTs on the flat state after consecutive 100 outward folding/unfolding cycles. **a)** Schematic representation of successive folding/unfolding cycles. **b)** I_{DS}–V_{GS} curves of three devices after

successive folding/unfolding cycles (V_{DS} = 1.2 V, V_{GS} scan rate = 0.2 V s^{-1}), and respective evolution of the electrical parameters: **c)** I_{OFF}, **d)** I_{ON}, **e)** V_{ON}, and **f)** μ_{Sat}. 129

Figure 6.26. Static and dynamic electrical characterization of the fabricated fully screen-printed ZnO NCGTs. **a)** I_{DS}–V_{GS} curves obtained after consecutive cycling without delay between each cycle (V_{DS} = 1.2 V, V_{GS} scan rate = 0.2 V s^{-1}). Arrows represent the sweep direction. **b)** Normalized electrical parameters for increasing cycles. Variation of I_{DS} with increasing cycles of V_{GS} pulses from -0.5 until 2.5 V for different frequencies: **c)** 0.1, **d)** 1, **e)** 10, and **f)** 25 Hz. **g)** Variation of I_{ON} and I_{OFF} with increasing cycles for a square-wave gate signal between -0.5 until 2.5 V for a fixed V_{DS} of 1.2 V and at different frequencies (open symbols correspond to I_{ON}, while closed symbols correspond to I_{OFF}). **h)** Evolution of I_{ON}, I_{OFF} and $I_{ON/OFF}$ with frequency for the tenth cycle (the data points show the average and corresponding errors bars obtained from four devices). 131

Figure 6.27. Logic gate applications of the planar fully screen-printed ZnO NCGTs with pencil-drawn load resistances. VTC curves of **a)** the NOT gate; **b)** NAND gate, and **c)** NOR gate, and respective |gain| for different V_{DD} = 1.5 V at a fixed voltage scan rate of 0.2 V s^{-1}. Truth tables of the fabricated logic gates are summarized as insets in the respective plots. 132

Figure 7.1. Circular sustainability loop for cellulose-based ionic conductors using repairing and recycling strategies that enable the endless reuse of the obtained ionic conductive membranes. 135

Figure 7.2. Electrical performance of IGZO EGTs gated by repeatedly reused L100 hydrogel. **a)** I_{DS}–V_{GS} curves, and **b)** respective electrical parameters obtained for five additional IGZO EGTs on multilayer-coated paper substrate gated by reused L100 membrane (V_{DS} = 1.2 V; V_{GS} scan rate = 25 mV s^{-1}). 136

Figure 7.3. Self-healing ability and recyclability of the freestanding CICHs**. a)** Photograph of the repaired N100 membrane after being cut into two pieces with a razor blade and then restored by gently pressing the pieces back into contact in the cutting region for 10 s (inset: optical microscope images of the N100 membrane in the cutting region after cut and repair). **b)** Ionic conductivity of the L100, L1N3 and N100 membranes after multiple cutting/healing cycles in the same position at RT. Photographs of the freestanding N100 ionic hydrogel **c)** before, and **d)** after formation of dendrites. Comparison of (**e, g**) C_{DL} and (**f, h**) σ_i for the different N100 membranes (pristine, recycled, healed – "hot-humid" environment, healed – "cold-dry" environment). The data points show the average and corresponding errors bars obtained from 4 samples. 137

Figure 7.4. Electrical performance of IGZO EGTs gated by pristine, healed, or recycled CICHs**.** Comparison between I_{DS}–V_{GS} curves of IGZO EGTs on glass gated by: **a)** pristine, recycled or healed N100 membranes recovered from exposure to hot-humid or cold-dry environment; **b)** pristine or recycled L100 membranes (V_{DS} = 1.2 V; V_{GS} scan rate = 50 mV s^{-1}). 139

Figure 7.5. SEM images of the recycled ACICC membrane, and EDS mapping of Zn. SEM images of the **a)** front side (surface in contact with air), **b)** back side (surface in contact with the container during the drying stage), and **c)** cross-section. **d)** EDS element identification of Zn. **e)** AFM characterization of the front and back side of the recycled ACICC membrane 141

Figure 7.6. Electrochemical characterization of the recycled ACICC membrane. **a)** Photograph of the recycled ACICC membrane. **b)** ECM used for data fitting, where R_c, R_b, R_p, C_p, C_{DL} correspond to contact resistance, bulk resistance, pore resistance, pore capacitance, and interface double layer capacitance, respectively. **c)** Capacitance and phase angle as a function of frequency, and respective **d)** nyquist plots for the pristine and recycled ACICC membrane, using carbon/membrane/carbon structure with an active area of 1 mm^2. The symbols and the dashed lines denote the experimental and the fitted data, respectively. **e)** Comparison of capacitance and σ_i for the pristine and recycled ACICC membranes (the data points show the average and corresponding errors bars obtained from five samples). **f)** Comparison of the CV curves of the pristine and recycled membrane for electrochemical cell with carbon/membrane/carbon layered structure. 142

Figure 7.7. Electrical performance of screen-printed ZnO transistors fabricated on the recycled membrane. I_{DS}–V_{GS} curve and respective I_{DS}–V_{DS} curve (the step for the V_{GS} was 0.25 V, starting

from -0.5 up to 2.5 V), collected with a V_{GS} scan rate of 0.2 V s^{-1}. Arrows represent the sweep direction, whereas continuous and dashed lines correspond to I_{DS} and $|I_{GS}|$, respectively. 143

Figure 7.8. Schematic representation of the depolymerisation process used for cork. **a)** Photograph of the collected cork stoppers. **b)** Cork powder obtained after sieving the recycled cork stoppers granulates with a 500 µm mesh. **c)** SEM image of the obtained cork powder. **d)** Resulting solutions after hydrolysis of cork for a starting amount of 4 or 15 wt.% in aqueous LiOH/urea solvent system and neutralization with acetic acid. **e)** Precipitation of a "muddy-like" phase after performing a centrifugation step. **f)** Separation of the "muddy-like" material from the liquid phase. 146

Figure 7.9. FTIR spectra of the cork raw materials (before and after perfoming the pre-treatment in ethanol and water and extracted materials from the depolymerization process of cork powder (15 wt.%) in aqueous alkali salt (LiOH or NaOH)/urea solvent system. The peaks assigned for suberin (S), lignin (L), and polysaccharides (P) are represented by dotted vertical lines......... 147

Figure 7.10. Features of the extracted materials from cork raw material and their potential applications. Photographs of the **a)** "resin-like" material obtained after drying the suberinic liquid phase extracted from cork, and of the **b)** developed composite membrane composed of a mixture of liquid phase and CMC (LP/CMC). **c)** Capacitance and phase angle as a function of frequency for LP/CMC membrane using stainless-steel discs with an active area of 1 cm^2**. d)** Comparison of the cyclic I_{DS}–V_{GS} curves of the fabricated screen-printed CMC/ZnO NPs EGTs fabricated on cork textile substrate, using LP/CMC membrane or CICH membrane (L100 hydrogel) as electrolyte-gate, collected at a fixed V_{DS} of 1.2 V and V_{GS} scan rate of 50 mV s^{-1}. Arrows represent the sweep direction, whereas continuous and dashed lines correspond to I_{DS} and $|I_{GS}|$, respectively. Antibacterial assays: suberinic liquid phase against **e)** Escherichia coli, and **f)** Staphylococcus aureus, and also **g)** "suberinic/lignocellulosic" paste against Staphylococcus aureus. The extracted suberinic materials were obtained from alkaline hydrolysis depolymerization process, with or without ZnO, using different amounts of cork powder (10 or 15 wt.)........ 150

Figure S1. Dynamic electrical characterization of IGZO EGTs on paper gated by M1C1 electrolyte. Variation of drain current with increasing cycles of gate voltage pulses from -0.6 until 2 V for different frequencies: **a)** 1 Hz, **b)** 10 Hz, **c)** 50 Hz, **d)** 80 Hz, **e)** 100 Hz and **f)** 200 Hz. 188

Figure S2. Electrical performance of L1N3 hydrogel-gated IGZO transistors on multilayer-coated paper after exposure to distinct environmental conditions. **a)** I_{DS}–V_{GS} curves obtained at different temperatures during heating (20 min of stabilization at each temperature before measuring). **b)** I_{DS}–V_{GS} curves obtained while cooling a device at ambient conditions, previously heated on a hotplate at 80 ºC for 20 min. I_{DS}–V_{GS} curves obtained **c)** under vacuum conditions, and **d)** during recovery at atmospheric pressure. All curves were acquired with a V_{GS} scan rate of 50 mV s^{-1} for saturation regime (V_{DS} = 1.2 V). 189

Figure S3. Dynamic response of N100 hydrogel-gated NOT gate with a pencil-drawn resistance of 36 kΩ. V_{OUT} vs. time to an input square-wave pulse from V_{IN} = -0.5 to 2.5 V and V_{DD} = 1 V for 20 Hz. 189

Figure S4. Electrochemical characterization of the ACICC membrane using a capacitor structure similar to the IGZO NCGTs. **a)** Schematics of the electrochemical cells, with or without IGZO layer. **b)** Capacitance and phase angle as a function of frequency for ACICC membrane using IZO/ACICC/Al structures with an area of 1mm^2, and respective **c)** Nyquist plot. **d)** Influence of the semiconducting layer in the CV curves (scan rate: 0.4 V s^{-1}). 190

Figure S5. Variation of I_{DS} with increasing cycles of gate voltage pulses from -0.5 until 2 V for different frequencies: **a)** 0.1 Hz, **b)** 1 Hz, **c)** 10 Hz, **d)** 50 Hz, **e)** 100 Hz, and **f)** 250 Hz. 191

Figure S6. Influence of V_{DD} and R_L on the electrical performance of the fabricated inverter with a pencil-drawn load resistance. Static VTC curves of the NOT gate for different R_L (from 50 kΩ to 150 kΩ) along the pencil-drawn graphite line for different V_{DD} (1, 1.5 and 2 V), and respective static |gain| characteristic curves for a V_{DD} of **b)** 1 V, **c)** 1.5 V and **d)** 2 V (voltage scan rate of 50 mV s^{-1}). 192

Figure S7. Electrochemical performance of the L100, L1N3 and N100 membranes before and after several cut/healing cycles at room temperature. **a-c)** Capacitance and phase angle versus frequency plots, and corresponding **d–f)** nyquist plots for L100, L1N3 and N100 membranes, respectively. The open symbols and the dashed lines denote the experimental and the fitted data, respectively. 193

Figure S8. Electrochemical performance of distinct N100 membranes (pristine, healed, and recycled) and comparison with recycled L100 membrane. **a)** Capacitance and phase angle versus frequency plots of the different N100 membranes (pristine, recycled, and healed). **b)** Respective nyquist plots. The open symbols and the dashed lines denote the experimental and the fitted data using Dasgupta's ECM, respectively. 194

List of Tables

Table 1.1. Comparison of different types of nanocellulose (CNCs, NFCs, BC).[13,60,75] 7

Table 1.2. Comparison of the features of most common printing techniques and inks requirements. Adapted from references [11,15,49,139,141–143,145,147–149,168]. 16

Table 2.1. Summary of all the developed ZnO-based composite inks. 35

Table 2.2. Summary of all the developed ClCHs membranes. 37

Table 4.1. Resume of the electrochemical characterization of Li-ClCHs with different proportions of CMC. 67

Table 4.2. Resume of the electrochemical characterization of the ClCHs. The values show the average and respective standard error of the mean obtained from four samples. 69

Table 5.1. Results of the electrical characterization of the IGZO EGT on paper gated by M1C1 electrolyte (V_{DS} = 1.2 V). 86

Table 5.2. Resume of the electrical performance stability of ACICC-gated IGZO transistors overtime. The values show the average and respective standard error of the mean obtained from six samples (V_{DS} = 1.5 V, V_{GS} scan rate: 0.4 V s^{-1}). 98

Table 6.1. Results of the electrical characterization of ClCH-gated screen-printed CMC/ZnO NPs EGTs on office paper. The values show the average and respective standard error of the mean obtained from twenty samples (V_{DS} = 1.2 V, V_{GS} scan rate: 0.05 V s^{-1}). 107

Table 6.2. Variation of the electrical performance of ClCH-gated screen-printed CMC/ZnO EGTs on office paper overtime. The values show the average and respective standard error of the mean obtained from three samples (V_{DS} = 1.2 V, V_{GS} scan rate: 0.05 V s^{-1}). 109

Table 7.1. Comparison of the electrochemical parameters for the different N100 membranes (pristine, healed, and recycled) and recycled L100, and their influence on the electrical performance of the fabricated IGZO transistors on glass (V_{DS} = 1.2 V, V_{GS} scan rate: 0.05 V s^{-1}). 139

Table 7.2. Comparison of the electrical parameters of the printed ZnO NCGTs using pristine or recycled ACICC membranes. The values show the average and corresponding standard error of the mean obtained from twenty-five and ten devices gated by pristine and recycled membranes, respectively (V_{DS} = 1.2 V, V_{GS} scan rate: 0.2 V s^{-1}). 143

Table 7.3. Comparison of the electrical parameters of the printed ZnO EGTs gated by the developed suberinic-based composite with those gated by Li-ClCH electrolyte (V_{GS} scan rate: 50 mV s^{-1}). 150

Table S1. Summary of processing routes (precursor method – PM, and/or nanoparticulate method - NM), and processing parameters (printing technique, and temperature of thermal annealing) adopted for printed n- or p-type TMOS materials, and features of the resulting printed TMOS transistors, including their configuration, channel dimensions, materials, and electrical performance. 196

Table S2. Summary of processing routes (PM and/or NM), and processing parameters (printing technique, and low-temperature annealing process) adopted for printed n- or p-type TMOS materials, and features of the resulting printed TMOS transistors, including their configuration, channel dimensions, materials, and electrical performance. 200

Table S3. State-of-the-art of cellulose (nano)paper-gated transistors. 201

Table S4. Results of the electrical characterization of IGZO transistors on glass gated by Li-ClCHs (V_{DS} = 1.2 V). 203

Table S5. Resume of the electrical performance of CICH-gated IGZO transistors on multilayer-coated paper. The values show the average and respective standard error of the mean obtained from five samples (V_{DS} = 1.2 V, V_{GS} scan rate: 0.05 V s^{-1})........203

Table S6. Variation of V_{ON} and S_S of the fabricated L1N3 hydrogel-gated IGZO transistor on multilayer-coated paper during heating at different temperatures (V_{DS} = 1.2 V, V_{GS} scan rate: 50 mV s^{-1}). 203

Table S7. Variation of V_{ON} and S_S of the fabricated L1N3 hydrogel-gated IGZO transistor on multilayer-coated paper during vacuum for various time intervals (V_{DS} = 1.2 V, V_{GS} scan rate: 50 mV s^{-1}). 204

List of Equations

Equation S1. Equation used for calculating the crystallinity index (CrI) from the empiric method proposed by Segal. $I_{(002)}$ is the maximum intensity (in arbitrary units – a.u.) of the (002) lattice diffraction taken at 2θ = 22º, and I_{am} is the intensity of the amorphous phase diffraction in the same units at 2θ = 18º. 206

Equation S2. Equation used for calculating the double layer capacitance from the Dasgupta's ECM. Y_0 is the capacitance associated to the CPE, R_c is the contact resistance, and α is a constant between 0 and 1 that determines how non-ideal the capacitor behaves (α = 1 corresponds to the case of an ideal capacitor). 206

Equation S3. Equation used for calculating the ionic conductivity from the Dasgupta's ECM. R_b is the bulk resistance, l is the thickness of the electrolyte membrane, and A is the surface area. 206

Equation S4. Equation used for calculating the subthreshold swing (S_S). I_{DS} and V_{GS} correspond to drain current and gate voltage, respectively. 206

Equation S5. Equation used for calculating the saturation mobility (μ_{Sat}). I_{DS}, V_{GS}, C_{DL}, W and L correspond to drain current, gate voltage, double layer capacitance of the CICHs, width and length of the channel, respectively. 206

Equation S6. Equation used for calculating the sheet resistance (R_s) from four-point probe measurements. V, and I correspond to the measured voltage between the two inner probes, and the current applied between the outer probes, respectively. 206

Equation S7. Equation used for calculating the bending strain (ε). r, $t_{CMC/ZnO}$, and $t_{office\ paper}$ correspond to the bending radius, and thicknesses of the CMC/ZnO film (≈ 8.65 μm) and office paper substrate (≈ 100 μm), respectively. 206

List of Symbols

2θ – Peak orientation angle (θ – Bragg angle)
A – Surface area
a.u. – Arbitrary units
C – Capacitance per unit area
C_b – Bulk capacitance
C_{DL} – Electric double layer capacitance
$C_{f=0.1\ Hz}$ – Capacitance value at 0.1 Hz
$C_{f=1\ Hz}$ – Capacitance value at 1 Hz
C_p – Pore capacitance
CrI – Crystallinity index
f – Frequency
$f_{\theta=-45^{\circ}}$ – Frequency value at $\theta = -45^{\circ}$
g_m – Transconductance
h – Hours
I – Current
$I_{(002)}$ – Maximum intensity (in arbitrary units) of the (002) lattice diffraction taken at $2\theta = 22^{\circ}$
I/A – Current density
I_{am} – Intensity of the amorphous phase diffraction in arbitrary units at $2\theta = 18^{\circ}$
I_{DS} – Drain current
I_{GS} – Gate leakage current
I_{OFF}– OFF current
I_{ON} – ON current
$I_{ON/OFF}$ – ON/OFF current ratio
L – Channel length
l – Thickness
min – Minutes
r – Bending radius
R_b – Bulk resistance
R_c – Contact resistance
R_{dark} – Dark resistance
R_L – Load resistance
R_{light} – Resistance under ultraviolet light
R_p – Pore resistance
rpm – Rotations per minute
R_s – Sheet resistance
S_S – Subthreshold swing
$t_{CMC/ZnO}$ – Thickness of the CMC/ZnO film
$t_{office\ paper}$ – Thickness of office paper substrate
V – Voltage
V_{DD} – Supply voltage
V_{DS} – Drain voltage
V_{GS} – Gate voltage
V_{IH} – Minimum value of input interpreted by the inverter as a logic “1”
V_{IL} – Maximum value of input interpreted by the inverter as a logic “0”
V_{IN} – Input voltage
V_{OH} – Output high level
V_{OL} – Output low level
V_{ON} – Turn-on voltage
V_{OUT} – Output voltage
V_{th} – Threshold voltage
W – Channel width
Y_0 – Capacitance associated to the CPE
Z_{imag} – Imaginary component of impedance
Z_{real} – Real component of impedance

α **–** Constant between 0 and 1 that determines how non-ideal the capacitor behaves ($\alpha = 1$ corresponds to the case of an ideal capacitor)
ε **–** Bending strain
θ **–** Phase angle
μ_{Sat} **–** Saturation mobility
σ_i **–** Ionic conductivity

List of Acronyms and Abbreviations

3D – Three-dimensional
AC – Alternate current
ACICC – All-cellulose ionic conductive composites
AFM – Atomic force microscopy
AGU – Anhydroglucose units
AJP – Aerosol-jet printing

BC – Bacterial cellulose

CBGT – Coplanar bottom gate transistor
CEMOP – Centre of Excellence in Microelectronics Optoelectronics and Processes
CENIMAT – Centro de Investigação de Materiais
CICHs – Cellulose ionic conductive hydrogels
CMC – Carboxymethyl cellulose
CMOS – Complementary metal-oxide semiconductor
CNCs – Cellulose nanocrystals
CPE – Constant phase element
CTGT – Coplanar top gate transistor
CV – Cyclic voltammetry

DIY – Do-it-Yourself
DP – Degree of polymerization
DPF – Dual-phase film

EC – Ethyl cellulose
ECM – Equivalent circuit model
EDLs – Electrical double layers
EDS – Energy-dispersive X-ray spectroscopy
EGT_D – Drive electrolyt-gated transistor
EGTs – Electrolyte-gated transistors
EHD – Electrohydrodynamic jet printing
EIS – Electrochemical impedance spectroscopy
E-wastes – Electronic wastes

FETs – Field-effect transistors
Flexo – Flexographic printing
FTIR – Fourier-transform infrared

GND – Ground
Gv – Gravure printing

IC – Inclusion complex
ICDD – International Centre for Diffraction Data
IGO – Indium gallium oxide
IGZO – Indium gallium zinc oxide
IJP – Inkjet-printing
IoT – Internet-of-Things
ITO – Indium tin oxide
IZO – Indium zinc oxide
IZTO – Indium gallium tin oxide

Li-CICHs – Cellulose ionic conductive hydrogels prepared from aqueous LiOH/urea solvent system
LN-CICHs – Cellulose ionic conductive hydrogels prepared from aqueous LiOH:NaOH/urea solvent system

MCC – Microcrystalline cellulose
MFC – Microfibrillated cellulose

Na-ClCHs – Cellulose ionic conductive hydrogels prepared from aqueous NaOH/urea solvent system
NFC – Nanofibrillated cellulose
NiO – Nickel oxide
NM – Nanoparticulate method
NMMO – N-methylmorpholine-N-oxide monohydrate
NPs – Nanoparticles
NRs – Nanorods
NWs – Nanowires

OER – optoelectrical resistor
OFETs – Organic field-effect transistors
OLEDs – Organic light-emitting diodes
OTFTs – Organic thin-film transistors

P3HT – Poly(3-hexylthiophene)
PC – Polycarbonate
PDF – Powder diffraction file
PEDOT:PSS – Poly(3,4-ethylenedioxythiophene) polystyrene sulfonate
PEG – Polyethylene glycol
PEN – Polyethylene naphthalate
PET – Polyethylene terephthalate
PI – Polyimide
PM – Precursor method
PVP – Poly(4-vinylphenol)

QDs – Quantum-dots

R2R – Roll-to-roll
RCFs – Regenerated cellulose films
RFID – Radio-frequency identification
RH – Relative humidity
RMS – Root mean square
RT – Room temperature

S2S – Sheet-to-sheet
SAP – Self-aligned inkjet printing
SBGT – Bottom gate transistor
SEM – Scanning electron microscopy
SP – Screen-printing
STGT – Staggered top gate transistor

TEMPO – (2, 2, 6, 6-tetramethylpiperidin-1-yl) oxidanyl
TFTs – Thin-film transistors
TGA – Thermogravimetric analysis
TMOSs – Transition metal oxide semiconductors

UV – Ultraviolet

VTC – Voltage transfer characteristic

XRD – X-Ray diffraction

ZnO – Zinc oxide
ZnO NPs – Zinc oxide nanoparticles
ZnO PNPs – Porous zinc oxide nanoplates
ZTO – Zinc tin oxide

Chapter 1

Designing a path for electronics to go "green"

1. Designing a path for electronics to go "green"...... 1

1.1. Motivation...... 2

1.2. State-of-the-art...... 5

1.2.1. Cellulose as a sustainable natural source 5

1.2.1.1. Sources and hierarchical structure of cellulose...... 5

1.2.1.2. Isolation of nanocellulose and its properties...... 7

1.2.1.3. Regenerated cellulose materials from aqueous alkali hydroxide-based dissolution solvent systems...... 8

1.2.1.4. Cellulose-based hydrogels: the potential of self-healing property...... 10

1.2.2. Cellulose-based paper substrates for printed electronics 11

1.2.3. Printed electronics 12

1.2.3.1. The interest behind printed electronics...... 12

1.2.3.2. Printing "intelligence" on lifeless objects or surfaces...... 14

1.2.3.3. Challenges hampering printed electronics...... 19

1.2.4. Printing TMOS materials for flexible electronics 20

1.2.4.1. TMOSs vs. organic materials...... 20

1.2.4.2. Strategies to formulate printable TMOS-based inks...... 21

1.2.4.3. State-of-the-art of printed TMOS materials on transistors...... 22

1.2.5. Electrolyte-gated transistors 27

1.3. Outlined objectives...... 30

1.1. Motivation

Modern society lives engulfed in a world strongly dependent on electronics, where consumerism allied with an inappropriate management at the end-of-life of products is causing a great stress in the planet resources, leading to the rapid growth of electronic-wastes (E-wastes).[1,2] According to a recent report,[3] more than 45 megatons of e-wastes were generated in 2016, and this value keeps increasing at an alarming rate of 3–4 % each year.

The pursuit of solutions to a society “consumed by consumerism” have boomed a worldwide effort to develop an innovative class of affordable, non-complex, portable, safe and sustainable smart systems that can play multiple functions with extremely low power consumption, while withstanding large mechanical deformations (bending, squashing, twisting and/or stretching).[4,5] At the end of their lifespan, reusability, repairing, recyclability, or disposability (biodegradability) are attractive solutions for reducing the environmental impacts. These key features are of major importance in the emerging field of “Zero-Waste” and “Internet-of-Things” (IoT), the networking of smart objects, as a tool to bring comfort and welfare to citizens.[4–9]

Abundant, renewable, highly stable materials, that are neither harmful nor polluting, together with simplified and economically efficient manufacturing processes performed at low-temperature are of great interest for the fabrication of these new-concept systems (**Figure 1.1**).[4,5,7,10,11] In particular, nature offers an exceptional diversity of biopolymers, including cellulose, starch, gelatin, chitin and their derivatives, to serve as a starting building block source for the development of eco-friendly advanced functional materials.[12] The interest and increasing trend of using these materials stems from their renewability, biodegradability and, often, their biocompatibility.

Among them, cellulose stands out as the most abundant biopolymer resource on Earth and the main component of paper.[13] This natural dielectric material can serve as an inexhaustible source of raw material in production of sustainable products.[10,12,14–19] The reengineering of cellulose with new functionalities allowed to extend its application beyond the conventional ones finding potential in electronics, photonics, energy and sensing.[1,5,15,17,20]

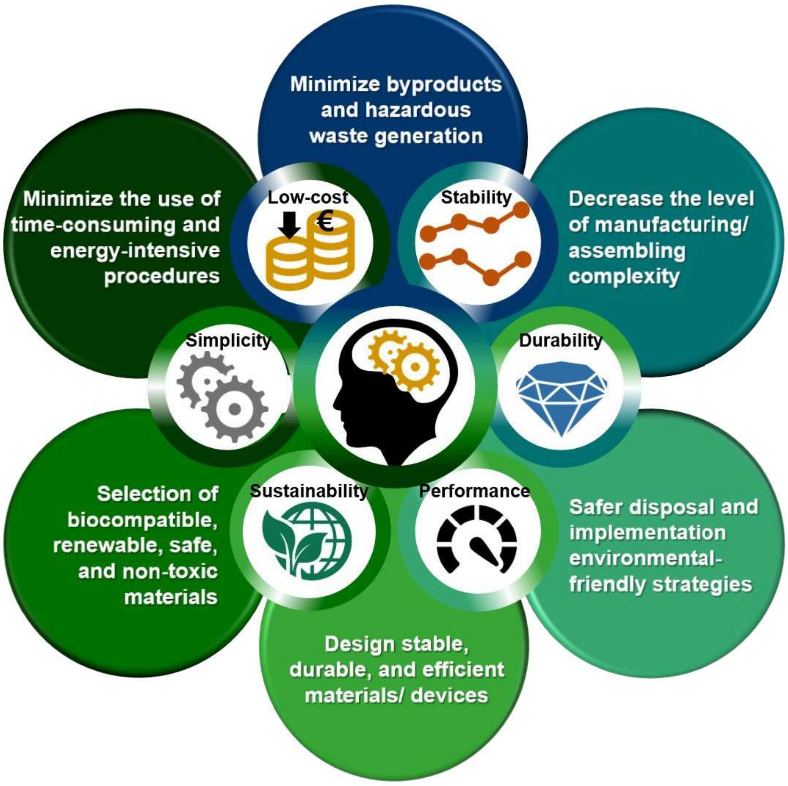

Figure 1.1. Design thinking of all the tasks needed to be fullfiled and unified, starting with a proper selection of raw materials and processes, to find the ideal conditions that combine efficiency, durability, stability, performance, and simplificity into the same materials and integrated devices, while boosting an enrironmental-conscious mentality through reusing, repairing, recycling or safer disposability (biodegradability).

The dielectric properties of this biopolymer has been explored in transistors and logic circuits in the form of cellulose derivatives,[21–27] nanofibrillated cellulose (NFCs),[28] cellulose nanocrystals (CNCs),[29] or even ionically modified CNCs,[30,31] and regenerated cellulose-based hydrogels.[32,33] Excitingly, pioneer work carried out in CENIMAT research group and, subsequently, its continuous update has received global attention due to the remarkable breakthroughs performed in the field of sustainable electronics by given an extra role to cellulose fibrous paper composed of micro (conventional paper) or sub-micrometric sized fibers (nanocellulose).[4,5,34–42]

For the first time, a new concept of paper electronics arises as a potential allied to silicon (Si)-based technologies, opening the way for an innovative class of low-cost, less complex, recyclable, flexible and lightweight products. The concept consists of giving an active function to paper, as the hydrophilic network of tangled hydrophilic cellulose fibers promotes simultaneously its excellent mechanical and dielectric properties.[43] Therefore, paper can be applied simultaneously as the substrate and as a solid-state dielectric in oxide semiconductor field-effect transistors (FETs),[34,35,40,41] write-erase and read memory transistors,[36] complementary metal-oxide-semiconductor (CMOS) devices,[37,39] logic gates,[4,44] and batteries.[38]

Despite its unquestionable versatility and outstanding potential as a “two-in-one solution” for such applications, porosity and large surface roughness of paper arises some obstacles to host electronic devices, especially when smoothness is a key criterion to reduce interfacial defects between active layers of transistors and integrated circuits towards better electrical performance.[5,15] Furthermore, the operating voltage of the paper-gated transistors and integrated circuits is still in the range of tens of volts to enable the creation of electrical double layers (EDLs), which depends on the mobile ions and absorbed water within the cellulose-based paper. An additional problem arises from the processes involved in the fabrication of such devices, which require sophisticated, complex, time-consuming, energy-intensive, and highly expensive vacuum-based deposition techniques (e.g., evaporation, and sputtering).

Regarding the latter issue, the substitution of conventional techniques by truly low-cost, simple and fast patterning techniques compatible with roll-to-roll (R2R), such as solution-phase printing or handwriting techniques,[11,45,46] offers competing advantages.

Plastic substrates and printable p-type polymer semiconductors have been the primary choice as channel of printed transistors owing to their mechanical flexibility, and easy solution processability and printability under less controlled environments than inorganic semiconductors.[47–51] The superior electrical properties and greater thermal and environmental stability of transition metal oxide semiconductors (TMOSs), usually electron conducting (n-type), make them better candidates for high-performance electronic devices, despite their limited mechanical strain tolerance, and higher processing temperature.[52–54] However, low-voltage, printed transistors and logic operations based on TMOSs with high performance on flexible substrates, such as paper, have eluded scientists up to date.

Usually, printed TMOS transistors are based on precursor-route, which requires high processing temperatures (>350 ºC) to chemically convert *in-situ* the precursor into metal-oxide-metal bonds, thus limiting the choice of substrates to rigid, heat-resistant substrates, such as Si or glass.[15,52,55] Despite their lower performance compared to the previous approach, as-synthesized TMOS nanostructures can be dispersed in a printable ink yielding a ready-to-use functional semiconductor layer yet with a rougher surface after printing and annealing at low temperature (<250 ºC) or near room-temperature (RT), which is a criterion for the use of flexible substrates.[11,56–58]

Progressive efforts in the development of high-mobility, printable TMOSs, together with recent advances in high-resolution printing technology and reengineered cellulose-based dielectrics will gradually close the gap towards real applications of sustainable, low-power, flexible, printed electronics with high-frequency operations on or within cellulose. The design of inks with long-term stability that can be printed/written under ambient conditions, in a simple way (no need of sophisticated facilities nor skilled individuals), and their direct instantaneous integration/application (*in-situ* fabrication and application) may usher in a new generation of customized electronic devices towards innovative concepts, such as “personal fabrication” (or “Do-it-Yourself”, DIY).[59] By doing so, ordinary people without any skills or training can freely design, produce and use their own product, turning the idea of “everywhere, everyone, anytime” a reality, where the concept from “Lab-to-Fab” starts at home.

1.2. State-of-the-art

1.2.1. Cellulose as a sustainable natural source

1.2.1.1. Sources and hierarchical structure of cellulose

A new era based on high-performing abundant and renewable materials has been set as the new world order to achieve a more sustainable future, to mitigate the devastating environmental impacts from the current fossil fuel era, such as greenhouse gases, climate change, plastic pollution and lack of renewable energy.[60] In this perspective, cellulose is a promising candidate as a sustainable material with low or even net-zero carbon emission.

Cellulose is commonly used in the form of paper for packaging or as a support for writing, record and store information.[5,15,61] Yet, this material and its derivatives can be envisioned to be used as stable hosting matrices, fillers, or coatings for the design of new composites with advanced functionalities, in the form of solution-processed films, fibers, freestanding membranes, beads or gels, by further functionalization and engineering.[17,62]

Cellulose is the most abundant biopolymer resource on Earth (annual yield of $\approx 10^{11}$ tons) that is forecasted to play a key role in (bio)economy.[20] This biopolymer is the major structural component in plant cell walls, such as wood (composed of 40–50 % of cellulose), and cellulose can also be found in some marine animal family of tunicates, certain species of fungi, and algae, as well as an extracellular product of some bacterias (e.g. *Gluconacetobacter*) (**Figure 1.2**).

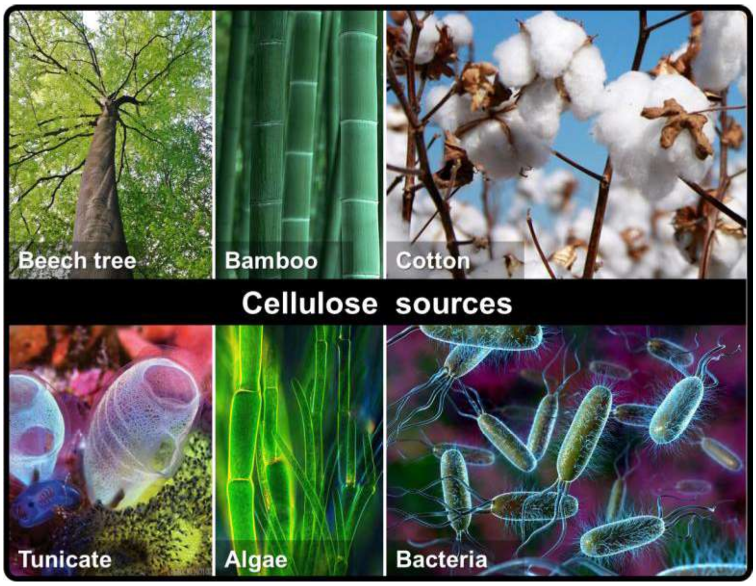

Figure 1.2. Cellulose sources available in nature, from wood, plants, seed fibers, marine animals, and algae to bacteria.

As depicted in **Figure 1.3**, cellulose, in its native state (termed cellulose I) in the cell walls of plants and trees, possesses an intriguing multi-level assembly, universally known as hierarchical structure.

At the molecular scale, cellulose is a linear polysaccharide composed of β-(1→4) linked D-anhydroglucopyranose units (AGU), the building blocks of cellulose polymer chain, with the molecular formula $[C_6H_{10}O_5]_n$ (n <20000).[63] The size of the cellulose molecules can be defined by the average degree of polymerization (DP), which varies depending on the cellulose source and processing methods.[12,13,64–66]

Each AGU has six carbon atoms with three hydroxyl groups at C2, C3, and C6 carbon atoms, giving a high degree of functionality to cellulose molecule.[64] The repeating unit of cellulose polymer is cellobiose composed of two AGU covalently linked via acetal functional groups between hydroxyl groups at C1 carbon atom of a glucose unit and C4 carbon of an adjacent glucose unit, which are arranged with a rotation of 180º in respect to each other.[12,67,68] Electrostatic attractions between oxygen and hydrogen atoms of adjacent rings (intramolecular hydrogel bonding), also occurring between polymer chains (interchain hydrogens bonds), along with van der Waals forces are responsible for the parallel stacking of cellulose elementary fibrils. [12,63,64,69]

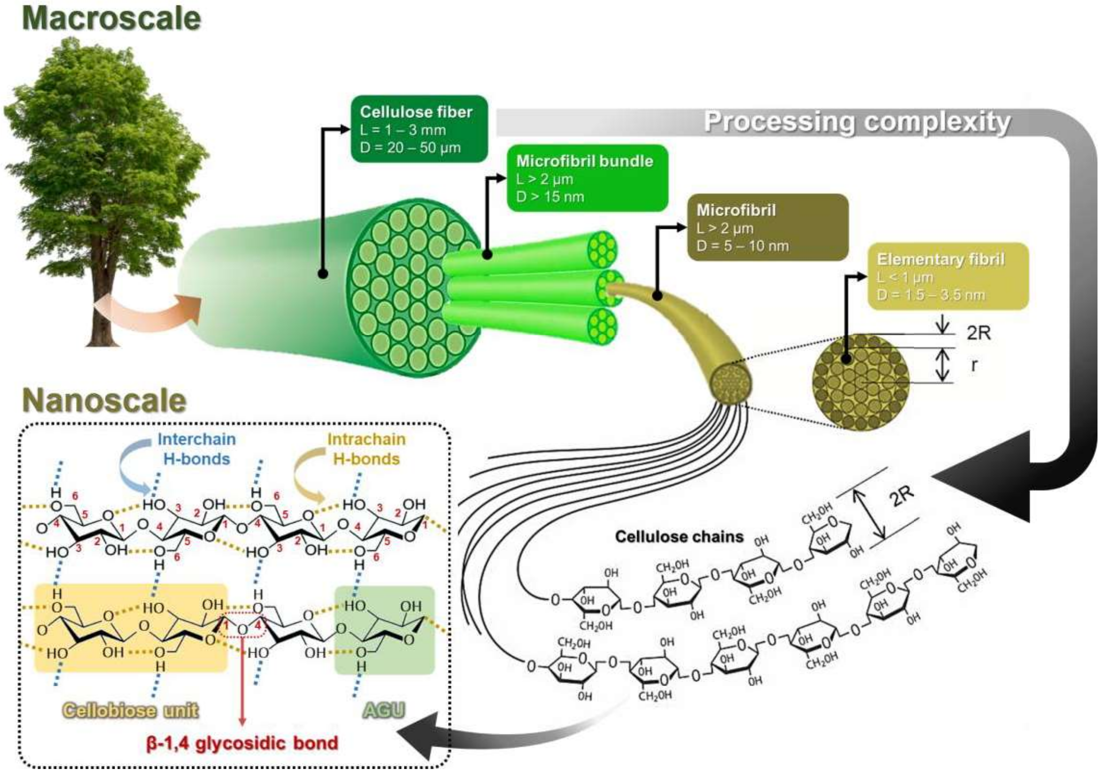

Figure 1.3. Schematic of the hierarchical structure of tree wood, from macroscopic to molecular dimensions, also illustrating the chemical structure of cellulose and the establishment of the intra/intermolecular interactions within cellulose chains through hydrogen-bonding (H-bonding). Image adapted from references [63,66,70].

Moving from nano- to macroscale, cellulose chains (composed of ≈36 individual cellulose molecules) are assembled to form elementary fibrils, which have nanoscale dimensions (≈1.5–3.5 nm in diameter) and are composed of highly ordered (crystalline) as well as disordered (amorphous-like) regions.[61,66] Usually the sizes of crystalline regions are in the order of 100–250 nm long and

3–10 nm wide, which can be isolated as individual crystallites.[71] Elementary cellulose fibrils, defined as the universal structural unit of natural cellulose fiber, are further packed into reasonably oriented microfibrils (micro/nanofibrillated cellulose – MFC/NFC) with a diameter larger than 15 nm and length of several micrometers, which then aggregate into macrofibrils, composed of thousands of microfibril bundles.[66] Cell walls of wood are composed of cellulose macrofibers, typically combined with lignin, hemicellulose, pectins, and water, thus forming a naturally occurring cellulose fiber composite.[61,66,71,72]

1.2.1.2. *Isolation of nanocellulose and its properties*

Taking advantage of the hierarchical structure of wood, the optical, mechanical, and morphological properties of cellulose paper are tuned through morphological engineering of cellulose fibers.[71] Therefore, appropriate processing strategies are needed to isolate and make use of the microfibrils and sub-microfibrils.

Two types of native cellulose nanomaterials, commonly referred to as nanocellulose, can be extracted from cellulose fibers. Acid hydrolysis is commonly used to isolate the cellulose crystallites through the selective degradation of the amorphous regions, producing rod-like CNCs with high crystallinity (≈90 %) and excellent mechanical properties at the cost of low yields (<30 %).[71,73] On the other hand, NFCs can be isolated from wood pulp by breaking the interfibril hydrogen-bonding, through intensive mechanical disintegration assisted by additional chemical and/or enzymatic treatments to reduce the energy demand during defibrillation, thus preserving both disordered and crystalline regions.[66]

Contrarily to the conventional top-down approaches used to isolate CNCs and NFCs from wood pulps, bacterial cellulose (BC) can be obtained by a bottom-up approach based on its natural production from bacteria species, thus producing highly pure cellulose hydrogels (nanofiber network structure composed of almost 99 % of water) with remarkable thermal and mechanical stability.[13,60,74]

A summary of the main features and respective differences of each type of nanocellulose is provided in **Table 1.1**.

Table 1.1. Comparison of different types of nanocellulose (CNCs, NFCs, BC).[13,60,75]

Type of nanocellulose	Length [nm]	Width [nm]	DP	Young's modulus [GPa]	Tensile strength [GPa]	Mass density [g cm^{-3}]	Crystallinity degree [%][a)]
CNCs	100–300	5–70	500–15000	20–50	9	1.5–1.6	54–88
NFCs	100–2000	4–100	≥500	0.5–10	0.1–1	1.3–1.4	59–64
BC	Various types of nanofiber networks	20–140	4000–10000	79–88	21	1.1	65–79

[a)] This parameter differs significantly depending on the technique and calculation method adopted.

Nanocellulose can be dispersed in a solution and then used as rheological modifiers in the formulations of inks, reinforcing materials in composites, and also to produce substrates (referred to as “nanopaper”).[76] In contrast to traditional paper, which is made from loosely packed microscale cellulose fibers, nanopaper is composed of densely packed nanoscale crystals or fibrils, thus featuring a unique set of properties. It exhibits nanoscale smoothness (≈5 nm), superior gas barrier resistance (pore size: 10-50 nm), higher tensile strength (200–400 MPa), larger Young’s modulus (7.4–14 GPa), greater transparency (≈90 %), and lower thermal expansion (12–28.5 ppm K^{-1}).[66,77] All these features trigger the interest of using nanopaper as an intrinsically insulating, flexible, lightweight and transparent substrate for R2R printed electronics and transparent electronic applications.[13,61,66,77,78]

The application of cellulose-based (nano)paper substrates in printed electronics will receive more attention in **section 1.2.2**.

1.2.1.3. Regenerated cellulose materials from aqueous alkali hydroxide-based dissolution solvent systems

Processing native cellulose though dissolution is a challenging issue, as a result of the rigid long-chain and strong inter-molecular and intra-molecular hydrogen-bonded structure of cellulose that hinders its solubility in water or common organic solvents.[12,79–81] For this reason, cellulose is usually chemically converted into derivatives, such as carboxymethyl cellulose (CMC), methyl cellulose, hydroxypropyl cellulose, hydroxypropylmethyl cellulose, ethyl cellulose (EC), among others, which can be used as thickener, binding agents, emulsifiers, film formers, suspension aids, surfactants, lubricants and stabilizers.[14,19,82]

Several kinds of multi-component solvent systems have been developed to prepare new regenerated cellulose materials, through dissolution, shaping and regeneration processes. These solvents are generally based on dissolved salts in either organic or aqueous solutions, such as lithium chloride/N,N-dimethylacetamide, N-methylmorpholine-N-oxide monohydrate (NMMO)/H_2O (used in “Lyocell” process), sodium hydroxide (NaOH)/carbon disulfide (CS_2) (used in “viscose” process), and ionic liquids.[14] However, these dissolution systems are limited to laboratory scale applications due to volatility, toxicity and high cost.[68,69,83]

Alternatively, a simple and rapid route based on inexpensive and less toxic solvent systems for cotton linter dissolution at low temperature was successfully developed, obtaining cellulose hydrogels without producing any hazardous byproducts.[84] This approach consists of dissolution of cellulose in aqueous alkali hydroxide solvent systems, such as NaOH/urea,[85–89] NaOH/thiourea,[83] NaOH/urea/thiourea,[83] NaOH/ polyethylene glycol (PEG),[90] NaOH/urea/zinc salts,[91–96] and lithium hydroxide (LiOH)/urea,[85,87,88,97,98] when pre-cooled to temperatures between -8 and -12 °C.

The mechanisms involved in cellulose dissolution using aqueous alkali hydroxide solvent systems are still poorly understood and efforts have been made toward its interpretation. The most accepted mechanism is the inclusion complex (IC) model,[84,87,89,97,98] which proposes that the dissolution of cellulose is only promoted at low temperatures since it plays a key role in the creation of stable hydrogen-bonded networks between cellulose, alkali hydroxide, urea, and water (**Figure**

1.4). Moreover, the surface of the alkali hydroxide hydrogen-bonded cellulose is surrounded with urea hydrates to form a stable IC. The urea channel IC aids in the reduction of the entanglement and self-association of the cellulose chains, which in turn leads to the rapid dissolution of cellulose, forming transparent solutions.[87,97] Owing to the relatively small ionic radius and high charge density of lithium ions (Li^+), they have the ability to penetrate easier into the cellulose chain than sodium ions (Na^+), thus presenting a superior dissolution power.[84,87]

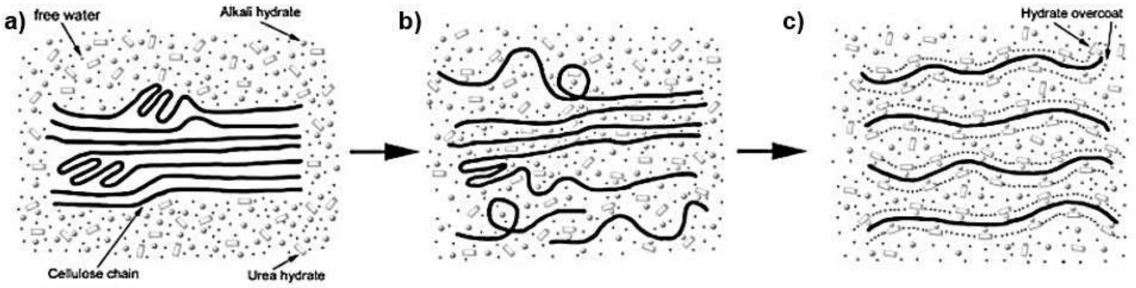

Figure 1.4. Schematic of the dissolution process of cellulose in aqueous alkali hydroxide/urea solutions at low-temperature: **a)** cellulose bundle; **b)** swollen cellulose; **c)** formation of a stable IC (transparent solution). Image obtained from reference [87].

Despite the superior efficiency of LiOH to dissolve cellulose compared to NaOH, some concerns arise regarding the use of lithium compounds as the global lithium consumption has increased exponentially over the last years driven by the high demand for lithium-ion batteries. In the long run, this will cause a huge stress in the environment from its extraction, which ultimately will dictate a huge increase in its cost and the quest for searching alternatives for this material that is forecasted to became scarce.[99–101] This issue revived the research work in abundant alternatives to lithium, such as sodium, due to its low cost (ratio of costs for carbonate Li:Na = 100:3),[100] non-toxicity, high abundance (the sixth most abundant element in the Earth's crust) and chemical similarity with lithium. The reviews from the authorship of Andrés Yaksic,[99] K. Vignarooban,[100] Gebrekidan Gebresilassie Eshetu,[101] and respective co-workers, give relevant insights in this topic.

The addition of acidic solution, pure or aqueous alcohols, or acetone, or the application of elevated temperatures breaks the cellulose IC, thus exposing the hydroxyl groups of cellulose that in turn induces the self-aggregation of cellulose to form rapidly physical regenerated cellulose hydrogels.[81,89] While the dissolution of cellulose destroys its crystallinity, the regeneration process leads to the conversion of thermodynamically metastable cellulose I into cellulose II type crystal with anti-parallel arrangement, which is also characterized of being the most stable crystalline structure.[18,87,93]

1.2.1.4. Cellulose-based hydrogels: the potential of self-healing property

Considering the abundant charged hydrophilic functional groups, including hydroxyl, carboxyl, and aldehyde groups, in the polymer chain of cellulose materials, they can be used to prepare hydrogels through physical and/or chemical cross-linking.[14,18,19,74,102]

Hydrogel materials consists of cross-linked three-dimensional (3D) hydrophilic polymeric networks capable of absorbing large amounts of water (or biological fluids) and swelling in a reversible manner.[14,19,74,102,103] These materials have both wet and soft appearance and can exhibit fascinating properties, such as high-water absorption capacity, stretchability, moldability, stimuli-responsiveness, and self-healing.[19,102]

Hydrogels with healing functionality is of foremost interest to the next generation electronic devices, from sensors, artificial electronic skins, tissue engineering, soft robotics, solar cells, actuators, and energy devices to transistors,[102,104–121] as they can repair themselves in response to an external stimulus (e.g. light, heat, solvent, pH, or pressure).[102,104–109,111,113] Thus, they can regain mechanical and functional properties upon local damage, which leads to waste reduction by extending the lifetime of products, while avoiding failure of materials during use and even safety problems.

This property can be achieved by introducing reversible chemical bonds, such as dynamic covalent bonding (chemical cross-linking), non-covalent interactions (e.g. hydrogen bonding, ionic bonding, hydrophobic bonding, supramolecular interactions, molecular diffusion, and chain entanglement), or multi-mechanism interactions.[102,105–108,113] Physical cross-linking yields mechanically weaker hydrogels compared to those based on covalent bonding.[19]

Self-healable hydrogels with combined toughness and elasticity are difficult to achieve, which is strictly related to the degree of cross-linking and amount of water retained.[122] Heavily cross-linked hydrogels are relatively rigid and brittle, exhibiting poor elasticity, while high amounts of water retained into the hydrogels may lead to their loss of dimensional stability, thus collapsing and dissolving. Hybrid physical-chemical cross-linking (dual-network cross-linking) emerged as a promising approach to address this issue by combining strong irreversible covalent bonds with weak yet reversible physical interactions within the hydrogels, thus obtaining tough and soft hydrogels with self-healing property.[19,102,106,122,123] Contrarily to physically cross-linked hydrogels, dual cross-linked hydrogels usually are not able to fully self-recover due to the contribution of the non-reversible character of the covalent linkages.[105]

Interestingly, the charged functional groups promote ionic interactions with ionic species (e.g. alkali metal ions) which in combination with the large amount of absorbed water result into hydrogels with liquid-like ionic conductivity, while preserving their dimensional stability.[102] This property arises further interest to be explored in healable ionic conductive hydrogels as essential functional elements for transistors with low-voltage operation based on electrolyte-gating mechanism (electrolyte-gated transistors, EGTs), which constitutes the target application of this PhD work (**sections 4.1** and **7.1**).

1.2.2. Cellulose-based paper substrates for printed electronics

Micro/nanostructured paper stands out as an attractive eco-friendly substrate for hosting electronics. This ubiquitous fibrous material, mainly composed of cellulose, combines a unique formula of properties. It is affordable ($\approx 10^{-3}$ € m^{-2}), flexible, foldable, lightweight, biodegradable, and recyclable.[4,5,7,15] Furthermore, it is compatible with R2R manufacturing processes, enabling large-area applications at reduced cost, and it is available in several textures, compositions, and coatings (more than 10000 different types of paper available).[45,46,61]

The idea of adding "intelligence" to ubiquitous paper or "paper-like" substrates as a suitable low-cost, flexible and robust support for various printed applications, outside the traditional graphical art industry, is no longer a novelty.[15] A wide range of applications have been demonstrated on cellulose paper as a suitable platform for printed and handwritten electronics from memory devices,[124] chromogenic displays,[125–127] photovoltaics cells, and paper-based microfluidic devices[128] to transistors and integrated circuits.[33,129–133]

Handwriting techniques, such as pencil drawing[46] and pen-on-paper,[45] answer to the emerging trend of using truly inexpensive and easily accessible techniques to design and fabricate "on-demand" electronic components or devices in just a few minutes using nothing more than a sheet of common office paper. While pen-on-paper approach relies on the design of printable functional inks compatible with readily available writing accessories, such as brush pens, markers, fountains pens, or rollerball pens, pencil-on-paper approach consists of a solvent-free method that enables the deposition of environmentally friendly graphitic tracks.[61] In the latter case, the naturally rough and irregular surface of office paper is ideal for the exfoliation of graphite particles from pencil to the cellulose fibers through mechanical abrasion, leading to the deposition of resistive graphitic tracks on paper.[46] Thus, smooth substrates are not compatible with pencil-drawing. Due to their reasonable electrical conductivity, pencil-drawn graphitic tracks on paper can be applied as electrode for sensors and energy storage devices, or as an active channel layer in transistors.[134]

Concerning the use of inks, the large surface roughness, high absorption capacity, porosity and the presence of chemical impurities in conventional fibrous paper arises major obstacles when printing electronic devices, especially for those where smoothness is a key criterion to reduce interfacial defects between active layers towards better electrical performance, as in the case of transistors and integrated circuits.[5,15,130,135]

The hydrophilicity of cellulose fibers speeds up lateral spreading that is particularly large when printing inks with low viscosity and slow evaporation rate, which promotes the swelling of the paper substrate during the printing process, thus leading to low-resolution, and irregular/deformed printed features. Besides, porosity and surface roughness of paper impact ink penetration and printed film continuity, which can result in inhomogeneous films.

Calendering, planarization though the use of barrier coating layers prior to the printing process, or the use of intrinsically smooth, transparent and less permeable nanopaper or regenerated cellulose films (RCFs) are suitable strategies to enhance substrate properties for printability.[61,66,77,78,136,137] In opposition to the complex, time-consuming, energy-intensive, and thus very expensive procedures involved in the production of cellulose nanopaper, RCFs present lower energy consumption during fabrication and yields membranes with a smoother surface, as they are free of fibrous structures. However, the mechanical, optical, and thermal properties of RCFs are slightly poorer due to the presence of cellulose II.[64,76,77,137,138]

An additional strategy to minimize the adverse effects of conventional cellulose-based paper substrates consists of printing viscous inks, such as the ones compatible with screen-printing technique (description in **section 1.2.3.2**), since they enable the deposition of thicker films, while preventing the excessive spreading, bleed out and swelling of the cellulose fibers.[78]

Contrarily to all these apparent “limitations” of traditional paper substrates, their fibrous and porous structure can be advantageous to promote a faster drying of the ink and allow a better adhesion of the printed film, from mechanical influences, when compared to non-absorbent substrates, such as glass or plastic. Paper also presents some advantages over plastic substrates upon heating, as it exhibits lower coefficient expansion (<40 ppm K^{-1}), does not melt, and usually withstands temperatures above 150 ºC, although cellulose fibers start darkening and degrading for such temperatures.[139]

In alternative to conventional high-temperature thermal treatments performed to optimize the percolation pathway between the functional particles of the printed film, some annealing/sintering processes compatible with flexible substrates have been already reported, as further mentioned in **section 1.2.3.2**.

Last but not the least, although paper has been merely seen as a passive support, the reengineering of paper with new functionalities can arise the concept of multifunctionality in a single material, being used as a support with “active” role. In particular, the natural dielectric properties of cellulose paper can be further enhanced with the introduction of ionic species within cellulose matrix and/or through surface functionalization by adding extra charged hydrophilic functional groups (e.g. carboxyl groups).[51] These properties arise interest for application as a flexible ionic conductive substrate in electronics devices, such as EGTs, as latter discussed in **section 6.2**.

1.2.3. Printed electronics

1.2.3.1. The interest behind printed electronics

Electronics industry is longing to produce high-performance products with extremely short switching times and high integration densities using low-temperature, or preferentially, RT processes.[140] Currently, these products are fabricated on non-flexible substrates using standard Si-based microfabrication technologies, which require sophisticated, complex, wasteful, time and high energy consuming techniques, such as high-vacuum deposition techniques (e.g. evaporation, sputtering, and chemical vapor deposition) and subtractive patterning processes (e.g. photolithography, and etching).[11,141,142] Therefore, large-area scaling is challenging and expensive, and these processes are restricted to rigid substrates.

Considering the ever-expanding technological demands, printed electronics is attracting a great deal of attention due to its promise of low-cost, high-volume, high-throughput production of electronic components and devices on soft, flexible, bendable, and stretchable systems, enabling concepts such as flexible electronics, and more recently stretchable and soft electronics.[49] Printed electronics has been extensively reviewed by several authors.[11,15,48,49,55,56,61,139–158]

The core of printed electronics refers to additive manufacturing processes inspired by graphical art printing technologies that allow selective deposition over large-areas (in the kilometers scale) and the patterning of functional inks or pastes containing soluble and/or dispersed materials (e.g. inorganic, organic, and bio-inspired materials) with different functionalities in a variety of designs and configurations, usually at low temperatures.[11,49,142,146]

These factors lower the degree of process complexity, reduce chemical and energy consumption, and the printing processes are not limited to rigid nor conventional substrates. However, the criteria for printed electronics are far distinct from traditional graphic printing, as continuous and homogeneous patterns with controlled thickness, roughness, and high-printing resolution are required in the prior case to yield high-performance functions.

In line with the benefits offered by printed electronics technology, it has been successfully demonstrated in several applications, from passive components (e.g. resistors, capacitors, and inductors) to active electronic devices, such as flexible organic light-emitting diode (OLED)-based displays, radio-frequency identification (RFID) tags, energy harvesting and storage devices, actuators, sensors (e.g. light, humidity, temperature, gas, and mechanical deformations), transistors, and even circuits (**Figure 1.5**).[49,142,148,149,155,159] In particular, printing techniques offer great advantages for fabricating transistors and integrated circuits at temperatures below 200 °C, making them compatible with flexible substrates, such as plastic or paper.[150]

In the long run, various possible future applications of printed electronics can be forecasted, such as smart packaging, healthcare monitoring and diagnosis, electronic-textiles, dynamic walls and lighting panels, dynamic newspapers, security devices, among others. These applications will fuel the growth of global printed electronics market, which is projected to grow from $9.8 billion in 2019 to $19.8 billion by 2024 at a compound annual growth rate of 15.1 % according to MarketsandMarkets™, a market research agency.

Furthermore, this technology may usher in a new generation of electronic devices towards innovative concepts, such as DIY, where ordinary people without any skills or training can freely design, produce and use their own product, turning the idea of “everywhere, everyone, anytime” a reality. An additional concept is the IoT, where a variety of sensors, communication devices, and displays are integrated to connect everyday objects to the network.[150,160]

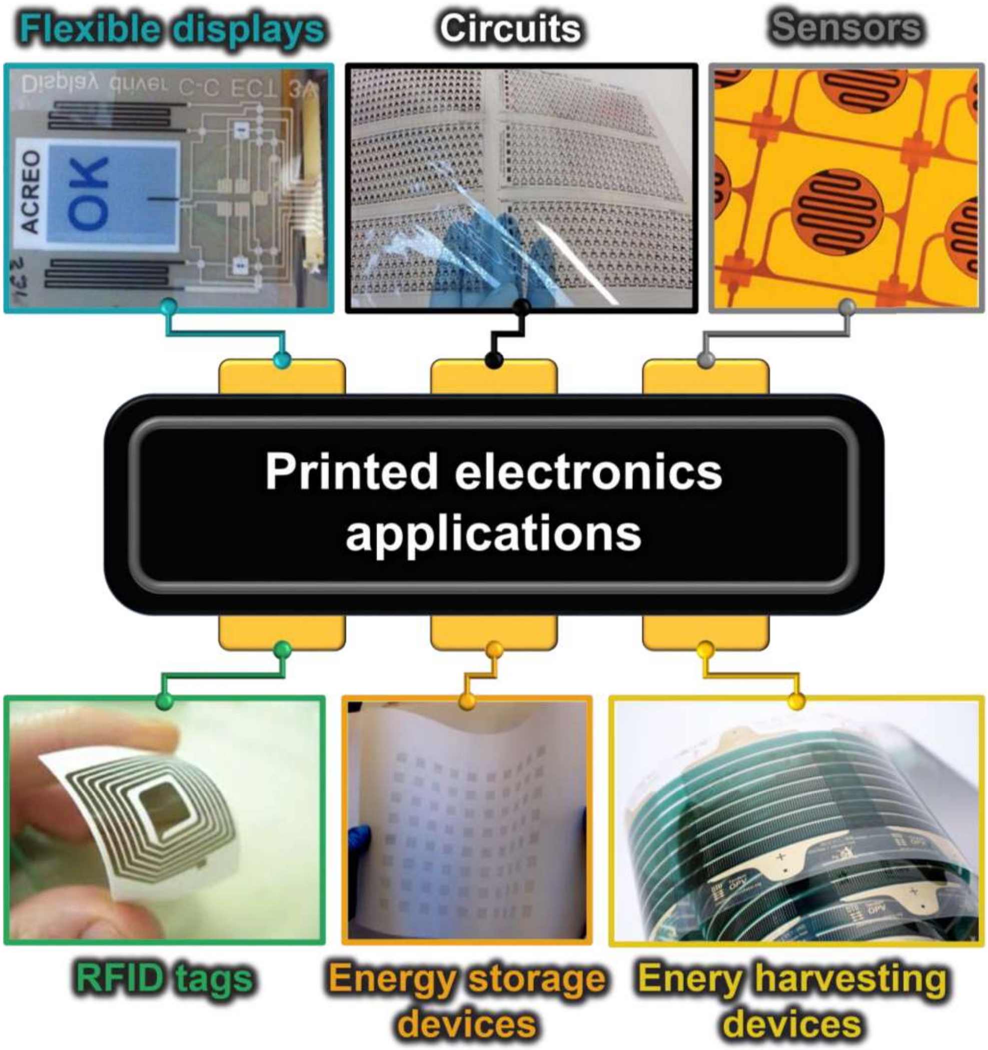

Figure 1.5. Overview of current applications of printed electronics. Adapted from references [161–166].

1.2.3.2. Printing “intelligence” on lifeless objects or surfaces

Printing process involves a sequence of tasks, starting with the selection of functional materials with the envisioned functionality, moving to the formulation of inks, and then selection of substrate (e.g. plastic, paper, textile, glass, and Si) and printing technique depending on the ink’s properties and intended features for the printed film.[143–145,151,156] Particular attention is paid to the most common printing techniques for deposition and patterning of solution-based materials, including screen-printing, which is the one in focus in this work. Finally, post-printing processes, usually thermal treatment, are performed to guarantee a functional layer and, consequently, provide the maximum performance of the resulting device.[11,144,167]

Inks’ formulation

In a similar way as the multiple layers that compose conventional devices, typically consisting of electrical conductors, dielectric materials, and semiconducting materials, distinct functional inks are needed to display such functions. Therefore, the development of stable, low-cost, non-toxic, and environmentally friendly printable inks with desired printability is crucial to deposit and pattern these materials onto a substrate to enable the production of a new class of devices that are extremely lightweight, affordable, readily customizable, thin, flexible, and disposable.[143]

Printable inks consist of a mixture of functional materials, binders, additives and solvents, which impact their viscosity, rheology, evaporation rate, and surface tension.[143,156]

An endless list of functional materials, from conductive polymers, ionic liquids, and carbon nanostructures to metallic nanoparticles (NPs), and metal oxide nanostructures can be used to formulate these inks (**Figure 1.6**).[143,144,151] Polymers for use as planarization or passivation layers can also be needed.[78,141] From this broad list, TMOSs, such as zinc oxide (ZnO), assume a particular interest in this work as the functional material for the development of printable TMOS inks compatible with flexible substrates for application in transistors and integrated circuits (**sections 1.2.4** and **6.2**).

The mixture of organic binder (e.g. acrylics, alkyds, rubber resins, and cellulose derivatives), additive (e.g. humectants, surfactants, and wetting agents) and solvent (e.g. water, and organic solvents) displays an important role in ink design.[143,156] This mixture promotes wetting of the functional material, dispersion stability, film formation, adhesion to the substrate, and regulates ink drying during and after printing, thus affecting the strength, density, and inner structure of the printed film. Hence, a proper selection of these components is needed to formulate an ink with suitable properties for the intended printing process, and depends on the target substrate, the drying conditions, and the final purpose of the printed films. Regarding the solvents, there is an increasing interest in the development of water-based inks, since water is a non-toxic, cheap and an environmentally friendly solvent.[144]

Printing techniques: screen-printing

A variety of printing techniques have been explored for the manufacturing of electrical components and devices, such as inkjet, aerosol-jet, gravure, flexographic, flatbed screen-printing, and rotary screen-printing (**Figure 1.6**). The selection of the printing technique depends on the required printing resolution, fabrication throughput, homogeneity, minimum layer thickness, ink characteristics (e.g. viscosity, rheological behavior, size and dispersion of the particles), and surface and mechanical properties of the substrate.[15,141,143,145,148]. A comparison of various printing techniques is displayed in **Table 1.2**.

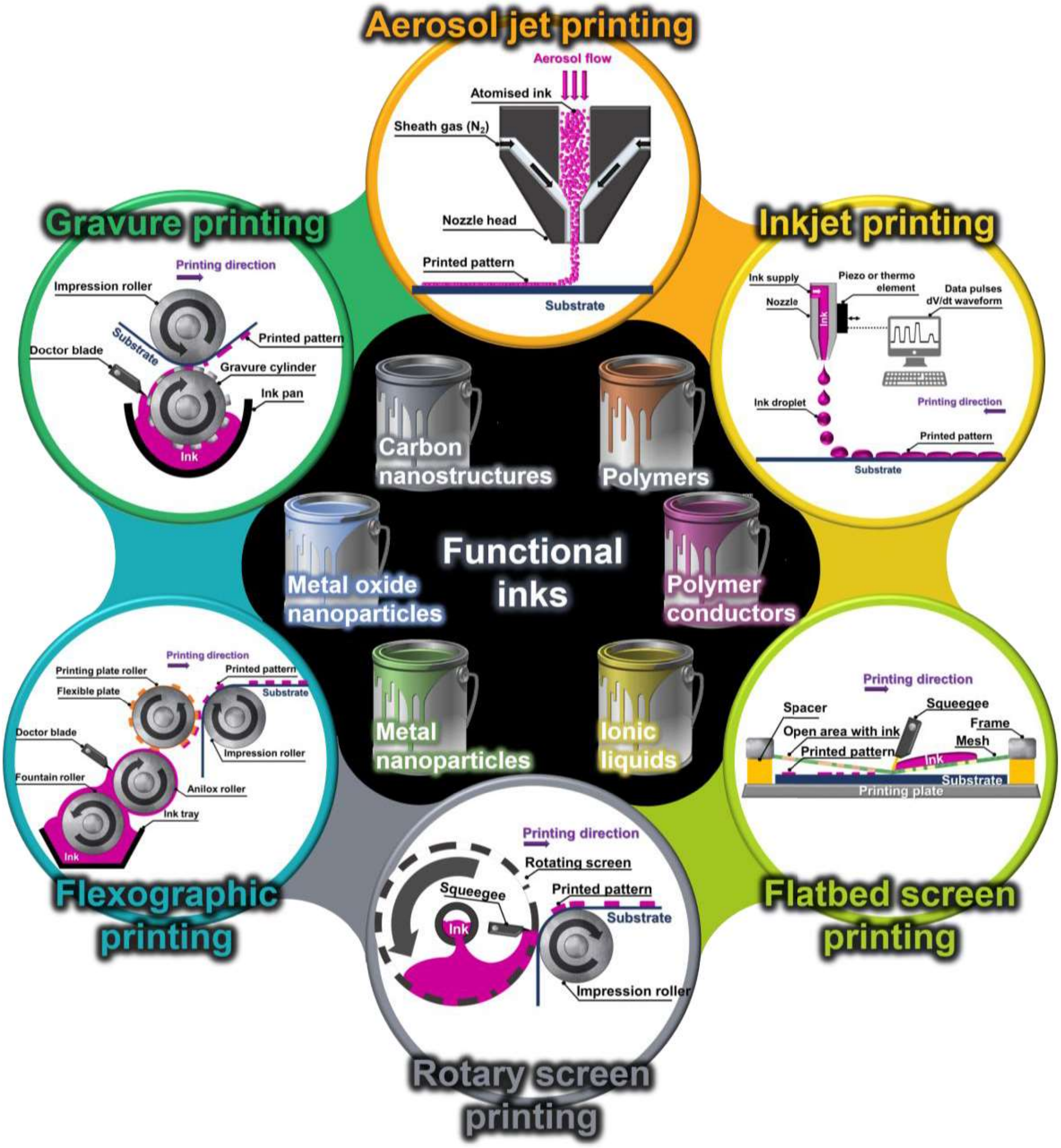

Figure 1.6. Schematic illustration of the most common printing techniques and typical functional materials used in inks' formulation.

Table 1.2. Comparison of the features of most common printing techniques and inks requirements. Adapted from references [11,15,49,139,141–143,145,147–149,168].

Printing technique	Surface tension (mN m^{-1})	Viscosity (Pa s)	Resolution (µm)	Thickness (µm)	Throughput (m^2 s^{-1})	Speed (m min^{-1})
Inkjet	15–50	0.001–0.1	10–100	0.01–20	0.01–0.5	0.02–500
Offset	-	5–100	20–50	0.5–10	3–30	0.6–1000
Gravure	25–45	0.01–1.1	20–200	0.01–12	3–60	0.3–1000
Flexography	10–30	0.01–2	30–80	0.005–8	3–30	5–500
Screen	35–50	0.03-50	30–100	0.015–100	2–3	0.6–150
Aerosol jet	-	0.001–2.5	10–250	0.01–5	<1	0.006–0.6

Of existing printing methods, screen-printing is widely used in printed electronics due to its simple operation, ease of prototyping, no need of complex equipment, fast printing speed (150 m min^{-1}), compatibility with substrates with tailored textures, and versatility of pattern designs (resolution around 30–100 µm). This technique is often used as a flat printing technique in batch processes, and it is also scalable to industrial level and suitable for high-volume R2R fabrication using rotary screen-printer for continuous processing, where the printing roller, substrate and impression roller move synchronously.[15,139,140]

In terms of functional materials, screen-printing is already used commercially for printing conducting layers and dielectric materials. For instance, Hyun et al.[129] reported the design and screen-printing of highly viscous pristine graphene inks compatible with glassine paper substrates. Instead of conventional thermal treatment at high temperatures (250–300 ºC) needed to decompose the stabilizer and achieve better electrical properties, which cause significant degradation of the paper substrate, the screen-printed graphene patterns were photothermally annealed. This low-temperature annealing treatment is quick (<1 ms), promotes localized heat generation on graphene patterns without degrading the underlying substrate, yielding graphene electrodes with a minimum width of 58 µm and an average electrical conductivity of 2.35×10^3 S m^{-1}. Besides the screen-printed graphene flakes withstand several cycles of folding deformations without peeling from the substrate and remains functional, and their electrical properties are suitable to explore as electrodes of transistors.

Though little effort has been made on screen-printing semiconductors for application on flexible transistors and integrated circuitry. The reason relies on the required printing resolution in electronics, which far exceeds the ones that screen-printing allows.[56] Up to date, mostly of the screen-printed semiconductors already reported rely on organic semiconductors, such as poly(3,4-ethylenedioxythiophene) polystyrene sulfonate (PEDOT:PSS), due to their low-temperature processing. [169–171]

Regarding the printing process, the functional ink is spread over the screen mask, and then a pattern is transferred to a substrate by pressing and moving forward the ink/paste with a squeegee (rubber or plastic blade) through a woven mesh (screen) or patterned stencil with open areas that define the design of the pattern. In rotary screen-printing, the rotating printing roller is equipped with a fixed squeegee and a mask, and it is loaded with the ink in the inner part to minimize exposure to the surrounding environment.

The screen mask is usually based on woven from threads that are made of several yarns twisted closely together, most frequently composed of polyester, although silk, nylon and metal nets are also used. The pores of the mesh are selectively blocked-up with a photo-polymerized emulsion that define the non-printing areas, whilst the open pores allow the ink to pass through mesh to define the intended pattern. Nevertheless, screen fabrics have some limitations to yield high-resolution screen-printed patterns, due to the poor lithography resolution of the photochemically defined emulsion coated on the screen mesh. Besides, the particles tend to form agglomerates that may clog the fine-mesh fabric openings, and the mesh thread tends to block the extremely thin openings.

In alternative, highly defined, non-woven, flexible, and smooth Si stencil (≈90 µm thick) with line openings as narrow as 5 µm, which are obtained by a photolithography process, have also been reported for superior resolutions.[172,173] Si stencils are prepared through photolithography to define the pattern, and wet etching process is performed to make the Si wafer thinner, and thus flexible enough to withstand the screen-printing process, while it thinner size facilitates the direct transfer of the ink from the stencil to the target substrate. Screen-printed conductive graphene, and silver patterns on PI substrate with a resolution of 40 and 22 µm, respectively, were successfully obtained using this approach.

The inks (also known as pastes) suitable for screen-printing exhibit “honey-like” viscosity (0.03–50 Pa s) and shear thinning thixotropic behavior (i.e. the viscosity of the ink decreases as the shear rate increases).[174–176] Before applying the squeegee, these inks must possess a high viscosity to remain on the screen mask without leaking through the permeable areas. Pressing and moving the squeegee across the ink promotes an increase in the shear rate and, consequently, a decrease in viscosity, thus allowing the ink to pass through the openings of the screen mask towards the substrate. After removing the stress or shear stress, the viscosity of the ink is gradually recovered overtime towards its initial value to allow the ink levelling and filling of the irregularities and voids of the substrate.[174–176]

Besides the properties of the ink and substrate, the printing resolution, thickness and functionality/performance of the screen-printed films are also affected by the features of the screen mask and printing conditions (e.g. pressure, angle, and the speed of the squeegee in respect to the screen mask during ink deposition, gap between screen mask and substrate).[5,15,175]

Ink-substrate interactions

One of the most important aspects during printing is related to the ability of the ink to wet, spread, and adhere to the surface of the substrate to enable the creation of smooth and continuous films with good resolution and performance. Therefore, when selecting a substrate for a given application, it is critical to consider its chemical endurance to solvents from the ink, roughness, surface energy, absorption capacity, and porosity, since such features have a substantial effect on ink characteristics during printing.[15,78] The surface tension of the ink must generally be lower (nearly 7–10 mN m^{-1} inferior)[143] than the surface energy of the substrate to ensure a good wettability and adhesion of the ink. Nevertheless, in the case of flexible, non-absorbing, and smooth plastic substrates, such as polyethylene terephthalate (PET), polyethylene naphthalate (PEN), polycarbonate (PC), and polyimide (PI), their low surface energy is challenging for printing, showing poor wettability in the case of water-based inks.

The interaction of the ink with the surface of the substrate can be improved by adding additives in the ink composition to lower its surface tension or by performing surface treatments on the substrate prior printing, such as surface plasma, or ultraviolet (UV) irradiation, to increase the surface energy of the substrate. The latter approach changes temporary the surface energy of the substrate by creating functional groups on its surface, yet it implies an extra step in the manufacturing process, thus increasing the time and cost of production.

Post-printing processes

After printing and deposition of the inks, post-printing procedures, such as drying, curing, annealing, and sintering, are performed to define the final morphology, uniformity, and functionality of the printed pattern. Drying and/or curing are needed to evaporate the solvents, and induce cross-linking of the binder, respectively. On the other hand, annealing or sintering process of the printed film is usually necessary, especially in the case of inorganic materials, to eradicate organic insulating components between the particles, such as organic binders and additives, that hinder an efficient percolation pathway, or to chemically convert the deposited precursor into the active material. The sintering treatment induces the merging and bounding between adjacent nanoparticles in the printed film.

A criterion for obtaining the desired functionality is the formation of direct contact between the particles in the printed pattern, which can be easily achieved by thermal decomposition of the organic insulating components at high temperatures, typically performed above 150 ºC.[15] Thus, it is of extreme relevance that the substrates possess dimensional and thermal stability during thermal treatment.[139] However, such thermal procedures are not compatible with flexible substrates, like paper or plastic, as the high temperatures required for the annealing/sintering process would deform, melt or burn flexible substrates. The low glass transition temperature or high thermal expansion coefficient limit the maximum process temperature of plastics usually to temperatures lower than 120 ºC.[139] High thermal expansion coefficient is an undesirable feature as it promotes the straining and cracking of the deposited layers. On the other hand, paper substrates present some advantages over plastic substrates upon heating, as they exhibit lower coefficient expansion, do not melt, and paper can still withstand temperatures above 150 ºC, although cellulose fibers start darkening and degrading for such temperatures.

Some annealing/sintering processes compatible with flexible substrates have been already reported, which involve the use of chemical agents (RT sintering), argon, plasma, microwaves, electrical voltage, or light sources (e.g. infrared, UV, laser, or flash lamps). Besides, combined annealing/sintering processes (e.g. thermal annealing/sintering and low wavelength far-UV irradiation) can be used to further enhance the degradation of organic residuals and improve densification without deteriorating the substrate.[15,148,158,177–179]

1.2.3.3. Challenges hampering printed electronics

Despite the compelling concept behind printed electronics, which progresses go hand-in-hand with flexible, conformable, and stretchable electronics, many challenges have hindered its development from a dormant idea to a thriving technology. The limited resolution, lower alignment precision, reduced lifetime, need for encapsulation with coatings or barrier layers to protect the device from environmental conditions, and both thermal and chemical sensitivity of the substrates during or after printing of inorganic materials leads to poorer performances compared to conventional Si-based technologies.[49,140,141] Therefore, in a first stage, printing technologies are not expected to be used as alternatives to conventional Si-based technologies, but as a complementary technology, and an entirely new market and industry.

As further discussed in **section 1.2.4**, in the case of transistors and integrated circuitry, which constitute the focus applications of this PhD thesis, the printing of TMOS transistors on flexible substrates is far to be a simple process as TMOS materials usually require high annealing temperatures (>350 ºC), which do not meet the thermal budget requirements of most flexible substrates. Besides, short-channel lengths and gate-to-contact overlaps with submicrometric dimensions to obtain high-speed circuits that operate at high frequencies in the GHz range are difficult to reach using printing techniques.[141,160,180]

Further advances in inks' design and processing as well as the development of both high-resolution printing techniques, capable of higher resolution, registration and uniformity, and alternative sintering procedures compatible with heat-sensitive substrates are vital to address such challenges to obtain “high-end” products, as projected by Guohua Hu et al. in 2018.[49,143]

1.2.4. Printing TMOS materials for flexible electronics

1.2.4.1. TMOSs vs. organic materials

Low-voltage, printed transistors and logic operations based on TMOSs with high performance on flexible substrates, such as paper, have eluded scientists up to date. Organic semiconductors, mostly relying in p-type semiconductors, have been the primary choice as channel of printed transistors owing to their mechanical flexibility, and easy solution processability and printability under less controlled environments than inorganic semiconductors, making them attractive for low-cost printed electronics.[47–51] Nevertheless, organic FETs (OFETs) still exhibit poor environmental stability, low field-effect mobility values (<10 $cm^2\ V^{-1}\ s^{-1}$), although higher than the ones obtained with amorphous Si transistors (<1 $cm^2\ V^{-1}\ s^{-1}$).[181–183] Besides, there is a lack of n-type organic semiconductors and their mobility is lower compared to p-type organic semiconductors (<0.1 $cm^2\ V^{-1}\ s^{-1}$).[52] The charge transport in organic semiconductors is poorer than inorganic semiconductors due to their weak intermolecular interaction based on secondary bonds (e.g. the van der Waals force), whilst the latter is based on stronger and shorter primary bonds, such as ionic and/or covalent bonds.[183]

On the other hand, the superior electrical properties, and both greater thermal and environmental stability of TMOSs, usually electron conducting (n-type), make them better candidates for high-performance electronic devices, despite their limited mechanical strain tolerance, and higher processing temperature.[52–54] Still, their performance is inferior compared to vacuum-processed inorganic-based devices counterparts due to the low film density with many defects and the presence of organic impurities from incomplete metal-oxide formation or non-conducting stabilizers shielding TMOS particles.[158,184] In a similar way as organic semiconductors, p-type TMOS transistors still display poorer electrical performance and stability, which is an issue for practical CMOS applications, where n- and p-type TMOSs are integrated into circuits.[185,186] Thus, one way to alleviate the problems from both categories of semiconductor materials to get functional CMOS would be the combination of n-type TMOSs with p-type organic semiconductors.

1.2.4.2. Strategies to formulate printable TMOS-based inks

Typically, printed TMOS transistors are fabricated by printing metal salt precursors (e.g. acetates, hydroxides, chlorides, and/or nitrates), as this strategy produces multi-compositional, homogeneous, and high-quality films.[11,154] Nevertheless, this method requires high-processing temperatures (>350 ºC) to activate semiconducting properties by burning-off the organic components, such as organic solvents, binders and/or additives, while chemically converting *in-situ* the precursor into metal-oxide-metal bonds, thus obtaining a high-quality TMOS.[154] Consequently, this approach limits the choice of substrates to rigid, heat-resistant substrates, such as Si or glass.[15,52,55]

Laser annealing,[187,188] far-UV annealing,[178,189] and microwave-assisted annealing[190] can be used in alternative to thermal treatment or combined to lower the processing temperature. Further strategies can be implemented to lower the processing temperature, such as doping of TMOS precursors (e.g. zirconium,[191] aluminum,[192] hafnium,[193] fluorine,[194] or metal alkali ions[194–196]), performing vertical diffusion technique,[184] controlling pH of solutions,[197] or changing conventional silica (SiO_2) dielectric oxide for high-k oxide dielectrics, polymer dielectrics, self-assembled monolayer dielectrics, organic-inorganic hybrid dielectric materials, or high-capacitance electrolytes.[198,199] An additional low-temperature processing strategy consists of using TMOS particles instead of precursors, which is the strategy selected to use throughout this thesis.

Since the synthesis of TMOS nanostructures and film deposition can be separated from each other, high temperatures can be applied during the synthesis to ensure the intended semiconducting functionality, while deposition is achieved at lower.[200] Therefore, synthesized TMOS nanostructures can be dispersed in a printable ink yielding a ready-to-use functional semiconductor layer after printing and annealing at low temperature (<250 ºC), which is a criterion for the use of flexible substrates.[11,56–58] However, smooth interface roughness between the nanoparticulate transistor channel and gate insulator is difficult to achieve due to the intrinsic morphology of the particles and their tendency to form agglomerates.[52] Therefore, small-sized nanoparticles are preferred to ensure smoother interface roughness to avoid the creation of charge traps responsible for the inhibition of charge transfer from drain to source.[52] Besides, stabilizers are usually needed to get stable nanoparticle dispersion, which remain in the printed layer after drying as a barrier that partially blocks the direct contact between oxide particles.[53] The semi-insulating nature of the stabilizer also hinders the electronic transport, thus compromising the device performance considerably. For these reasons, their performance is usually poorer compared to precursor-derived transistors.[11]

Better electrical performances can be achieved by blending TMOS precursors with nanostructures to aid in the film formation. This promotes the enhancement of the packing and percolation of the particles within a continuous dual-phase layer that displays superior performance to those obtained using these strategies individually.[58,201]

1.2.4.3. State-of-the-art of printed TMOS materials on transistors

General considerations

Several exceptional reviews on printed TMOSs and their application in transistors have been provided recently.[141,148,167,202] As shown in **Figure 1.7** (see **Table S1** and **Table S2** for more details), a variety of printed binary, ternary, and quaternary TMOSs have been studied, such as ZnO,[57,58,132,203–209] zinc tin oxide (ZTO),[210–214] indium gallium zinc oxide (IGZO),[187,188,215–220] indium gallium tin oxide (IZTO),[221,222] indium zinc oxide (IZO),[223–226] indium gallium oxide (IGO),[227] indium tin oxide (ITO),[52] indium oxide (In_2O_3),[53,54,178,189,228–239] and tin oxide (SnO_2).[240] Rare examples of transistors based on p-type TMOSs can be found in the literature, such as nickel oxide (NiO),[241] cupric oxide or tenorite (CuO),[54,190] and cuprous oxide or cuprite (Cu_2O).[230]

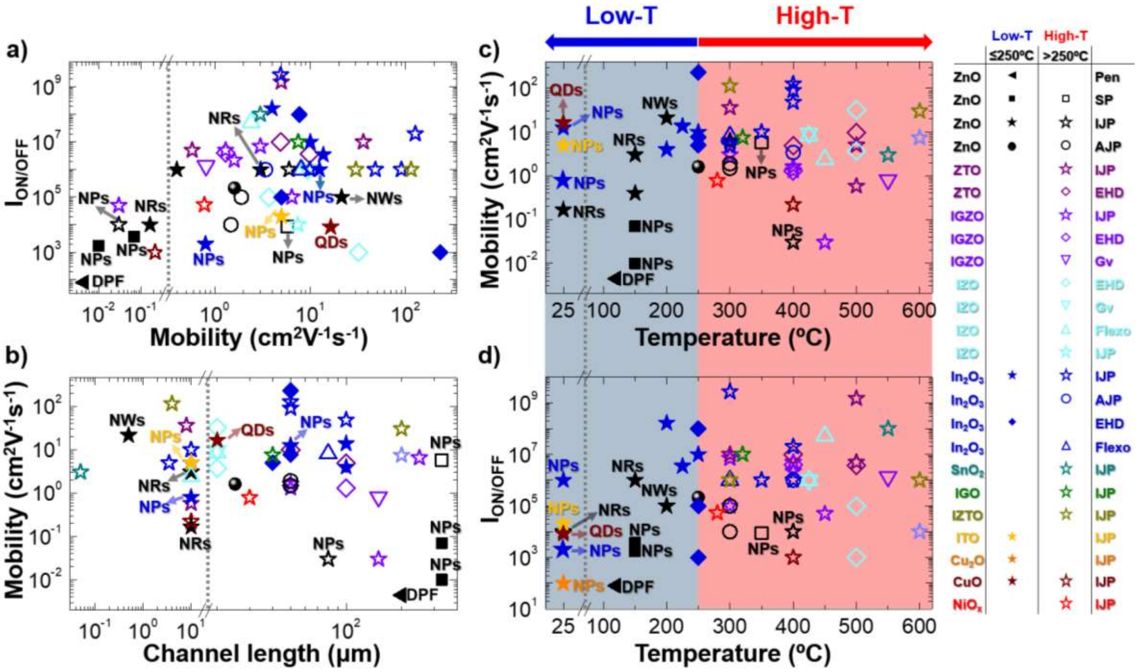

Figure 1.7. Graphical summary of several literature reports related with the topic of printed TMOS transistors, showing typical device's performance for different kinds of TMOS materials using different printing techniques and thermal treatments. **a)** Variation of $I_{ON/OFF}$ and mobility. **b)** Influence of channel length in mobility. Influence of thermal treatment after printing in **c)** mobility and **d)** $I_{ON/OFF}$. A distinction between low-temperature (Low-T) and high-temperature (High-T) post-printing processes is presented in the graphs to correlate their potential compatibility with heat-sensitive substrates. SP, IJP, AJP, EHD, Gv, Flexo, DPF, QDs, NPs, NWs, NRs stand for screen-printing, inkjet-printing, aerosol-jet printing, electrohydrodynamic jet printing, gravure printing, flexographic printing, dual-phase film (metal salt precursor combined with TMOS nanostructures), quantum-dots, nanoparticles, nanowires, and nanorods, respectively. Data taken from references [52–54,57,58,132,178,187,189,190,203–242]

In a transistor, there are two key device performance parameters, such as carrier mobility and on-off current ratio ($I_{ON/OFF}$), that heavily depend on the semiconductor material as well as transistor's design and must be maximized. Additionally, transistors with both high mobility and electrical modulation as well as short channel lengths are desired to display fast dynamic response when integrated in circuits comprising several interconnected transistors.[141] Therefore, these parameters are used as a means to get a fair comparison of the impact of the TMOS material on the electrical performance of the transistors, also considering the printing technique, temperature of the thermal annealing performed after printing of the semiconductor, and channel length of the transistors.

A big share of these works is still devoted to printed TMOS transistors on rigid substrates, such as Si wafer or glass, and inkjet printing stands out as the preferred printing technique to fabricate such devices. The attractiveness behind this digital printing technique is related to low material waste, the ability to print complex patterns with high-resolution, and compatibility with a variety of functional inks (either precursors or nanoparticulate inks).[243,244]

Some efforts have been made these devices fabricated onto plastic substrates, such as PEN[53,188,189] or PI[132,178,234,238]. Despite some advantages offered by paper or "paper-like" substrates over plastics, such as recyclability, lower cost, and lower thermal expansion, which is also a determining factor to define a uniform pattern, little progress has been made on these hosting materials using printing technology, specially implementing TMOS functional materials.

Interesting works were reported in the field of solution-processed or printed organic transistors on paper.[51,129,131,135,245,246] Bollström et al.[245] developed a recyclable, smooth, multilayer-coated paper-based substrate with good barrier properties suitable for printed functional devices. Later in 2013, the same author reported inkjet-printed organic poly(3-hexylthiophene) (commonly known as P3HT) semiconductor thin-film transistors (TFTs) on smoothed, multilayer curtain coated paper substrates.[135] The fabricated fully printed organic TFTs (OTFTs) gated by poly(4-vinylphenol) (PVP) dielectric displayed a mobility approaching 0.1 $cm^2V^{-1}s^{-1}$ and $I_{ON/OFF}$ of 3.2×10^4 at low-voltages (<2 V). Hyun et al.[129] demonstrated all-printed, in-plane, foldable organic EGTs on untreated, glassine paper substrates manufactured by supercalendering. The photonically annealed graphene electrodes, P3HT semiconducting channel, and ion-gel gate dielectric were printed using several printing techniques, such as screen-printing, aerosol-jet printing, and inkjet-printing, respectively. The paper-based organic EGTs show an $I_{ON/OFF}$ and mobility of 2.9×10^3 and 0.14 $cm^2V^{-1}s^{-1}$, respectively, and withstand at least 100 folding cycles without losing performance, due to the mechanical endurance of the graphene electrodes, intrinsic flexibility of the organic semiconductors, and the deformable nature of the ion-gel.

Beyond organic semiconductor materials, fully screen-printed nanoparticulate Si-based FETs were already demonstrated on paper, with no additional post-printing steps, where Si micro- and nanoparticles were obtained by mechanical milling of bulk n-type Si wafers.[247] Nevertheless, such devices still exhibit a poor electrical performance in comparison with OFETs, yet similar to amorphous Si-based devices, showing small electrical modulation (≈2000) and low mobilities (≈0.5 cm^2 V^{-1} s^{-1}).

Furthermore, the interconnect, gate, source, and drain electrodes of printed TMOSs transistors are often vacuum-deposited and patterned with photolithography to obtain short and well-defined channel lengths (<100 µm), targeting superior electrical performances. Only a few exceptions of fully printed transistors were reported to date on Si wafer,[209,218,232] glass,[203,227] including the recent developments made in our research group,[57,58] and the contribution of this PhD work, where (nano)paper-based materials and free-standing ionic conductive cellulose-based composites are used as suitable substrates to host transistors and circuits (see **chapter 5**).

Contrarily to typical photolithographic methods, downscaling of channel length towards submicron scale dimensions using standard printing techniques constitutes a critical challenge that remains to be solved. Thus, the switching speeds is usually limited to 1–100 Hz.[243,248] Strategies for printing submicrometric channel lengths were demonstrated using self-aligned inkjet printing (SAP), yielding devices with high frequency operation up to 18.21 GHz,[203,248,249] which is comparable to CMOS fabricated devices.[142] Baby et al.,[240] reported transistors with nanometric channel lengths based on an inkjet-printed TMOS channel layer sandwiched between two vertically overlapped source-drain electrodes. In this case, the thickness of the printed semiconductor below 50 nm defines the channel length, which is at least two orders of magnitude smaller than conventional inkjet-printing process. Although the dynamic response was not assessed in this publication, it is possible to predict their operation at high frequencies in the GHz range as those prepared using SAP process.

Printed ZnO transistors

From all the materials listed in **Figure 1.7**, In_2O_3 has been one of the benchmark n-type semiconducting materials in these studies.[53,54,178,189,228–239] The highest mobility value achieved to date of 230 cm^2 V^{-1} s^{-1} was obtained for printed TMOS transistors processed at low-temperatures (≈250 ºC) on Si using electrohydrodynamic jet printing (EHD) to define In_2O_3 channel layer and spun-coated high-k dielectrics.[238]

Regardless the superior performance observed in printed In_2O_3 transistors compared to other TMOS materials, its high-cost and rarity arises economic and environmental issues. In alternative, ZnO is another well-explored n-type oxide semiconductor, due to its tendency to form oxygen vacancies and/or zinc interstitials, with a direct wide bandgap (3.2–3.4 eV) and large exciton binding energy (60 meV) at RT.[11]

A variety of synthetic techniques, from chemical, physical to biological methods, have been used for the synthesis of ZnO nanostructures with tailored sizes and morphologies, such as nanorods (NRs), quantum dots (QDs), nanoplates, nanoneedles, nanotubes, nanoflowers, nanobelts, and nanowires (NWs).[250–253] Besides, its low-temperature processability (<300 ºC), chemical and thermal stability, abundant availability, non-toxic nature, among several other features, which were discussed in detail in recent reviews,[250,253–258] have encouraged its investigation.

Several reports on printed ZnO transistors using different printing techniques, from screen-printing,[57] inkjet-printing,[203–206] nozzle-jet printing,[207] aerosol-jet printing[132,208,209] to simple approaches, such as pen-writing[58] towards personal fabrication, are available in the literature. Field-effect mobilities of up to 21.3 cm^2 V^{-1} s^{-1} at a maximum processing temperature of 200 ºC were demonstrated for inkjet-printed ZnO NWs on glass. Other nanosized ZnO nanostructures, such as NPs,[57,58,204] and NRs,[205] have been explored as attractive candidates for manufacturing printed ZnO transistors at low-cost and low-temperature on flexible substrates, away from Si.

In our research group, some breakthroughs have been made in exploring cellulose-based paper substrates as a suitable platform to host fully printed TMOS transistors, despite their poor mobility values (<0.1 cm^2 V^{-1} s^{-1}). Carvalho et al[57] developed a screen-printable ZnO ink composed of a high concentration of nanoparticles blended with ethyl cellulose, which provides printability and excellent adhesion to paper substrates, including office paper and MFC. The high amount of particles is enough to produce an interconnected ZnO NPs matrix with a single screen-printing pass, thus enabling the fabrication of printed ZnO EGTs with a turn-on voltage of 1.90 V, saturation mobility of 0.07 cm^2 V^{-1} s^{-1}, and an $I_{ON/OFF}$ of more than three orders of magnitude. In a different work of the same group, [58] an aqueous solution of ZnO NPs was combined with a precursor solution of zinc nitrate and hexamethylenetetramine with the purpose of aiding in the process of particles interconnectivity. The viscosity of the mixed route ZnO inks (precursor mixed with NPs) is compatible with pen-writing, enabling the deposition of a continuous dual-phase layer with good adhesion to the paper surface. Nevertheless, when applied as a channel layer on paper, acting simultaneously as substrate and ionic conductor, they suffer from a lack of electrical performance due to interface inhomogeneities, and partial conversion of the precursor into ZnO.

Printed p-type TMOS transistors

Despite the exceptional performance exhibited by printed n-type TMOSs, the performance of p-type oxide transistors is still lagging as they have very low carrier mobility.[185] Oxides of copper and nickel are known to show p-type conductivity and are attracting renewed interest as promising printable p-type TMOS materials for transistor applications and integrated CMOS circuits.[54,190,230,241]

Recently, high-performance inkjet-printed NiO_x TFTs on Si with 50-nm-thick alumina (Al_2O_3) high-k dielectric layer deposited by plasma-enhance atomic layer deposition have been fabricated.[241] The optimized electrical performance was obtained for annealing temperatures of 280 ºC, showing a hole mobility of 0.78 cm^2 V^{-1} s^{-1} and $I_{ON/OFF}$ exceeding 4 orders of magnitude. In 2013, Vaseem and co-authors[39] demonstrated that it is possible to inkjet-print functional CuO QDs transistors on Si/SiO_2 without performing any type of post-printing treatment. The devices showed p-semiconductor behavior with a high carrier mobility of 16.4 cm^2 V^{-1} s^{-1}, which performance is intriguingly comparable or even better that previous reported printed n-type TMOS transistors. Further improvements were demonstrated by performing microwave-assisted annealing to produce defect-free, smooth, interconnected CuO QDs nanofilms. By doing so, the devices showed 2-times higher mobility of 28.7 cm^2 V^{-1} s^{-1} after microwave-assisted annealing, which is the best among the p-type inorganic-based FETs. This value is comparable or even better than previous reported thermally treated n-type equivalents, which is quite impressive considering the typical lower performance obtained for nanoparticulated TMOS transistors. Therefore, this work arises a new hope in the field of high-performance p-type TMOS semiconductors by allowing the production of highly compact CMOS circuits with low power consumption that will fuel IoT revolution. A different group used precursor-route to demonstrate printed CuO FETs, where a composite solid polymer electrolyte (CSPE) was used as the gate dielectric to create a highly conformal interface with the oxide semiconductor layer. Annealing temperatures of 400º C are needed to activate semiconductor functionality of CuO, and the resulting electrical performance of the EGTs is not as good as the previous approach using CuO QDs.

Printed integrated circuits

The lack of high-performance p-type oxide semiconductors with similar performance to n-type counterparts is the main obstacle in obtaining functional CMOS inverters, a key component in analog and digital electronic systems for logic functions, that demands co-integration of both types of semiconductors (n-type and p-type semiconductors). The motivation behind CMOS in comparison with unipolar logics, in which a single type of semiconductor is used, is regarded to its low static power dissipation, as the steady state current is limited by the OFF current of one of the single transistors.[208] Additional advantages are superior signal gain, high noise immunity, and low degree of design complexity, thus allowing higher density of logic functions on a chip.[37,39,259]

To date, there has been hardly any report published on printed all-oxide CMOS logics. In this regard, in collaborative works, Baby et al.[230] and Garlapati et al.[54] demonstrated inkjet-printed oxide-based CMOS inverters prepared from nanoparticle-route, and precursor-route, respectively. Despite the limited performance of the p-type Cu_2O and CuO semiconductors, the CMOS inverters exhibited low static power dissipation and high signal gains of 18 and 21, respectively, at a very low supply voltage of only 1.5 V, due to the use of high-capacitance CSPE.

In alternative to p-type TMOS semiconductors, hybrid CMOS circuits have been constructed by combining n-type TMOSs with organic p-type semiconductors. Aerosol-jet printed CMOS inverters onto Si substrates based on organic p-type P3HT and n-type ZnO EGTs with similar carrier mobilities of 2 cm^2 V^{-1} s^{-1} were demonstrated.[208] The fabricated CMOS inverters operate for supply voltages as low as 1.5 V, showing negligible hysteresis, large signal gain of 15, and static power consumption below 10 nW. Additionally, the circuits can switch continuously for 22 h at 1 kHz with stable operation. Five-stage ring oscillators were successfully fabricated with five CMOS inverters and an output buffer, oscillating at maximum frequencies of 2.2 kHz at 2 V supply biases with propagation delays of 40–50 µs.

Though simple resistive-load inverters with n-type semiconductors have often been fabricated.[53,58,132,210,238,260] Unipolar resistive-load inkjet-printed In_2O_3 nanoparticles inverters on flexible PEN foils with small gains of 1.4 under 1 V were reported.[53] Hong et al.[132] have demonstrated a resistive-load inverter by connecting aerosol-jet printed ZnO EGTs in series with 10 kΩ printed PEDOT:PSS-based resistors with better performance. Compared to the previous work, the circuit displays a higher signal gain of 8, and responded well to a 1 kHz square-wave input signal for a supply voltage of 2 V. Besides electrolyte-gating approach, high signal gains of 9.2 and 16 can be obtained for supply voltages of 2 V and 4 V, respectively, by using a spun-coated high-k dielectric combined with EHD-printed, high mobility In_2O_3 TFTs on Si connected to a load resistor of 80 kΩ.[238] On the other hand, Grey et al.[58] proposed a user-friendly approach to boost DIY concept, where ubiquitous handwriting and printing tools enabled the design and fabrication of ZnO transistors and logic gates on a sheet of office paper, where graphitic pencil-drawn tracks were used as load resistances. Despite all the issues related to paper's surface, it was used successfully as an ionic conductive substrate compatible with printing/handwriting techniques, thus simplifying considerably the design of the devices. Nevertheless, input voltages of tens of volts are needed to trigger signal inverting behavior, and the gain is inferior to one. This concept can be extended to smoother paper or paper-like substrates to improve semiconductor/dielectric surface, targeting superior performances.

Complex circuits, such as ring oscillators, were also demonstrated. Marques et al.[260] have recently demonstrated inkjet-printed three-stage ring oscillators using resistive-load In_2O_3 electrolyte-gated FETs, which are able to operate at supply voltages as low as 2 V. The individual inverters show a gain of 4.4 and 2.3 ms propagation delay time at 1 V supply voltage, while the ring oscillators show a reasonable oscillation frequency of the order of 350 Hz at 2 V supply voltage and a power consumption of 138 μW. Although CMOS circuit design displays superior performances, a greater gain can be easily achieved for unipolar circuits by applying higher voltages, increasing the width of the channel, and shortening its length.

Progressive efforts in the development of high-mobility, printable TMOSs, together with recent advances in high-resolution printing technology will gradually close the gap towards real applications of low-power, flexible, printed electronics with high-frequency operations.

1.2.5. Electrolyte-gated transistors

One important challenge in developing transistors and integrated circuits is reduction of operating voltage. The use of electrolytes, consisting of electrically insulating yet ionically conductive materials, in alternative to inorganic oxide gate dielectrics of conventional FETs, such as SiO_2, titania (TiO_2), and Al_2O_3, is promising in this regard, thus introducing an innovative class of transistors, known as EGTs.[47,261]

As sketched in **Figure 1.8**a, EGTs are composed of three fundamental layers, the semiconductor, electrolyte, and electrodes (source, drain, and gate), in a similar way as typical FETs. The electrolyte separates the semiconductor material from the gate electrode, and it can control electrical isolation and regulate the number of charge carriers induced in the semiconductor channel layer.[198] Depending on the location of the electrodes to the semiconductor layer and on the position of the gate electrode (on the top or bottom of the EGTs), the devices can be classified either as coplanar or staggered top/bottom gate.[259] Their configuration is selected depending on the processing strategy of the materials and the operation conditions of the devices.[185]

As illustrated in **Figure 1.8**b, for the electrolyte-gating case, by applying a positive (negative) voltage to the gate electrode, electrons (hole) carriers accumulate in the semiconductor, while anions (cations) and cations (anions) from the electrolyte migrate and accumulate at the gate/electrolyte and semiconductor/electrolyte interfaces, respectively, forming nanoscale electric EDLs, known as Helmholtz double layer.[47,262] Therefore, EGTs can be compared to a two-electrode EDL capacitor.[11] The entire gate voltage is dropped across the EDLs, leading to large gate-to-channel capacitances. Depending on the permeability of the semiconductor, they can be classified as EDL transistors, if the semiconducting layer is impermeable to ions (as exemplified in the figure), causing a field-effect mode, or electrochemical transistors, if ions can migrate into the semiconductor (3D channel), causing electrochemical reactions (Faradaic processes).[47]

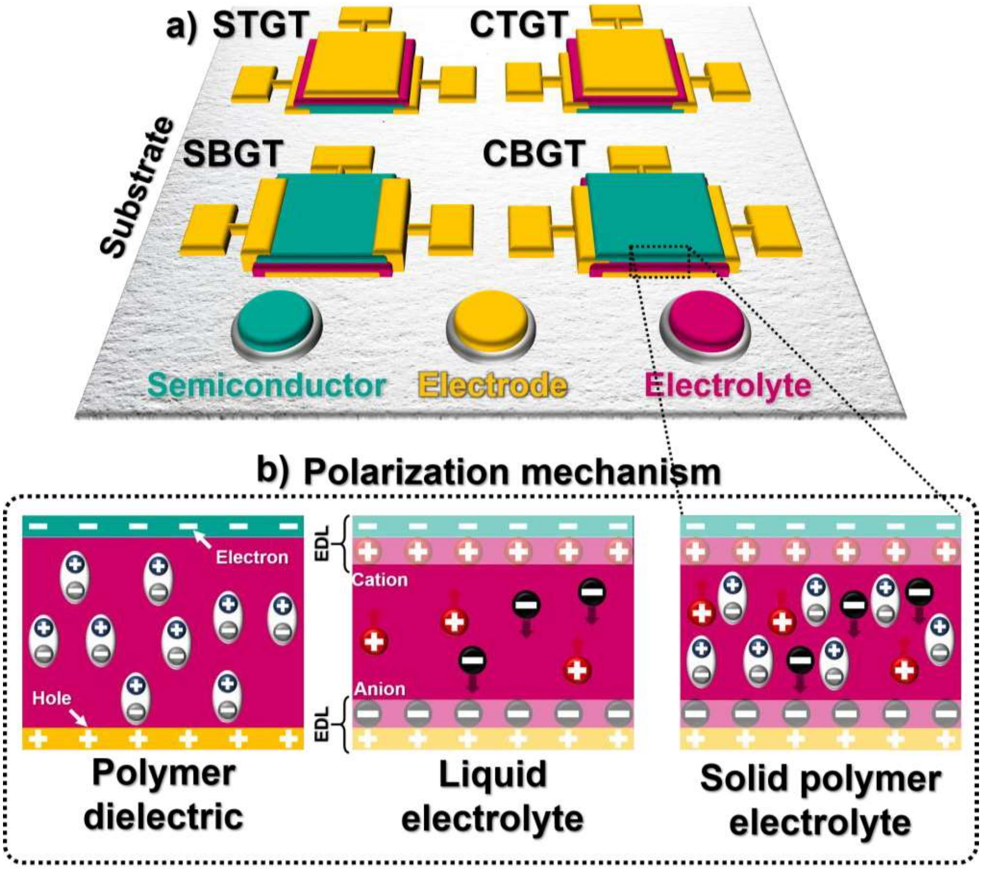

Figure 1.8. Overview of transistors configurations and gating mechanism. **a)** Schematic illustration of typical configurations of transistors: staggered top gate (STGT) or bottom gate (SBGT), coplanar top gate (CTGT) or bottom gate (CBGT) transistors. **b)** Cross-section of transistors depicting the semiconductor (n-type)/dielectric/gate electrode interfaces for different polarization mechanisms when using polymers dielectrics (dipole polarization), liquid electrolytes (ionic polarization), or solid polymer electrolytes (dipole and ionic polarizations).

Contrarily to electrolyte-gating, the working mechanism of polymer dielectrics relies on dipole polarization.[198] While the large specific capacitance of the electrolytes is independent of their thickness, meaning that relatively thick layers with several micrometers can be deposited, polymer dielectrics only achieve high-capacitance for reduced thicknesses in the submicrometric scale to allow low-voltage operation in transistors, which clearly constitutes a processing disadvantage.[263]

Common drawbacks of the EGTs are high parasitic capacitances, large gate-source leakage currents, and the use of electrochemically stable conductors (e.g. noble metal electrodes, and carbon-based materials) to avoid high off currents and device degradation.[47] Besides, the maximum speed is also limited by the polarization response time of the electrolyte, and high bias stress (usually above 5 V) lead to electrochemical doping of the semiconductor layer that also pose a critical limitation on the switching speed and leads to device instabilities.[198,262]

In a similar way as traditional transistors, EGTs can be integrated into analog/digital circuits.[181] Yet, the ion movement principle of EGTs allied with their high signal amplification capability at low operating voltages make them find far greater potential as promising building block for biosensors capable of detecting biophysical (e.g. light, cardiac rhythm, and brain activity) or chemical signals from biochemical species (e.g. glucose, cell receptors, enzymes, antibodies, and nucleic acids), and neuromorphic computing based on artificial synaptic devices.[47,261,264] Hence, EGTs can provide a platform that simultaneously integrate sensing and computing ability toward artificial intelligent sensory systems, thus serving the purpose of IoT.

Ionic liquids, electrolytic solutions, ion gels, polyelectrolytes, and solid polymer electrolytes have been used as gate dielectrics for EGTs.[47,198] In a similar way as in solid-state electrolytes, ionic hydrogels can be considered a good approach for EGTs since they are free from liquid-leakage, thus easily applied and safe for users, minimizing one of the main problems associated to electrolytes in the liquid form.[265] Nevertheless, the ionic conductivity and contact at electrode/electrolyte interface are poorer when compared with liquid electrolytes.[266] Furthermore, ionic hydrogels are compatible with solution processing (printability/coating), and are able to drastically reduce the transistors‘ operation voltage from tens of volts to just less than 3 V with high operating frequencies up to the kHz range, due to their large capacitance (typically in the order of 1–10 μF cm^{-2}), fast polarization times (within a few milliseconds), and high ionic conductivity (>0.1 mS cm^{-1} at RT).[33,47,132,263,267,268]Their low operating voltage aspect is of foremost interest from a power consumption perspective, offering the possibility of powering these devices by thin-film batteries, external radio frequency fields, supercapacitors, solar-cells.[4–6,43,263,269]

Until now, not much can be found in the literature regarding EGTs relying on cellulose-based electrolytes. Thiemann et al.[33] introduced a new class of regenerated cellulose ion-gels based on microcellulose and various methylphosphonate ionic liquids, which exhibit transparency, flexibility, transferability and high capacitance (5-15 μF cm^{-2}), finding pioneer applications in flexible electronics as high capacitance gate dielectrics for EGTs. Solid-state cellulose electrolytes with additional photonic properties were proposed by Grey et al.[30,31], where intrinsically chiral nematic photonic CNC films were ionically modified through ion infiltration with aqueous solutions of alkali hydroxides. These multifunctional cellulose-based electrolytes were successfully integrated into photo-responsive transistors capable of sensing distinct polarization states of circular polarized light. In addition, multifunctionality was also explored on (nano)paper as it can be used simultaneously as substrate and gate dielectric layer in FETs.[4,34–37,39–41,44,270–275]

Despite the considerable studies on exploring cellulose-based paper substrates with different textures and compositions as intrinsically ionic conductive substrates in transistors and integrated circuits, their electrolytic performance is by far satisfactory enough for low-power applications (**Table S3**). Their electrochemical behavior relies on the abundant charged hydrophilic functional groups in the polymer chain of cellulose as well as the presence of hygroscopic species in the cellulose fibers of paper that can retain water. As demonstrated by Pereira et al.,[41] the water sorption mechanism promotes the formation of the EDL in paper, providing cations (protons, H^+) and anions (hydroxide anions, OH^-), that are responsible for the ionic conduction and build-up of the capacitance at low frequencies.

One way to enhance the electrolytic performance of the cellulose nanopaper consists of adding ionic species that can increase the amount of water retained into its framework. Up to now, Dai et al.[51] reported low-voltage (<5 V) organic FETs and complementary inverters fabricated on flexible, transparent and intrinsically ionic conductive cellulose nanopapers, which were prepared from a chemically modified NFC pulp using (2, 2, 6, 6-tetramethylpiperidin-1-yl) oxidanyl (TEMPO) oxidation process assisted by sodium salts responsible for the ionic conduction.

1.3. Outlined objectives

Considering the motivation of this PhD work together with the knowledge acquired during a deep research made in the current state-of-the-art in the field of cellulose advanced functional materials, paper electronics, and printed TMOS electronics, several objectives were set in order to merge all these concepts and design a path composed of numerous tasks to concretize the vision of this work: ***a new Era of eco-sustainable, low-power, affordable, flexible, and customizable, printed smart-systems onto paper/“paper-like” platforms to serve the comfort and welfare of citizens.***

Throughout this work, the importance of the implementation of sustainable procedures, starting with a proper selection of raw materials and compatible low-temperature processing and manufacturing methods, is systematically addressed targeting solutions for reducing the environmental impact, while boosting an environmental-conscious mentality.

The objectives of this work are focused on two key essential pieces of a transistor, the semiconductor (“*heart*”) and dielectric (“*brain*”). These materials are designed using cellulose-based materials as suitable matrix hosting the active material, which are integrated on paper substrates or reengineered cellulose “paper-like” ionic conductive substrates targeting low-power operation and low-temperature processing, while ensuring flexibility, recyclability/biodegradability. User-friendly manufacturing processes, such as screen-printing and handwriting techniques as well as simple lamination processes, are used to create “on-demand” personal printed/handwritten transistors and circuits, while having fun at it.

In the first place, a proper selection of cellulosic materials and ZnO nanostructures, and respective compatible processing routes must be made towards the development of cellulose composites with semiconducting or ionic conductive functionality, processable at low temperatures (preferably <150 ºC) to enable the use of flexible substrates. Water-based formulations are highly attractive for reducing environmental impact as well as both processing and integration costs.

Secondly, several features must be evaluated and optimized during their formulation and further integration onto cellulose-based materials:

- To formulate cellulose composite semiconducting inks, a compromise should be found between the ink’s components, while ensuring percolation between the functional particles with minimal defects after drying, such as voids, agglomerates and/or cracks. Thus, the inks’ characteristics as well as surface, compositional, thermal, and mechanical properties of the target cellulose-based substrate are of extreme relevance as they affect the printing resolution, thickness, and functionality of the screen-printed pattern. In this work, cellulose derivatives, such as CMC and EC, were tested as binders and their compatibility with ZnO nanostructures to formulate stable inks compatible with screen-printing process was addressed. The amount, morphology, and dimensions of the ZnO nanostructures were considered as they impact the surface roughness, percolation network, and mechanical properties of the screen-printed films.
- Regarding the cellulose-based ionic conductors, aqueous alkali hydroxide (LiOH and/or NaOH) systems combined with urea are a suitable strategy to easily prepare new regenerated cellulose materials in the form of hydrogels. This strategy can be combined with water-soluble derivatives, such as CMC, or nanocellulose materials, such MFC/NFC, as reinforcing agents to improve their robustness. The study of their electrochemical properties (e.g. capacitance and ionic conductivity) assumes great interest to evaluate their suitability to ionic responsive devices with low-power operations, such as EGTs.

The accomplishment of these goals leads to the ultimate objective of integration of the produced cellulose-based composites with the optimized formula into flexible, printed/written ZnO EGTs and logic gates onto conventional paper substrates or developed “paper-like” ionic conductive substrates.

Last but not the least, resource-conscious strategies, such as repairing, reusing, recycling, and biodegradability, must be assessed to evaluate the environmental impact of the fabricated devices.

Chapter 2

Materials and Methods

2. Materials and Methods **33**

2.1. Screen-printable cellulose composite inks 34

2.1.1. Chemical synthesis and characterization of porous ZnO nanostructures 34

2.1.2. Preparation and characterization of cellulose composite semiconducting inks 35

2.1.3. Inks' printability on office paper 36

2.2. Iontronic cellulose-based membranes 36

2.2.1. Preparation of self-healable cellulose iontronic stickers 36

2.2.2. Preparation of iontronic cellulose nanopaper composite 37

2.2.3. Characterization of the iontronic cellulose-based membranes 38

2.3. Oxide-based transistors and integrated circuits based on electrolyte-gating mechanism 38

2.3.1. Fabrication of CICH-gated IGZO transistors and inverters 38

2.3.2. Fabrication of ACICC-gated IGZO transistors 39

2.3.3. Fabrication of screen-printed ZnO EGTs and circuits on paper 39

2.3.4. Fabrication of ACICC-gated screen-printed ZnO transistors and logic gates 40

2.3.5. Electrical characterization of EGTs and integrated circuits 41

2.3.6. Electrical characterization of UV-responsive screen printed ZnO circuits 41

In this chapter, a detailed description of all the steps required to successfully accomplish the processing, manufacturing, and characterization of the engineered advanced cellulose composite materials and integrated devices will be given.

The research activities were entirely developed using existing technological facilities and scientific competences at the host institution (CENIMAT|I3N and CEMOP/UNINOVA). The methodology used throughout this work consisted of several scientific tasks that covered the selection of materials and synthesis methods targeting the formulation of printable functional semiconductor materials based on ZnO nanostructures and development of ionic conductive membranes for the design and fabrication of the individual transistors and circuits. An intermediate additional task was addressed throughout this work that concerns the implementation of environmental-responsible strategies to address the negative impact of e-waste on the natural environment. All these tasks were strongly coupled with characterization and validation procedures at all levels from materials to devices.

2.1. Screen-printable cellulose composite inks

2.1.1. Chemical synthesis and characterization of porous ZnO nanostructures

Porous ZnO nanostructures were synthesized by hydrothermal method assisted by microwave radiation. Zinc nitrate hexahydrate ($Zn(NO_3)_2$ $6H_2O$, from Sigma-Aldrich 98 %) and urea (Sigma-Aldrich 99.0–100.5 %) were used without further purification. In a typical synthesis, 0.05 M of zinc nitrate was first dissolved in deionized water (Millipore), and after its total dissolution, urea was added to the aqueous solution. The molar ratio of zinc to urea was kept at 1:5. Then, 25 mL of the obtained solution was transferred to a 35 mL Pyrex vessel, which was placed in a Discovery SP microwave (CEM corporation). The synthesis was carried out at 140 °C for 15 min under a power of 100 W.

The resulting white precipitates were washed with deionized water, followed by isopropanol, and centrifuged at 4500 rotations per minute (rpm) for 5 min each. This washing process was repeated three times. The powders were dried in air at RT for 48 h, and then calcinated in a furnace (Nabertherm muffle furnace) at 700 °C in air for 2 h at a heating rate of 250 °C h^{-1}.

The morphology of the porous ZnO nanoplates (ZnO PNPs) was evaluated and compared with commercial ZnO nanopowder (Aldrich, <100 nm particle size) by scanning electron microscopy (SEM) using a Carl Zeiss AURIGA CrossBeam FIB-SEM workstation. The structural analysis was done via X-Ray diffraction (XRD) using a PANalytical X'Pert Pro, with Bragg–Brentano geometry and Cu Kα line radiation ($\lambda = 1.5406$ Å). Fourier-transform infrared (FTIR) spectroscopy acquisitions were performed at RT, using an attenuated total reflectance sampling accessory (Smart iTR) equipped with a single-bounce diamond crystal on a Thermo Nicolet 6700 spectrometer. The spectra were acquired between 4000 and 525 cm^{-1} with a 4 cm^{-1}.

2.1.2. Preparation and characterization of cellulose composite semiconducting inks

ZnO nanostructures were blended with different concentrations (10–40 wt.%) into a previously prepared cellulose derivative solution used as binder. The mixture was slowly stirred (200 rpm) for 4 h to obtain a well dispersed and homogeneous white viscous solution. The ink was stored in a refrigerator at 3 ºC, until being used.

Two types of ZnO nanostructures were tested, including commercial ZnO nanopowder and the synthesized ZnO PNPs. Regarding the binders, distinct cellulose derivatives were investigated, such as CMC (Sigma-Aldrich, $M_w \approx 250000$), and EC (Sigma-Aldrich, 5 % in toluene/ethanol 80:20(lit.), extent of labelling: 48% ethoxyl). An aqueous solution of CMC was prepared with a content of 3 wt.%. The EC solution was prepared by dissolving 5 wt.% EC in a solvent mixture (80:20 v/v%) of toluene (Merck, ≥99 %) and ethanol (Fisher Scientific).

Table 2.1 summarizes the developed inks and their composition, including the nomenclature given for each ink to simplify description.

Table 2.1. Summary of all the developed ZnO-based composite inks.

Ink	Cellulose derivative/ weight ratio in the binder solution [wt.%]	Solvents	ZnO nanostructure/ weight ratio in the ink [wt.%]
EC5Z40	EC/ 5	Ethanol/ toluene (80:20 v/v%)	Commercial NPs/ 40
C3Z10	CMC/ 3	H_2O	Commercial NPs/ 10
C3Z20			Commercial NPs/ 20
C3Z30			Commercial NPs/ 30
C3Z40			Commercial NPs/ 40
C3ZPN10			Synthesized PNPs/ 10
C3ZPN20			Synthesized PNPs/ 20
C3ZPN30			Synthesized PNPs/ 30
C3ZPN40			Synthesized PNPs/ 40

Viscosity of the binder solutions was measured on Bohlin Gemini HRnano rheometer, in parallel plate's geometry (20 mm diameter and 500 µm gap) for steady-state measurements. Temperature was kept at 25 °C and, before starting the measurements, samples were subjected to a pre-shearing stage, with a pre-shear of 1 s^{-1} applied for 30 s, followed by a stabilization time of 180 s. A solvent trap was used to avoid evaporation. The steady-state measurements were performed for shear rates up to 1000 s^{-1}.

The inks' rheologic properties were analyzed with a Brookfeld CAP 2000+ Viscometer for steady-state measurements under heating from 25 to 30 ºC. Before starting the measurements, the ink was subjected to a pre-shearing stage of 300 s^{-1} for 30 s, followed by a steady-state measurement with the same parameters as the pre-shear. A solvent trap was used to avoid evaporation.

The thermal characterization of the formulated cellulose semiconducting composite inks was performed by thermogravimetric analysis (TGA) (TGA-DSC- STA449 F3 Jupiter, under air temperature.

2.1.3. Inks’ printability on office paper

Standard office paper (The Navigator Company, 80 g m^{-2}) was tested as printing substrate. The morphological, thermal, and structural characterization of the paper substrate was performed by SEM, TGA, and XRD, respectively. The surface roughness of paper substrate was performed with an Ambios XP-Plus 200 Stylus Profilometer and the software data compilation from TrueMap. The formulated cellulose composite inks were screen-printed on standard office paper, using a custom-made screen-printing station. The inks were printed with a polyester screen with the following features: mesh model: 77–55; mesh count: 190 mesh/inch; aperture: 81 µm; thread diameter: 55 µm; opening: 30%; thickness: 88–97 µm). The printed films were dried at RT in less than 10 s.

The morphological and compositional characterization of the printed layers was performed by SEM and FTIR, respectively. Thickness of the printed layers was estimated from the average of 10 measurements collected from the SEM cross-section images that were processed using ImageJ software. Optical microscopes (Leica M80 or Olympus BX51) were used to observe the topography of the printed films, and their printing resolution was estimated from the average of 10 measurements collected from optical microscope images that were processed using ImageJ software.

The surface roughness of the printed films composed of commercial ZnO NPs was evaluated by atomic force microscopy (AFM) using an Asylum Research MFP-3D operated in alternate contact mode. The resolution of the image was 256 lines by 1024 columns and the scan size was 5 × 5 µm^2.

2.2. Iontronic cellulose-based membranes

2.2.1. Preparation of self-healable cellulose iontronic stickers

Inspired in the procedures reported in the literature for the dissolution of cellulose,[88,89] different strategies were employed to prepare cellulose ionic conductive hydrogels (CICHs). Cellulose dissolution medium was prepared by mixing 4.6 wt.% LiOH (0.46 g, Sigma-Aldrich, ≥98 %) or NaOH (0.46 g, Labkem, ≥98 %), 15 wt%. urea (1.5 g, Carl Roth, ≥99.5 %) in 80.4 wt%. deionized water (8.04 g, Millipore). Different alkali hydroxide mixtures of LiOH and NaOH (LiOH:NaOH = weight ratio of 3:1, 1:1, 1:3, 1:19) were also prepared, while keeping the weight ratio of 4.6 wt.% alkali hydroxides mixture, 15 wt.% urea and 80.4 wt.% of water (0.46 g of LiOH:NaOH, 1.5 g of urea and 8.04 g of water in 10 g of solution). The solvent mixtures were precooled in a freezer at -25 ºC, until they became a frozen solid. The frozen solutions were then allowed to thaw at ambient conditions and 4 wt.% of microcrystalline cellulose (MCC, 0.4 g in 10 g of solution, Sigma-Aldrich, powder: 20 µm) was immediately added into the solvent system (9.6 g in 10 g of solution) under vigorous stirring at -8 ºC until its complete dissolution (≈30 min). A freezing-thawing cycle was performed to improve cellulose dissolution.

Mixtures of MCC and CMC were prepared by adding different amounts of CMC to the previous cellulose solution obtained from aqueous LiOH/urea solvent system in the following MCC:CMC weight ratios: 2:1 (0.4 g of MCC, 0.2 g of CMC, 9.6 g of aqueous alkali salt/urea solvent system) and 1:1 (0.4 g of MCC, 0.4 g of CMC, 9.6 g of aqueous alkali salt/urea solvent system). For the remaining MCC solutions prepared from aqueous NaOH/urea or LiOH:NaOH/urea solvents, mixtures of MCC:CMC were prepared with a weight ratio of 1:1.

The mixtures were stirred at RT conditions until complete dissolution of CMC, and then at -8 ºC to ensure MCC dissolution. The transparent solutions were kept overnight in a freezer at -25 ºC. The last step consists of neutralization of the solutions and simultaneous regeneration of cellulose with acetic acid (≈1 mL, Sigma-Aldrich, ≥ 99). This process was performed in an icy bath by slowly adding acetic acid “drop-by-drop” to the cellulose solution under stirring to avoid overheating. The resulting solutions were shear-casted on a glass plate. The ≈1 mm-thick electrolyte films were dried in a closed box with controlled environment (SICCO, T = 24 ± 2 ºC, 33 ± 2 %RH – relative humidity) for 3 days and stored in air. The thickness of the resulting membranes was estimated from the average of five measurements made using a Mitutoyo digital micrometer.

The CICHs prepared from LiOH, NaOH, and mixtures of LiOH and NaOH will be referred to as Li-CICHs, Na-CICHs, and LN-CICHs, respectively. A summary of all the developed CICH membranes, including their formulation details and respective nomenclature, are displayed in **Table 2.2**.

Table 2.2. Summary of all the developed CICHs membranes.

CICH membrane	MCC:CMC [weight ratio]	Alkali hydroxide	Alkali hydroxide [wt.%] in urea/water mixture
MC0	4:0	LiOH	4.60
M2C1	4:2	LiOH	4.60
M1C1 (or L100)	4:4	LiOH	4.60
L3N1	4:4	LiOH:NaOH	3.45:1.15
L1N1	4:4	LiOH:NaOH	2.30:2.30
L1N3	4:4	LiOH:NaOH	1.15:3.45
L1N19	4:4	LiOH:NaOH	0.23-4.37
N100	4:4	NaOH	4.60

2.2.2. Preparation of iontronic cellulose nanopaper composite

A “paper-like” all-cellulose ionic conductive composites (ACICC) was prepared by blending 5 wt.% of Li-CICH slurry (0.5 g), corresponding to L100 membrane, with 95 wt.% of a cellulose pulp (0.95 g) provided from *Centre Technique du Papier*, consisting of an aqueous kraft pulp suspension containing 2 wt.% of MFC/NFC. The slow casting and evaporation of water was performed from 5 mL of the all-cellulose nanocomposite solution mixture in polystyrene Petri dishes (55 mm diameter) in a closed box with controlled environment (SICCO, T = 24 ± 2 ºC, 33 ± 2 %RH) for 3 days and stored in air. Freestanding membranes were also prepared by solvent casting the nanocellulose pulp without adding the Li-CICH slurry (referred to as cellulose nanopaper), and by shear-casting the Li-CICH slurry on a glass plate. Both membranes are obtained after drying in the same conditions as the ACICC membrane. The thickness of the resulting cellulose nanopaper, ACICC and CICH membranes was estimated from the average of ten measurements made using a Mitutoyo digital micrometer around 63.5 ± 1.59 μm, 78.3 ± 0.78 μm and 336 ± 31.0 μm, respectively.

2.2.3. Characterization of the iontronic cellulose-based membranes

The optical transmittance measurements were performed with a Perkin Elmer Lambda 950 spectrophotometer in the wavelength range from 400 to 800 nm, with a scan of 1 nm and using air as the reference.

The morphological, structural, thermal, and compositional characterization of the membranes was performed by SEM, XRD, TGA, and FTIR, respectively.

The surface roughness of the cellulose-based nanopapers was analyzed by AFM, and the resolution of the image was 256 lines by 1024 columns and the scan size was 5 x 5 μm^2.

Electrochemical characterization of the CICHs was carried out at RT (23 ± 2 ºC, ≈40 %RH) in a typical capacitor structure by depositing the electrolyte between two stainless-steel discs with an active area of 1 cm^2, using a Gamry Instruments Reference 600 potentiostat. For the ACICC membrane, two electrochemical cells with an active area of 1 mm^2 were prepared depending on the material's composition of the transistors: carbon/membrane/carbon, and Al/membrane/IZO.

Electrochemical impedance spectroscopy (EIS) measurements were performed with 10 mV AC voltage in a frequency range of 0.1 up to 10^6 Hz. Cyclic voltammetry (CV) measurements were performed in a potential range between -3 and 3 V at distinct scan rates and a collection of five successive cycles were acquired before analysis. To test the electrochemical stability of the oxide semiconductors (IGZO and ZnO), CV measurements were also performed including the semiconducting layer in the capacitors' structure.

2.3. Oxide-based transistors and integrated circuits based on electrolyte-gating mechanism

2.3.1. Fabrication of CICH-gated IGZO transistors and inverters

A planar configuration was adopted based on titanium/gold (Ti/Au) bottom electrodes (source, drain and gate) deposited on glass (Marienfeld) or multilayer-coated paper (Felix Schoeller type 3) in an interdigital architecture by electron-beam evaporation, followed by sputtering process of amorphous IGZO, working as the active oxide semiconductor, and lamination of the CICHs as gate dielectric.

Glass substrates were cleaned in an ultrasonic bath for 5 min, first in acetone and then in isopropanol, after that rinsed off in deionized water and dried using nitrogen. The electrical contacts, double layer of Ti/Au with 6 and 65 nm, respectively, were deposited on the substrate by electron-beam evaporation. Then a 35 nm IGZO (In_2O_3–Ga_2O_3–ZnO; 1:2:2 mol%) layer was deposited by radio-frequency magnetron sputtering, at RT in an AJA ORION system. The semiconductor channel and the electrodes were patterned by shadow masks with a channel width (W) of 6800 µm and length (L) of 40 µm (W/L = 170). Gate-to-semiconductor gap is 50 µm. The EGTs were annealed in air at 150 °C for 30 min. The CICHs were laminated onto the devices to connect the transistors' channel and gate electrode.

An optical microscope was used to observe the surface topography of the devices. Images were processed using ImageJ software to estimate transistor's real dimensions.

For circuits demonstration, CICH-gated EGTs on multilayer-coated paper were glued with double-sided tape to a sheet of office paper. A resistive-load inverter was fabricated by exploiting pen-on-paper and pencil-on-paper approaches. Thick conductive tracks were drawn with a silver conductive ink rollerball pen (CircuitScribe) to establish the electrical connections between the drain electrode and the load resistance. Graphitic line tracks were hand-drawn with a HB-2 pencil (Black'Peps, Maped) to define the load resistances.

2.3.2. Fabrication of ACICC-gated IGZO transistors

The devices were produced with a staggered-bottom gate structure, and all the deposition steps were performed at room temperature without any intentional substrate heating. The semiconductor layer of amorphous IGZO was deposited by RF magnetron sputtering with a thickness of 40 nm on the smoothest side of the ACICC membrane. Aluminum (Al) drain and source contacts (200 nm thickness) were deposited by e-beam evaporation. Both layers were patterned using shadow masks with a channel width of 2.3 mm and length of 230 µm (W/L = 10). The bottom gate electrode consists of a 200 nm thick layer of IZO (In_2O_3–ZnO; 89.3:10.7 wt%) that was deposited by RF sputtering on the opposite side of the membrane.

2.3.3. Fabrication of screen-printed ZnO EGTs and circuits on paper

Screen-printed ZnO EGTs with a planar configuration in a conventional architecture (theoretical: W = 500 µm, L = 200 µm, W/L ≈2.5, gap between the gate electrode and the printed semiconductor layer = 300 µm) were produced onto office paper, using a custom-made screen-printing station. The active layers were sequentially deposited on paper, starting with the printing of the electroconductive ink for the patterning of source, drain and gate electrodes on paper, followed by the printing of the formulated semiconducting composite inks between the source and drain carbon electrodes.

A commercial conductive carbon paste (CRSN2644 C INK, Sun Chemical) was used for printing the electrodes, and a polyester screen was used with the following features: mesh model: 120–34; mesh count: 305 mesh/inch; aperture: 45 µm; thread diameter: 34 µm; opening: 30.5 %; fabric thickness: 52–57 µm. The carbon patterns were cured at 100 ºC for 30 min in air, and their sheet resistance (R_s) was determined by four-point probe technique (Jandel Engineering Ltd.) and estimated from the average of ten measurements. An optical microscope was used to determine the printing resolution of the ink from the average of 10 measurements collected from the optical microscope images that were processed using ImageJ software.

The formulated semiconducting composite inks (detailed formulation is available in **section 2.1.2**) were printed with a different polyester screen (mesh model: 77–55; mesh count: 190 mesh/inch; aperture: 81 µm; thread diameter:55 µm; opening: 30 %; thickness: 88–97 µm), and dried at RT in less than 10 s.

To conclude the EGTs' fabrication, L100 electrolyte (detailed formulation is available in **section 2.2.1**, corresponding to Li-ClCHs prepared from aqueous LiOH/urea solvent system) was laminated onto the devices to connect the transistor's channel and gate electrode.

An optical microscope was used to observe the surface topography of the printed devices. Images were processed using ImageJ software to estimate transistor's real dimensions from the average of 10 measurements. Cross-section images of the EGTs were obtained by SEM-EDS (energy-dispersive X-ray spectroscopy).

For circuits demonstration, silver tracks were handwritten using a conductive silver ink rollerball pen (CircuitScribe) to establish the electrical connections between the fabricated screen-printed ZnO EGTs on office paper and the load resistances, either based on pencil-drawn graphitic tracks or screen-printed optoelectrical resistor (OER) switches.

Regarding the patterning of the load resistances, graphitic line tracks were hand-drawn using a HB-2 pencil (Black'Peps, Maped). A more complex strategy was adopted to fabricate the OERs. For the OERs, planar electrodes were screen-printed with an interdigital architecture composed of one pair of 4 interdigital fingers with a width of 300 µm and length of 7.5 mm, spaced from each other with a gap of 300 µm. The carbon electrodes were dried at 100 ºC for 15 min in air. Then, the formulated C3ZPN10 ink was screen-printed in a square shape (6.6 x 6.6 mm^2) between the planar carbon electrodes and dried at room temperature in less than 10 s. A piece of office paper was laminated on top of the electrolyte to avoid the influence of the light source on the electrical performance of the EGTs.

2.3.4. Fabrication of ACICC-gated screen-printed ZnO transistors and logic gates

Planar carbon electrodes were screen-printed on the smoothest side of the ACICC membrane using a conductive carbon paste (CRSN2644 C INK, Sun Chemical), and a screen mold made of polyester with the following conditions: mesh model, 120-34; mesh count, 305 mesh/inch; aperture, 45 µm; thread diameter, 34 µm; opening, 30.5 %; fabric thickness, 52–57 µm. The carbon electrodes were dried at 70 ºC for 15 min in air.

The R_s of the screen-printed carbon electrodes on ACICC membrane was determined by four-point probe technique (Jandel Engineering Ltd.) and estimated from the average of ten measurements.

Before printing the next layer, the membrane with the printed electrodes was stored for 1 h at ambient conditions to restore its moisture. The C3ZPN30 ink (detailed formulation of this ink is available in **section 2.1.2**) was screen-printed between the source and drain carbon electrodes (W = 1 mm, L = 200 µm, W/L = 5) with a different polyester screen (mesh model: 77–55; mesh count: 190 mesh/inch; aperture: 81 µm; thread diameter: 55 µm; opening: 30 %; thickness: 88–97 µm) and dried at RT in less than 10 s.

An optical microscope was used to observe the surface topography of the devices. Images were processed using ImageJ software to estimate transistor's real dimensions from the average of 10 measurements. SEM images were also acquired.

To fabricate logic gates, the ACICC membrane was glued with double-sided tape to a sheet of office paper. Graphitic line tracks were hand-drawn with a HB-2 pencil (Black'Peps, Maped) on the office paper to define the load resistances. After printing the planar carbon electrodes, thick carbon tracks were drawn with a pencil brush to establish the electrical connections between the transistors and the load resistance, using the same ink to print the carbon electrodes. The screen-printed electrodes and hand-drawn tracks were dried simultaneously at 70 ºC for 15 min in air.

To conclude the circuits' fabrication, the ACICC membrane with the patterned carbon layers was stored for 1 h under ambient conditions, and then C3ZPN30 ink was screen-printed between the source and drain carbon electrodes, and dried at RT in less than 10 s.

2.3.5. Electrical characterization of EGTs and integrated circuits

The EGTs and circuits were electrically analyzed in the dark in air at RT (24 ± 2 °C, 43 ± 4 %RH) using a microprobe station (Cascade Microtech M150) connected to a semiconductor parameter analyzer (Agilent 4155C) controlled by the software Metrics ICS. In-situ temperature and bending measurements were also performed using this apparatus.

The electrical characterization under vacuum was done in a Keithley 4200-SCS semiconductor parameter analyzer connected to a JANIS ST-500 microprobe station.

For dynamic characterization, a microprobe station (Cascade Microtech MPS150) connected to a semiconductor parameter analyzer (Keysight B1500A) controlled by the software Keysight EasyEXPERT was used for biasing the circuit. A waveform generator was connected for input signal (Keysight 33500B Series) and the output signal was measured with an oscilloscope (ISO-TECH IDS 8062) with a high impedance probe (10 MΩ). The oscilloscope cable and each probe of the microprobe station have a parasitic capacitance of 15 and 160 pF, respectively.

2.3.6. Electrical characterization of UV-responsive screen printed ZnO circuits

The fabricated OERs and UV-responsive circuits were electrically analyzed at room temperature (24 ± 2 °C, 38 ± 4 RH%) using a microprobe station (Everbeing) connected to a semiconductor parameter analyzer (Agilent 4155C) controlled by the software Keysight EasyEXPERT for biasing the devices.

The screen-printed OERs were irradiated with a fiber-coupled LED with a well-defined wavelength controlled by a DC2100 Controller from Thorlabs, with a pulse train generator (Pulse Pal) programmed to turn on and off the LED. A fiber-coupled LED with a nominal wavelength of 365 nm (M365F1 Thorlabs, 4.1 mW) was used as light source. The OERs were placed at 2 cm from the light source and irradiated for 150 s (LED ON), followed by 150 s in the dark (LED OFF), during five ON/OFF cycles. Simultaneously, chronoamperometry measurements were carried out with an applied bias of 1.5 V for three light intensities (0.3, 2.0, and 8.7 mW cm^{-2}). The light intensity for each configuration was measured with a Suss MicroTec UV-Optometer.

For the OER-loaded inverters, consecutive voltage transfer characteristic (VTC) curves were acquired overtime before (as-prepared), during and after exposure to the light source for a period of 180 s in each state. The circuits were tested for a drain voltage of 1.5 V for three light intensities (0.3, 2.0, and 8.7 mW cm^{-2}). Dynamic electrical characterization of the inverters was performed by applying a fixed V_{IN} (0 or 3 V) and V_{DS} (1.5 V), while irradiating the OER for 60 s (LED ON), followed by 60 s in the dark (LED OFF), during ten ON/OFF cycles.

Chapter 3

Cellulose composite semiconducting inks

3. Cellulose composite semiconducting inks 43
3.1. Characterization of ZnO nanostructures 44
3.2. Characterization of office paper substrate 46
3.3. Formulation and screen-printing of cellulose composite inks 47
  3.3.1. Formulation of cellulose composite inks 47
  3.3.2. Printing trials on office paper 48
    3.3.2.1. Influence of cellulose derivatives and ZnO content 48
    3.3.2.2. Influence of drying conditions 51
    3.3.2.3. Influence of ZnO nanostructures 53

Regarding the development of printable cellulose composite semiconducting inks, a deep research in the literature was performed to identify typical TMOS materials compatible with low-temperature printing processes that yield transistors with high performances, while ensuring compatibility with heat-sensitivity substrates, such as paper. Especial attention was given to those prepared from nanoparticles-route as this approach enables low-temperature processing, contrarily to metal salt precursor approach that do not meet the thermal budget requirements of most plastic substrates or paper substrate.

From a huge list of printed TMOS transistors, ZnO was identified as a well-explored n-type TMOS material that can be prepared from various synthetic approaches, including hydrothermal method assisted by microwave radiation,[254,276] thus encouraging its investigation. The starting point of the laboratory activities consisted of the use of commercially available ZnO NPs, and subsequent analysis of their structural, compositional, and morphological properties, before moving to the preparation of ZnO PNPs using hydrothermal synthesis assisted by microwave.

Secondly, binders are an essential component of printable inks to aid in the printing process, while ensuring adhesion to the paper-based substrate and mechanical integrity of the printed film. Aqueous, and non-aqueous soluble cellulose derivatives, such as CMC and EC, respectively, have been reported as suitable binders to host functional materials.[57,129,172,277–286] These materials were tested as potential binders to formulate screen-printable ZnO-based inks.

Prior mixing the cellulose derivatives with the functional ZnO particles, the rheological behavior of the binders was studied to evaluate their compatibility with screen-printing technique. The critical point was the adjustment of the cellulose derivatives and ZnO particles, and the optimization of drying conditions to obtain screen-printed films with semiconducting functionality on naturally rough, and porous paper-based substrates, such as regular office paper that is commonly used in our daily-life. No additional coating or calendering treatments were adopted to office paper to simplify the manufacturing process, while preserving its intrinsic advantageous properties, such as low-cost and recyclability.

The surface morphology and roughness, substrate/printed film interface, printing resolution, and thickness of the screen-printed films on office paper was exhaustively investigated. The influence of the drying conditions, and morphology of ZnO particles was also assessed, as the size, shape, and loading coating of the functional material affect the percolation network, and thus their functionality/performance.

3.1. Characterization of ZnO nanostructures

In this work, ZnO powders from two different sources, including commercial ZnO NPs and ZnO PNPs, were tested as semiconducting functional material. The latter were synthesized through a facile and fast hydrothermal method assisted by microwave radiation, followed by a washing step to remove remnants of reagents from the synthesis, and a calcination step in a furnace at 700 ºC to thermally convert the hydrozincite precursor into ZnO. Microwave hydrothermal/solvothermal synthesis presents several advantages over conventional heating due to the absorption of microwave radiation by the materials, which results in high reaction rates and in a homogeneous and fast volumetric heating.[287,288]

As shown in **Figure 3.1**a, commercial ZnO NPs exhibit distinct morphologies and sizes that can reach 200 nm. Regarding the obtained ZnO PNPs powder, sharp porous nanoplates with serrated edges are visible in **Figure 3.1**b, although these particles tend to be tightly packed into 3D hierarchical structures in the form of flower-like microstructures. The nanoplates are thin (<100 nm thickness), elongated (maximum length: <3.5 µm) and exhibit a highly porous surface with a large pore size in the range of hundreds of nanometers that are formed during calcination at 700 ºC.

In **Figure 3.1**c, the diffraction peaks for both ZnO powders can be attributed to hexagonal wurtzite ZnO structure (International Centre for Diffraction Data (ICDD) Powder Diffraction File (PDF): 00-036-1451).[251,252,276] The three highly narrow and intense peaks observed within the range 30–40º imply that the ZnO powders are well-crystallized. There are not additional peaks related to the presence of impurities in the ZnO PNPs, which suggests their high purity.[289] On the other hand, the bands between 1500–1300 cm^{-1} and 1100–700 cm^{-1} in the FTIR spectra confirm the presence of carbonate groups, which implies the incomplete pyrolysis of the hydrozincite precursor (**Figure 3.1**d).[251,289,290]

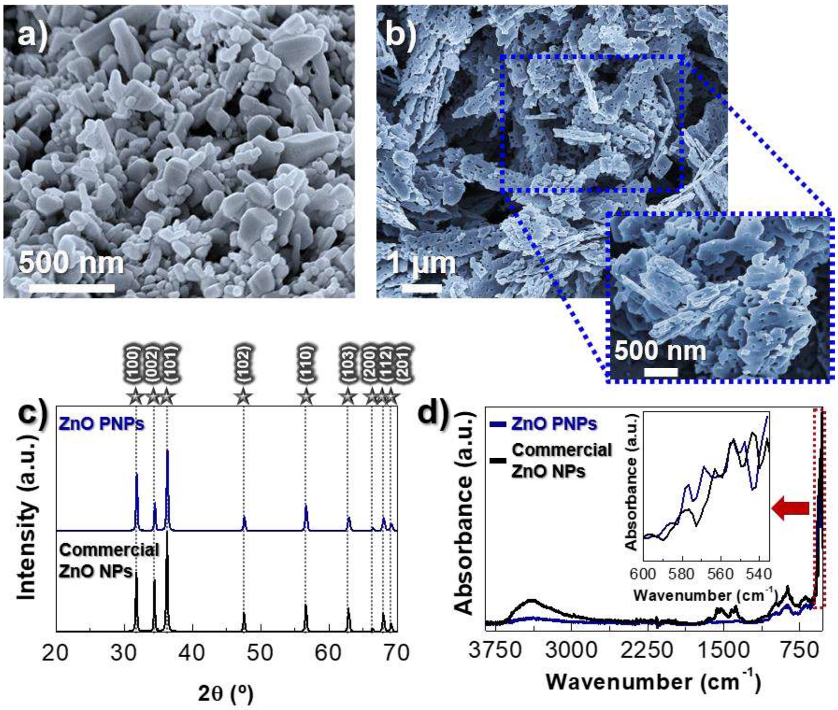

Figure 3.1. Characterization of ZnO nanostructures. SEM images for different magnifications of **a)** commercial ZnO NPs, and **b)** synthesized ZnO PNPs. **c)** XRD diffractograms. **d)** FTIR spectra (inset: magnification of the absorption band at 600–530 cm^{-1}).

FTIR spectra also shows a broad and intense band for low wavenumbers (<600 cm^{-1}) attributed to the Zn–O stretching vibrational mode.[276] The broad absorption peak at 3700–3000 cm^{-1} and small band at 1633 cm^{-1} correspond to stretching and bending modes of hydroxyl groups of absorbed water at the surface of the particles, respectively, which is related to atmospheric moisture.[291] All the referred bands are very pronounced in commercial ZnO NPs in opposition to ZnO PNPs, which clearly indicates a higher degree of contamination by the remaining precursor.

3.2. Characterization of office paper substrate

Figure 3.2a-b depicts SEM images of the office paper's morphology. Individual, heavily entangled cellulose fibers can be clearly distinguished, which are held together by hydrogen bonding between the hydroxyl groups, aiding the mechanical robustness of office paper. The hydrogen bonding and mechanical entanglement of the fibers yield a layered and relatively compact porous network, as shown in the cross-section image in **Figure 3.2**b. The long and wide cellulose fibers exhibit varied sizes, surpassing the microscale in length, while their width is in the range of 10–25 μm. Also, some hygroscopic fillers are visible among the fibrous network of paper, corresponding to calcium carbonate ($CaCO_3$), as confirmed by XRD (inset in **Figure 3.2**a). Besides, XRD diffractogram also reveals the characteristic peaks for $(1\bar{1}0)$, (110) and (002) crystallographic planes at 2θ = 15, 16.5, and 23.2°, respectively, correspond to cellulose I. According to the empiric method proposed by Segal et al.[292], the crystallinity index (CrI) of office paper was calculated using **Equation S1**, and it was estimated to be around 78 %.

As observed in **Figure 3.2**c, the surface defects existent in the office paper are responsible for its high roughness (root mean square (RMS) roughness: ≈2.21 μm).

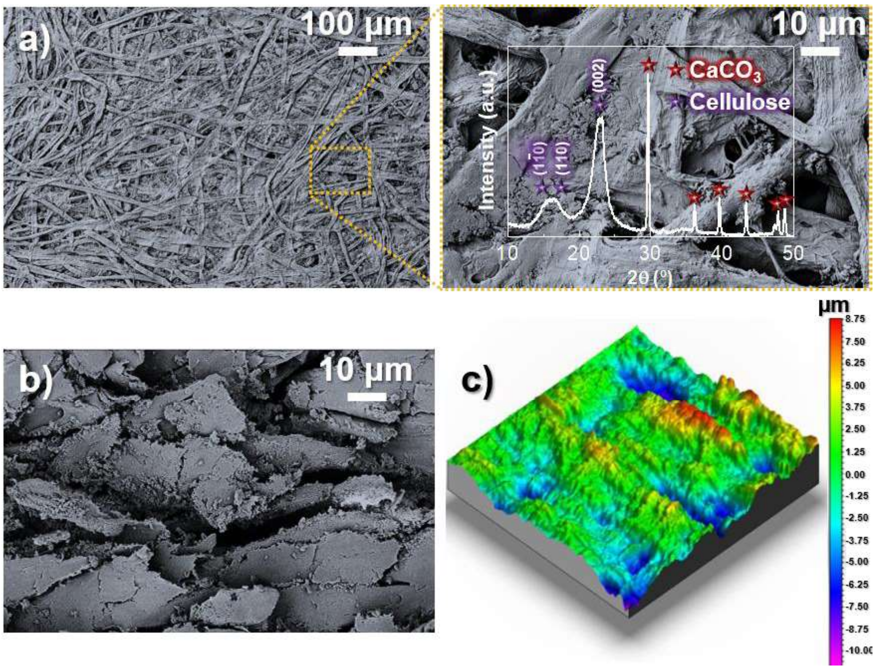

Figure 3.2. Morphological and structural characteristics of office paper substrate. **a)** SEM images of the surface of office paper for different magnifications (inset: XRD diffractrogram of office paper). **b)** Cross-section image of office paper. **c)** 3D profilometry of office paper (area: 0.5 x 0.5 mm^2).

3.3. Formulation and screen-printing of cellulose composite inks

3.3.1. Formulation of cellulose composite inks

Before mixing the organic binder with the inorganic nanostructures, a first attempt to optimize the cellulose derivative content was performed towards better printability on office paper substrate. Several aqueous solutions of CMC with different contents (1–3 wt.%) were prepared. For contents lower than 3 wt.% the binder solution drains through the mesh openings without applying a shear stress, therefore no further studies were carried for such concentrations.[278] On the other hand, the supplier already reports a viscosity of 0.3 Pa s for 5 wt% of EC in a mixture of organic solvents (80/20 v/v.% of toluene/ethanol), which value is within the typical range of values reported for screen-printable inks.[11,155] Superior amounts of EC were not tested due to the high volatility of the organic solvents used to dissolve EC. Therefore, the chosen contents for CMC and EC were 3 and 5 wt.%, respectively.

The rheological behavior of the selected binders was first investigated (**Figure 3.3**a). It is clear from the results that both binder solutions displayed a shear thinning thixotropic behavior. The corresponding viscosities at a fixed shear rate of 1 s^{-1} for the CMC and EC solutions are 3.9 and 21 Pa s, respectively. The rheological behavior and high viscosity (>1 Pa s) presented by both binders is appropriate for screen-printing.[11,155]

The balance between the proportion of functional material and binder/solvent to yield good printability on paper and achieve the intended functionality was further studied by changing the content of commercial ZnO NPs from 10 to 40 wt.%. Higher loading contents were not tested as the resulting inks are too viscous and pasty to be printed, drying almost instantly in the mesh. As verified in **Figure 3.3**b, the incorporation of functional ZnO particles increases the viscosity of the inks. Using as example the formulated water-based highly loaded C3Z40 ink, which is composed of a 40 wt.% of commercial ZnO NPs, the viscosity is around 1.2 and 1.1 Pa s at 25 and 30 ºC, respectively, for a shear rate of 300 s^{-1}. This feature is required to prevent the excessive spreading of the ink on the paper surface, allowing the formation of a continuous film.

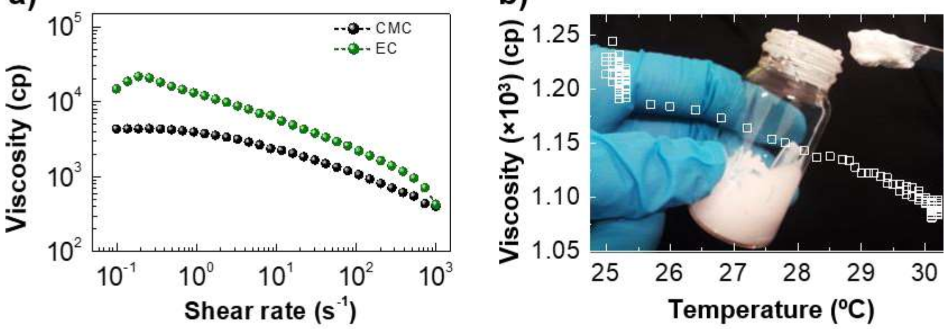

Figure 3.3. Inks' characteristics. a) Rheological behavior of CMC and EC binder solutions. **b)** Viscosity as function of the temperature for C3Z40 ink (Inset: photo of the cellulose composite semiconducting ink).

3.3.2. Printing trials on office paper

3.3.2.1. Influence of cellulose derivatives and ZnO content

Figure 3.4 depicts SEM images of the office paper's surface after performing printing trials with the developed inks using a polyester screen mesh with an aperture width of 81 μm at ambient conditions (40–45 %RH), which clearly demonstrates how the binder as well as the amount of functional material affect the printability on paper and the formation of percolative paths. The samples were dried at RT for 1 h before analysis.

Regarding the inks with CMC in their composition, these inks do not enable a uniform coverage of the highly fibrous surface of office paper for ZnO contents lower than 40 wt.%, as individual cellulose fibers as well as occasional uncovered areas can still be distinguished. The presence of some poorly coated fibers with ZnO particles disrupts percolation paths that are crucial for the intended functionality of the printed films as channel layer in transistors. Furthermore, the contribution from CMC binder should also not be disregarded as its presence around the particles also impairs part of their functionality, and it is more pronounced in the films composed of low amounts of particles. As a result, these poorly percolated films do not display a satisfactory performance when working as semiconducting layer in EGTs, as the number of percolative paths are not enough to promote electrical modulation of the transistors.

A balance between the amount of CMC and ZnO must be found to ensure the printing of a densely packed and reasonably uniform film along the irregular and rough surface of paper, while providing a continuous path between small-sized nanoparticles. From all the formulated inks, the ink that endows such features is the one composed of 40 wt.% of ZnO nanoparticles. Some agglomerates are still visible along the surface of the printed films, which could be avoided with heavy functionalization of the particle surfaces, although the semi-insulating nature of the stabilizers would later compromise RT functionality.

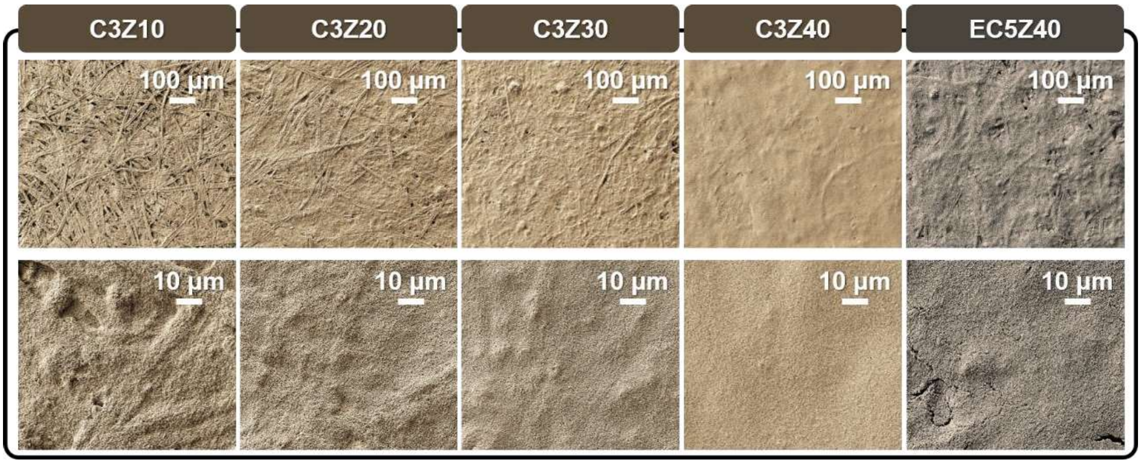

Figure 3.4. SEM images of the screen-printed cellulose/ZnO composite films on office paper.

Concerning the influence of the binder, a comparison between C3Z40 ink and EC5Z40 ink was performed for the optimized content of ZnO particles, set as 40 wt.%. When EC is used as binder, the high volatility of the solvents promotes the formation micro-cracks during drying because of the reduced network strength between the inorganic particles. Although a slight increase on the EC content could promote a better coating of office paper, a thicker organic layer involving the functional particles would compromise the functionality of semiconductor or introduce excessive leakage in the devices. In alternative, the replacement of toluene and ethanol by solvents with slower evaporation rate, such as diacetone alcohol, could promote a better film formation.

Higher magnifications of the screen-printed films prepared from C3Z40 ink and EC5Z40 inks show a compact close-packing of particles and some agglomerates (**Figure 3.5**a,b). Particle bridging occurs through the development of hydrogen bonding between hydroxyl groups existent within the cellulosic materials and surface oxygen of ZnO particles.[283,293] Despite the presence of the insulating cellulosic matrix wrapping the semiconducting material that hinders the electronic transport, the high content of ZnO in both inks provides a continuous path through small contact points between adjacent individual particles for electron percolation. Some voids are formed between the particles, when non-ideally packed, that are more evident and larger in printed films composed of EC, due to the fast evaporation of the organic solvents. As verified by AFM measurements, the presence of such defects contributes for unwanted surface roughness, which was measured to be of 106 and 166 nm for C3Z40 ink and EC5Z40 ink, respectively (**Figure 3.5**c,d).

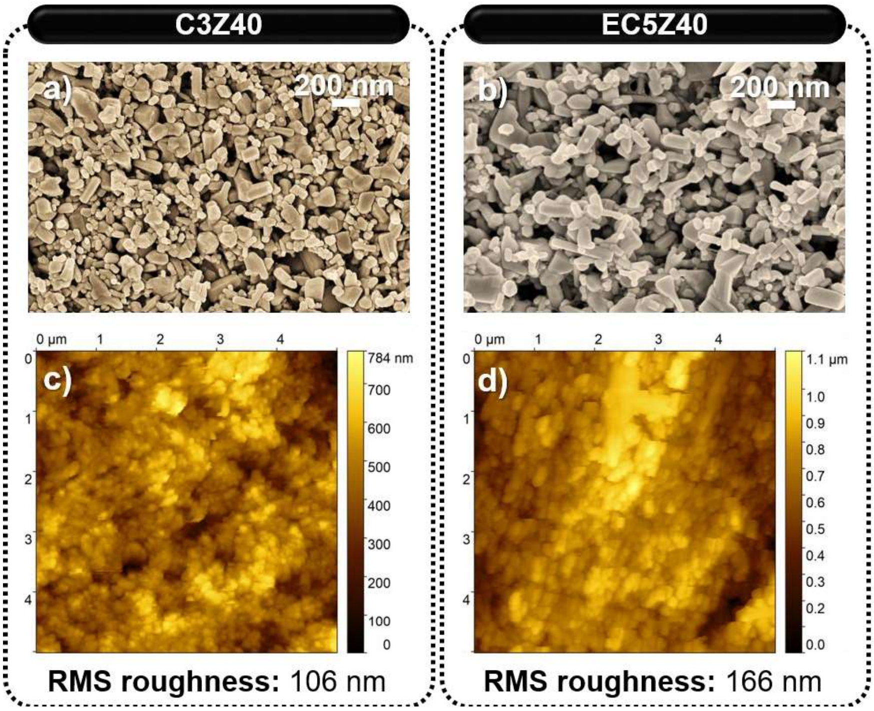

Figure 3.5. Surface defects of the screen-printed ZnO films on office paper. SEM images for higher magnifications of screen-printed film on office paper using **a)** C3Z40 ink, and **b)** EC5Z40 ink. AFM images of the screen-printed films on office paper using **c)** C3Z40 ink and **d)** EC5Z40 ink.

The interface between the printed layer and the paper surface was evaluated through the analysis of cross-sectional SEM images (**Figure 3.6**). Despite all the challenges related to paper surface roughness and absorption, a continuous composite thick film with good adhesion to the hydrogen-bonded cellulose fiber network is formed with a single printing pass. There are no signs of cracks nor peeling alongside their thickness. The cracks observed in the EC5Z40 film are formed at the surface, thus maintaining its mechanical integrity. The high viscosity of the inks prevents excessive swelling of the paper structure, allowing the formation of continuous thick films on paper's surface with a thickness of 18.8 ± 0.33μm and 17.4 ± 0.16 μm for C3Z40 ink and EC5Z40 ink, respectively. The small error observed when measuring the thickness of the printed layer indicates that screen-printing technique is suitable to form a uniform and relatively smooth interconnected particle monolayer, even on highly textured substrates, like paper.

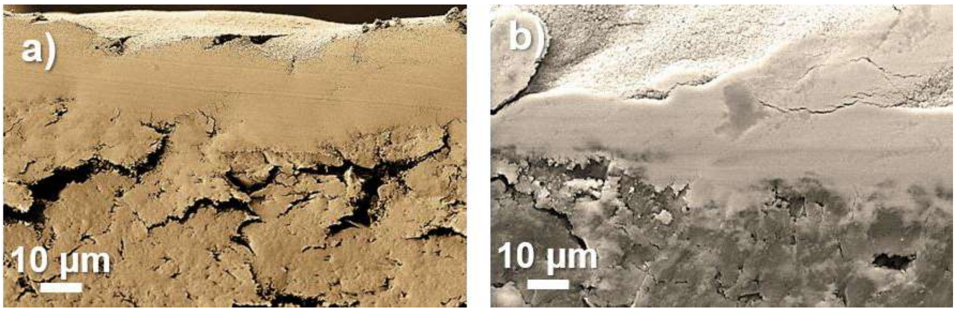

Figure 3.6. Quality of the interface between the screen-printed films and office paper. Cross-section SEM images of the screen-printed films on office paper using **a)** C3Z40 ink, and **b)** EC5Z40 ink.

Figure 3.7a,c show the optical microscope images of screen-printed lines on office paper with various line widths (≈150–350 μm), which were obtained from a polyester screen with the same line openings. Despite the high viscosity of the inks and the slight hydrophobic behavior of paper's surface (contact angle around 101 and 106 º),[42,278] the swelling of the paper can take place due to the solvent absorption during the printing process and due to slight changes in the RH. This hygroexpansion effect can promote the lateral spreading of the inks, which varies from 2.5 to 19 % and 1.3 to 15 % for EC5Z40 ink and C3Z40 ink, respectively. The lower spreading observed for the water-based ink is possibly promoted by the hydrophobic behavior of paper, although this effect decreases overtime owing to the absorptive porous surface of paper and slow evaporation of water in comparison with the ethanol/toluene solvent mixture used on the EC5Z40 ink.[278] Furthermore, these variations are more significative for smaller line widths, where the micrometric size (>10 μm wide) of the entangled cellulose fibers has a more notorious influence. The printed lines exhibit wave-like edges and blank areas are also visible, which can be attributed to fast printing and non-uniform pressure.[139]

The maximum printing resolution achieved for each ink was obtained for a line width of 150 μm, enabling the printing of well-defined lines on office paper with a minimum width of and 167 ± 6.91 μm and 162 ± 2.68 μm for EC5Z40 ink and C3Z40 ink, respectively (**Figure 3.7**b,d). The obtained values are within the typical printing resolution of screen-printing method, which ranges from 50 to 150 µm when using conventional screen-printing meshes with line openings of 40 to 120 µm.[172] Despite the sub-micrometric size of the ZnO particles, they tend to form agglomerates with larger size that are prevented from passing through the screen woven mesh to the substrate, creating defects in the printed film. Furthermore, the quality of the screen mask based on woven mesh has inherent limitations, which hinders high-resolution screen-printed patterns.

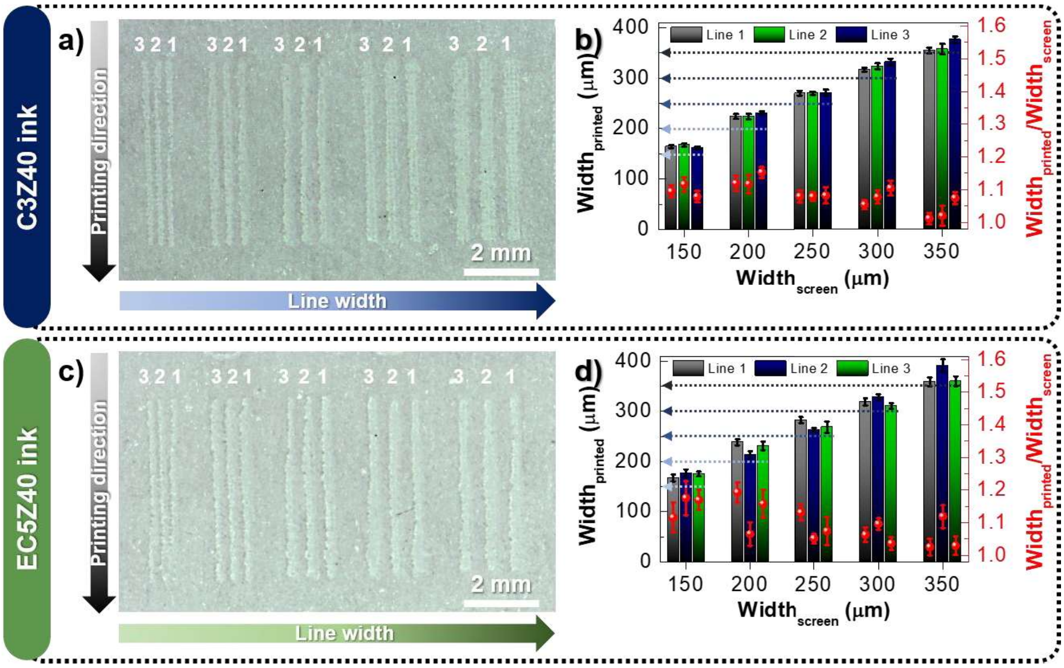

Figure 3.7. Printing resolution of the screen-printed films on office paper. Optical microscope image of screen-printed lines on office paper with different spacings (150 – 350 µm) for **a)** C3Z40 ink and **c)** EC5Z40 ink. Measured line width (width$_{printed}$) as a function of theoretical line width (width$_{screen}$) for **b)** C3Z40 ink and **d)** EC5Z40 ink, and respective lateral spreading (width$_{printed}$/width$_{screen}$). The values show the average and respective standard error of the mean obtained from ten measurements for each line.

3.3.2.2. Influence of drying conditions

The possibility to print a functional inorganic semiconductor under ambient conditions without the need of thermal annealing is highly appealing in terms of compatibility with paper, thus ensuring at the same time low energy consumption and less time expended in the manufacturing process. Still, the time and temperature required to ensure the evaporation of solvents from the printed film must also be considered.

TGA measurements were performed in air to study the thermal behavior of the inks and office paper substrate (**Figure 3.8**a). Heating promotes an initial weight loss at temperatures lower than 100 ºC on office paper, which is related to water desorption from hygroscopic fillers and hydrophilic functional groups of cellulose fibers. The small weight loss is inferior to 5 %, thus the printed layers are not expected to be significantly deformed during heating within this range of temperatures. A sharp weight loss occurs between 240–325 ºC related to the thermal degradation of cellulose.

Regarding the thermal behavior of the inks, the solvents in their composition have a major influence. For EC5Z40 ink, the evaporation of organic solvents occurs almost instantly due to their high volatility, as verified by the significant weight loss (≈46 %) shortly after starting the measurement. On the other hand, it is possible to get a better control on the evaporation of solvents from C3Z40 ink with heating. In this case, a considerable weight loss occurs at a slower rate as temperature rises until 100 ºC, corresponding to the boiling point of water. The thermal degradation of the cellulose derivatives of the inks occurs for temperatures above 250 ºC.[57,278]

Considering the slower evaporation rate of C3Z40 ink, a detailed study was carried out by FTIR to understand the effects of drying time and temperature on the water evaporation rate of the screen-printed films (**Figure 3.8**b-e). The drying temperature was limited to 120 ºC to ensure water evaporation, while preserving the integrity of the binder and substrate. For this purpose, C3Z40 ink was screen-printed on glass, since FTIR spectra of paper is deeply influenced by the adsorbed water.[41] FTIR spectrum of CMC powder is also represented for comparison. The spectra were baseline corrected to 0 at 1845 cm^{-1} and 3739 cm^{-1} and normalized to 1 at 2900 cm^{-1}, which forms a common baseline for the study of water content inside the printed films.[294]

Looking at the FTIR spectra in **Figure 3.8**b, the slight changes observed in the intensity and shift of FTIR bands in the nanocomposite are related to the formation of interactions between ZnO nanopowder and functional groups of CMC matrix through hydrogen bonding.[295–297] This is also confirmed by the presence of a wide peak for low wavenumbers (<570 cm^{-1}) related to the presence of a metal oxide bond (Zn–O stretching vibrational mode), as observed in **Figure 3.8**c.[276] Several characteristic absorption bands for CMC are visible in the printed composite films.[296–299] The absorption bands at 2920, 1593, 1413 and 1056 cm^{-1} correspond to asymmetric C–H stretching from $-CH_2$ group, asymmetrical vibration stretching of COO–, symmetrical vibrational stretching of COO–, and stretching vibration of C–O group, respectively. The peak around 1320 cm^{-1} can be assigned to C–O–C stretching vibration. A new absorption peak around 1500 cm^{-1} appeared in the CMC/ZnO composite that can be attributed to H–O–H bending vibration mode of ZnO due to the adsorption of moisture.[300] The broad absorption band at 3700–3000 cm^{-1} increases significantly and shift to higher wavenumber with the addition of ZnO NPs (**Figure 3.8**d).[295] This band is assigned for –OH stretching vibration, which can be associated to the water content within the printed patterns, giving a valuable information about the evaporation rate.

The high loading content of ZnO NPs leads to faster drying of the printed film, even at RT. Although there is a small decrease in the absorption bands in the range 3700–3000 cm^{-1} for longer drying times at RT, there were no significant variations after 19 h of storage under RT. This suggests that the printed film establishes an equilibrium with the ambient moisture. These variations are almost imperceptible at 120 ºC, which indicates that the sample dried instantly when heated (**Figure 3.8**e).

The drying conditions were selected to obtain an economically efficient and simplified manufacturing process. Thus, the inks were printed and dried at ambient conditions for a period of less than 10 min for subsequent integration in EGTs and integrated circuits (**chapter 6**).

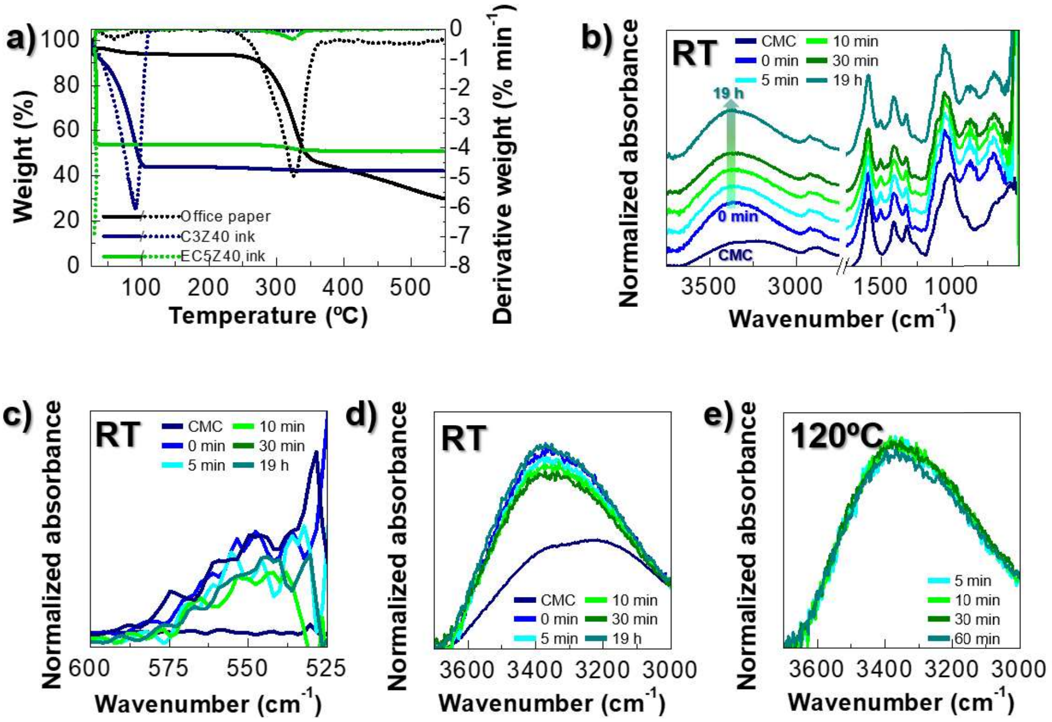

Figure 3.8. Influence of the drying conditions. **a)** TGA curves of C3Z40 ink, EC5Z40 ink, and office paper, and respective derivatives. Normalized FTIR spectra of C3Z40 ink screen-printed on glass and dried at **b)** RT, and **e)** 120 ºC for different times. Magnifications of the normalized absorption bands at **c)** 600–525 cm^{-1}, and **d)** 3700–3000 cm^{-1} for C3Z40 ink screen-printed on glass and dried at RT for different times. Magnifications of the normalized absorption bands at **e)** 3700–3000 cm^{-1} for C3Z40 ink screen-printed on glass and dried at 120 ºC for different times.

3.3.2.3. Influence of ZnO nanostructures

In this work, synthesized ZnO PNPs were used in alternative to the small commercial ZnO NPs to form percolation network at lower contents. Interestingly, ZnO nanostructures with a porous morphology is advantageous for sensing applications, as a high number of pores result in high specific surface areas for the adsorption of molecules, thus enhancing their sensing responsivity. Although there are several reports that demonstrate the superior performance of ZnO PNPs in gas sensors, dye-sensitized solar cells, photodegradation, and biosensing, their performance in transistors and circuits has never been tested.[301]

To formulate inks with ZnO PNPs, CMC was selected as binder since it allows the printing of smoother and less defective films on office paper in comparison with EC, as previously observed. Different water-based CMC/ZnO PNPs inks were prepared by varying the amount of ZnO PNPs (10–40 wt.%), and then screen-printed on office paper in the same conditions, as previously described, and dried at RT for 10 min before analysis.

A closer examination of the SEM images in **Figure 3.9** reveals a reasonably dense and compact network structure of stacked ZnO PNPs, randomly oriented with dispersed sizes and shapes. The mechanical stress induced during preparation of the inks under stirring promotes the disassembling of the 2D nanostructures, thus destroying their arrangement in the form of flowers. On the other hand, the shear stress induced during the printing process can severely damage the particles, breaking some of the dispersed ZnO PNPs.

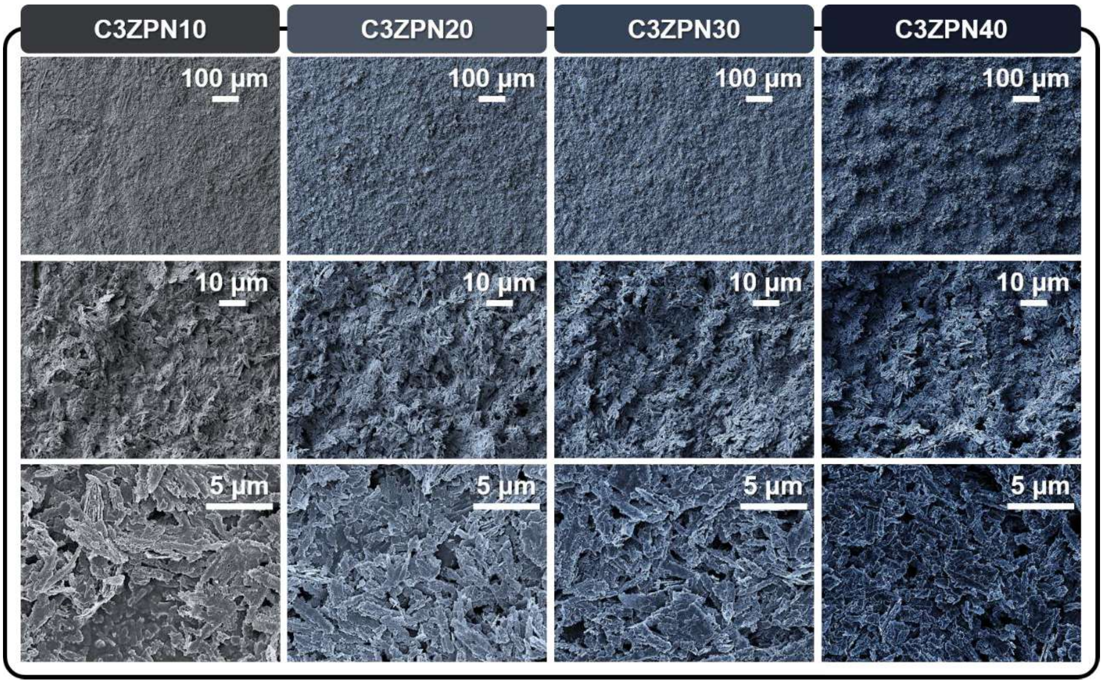

Figure 3.9. SEM images of screen-printed CMC/ZnO PNPs films on office paper.

For the smallest amount of ZnO PNPs, it is still possible to observe the fibrous surface of paper as well as the binder surrounding the particles, which compromises their efficient percolation. Larger amounts of ZnO PNPs yield better coating of office paper and a more direct percolation path between the elongated structures, enhancing their conductivity thanks to the anisotropic diffusion of electrons. On the other hand, extreme amounts of ZnO PNPs (≈40 wt.%) make the ink too viscous and pasty to be printed. Consequently, the texture of the woven mesh is transferred to the film during printing, yielding a wave-like rough surface from the crossed threads of the mesh.

In comparison with commercial ZnO NPs, the elongated size of the ZnO PNPs can form a percolation network at considerably lower particle loading, decreasing 50 % of the amount of functional material in the ink. Nevertheless, despite the better percolation achieved for printed films composed of ZnO PNPs, their morphology creates micro-sized voids that contribute to large surface roughness. Bundles and aggregates responsible for the slightly rough and irregular surface are also visible.

Regarding the printing resolution of the developed CMC/ZnO PNPs inks, printed lines with a minimum width of 147 ± 3.92, 152 ± 2.65, and 132 ± 6.24 µm can be obtained for C3ZPN10, C3ZPN20, and C3ZPN30 inks, respectively. Some variations in the width of the lines can be observed for the same ink, which can be related to defects or poor resolution of the screen mesh (**Figure 3.10**). Larger amounts ZnO PNPs lead to narrower lines, as the particles tend to be close to each other.

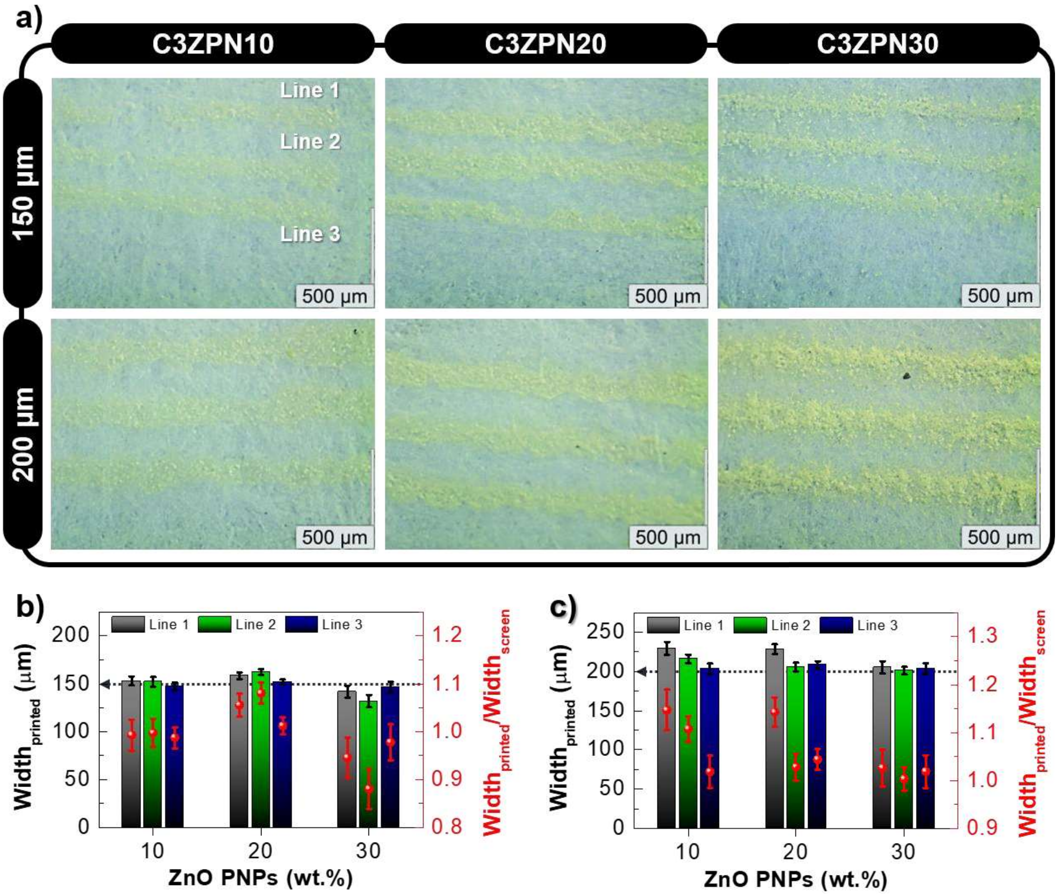

Figure 3.10. Printing resolution of screen-printed CMC/ZnO PNPs films on office paper. **a)** Optical microscope image of screen-printed lines on office paper with different spacings (150 and 200 µm) for C3ZPN10 ink, C3ZPN20, and C3ZPN30 inks. Measured width$_{printed}$ as a function of the loading content of ZnO PNPs in the ink composition for a spacing of **b)** 150 and **c)** 200 µm, and respective lateral spreading (width$_{printed}$/width$_{screen}$). The values show the average and respective standard error of the mean obtained from ten measurements for each line.

Chapter 4

Cellulose-based iontronic membranes

4. Cellulose-based iontronic membranes 57
  4.1. Development of self-healable cellulose iontronic hydrogels 58
    4.1.1. Formulation using aqueous alkali hydroxide/urea dissolution system 58
      4.1.1.1. Aqueous LiOH/urea solvent system 58
      4.1.1.2. Aqueous mixed alkali salts/urea solvent system 60
    4.1.2. Optical, structural, compositional, and morphological properties 61
    4.1.3. Electrochemical properties 65
      4.1.3.1. Influence of the addition of CMC 66
      4.1.3.2. Influence of the alkali hydroxide 68
  4.2. Development of iontronic cellulose nanopaper composites 70
    4.2.1. Optical, structural, compositional, and morphological properties 70
    4.2.2. Electrochemical properties 74

This chapter is devoted to the results that cover the development of cellulose composites with electrolytic properties targeting their application as electrolyte-gate layer in transistors and circuits with low-voltage operation.

Regenerated cellulose-based electrolytes were strategically designed taking into consideration the arise of a new worldview of modern society that demands the adoption of sustainable concepts by making greater use of abundant, renewable and environment friendly raw materials. Despite the challenges involved in the reengineering of cellulose through chemical processing, many strategies have been reported over the last years to successfully dissolve this biopolymer and prepare new regenerated cellulose materials. Among a broad range of solvent systems capable of dissolving cellulose, it is known that cellulose is soluble in aqueous alkali hydroxide systems combined with other additives such as PEG, urea, and/or thiourea, when precooled to temperatures below -5 ºC.[83,85–98] In comparison with other methods that generally require time- and energy-consuming procedures as well as toxic and expensive chemicals, this low-temperature strategy is considered an economically efficient dissolution method of native cellulose. This route fits the compromise of environmental awareness as it is fast, non-polluting, easy to handle and uses common chemicals that do not produce any hazardous byproducts.[67]

Having this in mind, regenerated cellulose-based hydrogels were produced from dissolution of MCC in pre-cooled aqueous alkali hydroxide/urea solvent systems. The hydrogels were prepared by varying the alkali hydroxide, such as LiOH/urea and/or NaOH/urea,[84] to result in Li^+ and/or Na^+, respectively, insertion within the cellulose matrix after regeneration. The influence of the addition of a water-soluble cellulose derivative as a mechanical strengthener was also studied.

An additional strategy was implemented to further improve their robustness towards their application as an ionic conductive substrate. For this purpose, a “paper-like” ACICC was prepared by combining the intrinsic mechanical robustness and smoothness of MFC/NFC (nanopaper) with the appealing electrochemical properties of the prepared CICHs.

The developed cellulose-based electrolytes will be under focus in the following sections, where a deep understanding of the impact of their formulation on the compositional, morphological, structural, thermal, and optical properties will be addressed. More importantly, the study of their electrochemical properties assumes great interest to validate their suitable use as electrolyte-gate in transistors.

4.1. Development of self-healable cellulose iontronic hydrogels

4.1.1. Formulation using aqueous alkali hydroxide/urea dissolution system

4.1.1.1. Aqueous LiOH/urea solvent system

CICHs were produced from a simple, fast, low-cost, and environmentally friendly dissolution method of MCC at low temperature, which involves an aqueous alkali hydroxide/urea solvent system. The first attempts to develop the CICHs started with the use of LiOH as the alkali hydroxide component of the solvent system for the dissolution of MCC, due to its superior dissolution efficiency compared to NaOH.[84,87]

The transparency of the solutions can be related with the efficiency of the dissolution process of cellulose. As shown in **Figure 4.1**a, a fully transparent slightly viscous solution is obtained due to the good solubility of cellulose in the precooled aqueous solution LiOH/urea, using a freezing-thawing process that promotes the fast dissolution of cellulose in a few minutes (≈5 min) under vigorous stirring at low temperatures (below -8 °C).

The dissolution of cellulose in the presence of an alkaline salt, urea, and water provides ions which serve as charge carriers that contribute to ionic conductivity under the influence of an electric field. Thus, Li^+ is already trapped in the cellulose solution but the presence of OH^- turn the solution highly alkaline (pH = 14), impeding its direct application onto devices without damaging the deposited layers.

A three-in-one step was conducted on the cellulose solution in alkali/urea aqueous system, which consists of its neutralization, simultaneous cellulose regeneration, and additional incorporation of protons with acetic acid. The acetic acid was slowly added “drop-by-drop” to the cooled cellulose solution, under stirring, to avoid the overheating of the solution.

Figure 4.1b shows the resulting whitish liquid solution having a solid phase well dispersed in the aqueous-based solution that is associated to the regenerated cellulose. Unlike the conventional method of immersion of the dissolved cellulose solution in a regeneration bath, the regeneration of cellulose under stirring conditions leads to the formation of a regenerated cellulose pulp instead of a robust “sheet-like” hydrogel. Furthermore, it is also worth noting that after obtaining regenerated cellulose materials from this dissolution method, a washing step with excess in deionized water is commonly performed to remove the residual chemical reagents, thus removing the mobile ions yielded from the dissociated salts in water. In this work, the washing step in water was skipped to trap the mobile ions within cellulose network that will deeply contribute to the ionic conductivity of the resulting electrolyte.

The regenerated cellulose pulp was shear-casted on glass and dried at RT, yielding a sticky hydrogel membrane (**Figure 4.1**c). The produced hydrogel membrane (referred to as MC0) can be delaminated from the glass and due to its gel-state, further it is possible to cut the hydrogel into stripes and manipulate its shape. However, the smooth and sticky membrane is slightly cracked, thus it is necessary to improve its mechanical properties to obtain a flexible yet robust free-standing hydrogel membrane that can be easily applied on bendable substrates, such as paper.

The development of composite hydrogels with reinforcing fillers or hybridizing of different polymers can improve the mechanical properties of the original hydrogel without sacrificing the ionic conductivity.[102] For this purpose, sodium-salt CMC was chosen due to its polymeric structure and high molecular weight that enables a wide range of possible chemical reactions offered by the presence of reactive carboxyl groups.[302,303] . It is as water-soluble anionic polyelectrolyte usually used as a thickener and rheology modifier.[302,303]

Different amounts of CMC were added to the MCC solution, where the resulting solution is transparent and slightly yellowish (see **Figure 4.1**b) and its viscosity increases with the amount of CMC added. The Li-CICHs obtained from MCC:CMC mixtures with a weight ratio of 2:1 and 1:1 were coded as M2C1 and M1C1, respectively. The addition of CMC improves the mechanical properties of the resulting Li-CICHs, where the regenerated cellulose pulp is dispersed into a CMC matrix, decreasing the formation of fractures. Only for the highest CMC amount (M1C1 membrane), a flexible, robust and sticky regenerated cellulose-based membrane with high conformability is obtained, as it can be easily molded and folded (**Figure 4.1**c,d). The membrane can be cut in the desired size and shape, peeled-off from glass and transferred using tweezers to a device, like a sticker, decreasing considerably the time and degree of manufacturing. Thus, the formulation of M1C1 hydrogel will be the prime focus on the following sections.

Considering possible concerns over rising lithium costs in the future, sodium salts emerge as a more environmentally friendly and less expensive alternative. Thus, CICHs were also prepared by replacing or combining LiOH with NaOH for cellulose dissolution.

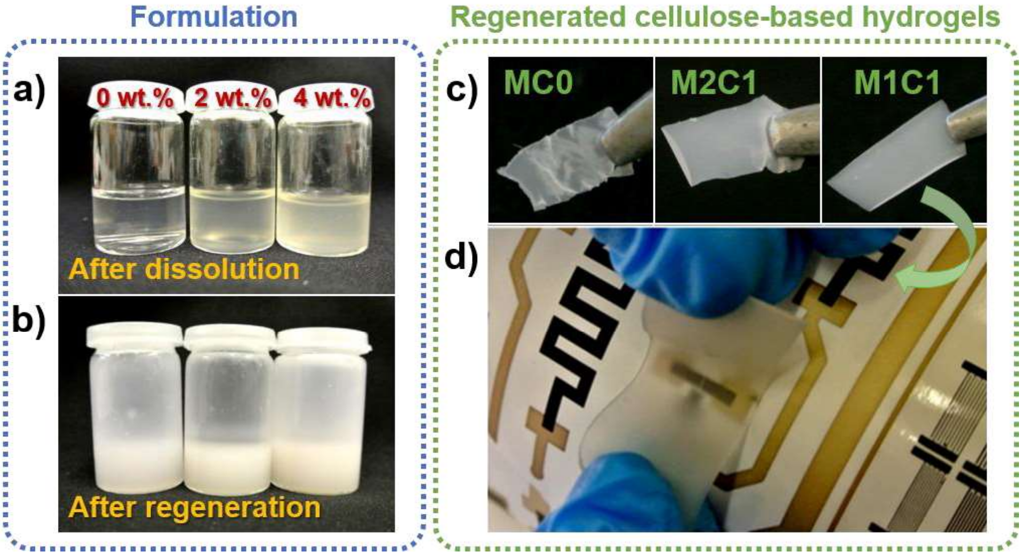

Figure 4.1. Photography of different stage steps of the developed Li-CICHs with different proportions of MCC:CMC. Photograph of the MCC:CMC solutions with different weight ratios of CMC (0, 2, and 4 wt.%) **a)** before and **b)** after regeneration. **c)** Resulting flexible, freestanding Li-CICHs, referred to as MC0 (0 wt.% of CMC), M2C1 (2 wt.% of CMC), and M1C1 (4 wt.% of CMC). **d)** Demonstration of the high conformability and adhesion of the M1C1 hydrogel.

4.1.1.2. Aqueous mixed alkali salts/urea solvent system

As illustrated in **Figure 4.2**, the optimized formulation of CICHs consists of the dissolution of mixtures of MCC and CMC in pre-cooled aqueous alkali hydroxide solvent systems, such as LiOH/urea and/or NaOH/urea, followed by regeneration with acetic acid under stirring. In order to get a reliable comparison on the influence both alkali hydroxides in the properties of the CICHs, the concentration of NaOH used for dissolution of cellulose was the same as the typically reported for LiOH (4.6 wt.%) in urea (15 wt.%)/water solvent system.[84,88,89] Several mixtures of LiOH and

NaOH were also prepared (LiOH:NaOH = weight ratio of 3:1, 1:1, 1:3, 1:19), maintaining the weight ratio of alkali hydroxide in urea/water solvent system constant. The hydrogels obtained from LiOH:NaOH mixture were named as L3N1, L1N1, L1N3 and L1N19, respectively. The hydrogels obtained from this method were compared with those prepared using just LiOH (also referred to as L100) or NaOH (referred to as N100) in the cellulose dissolution.

The dissolution of MCC has shown to be less effective in the aqueous NaOH/urea solvent system in comparison with the use of LiOH, since the smaller ionic radius of Li^+ and its high charge density promotes an easier diffusion into the cellulose chain. One freezing-thawing cycle was performed to optimize cellulose dissolution since the concentration of NaOH used is lower than the ideal for an efficient dissolution, which according to literature is between 6–10 wt.% at temperatures between -15 and 4 ºC.[83] Still, the resulting viscous MCC:CMC solutions after regeneration with acetic acid were shear-casted on glass and dried at RT, yielding flexible, robust and sticky regenerated cellulose-based membranes with high conformability, as they can be easily molded and folded (**Figure 4.3**a).

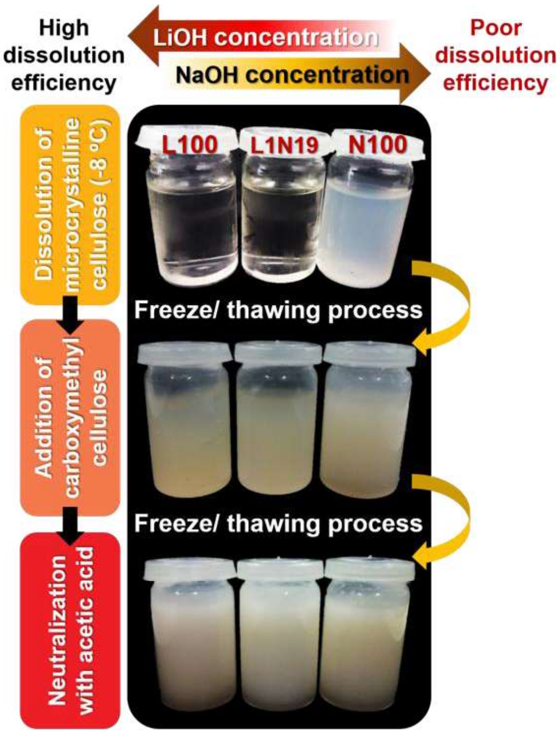

Figure 4.2. Photography of the different stage steps of the developed cellulose-based solutions with different proportions of LiOH and NaOH. The procedure starts with the dissolution of MCC powder in the aqueous alkali hydroxide/urea solvent system, followed by the addition of CMC and regeneration/ neutralization of the cellulosic solution with acetic acid. A freeze-thawing process is performed between each step in order to improve MCC dissolution.

4.1.2. Optical, structural, compositional, and morphological properties

As depicted in **Figure 4.3**b, the CICHs exhibit reasonable transparency, presenting a total transmittance of 88, 87 and 86 % at 700 nm for L100, L1N3, and N100 electrolytes, respectively, making them suitable for applications where transparency is a desirable feature.

Figure 4.3c displays the XRD patterns of both L100 and N100 membrane, where are visible two peaks at 20 and 22º for (110) and (200) planes, respectively, which are characteristic for cellulose II crystal, thus confirming the regeneration of cellulose with acetic acid.[87,304]

Figure 4.3d shows the thermal degradation of the different CICHs, which starts with the desorption of moisture adsorbed in the cellulose-based matrix at temperatures below 100 ºC, followed by a steep weight loss up to nearly 240 ºC related to the thermal degradation of the composite material. The pronounced weight loss observed at low temperature corresponds to 11 and 14 % at 100 ºC for the L100 and L1N3 membranes, respectively, which corroborates their hydrogel character due to their ability to retain a high amount of weakly bonded water that is adsorbed in the cellulose network.

FTIR spectra of CICHs are displayed in **Figure 4.3**e, and the spectrum of MCC powder is used as reference The spectra were baseline corrected to 0 at 1845 and 3739 cm^{-1}, and normalized to 1 at 2900 cm^{-1}, which forms a common baseline for the study of water content inside the membranes.[294]

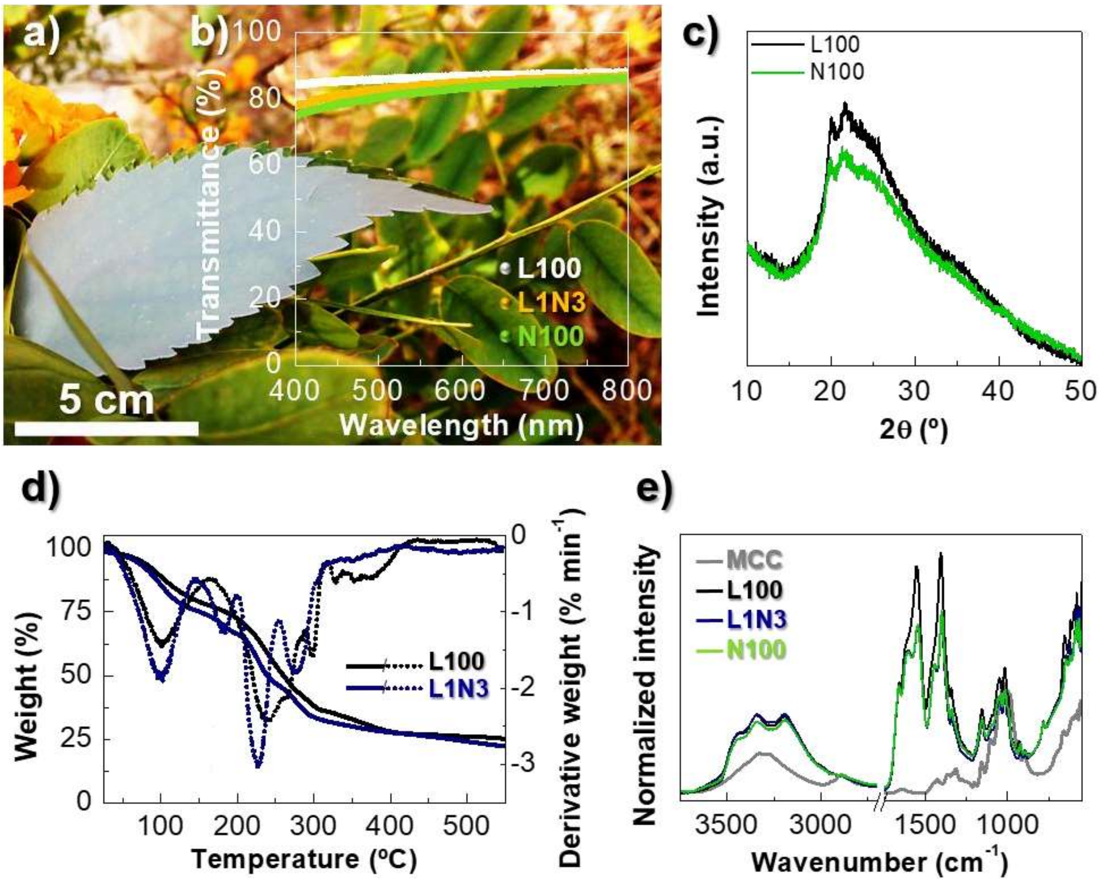

Figure 4.3. Optical, structural, thermal, and mechanical properties of CICHs. **a)** Photography of the developed highly conformable and sticky Na-CICH, which was cut with the same shape of a leaf. Main properties of CICH membranes: **b)** Total optical transmittance, **c)** XRD diffractograms, **d)** TGA curves and respective derivatives (dotted lines), **e)** FTIR spectra (MCC powder used as reference).

A series of characteristic absorption bands for cellulose are visible in MCC powder at 3600–3000 cm^{-1}, 2893 cm^{-1}, and 1641 cm^{-1}, which are assigned for stretching vibration of H-bonded O–H groups, C–H stretching, and O–H bending of adsorbed water, respectively.[304–306] Typical bands assigned to cellulose at 1159 cm^{-1} and 894 cm^{-1} are due to C–O–C stretching vibrations of the β(1→4)-glycosidic links in cellulose.[304,307] The absorbance at nearly 1051 and 1028 cm^{-1} is attributed to C–O–C pyranose ring skeletal vibrations, while the band at 661 cm^{-1} corresponds to O–H bending out of plane.[307]

On the other hand, the CICHs' spectra are very distinct from the MCC powder due to the regeneration of cellulose and contribution of urea hydrates. An overlapping of bands occurs in the range of 3600–3000 cm^{-1} related to N–H stretching vibration of urea molecules (asymmetric stretching at 3449 cm^{-1} and symmetric stretching at 3342 cm^{-1}) and O–H stretching vibration of water molecules.[308,309] The shoulder band at 3448 cm^{-1} is a characteristic band of cellulose II, assigned to O–H groups forming intramolecular hydrogen bonds.[304] Additional overlapped bands in the region between 1750 cm^{-1} and 1520 cm^{-1} are visible, corresponding to O–H bending vibration of water molecules as well as Amide I and Amide II of urea molecules. The band at 1456 cm^{-1} is attributed to the C–N asymmetric stretching and N–H deformation of Amide III, while the overlapping band at 1157 cm^{-1} assigns for rocking vibration of NH_2.[308,309]

The evolution of water retention can be compared by looking closer to the broad band at 3600–3000 cm^{-1} and 1635 cm^{-1}.[41] These bands are more pronounced in the L100, followed by L1N3, and N100 membranes, as smaller lithium ion tend to capture more water molecules than heavier alkali metal ions that are weakly hydrated, thus promoting a better water retention within the regenerated cellulose composite matrix.[31,310]

SEM images in **Figure 4.4** show that the L100 hydrogel is slightly rough with a wavy-like texture, and a dense and highly packed morphology, which indicates its high toughness and dense physical cross-linking. The cross-sectional images confirm a heavily wrinkled and lamellar morphology, which may arise from the incorporation of metal ions.[311] The incorporation of NaOH into the dissolution solvent system increases considerably the roughness of the hydrogel due to a poorer dissolution of cellulose, which can also explain its slightly lower transparency.

The CICHs exhibit a smoother surface on the side that is in direct contact with the flat surface of the glass and exhibits better adhesion. The smoothest surface of the CICHs is the one in contact with the semiconductor layer when used in EGTs to minimize the creation of interfacial defects between the functional layers.

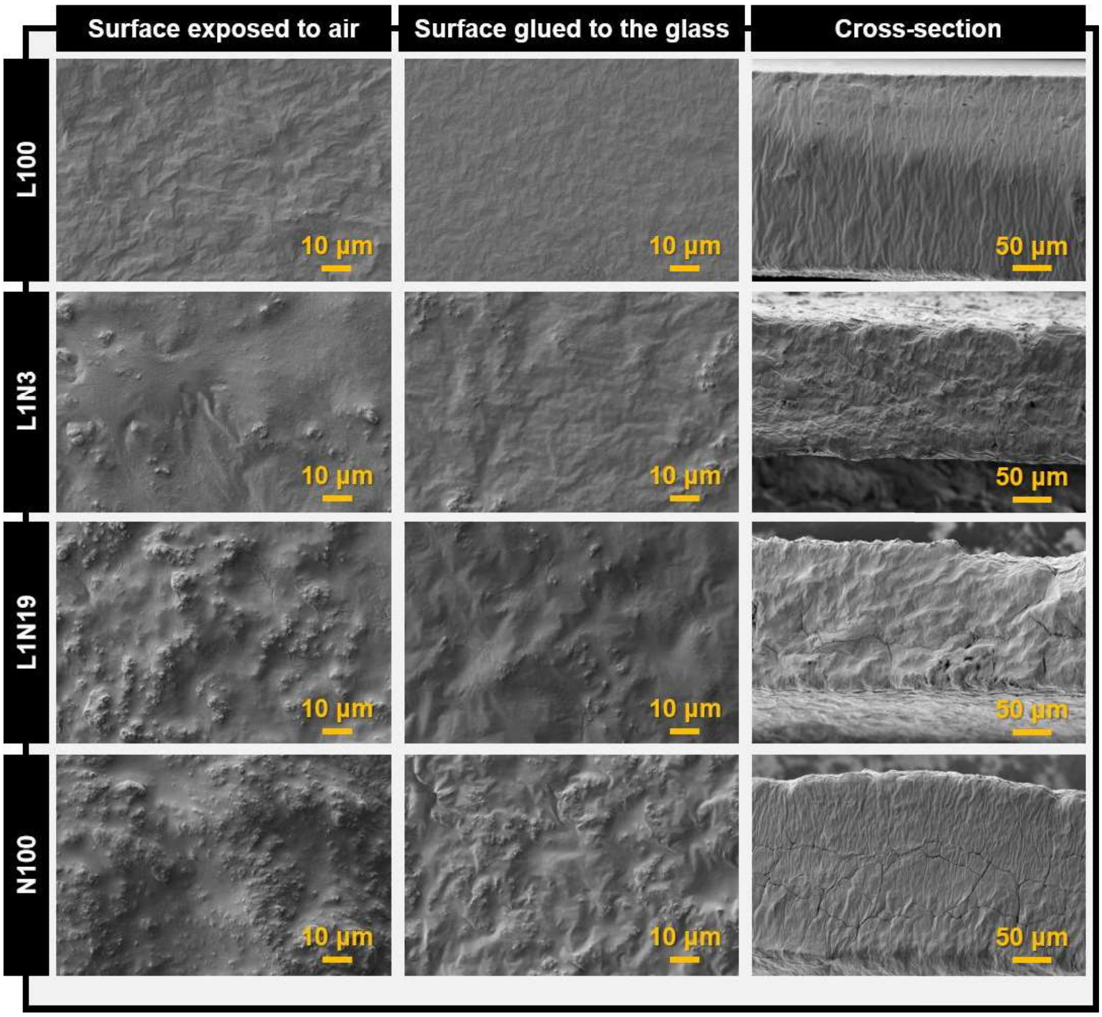

Figure 4.4. SEM micrographs of the different ClCHs for different magnifications.

One side back of the use of NaOH in the formulation of ClCHs is their poorer air-stability overtime. As shown in **Figure 4.5**a,c, right after cutting the hydrogels composed of higher contents of NaOH, “tree-like” structures start forming in a relatively short time (less than 28 h) on the top surface (exposed to air during drying) of the membranes. Once the dendrites formation has started, the growth is spontaneous and continuous, leading to a gradual loss of transparency while the membranes become more brittle. Therefore, there is a clear reduction of their conformability and adhesion to the substrate. XRD diffractogram in **Figure 4.5**b confirms the origin of the dendrites, where new peaks are introduced corresponding to urea (ICDD PDF: 00-028-2015).

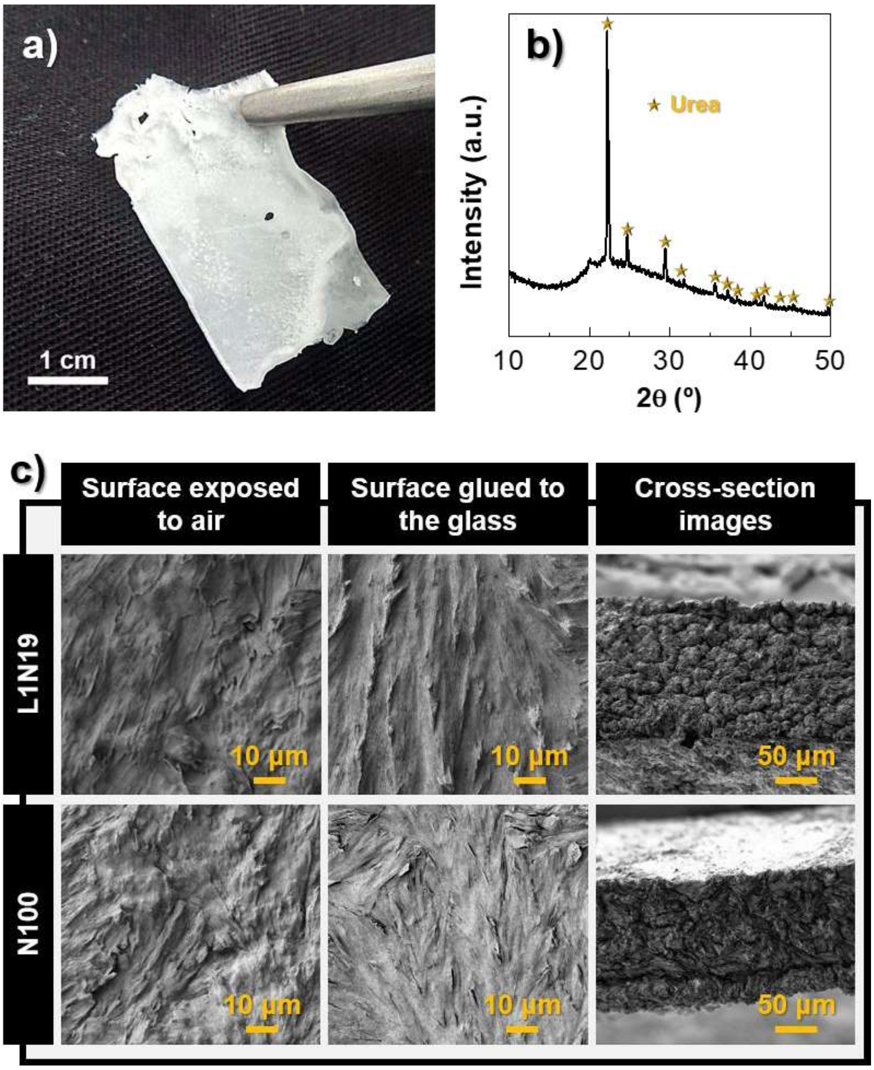

Figure 4.5. Air-stability of the CICHs. **a)** Photography of a slice of N100 hydrogel after one day of storage at ambient conditions. **b)** XRD diffractogram of N100 hydrogel after formation of urea dendrites. **c)** SEM images of L1N19 and N100 membranes obtained 28 hours after being cut and stick on the electrodes.

Aiming the application of CICHs as high capacitance dielectric in iontronic devices, such as EGTs and integrated circuits, the study of their electrochemical properties gains great importance, being the focus of the next section.

4.1.3. Electrochemical properties

Figure 4.6 displays a schematic of the electrochemical cell's assembly for electrochemical measurements, where the electrolyte is cut into the same shape of the stainless-steel discs (active area of 1 cm^2), delaminated, and transferred with a tweezer onto one electrode disc, and then sandwiched, obtaining a typical capacitor structure. Here, the role of the CMC and alkali hydroxide used in the CICHs' formulation was highlighted and their consequent impact in the resulting electrochemical properties was discussed.

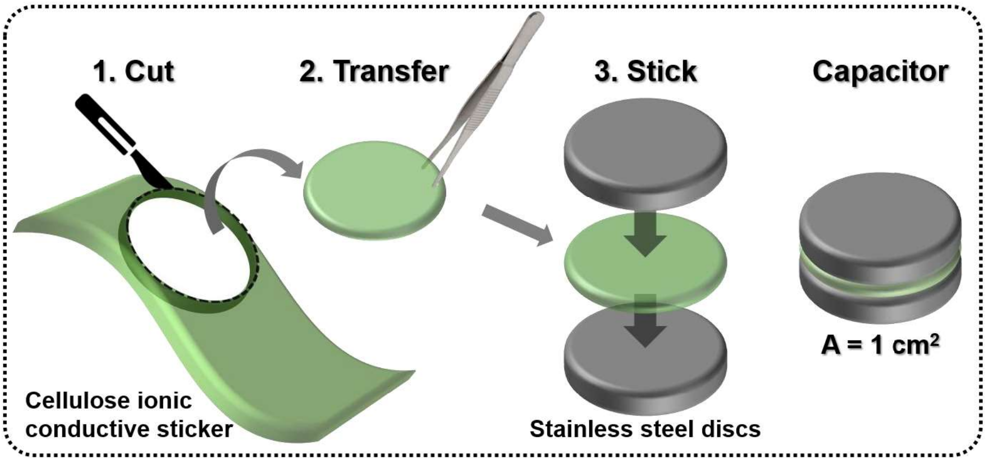

Figure 4.6. Schematic representation of the electrochemical cell assembly in a typical capacitor structure (metal/CICH/metal) to perform the electrochemical characterization of the developed CICHs.

4.1.3.1. *Influence of the addition of CMC*

As shown in **Figure 4.7**b, the specific capacitance (C) and phase angle (θ) were measured as a function of frequency (f) in the range of 0.1–10^5 Hz for the Li-CICHs with different concentrations of CMC, and the respective Nyquist plots are displayed in **Figure 4.7**c.

An equivalent circuit model (ECM) is necessary to analyze the EIS results. Hence, the ECM suggested by Dasgupta et al.[52] (**Figure 4.7**a), which consists of a contact resistance (R_c) in series with a RC circuit (related to the bulk resistance and bulk capacitance **–** R_b and C_b, respectively) and a constant phase element (CPE), was chosen for data interpretation as it produces a reasonably good fitting to the obtained data. Some important parameters can be obtained from the ECM, namely the electric double layer capacitance (C_{DL}) and ionic conductivity (σ_i), which are listed in **Table 4.1**.[312,313] These parameters were calculated using **Equation S2** and **Equation S3**, respectively.

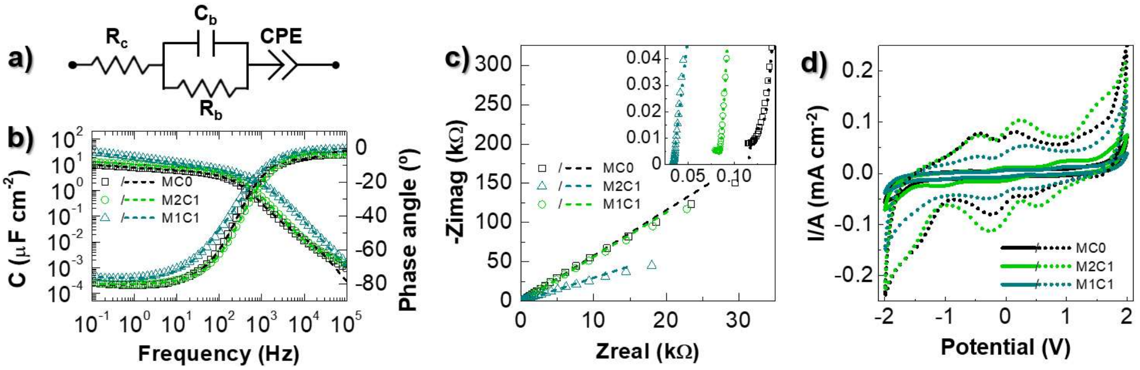

Figure 4.7. Electrochemical characterization of Li-CICHs with different proportions of MCC:CMC. **a)** Electrical equivalent circuit of the proposed impedance model, where C_b is the bulk capacitance, R_c and R_b are the electrical contact and bulk resistances, respectively, and CPE is the constant phase element. **b)** Capacitance and phase angle versus frequency plots for the developed Li-CICHs (MC0, M2C1, and M1C1), and respective **c)** nyquist plots. The symbols and the dashed lines denote the experimental and the fitted data, respectively. **d)** CV measurements of the Li-CICHs from -2 to 2 V at different scan rates, whereas continuous and dashed lines correspond to 25 mV s^{-1} and 400 mV s^{-1}, respectively.

Table 4.1. Resume of the electrochemical characterization of Li-ClCHs with different proportions of CMC.

Li-ClCHs	CMC [wt.%]	$C_{f=0.1\ Hz}$ [µF cm^{-2}]	C_{DL} [µF cm^{-2}]	σ_i [mS cm^{-1}]	$f_{\theta=-45}$ [Hz]
MC0	0	10.2	3.8	1.9	199
M2C1	2	13.4	5.3	4.2	252
M1C1	4	30.4	5.0	7.2	126

For frequencies above 126–252 Hz, a phase angle between voltage and current higher than -45° suggests the predominance of a resistive behavior that is associated with ionic relaxation, and this value gets close to zero for increasing frequencies. In this region, the specific capacitance is low and increases rapidly when the frequency decreases until level out at intermediate frequencies. A different mechanism takes place at lower frequencies associated to the EDL formation due to ion accumulation at the electrode/electrolyte interfaces. A decrease in phase angle for values lower than -45° and the leveling near -80° clearly indicates a transition from a resistive to a dominant capacitive regime. Even at low frequencies the phase angle never reaches -90°, as the electrolyte does not behave as a purely capacitive element. High specific capacitance up to the order of tens of µF cm^{-2} can be achieved at 100 mHz, and this value increases from 10 to 30 µF cm^{-2} for higher CMC contents, which is far greater than typical dielectrics[47]. A possible explanation for the high capacitance is that the addition of CMC provides some extra Na$^+$ that can aid in water retention, thus increasing the number of ionic species available that will also contribute to the formation of the EDL at low frequencies.[31,32,41,314]

According to some authors,[312,313] C_{DL} values should be considered instead of the specific capacitance values obtained directly at low frequencies, where EDL formation occurs. Although the calculated C_{DL} values for Li-ClCHs are slightly lower, they situate still in the typical reported values, usually around 1–10 µF cm^{-2}.[18] Additionally, the Li-ClCHs exhibit ionic conductivity in the range of ≈10^{-3} S cm^{-1}, which is far superior than that of usual solid polymer electrolytes at RT (≈10^{-5}–10^{-4} S cm^{-1}).[47] Typically, the ionic conductivity of the solid polymeric electrolytes limits the switching speeds of the transistors usually to less than 100 Hz owing to their slow polarization response time.[268] Thus, electrolytes with high ionic conductivity are desirable for faster switching EGTs. In this case, the Li-ClCHs can reach a high specific capacitance around 2–6 µF cm^{-2} for operating frequencies (when $\theta = -45°$) of 199, 252, and 126 Hz for MC0, M2C1, and M1C1, respectively.

As depicted in **Figure 4.7**d, CV measurements were performed in the potential range of ±2 V using different scan rates. An enlargement of the hysteresis as well as an increasing time to reverse the sign of the charging current tending toward higher scan rates relies on the incomplete charging of the electrodes.[52] The presence of faradaic currents is dominant and multiple peaks are visible during forward and reverse scans, which can be related to reversible redox reactions in the range of the voltages under study at the electrode/Li-ClCH interface. These peaks are less intense for increasing levels of CMC.

4.1.3.2. Influence of the alkali hydroxide

Figure 4.8a shows the frequency dependence of the specific capacitance and phase for the different CICHs (nyquist plots are also presented in **Figure 4.8**b). In this section, the developed M1C1 electrolyte, associated to the optimized formulation of CICHs prepared from LiOH (Li-CICHs), will be often referred to as L100 electrolyte.

At low frequency (f <1 kHz) the specific capacitance is between 6 and 13 µF cm^{-2} due to the formation of EDLs at the electrodes/CICH interfaces. The phase angle levels around -80° due to a slightly non-ideal capacitive behavior. The large specific capacitance values obtained for Li-CICH, Na-CICH and LN-CICHs are superior than traditional dielectrics and comparable with values typically reported for ion gels.[47,264] Such values persist up to the order of hundreds of Hz, decreasing significantly for higher frequencies, where ionic relaxation takes place.

In a similar way as the previous electrolytes, the ECM suggested by Dasgupta et al.[52] also produces a good fitting to the obtained data. The estimated C_{DL} and σ_i were plotted as a function of the amount of NaOH used for cellulose dissolution (**Figure 4.8**c). All the results are listed in **Table 4.2**.

The LN-CICHs exhibit high RT σ_i in the order of ≈10^{-3} S cm^{-1} comparable to those of single small cation salt systems (Li^+). Nevertheless, there is a decrease in the σ_i for the CICHs obtained from high amounts of NaOH (L1N19 and N100 membranes), which can be related to a poorer water retention into these hydrogels, as verified by FTIR spectra in **Figure 4.3**e. The superior water retention ability of lithium compared to sodium leads to additional free ionic species (protons and hydroxide anions) that aid in the process of ionic conduction.[31,32,41,314]

In this regard, some controversial results have been reported in literature and, therefore, there is not a consensual explanation.[315,316] Typically, smaller ions, such as Li^+, have greater conductivity than larger ions. However, the degree of hydration in aqueous medium is superior in alkali metal ions with smaller size, thus increasing the effective size of ionic radii of Li^+ in water (hydrated ionic radii),[310] being less mobile. Although water molecules can lead to an increase in the amount of free ions, when in excess it will reduce their mobility and hamper ion diffusion.[314] We must also consider the affinity of the hydrated ions with hydrophilic functional groups existing in the structuring polymers, such as the case of the hydroxyl and carboxymethyl, and the contribution of protons for the measured σ_i.

Despite such controversy, the lower values of σ_i obtained for the electrolytes that are highly enriched with Na^+ can also be related to a less efficient dissolution of cellulose in aqueous alkali hydroxide/urea systems with higher contents of NaOH, which are also more prone to formation of dendrites composed of urea, as aforementioned. The dendrites lead to large interfacial resistances that jeopardizes the electrochemical properties of the electrolytes.

The voltage window stability of the developed CICHs was evaluated by CV measurements (**Figure 4.8**d), which has been found in the range from -2.5 to 2.5 V, that is suitable for the intended application as gate dielectric in transistors. The presence of faradaic currents is dominant and multiple peaks are visible during forward and reverse scans, which can be related to reversible redox reactions at the electrode/CICH interface.

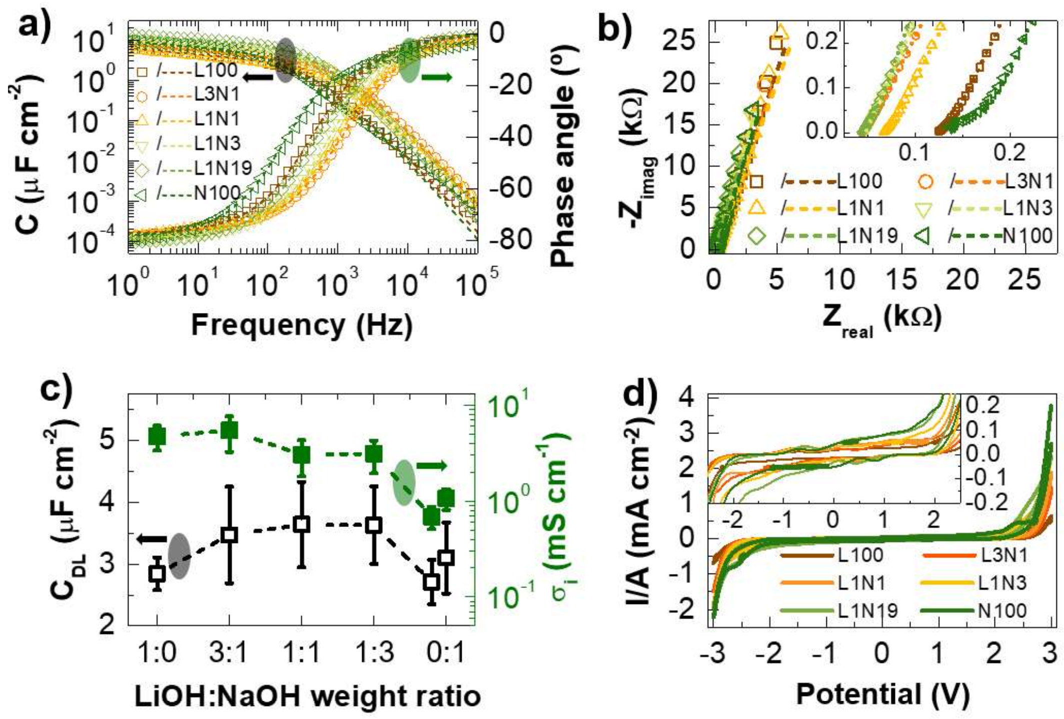

Figure 4.8. Electrochemical performance of the CICHs. **a)** Capacitance and phase angle versus frequency plots of the developed CICHs, and respective **b)** nyquist plots. The open symbols and the dashed lines denote the experimental and the fitted data, respectively. **c)** Representation of C_{DL} and σ_i as a function of LiOH:NaOH contents used for cellulose dissolution. The data points show the average and corresponding errors bars obtained from 4 samples. **d)** CV measurements of the CICHs (the potential sweep was performed with a scanning rate of 50 mV s^{-1} in a potential range between -3 and 3 V).

Table 4.2. Resume of the electrochemical characterization of the CICHs. The values show the average and respective standard error of the mean obtained from four samples.

CICH	$C_{f=1\ Hz}$ [μF cm^{-2}]	C_{DL} [μF cm^{-2}]	σ_i [mS cm^{-1}]	$f_{\theta = -45}$ [Hz]
L100	6.4 ± 0.4	2.8 ± 0.3	4.7 ± 1.4	257 ± 33.7
L3N1	6.3 ± 1.1	3.5 ± 0.7	5.4 ± 2.2	588 ± 131
L1N1	9.3 ± 2.2	3.6 ± 0.7	3.1 ± 1.3	456 ± 100
L1N3	8.6 ± 0.3	3.6 ± 0.6	3.1 ± 1.2	462 ± 67.7
L1N19	13 ± 0.7	2.7 ± 0.4	0.7 ± 0.2	482 ± 54.7
N100	8.2 ± 0.6	3.1 ± 0.6	1.1 ± 0.3	288 ± 63.9

Considering the superior electrochemical performance and stability of the L100 electrolyte, a more in depth-study was performed towards its application as gate dielectric in printed transistors and logic gates (**chapters 5** and **6**). Its formulation is also used to aid in the development of a new class of “paper-like” ionic conductive substrates, as discussed in the following section.

4.2. Development of iontronic cellulose nanopaper composites

Despite the appealing electrochemical properties of the developed CICH stickers, their sticky, soft, and easy deformable surface is very challenging to host a device, as their hydrogel-nature makes them highly sensitive to environmental conditions, thus deforming the layers deposited on them. Within this context, an ionic responsive cellulose-based membrane that combines the mechanical robustness and smoothness of cellulose nanopaper, composed of MFC/NFC, with the high capacitance of the CICHs was developed.

The ACICC membrane was prepared by slow casting and evaporation of water from a mixture of MFC/NFC pulp with the optimized Li-CICH formulation.

4.2.1. Optical, structural, compositional, and morphological properties

Figure 4.9a-b display a photograph of the ACICC membrane and the comparison of its optical transmittance with the cellulose nanopaper. Both membranes possess high total optical transmittance in the visible region of the spectrum (400 – 800 nm), mostly above 80 %, due to their micro/nanosized fibers that contribute to a denser structure, as verified by the SEM images (**Figure 4.10**). The total transmittance of cellulose nanopaper can be tuned by filling its porous cavities with the cellulose-based hydrogel, leading to a slight shift of the total transmittance from 86 % (cellulose nanopaper) to 88 % (ACICC membrane) at 700 nm. Such feature makes them suitable for applications where transparency is of great importance.

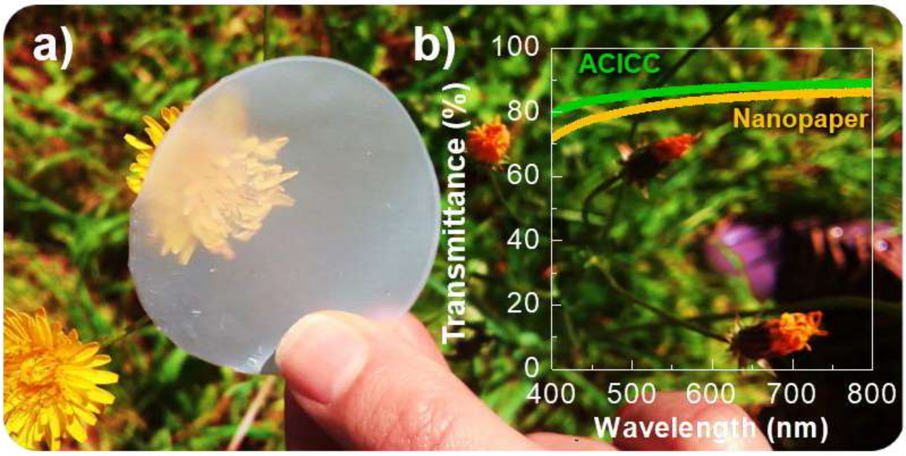

Figure 4.9. Optical characterization of the engineered nanopapers. **a)** Photograph of the developed ACICC membrane, and **b)** its total transmittance compared with cellulose nanopaper.

As show in **Figure 4.10**, the hydrogel electrolyte promotes the swelling of the narrow (≈20 – 90 nm range), tightly packed, and entangled hydrogen bonded micro/nanofibrils of the nanocellulose matrix. Some microfibrils are visible, reaching in some cases hundreds of nanometers in width and a length of several micrometers. The cross-section images show that the nanopaper exhibits a layered and unique porous network structure with a pore size with tens of nanometers. This type of network is beneficial for relieving the mechanical stress induced in the functional layers deposited on its surface, which contributes to its excellent flexibility.[66] In the case of the ACICC membrane, the hydrogel fills the layered porous structure increasing its impermeability.

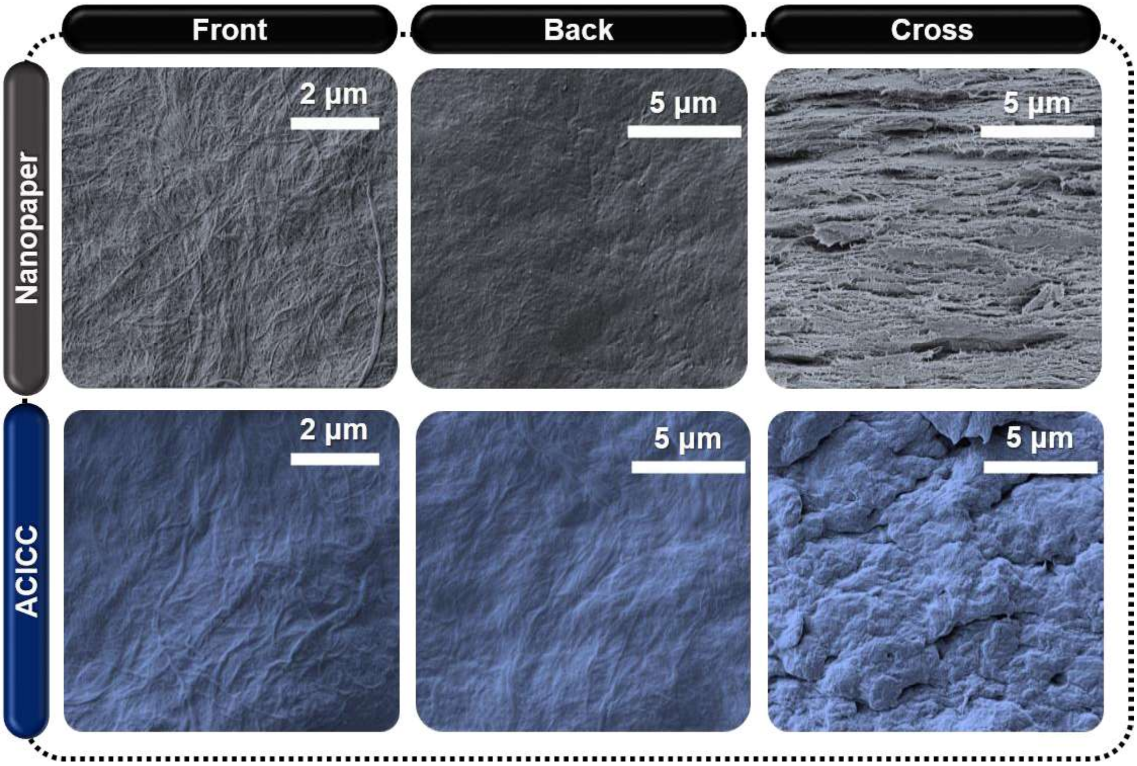

Figure 4.10. Morphological characterization of the engineered nanopapers.SEM micrograph images of cellulose nanopaper and ACICC membrane on distinct surfaces (front, back surfaces, and cross-section).

As confirmed by AFM measurements (**Figure 4.11**), the soaking of the fibers in the ACICC membrane leads to smoother and less permeable surfaces, reducing the RMS roughness nearly 11 % (from 77 to 68 nm) when compared with cellulose nanopaper. The smoothest surface of the ACICC membrane, related to the side dried in contact with the container, is the one used to fabricate the iontronic devices. Their smoothness can be further improved by downsizing fibril's dimension through combined mechanical, enzymatical and/or chemical pre-treatment of cellulose fibers' pulp before mechanical shearing to obtain a nanocellulose pulp.[13]

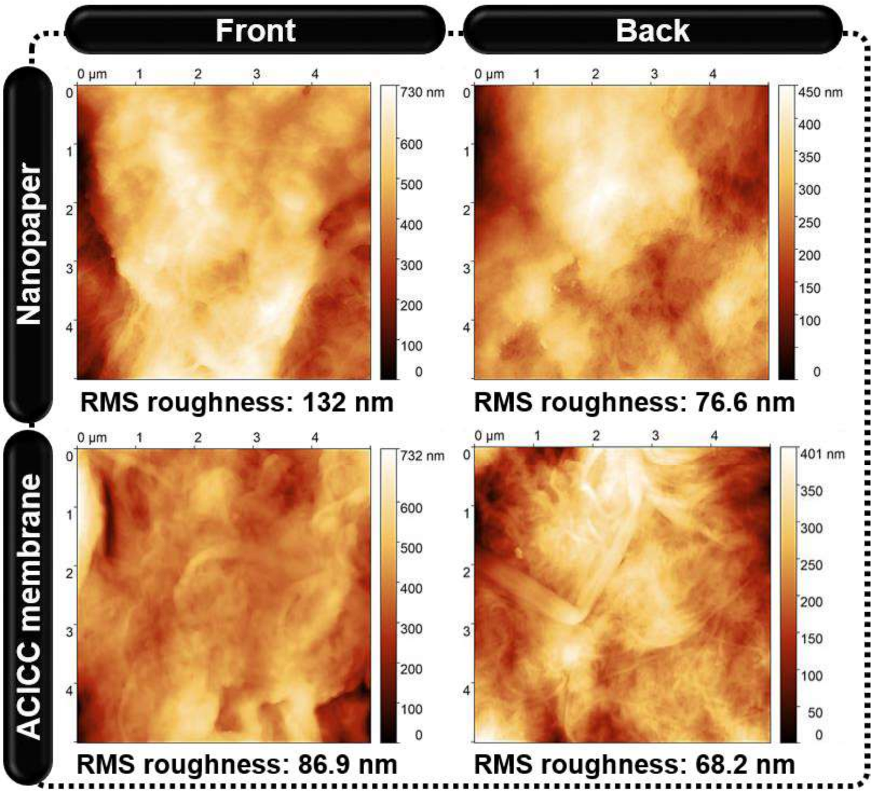

Figure 4.11. AFM characterization of engineered nanopapers. Surface roughness of the front and back side of cellulose nanopaper and ACICC membrane.

Figure 4.12a confirms that the crystalline structure and respective crystallinity index (CrI) of the ACICC membrane are not affected with the addition of the ClCH-based slurry into the nanocellulose pulp. The characteristic peaks for $(1\bar{1}0)$, (110) and (002) crystallographic planes at 2θ = 14.3, 16.3, and 22.4°, respectively, corresponds to cellulose I. According to the empiric method proposed by Segal et al.[292], the CrI was estimated to be around 61 and 65 % for ACICC and nanopaper, respectively. It is noteworthy to mention that the values estimated for the CrI of both nanopaper-based membranes are useful just for comparison of their relative differences, as the CrI differs significantly depending on the technique and calculation method adopted.[41,317]

The amount of water retained within the cellulose-based membranes was evaluated by FTIR (**Figure 4.12**b). The spectra were baseline corrected to 0 at 1845 cm^{-1} and 3739 cm^{-1} and normalized to 1 at 2900 cm^{-1}, which forms a common baseline for the study of water content inside the membranes.[294] FTIR spectra of cellulose nanopaper and ACICC membrane reveal a series of characteristic absorption bands for cellulose, which are identical to the ones identified in the FTIR spectrum of MCC powder (**Figure 4.3**e) and discussed in previous **section 4.1.2**. Some additional bands are also visible in the ACICC membrane, due to the contribution of urea hydrates and regenerated cellulose from the hydrogel electrolyte. The bands in the region between 1750 and 1520 cm^{-1} can be related to Amide I and Amide II of urea molecules, whereas the small shoulder band at 3448 cm^{-1} corresponds to a characteristic band of cellulose II, assigned to O–H groups forming intramolecular hydrogen bonds.[304,308,309]

The evolution of water retention can be compared by looking closer to the broad band at 3600–3000 cm^{-1} and 1635 cm^{-1}.[41] The addition of the cellulose-based hydrogel enriched with hygroscopic species in the micro/nanofibrous matrix results in an increase in the amount of adsorbed water species, showing a water retention behavior located between the Li-CICH membrane and the cellulose nanopaper.

Figure 4.12c shows the thermal degradation of the individual materials that compose the engineered nanocellulose composite. According to the weight loss curves, the thermal degradation of the ACICC membrane occurs in two steps, starting with the desorption of moisture adsorbed in the cellulose matrix at temperatures below 100 ºC, followed by a steep weight loss up to 295 ºC related to the thermal degradation of the material. The cellulose nanopaper was found to have better thermal stability nearly up to 325 ºC, while the thermal degradation in the Li-CICH membrane occurs for earlier temperatures (<240 ºC). TGA measurements also confirms that the amount of adsorbed protonic species in the cellulose nanopaper is inferior compared to the Li-CICH and ACICC membranes, which is in line with the FTIR results.

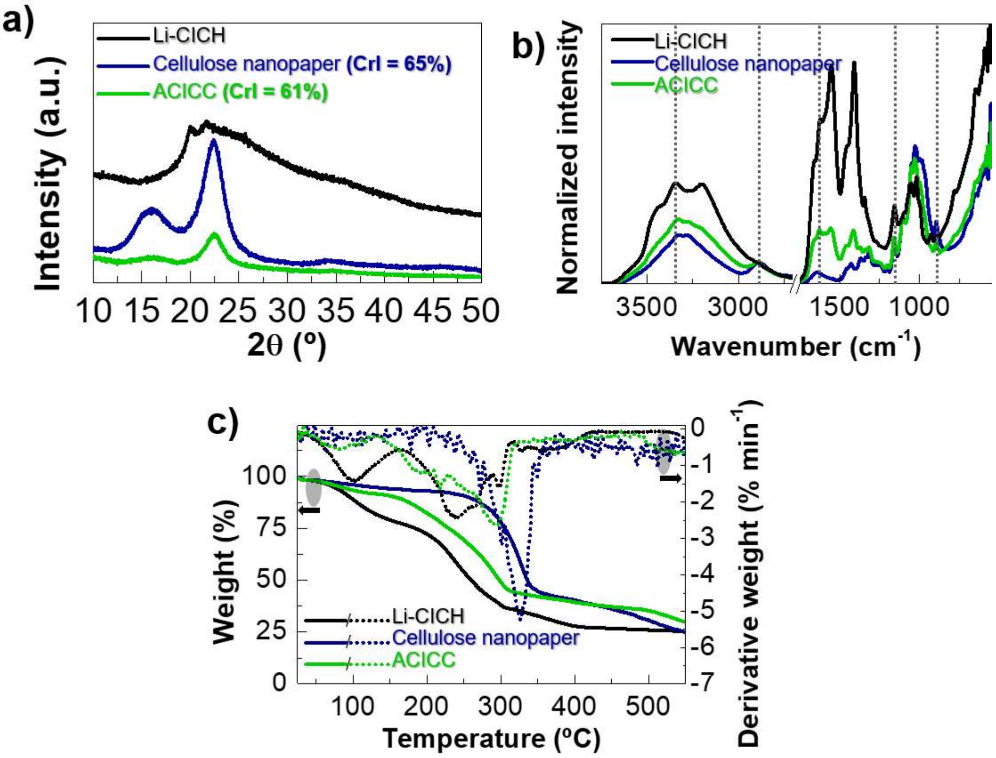

Figure 4.12. Structural, chemical, and thermal characterization of the engineered nanopapers and comparison with the Li-CICH membrane. a) XRD diffractograms. b) Normalized FTIR spectra. c) TGA curves and respective derivatives.

Therefore, the ACICC membrane combines the thermal resistance from MFC/NFC and superior water adsorption ability from the Li-CICH membrane, thus confirming its "composite" character. The latter feature has a tremendous impact in the electrochemical properties, since water retention is the main source of H$^+$ and OH$^-$ responsible for the high capacitance values obtained at low frequencies.[32]

4.2.2. Electrochemical properties

Here, the enrichment of the cellulose nanopaper with a hydrogel electrolyte composed of alkali ionic species was assessed by EIS and CV. The electrochemical characterization of the cellulose nanopaper and the developed ACICC membrane was carried out under ambient conditions, using a typical capacitor structure (**Figure 4.13**a), where the carbon electrodes were screen-printed on both sides of the membranes with an area of 1 mm^2 to simulate the printed EGTs structure implementing this membrane as gate dielectric (**Figure 6.18**).

Figure 4.13c,d display the measured specific capacitance and phase angle as a function of frequency in the range of 0.1 Hz to 1 MHz, and the respective Nyquist plot is displayed in **Figure 4.13**b.

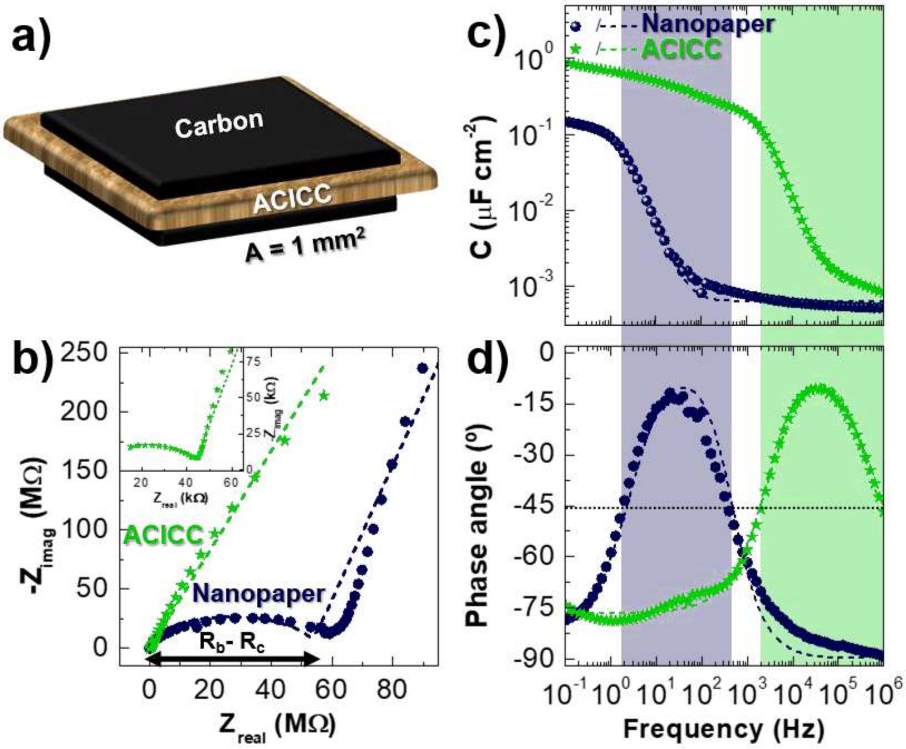

Figure 4.13. Electrochemical characterization of the engineered nanopapers. a) Design of the capacitor structure (carbon/membrane/carbon) with an active area of 1 mm^2. **b)** Nyquist plots for the engineered nanopapers, and respective. **c)** capacitance and **d)** phase angle as a function of frequency, where the ionic relaxation region is highlighted in blue and green for the cellulose nanopaper and ACICC membrane, respectively. The symbols and the dashed lines denote the experimental and the fitted data, respectively.

Distinct polarization mechanics occurs depending on the range of frequencies under consideration as well as the “degree” of ionic enrichment of the membranes. For the nanopaper, three regimes can be clearly distinguished, starting with the dipole relaxation that occurs for higher frequencies (≈0.5 kHz–1 MHz, θ <-45°), moving sequentially to ionic relaxation (2 Hz–0.5 kHz, θ >-45°, highlighted in blue in the plot) related to a dominant resistive behavior, and then a transition to a dominant capacitive regime occurs as frequency decreases (<2 Hz, θ <-45°) due to the EDL formation. In the latter regime, the mobile ionic species trapped within the nanopaper matrix, which are mainly responsible for protonic conduction (the Grotthuss mechanism),[318] migrate towards the nanopaper/carbon interfaces promoting an abrupt increase in the capacitance up to 0.15 µF cm^{-2} at 0.1 Hz, whilst the phase angle levels near -80° since the nanopaper does not behave as a purely capacitive element.

The ionic performance is considerably improved when mixing the nanocellulose pulp with a small amount of hydrogel electrolyte enriched with hydrated alkali ionic species that aids water retention within the membrane matrix, as demonstrated previously by FTIR and TGA measurements. The EDL formation occurs for higher frequencies (<2 kHz), reaching a maximum capacitance of 0.8 µF cm^{-2} at 0.1 Hz, where the phase angle levels around -75º due to a slightly non-ideal capacitive behavior. The Nyquist plot of the ACICC membrane reveals a shrinkage of the semicircle width, correspondent to the difference between R_b and R_c (as indicated in the plot), when comparing with the nanopaper, which indicates a clear enhancement of both capacitance and σ_i.

A reasonably good fitting is obtained to the data by using the ECM suggested by Dasgupta et al.,[52] and respective σ_i values were determined from five samples. The cellulose nanopaper yields a low value of σ_i around (9.38 ± 0.88) $\times$ 10^{-9} S cm^{-1}, which is increased more than three orders of magnitude to (4.18 ± 0.36) $\times$ 10^{-5} S cm^{-1} for the ion enriched ACICC membrane.

Regarding the electrochemical stability of the membranes, there are no evidence of redox peaks in the CV measurements in the range of voltages under consideration between -2.5 and 2.5 V at a fixed scan rate of 0.2 V s^{-1}, which are the same parameters used in the electrical characterization of the printed ZnO PNPs transistors gated by the ACICC membrane (**Figure 4.14**a), as further discussed in **section 6.2.2**. The ACICC membrane exhibits superior current values when compared to nanopaper, yet the currents observed for both membranes are mainly related to the double layer charging.

It should not be disregarded the possibility of electrochemical reactions between the electrolyte and the oxide semiconductor, which will ultimately influence the operation mode of the transistors as well as their switching speed. Therefore, the electrochemical stability of the carbon/ACICC/semiconductor/carbon layered structure, which simulates the structure of the printed ZnO PNPs displayed in **Figure 6.18**, was also evaluated (**Figure 4.14**b). The interface between the electrolyte and the semiconductor leads to the appearance of redox peaks that can evidence the permeability of the semiconductor to ions existent within the ACICC membrane. Therefore, it is possible to predict the working mechanism of the fabricated ZnO EGTs consisting of a mixed operating mode (field effect and electrochemical doping), which is also influenced by the adsorption of ambient species (e.g. O_2 and H_2O) that accelerate the chemical reactions in the oxide semiconductor.[319]

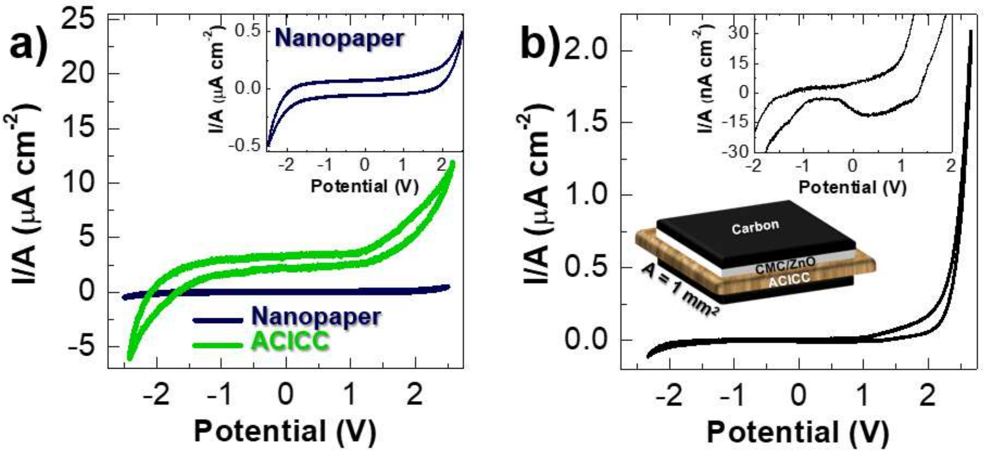

Figure 4.14. Electrochemical stability of the engineered nanopapers. **a)** CV curves of the cellulose nanopaper and ACICC membrane using carbon/membrane/carbon structure. **b)** Influence of the CMC/ZnO PNPs layer in the CV curve of the ACICC membrane (inset of the capacitor structure similar to the fabricated screen-printed ZnO PNPs NCGTs, including the semiconductor layer). All the curves were acquired for a scan rate of 0.2 V s^{-1}

In conclusion, ACICC membrane combines a unique set of features from smooth surface, semi-transparency, and temperature resistance to good electrochemical properties, which lead us to explore its full potential as an ionic conductive substrate in low-voltage transistors and logic gates.

Chapter 5

Ion-controlled IGZO transistors and circuits

5. Ion-controlled IGZO transistors and circuits 77
  - 5.1. CICH-gated IGZO transistors and logic gates 78
    - *5.1.1. Design and architecture 78*
    - *5.1.2. Electrical performance of CICH-gated IGZO transistors 80*
      - *5.1.2.1. Li-CICHs as electrolyte-gate in IGZO EGTs on glass 80*
      - *5.1.2.2. Li-CICHs as electrolyte-gate in flexible IGZO EGTs 85*
      - *5.1.2.3. LN-CICHs and Na-CICHs as electrolyte-gate in flexible IGZO EGTs...... 90*
    - *5.1.3. Electrical performance of CICH-gated IGZO circuits on paper 95*
  - 5.2. “Interstrate” ACICC-gated IGZO transistors 97

To put the attributes of the developed electrolytes in perspective, a first attempt was made to study EGTs based on the benchmark amorphous IGZO n-type semiconductor prepared by conventional vacuum-based deposition techniques on glass, and then on smooth, impermeable, and flexible multilayer-coated paper. Two types of electrolyte-gating were tested, either based on hydrogels or ionic conductive substrates. Regarding the first case, the sticky, soft, and easy deformable surface allied with some mechanical robustness of the ClCH membranes enable their application directly onto iontronic devices as stickers. On the other hand, the AClCC membrane combines a “two-in-one” functionality into a single material, as it works not only as the support but also as a vital constituent of the devices themselves, thus making the manufacturing process easier.

5.1. ClCH-gated IGZO transistors and logic gates

This section is focused on the design and electrical characterization of the fabricated ClCH-gated IGZO transistors and resistive-load inverters. Firstly, the influence of CMC content of the Li-ClCHs on the electrical performance of the IGZO EGTs fabricated on glass is addressed. A better understanding on the operation mechanisms behind their performance is given by controlling the applied gate voltage (V_{GS}) and V_{GS} scan rate of the EGTs. The ageing of the devices on glass, stored under ambient conditions, was also investigated.

Due to the superior electrical performance observed on the devices gated by L100 membrane, which also combine the best combination of mechanical/electrochemical properties (as previously discussed in **section 4.1)**, further studies were carried out with this membrane as gate dielectric in flexible IGZO EGTs. The endurance of the flexible IGZO devices was studied under different conditions (temperature, humidity, bending, and electrical stress) and their performance was compared with the ClCHs prepared using NaOH or mixtures of LiOH:NaOH as the alkali hydroxides of the solvent system for the dissolution of cellulose.

If not mentioned otherwise, the IGZO EGTs and inverters were tested in air under ambient conditions, right after transfer and stick the electrolyte onto the devices.

5.1.1. Design and architecture

As illustrated in **Figure 5.1**, the devices here reported rely on an electrolytic gate insulator based on a new class of ClCHs coupled with an oxide semiconductor based on amorphous IGZO as the transistor’s channel and gold bottom electrodes deposited in an interdigital architecture.

Gold was the material of choice for the electrodes, due to its well-known electrochemical stability and corrosion resistance.[47] The efficient use of sputtered amorphous IGZO as active n-channel layer in rigid and flexible transistors was already extensively reported in the literature, being also used throughout this work.[320–322] The incorporation of oxide semiconductors with an amorphous microstructure offer advantages on low-temperature processing and the ability to produce films with highly smooth surfaces that eradicate grain boundaries effects, which have unfavorable effects on the mobility of the devices.[259]

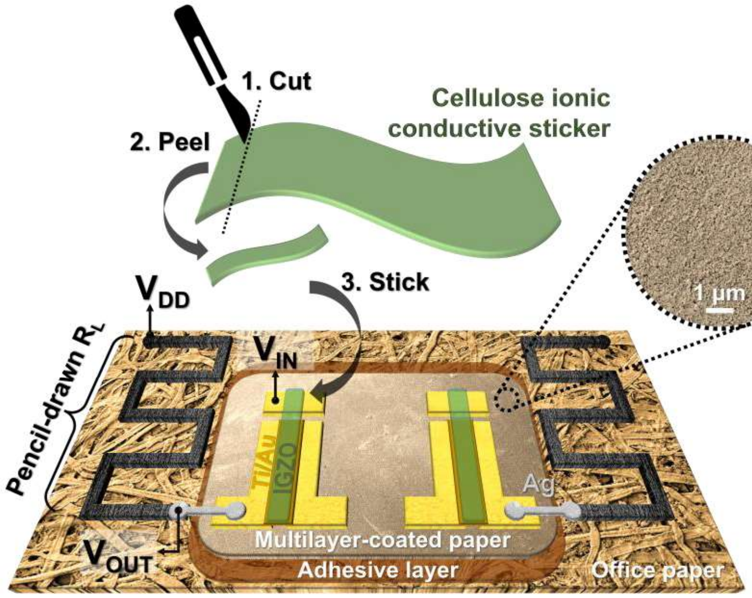

Figure 5.1. Schematic illustration of two planar CICH-gated IGZO EGTs fabricated on multilayer-coated paper integrated onto NOT gates with conductive/resistive tracks hand-drawn on office paper. Inset: SEM image of the smooth and impermeable surface of the multilayer-coated paper substrate used for fabrication of the EGTs. R_L, V_{DD}, V_{OUT}, and V_{IN}, stand for load resistance, supply voltage, output voltage and input voltage, respectively.

Contrarily to conventional dielectric gating, where the dipolar polarization is unidirectional, electrolyte gating enables the formation of EDLs at the electrode and semiconductor surfaces that are in direct contact with the electrolyte, being possible to adopt an in-plane-gate device configuration for fabrication of the EGTs. Such design offers some advantages as it allows to reduce the mechanical stress applied to the device compared to the vertical structure, and simplifies substantially the device fabrication, since the source, drain, and gate electrodes are deposited simultaneously in a single deposition step, and thus they are disposed in the same plane. Hence, time consuming procedures, such as the alignment of subsequent layers prior deposition as well as the number of deposition steps needed to pattern all the functional layers are minimized.

The devices were fabricated on rigid (glass) or flexible substrates (multilayer-coated paper). In the latter case, the nanoporous top-coating layer of the multilayer-coated paper substrate (inset of **Figure 5.1** was used to host the iontronic devices owing to its smoother and hydrophilic surface as well as good barrier properties.[278] Such properties make this paper-based substrate suitable for applications that demand molecularly smooth interfaces.

Furthermore, we also demonstrate that the IGZO EGTs fabricated on multilayer-coated paper can be easy and quickly integrated into simple logic gates. An example of a logic gate is the logic inverter (or NOT gate), which is the basic building block in digital electronics, able to invert an input signal.

To do so, a hybrid manufacturing process was implemented that combines high-vacuum deposition techniques with user-friendly RT processes that allow the readily integration of transistors into circuits, and their application. Although the prior set of manufacturing techniques is characterized for being sophisticated, complex, time- and high-energy consuming techniques that require skilled individuals, they ensure the deposition and patterning of pure, thin, and high-quality electrodes and semiconductor materials that will define the transistors on reasonably smooth and impermeable multilayer-coated paper substrates. Regarding the adopted RT processes, a transfer-lamination process is used to apply the electrolyte-sticker, while ubiquitous and portable calligraphy accessories allow to easily draw the conductive and resistive tracks of the circuits.

Since the plastic coating of the multilayer-coated paper is not compatible with pencil-drawing, conventional office paper was used instead. Thereby, a resistive graphitic track is pencil-drawn on a sheet of regular office paper, where the paper transistors are glued with a double-sided tape, and then the electrolyte-gate sticker is laminated directly onto the devices. Thick electroconductive silver tracks are handwritten with a commercial pen to establish the connection between the drain electrode of the transistor fabricated on multilayer-coated paper and the pencil-drawn load resistance (R_L) on office paper.

5.1.2. Electrical performance of CICH-gated IGZO transistors

5.1.2.1. Li-CICHs as electrolyte-gate in IGZO EGTs on glass

Influence of CMC content

Figure 5.2 show the schematics illustration of the EGTs on glass with laminated Li-CICHs, and respective cyclic transfer (drain current I_{DS} vs. V_{GS}) and output (I_{DS} vs. drain voltage V_{DS}) characteristic curves in the saturation region (V_{DS} = 1.2 V). **Table S4** provides the resume of the main results obtained for IGZO EGTs on glass, which are represented in **Figure 5.3**, including ON/OFF current ratio ($I_{ON/OFF}$), turn-on voltage (V_{ON}), transconductance ($g_m = \partial I_{DS}/\partial V_{GS}$), subthreshold gate voltage swing (S_S) and saturation mobility (μ_{Sat}). The electrical parameters were calculated in the forward sweep direction, from negative to positive gate voltage, in the saturation regime (V_{DS} = 1.2 V) and obtained at different scan rates. The parameters Ss and μ_{Sat} were calculated according to **Equation S4** and **Equation S5**, respectively.

Some considerations must be done regarding the calculation of μ_{Sat}. As observed in **Figure 5.8**, the use of shadow masks often leads to misalignments of the patterned IGZO with the source and drain contacts, which affects the real dimensions of the devices, thus being one limiting factor in calculating the device's mobility. An additional parameter that impacts the mobility values is the capacitance of the gate dielectric. Although the capacitance values obtained directly from the EIS data at 0.1 Hz ($C_{f=0.1\ Hz}$), where occurs the EDL formation, are in the same order of magnitude as those estimated from the fitting of the experimental data (C_{DL}) with the ECM used for data interpretation, they are still much higher. To demonstrate how these values lead to miscalculated values of mobility, we can exemplify by comparing the mobility calculated for the devices gated by M1C1 hydrogel for a scan rate of 25 mV s^{-1}. In this case, the mobility can shift from 21 to merely 5.3 cm^{2}V^{-1}s^{-1}, when using the capacitance values from the fitting and experimental data at low-frequencies, respectively. For data interpretation, the mobility values considered will be those determined using the C_{DL} values, as previously explained in **section 4.1.3.1**.

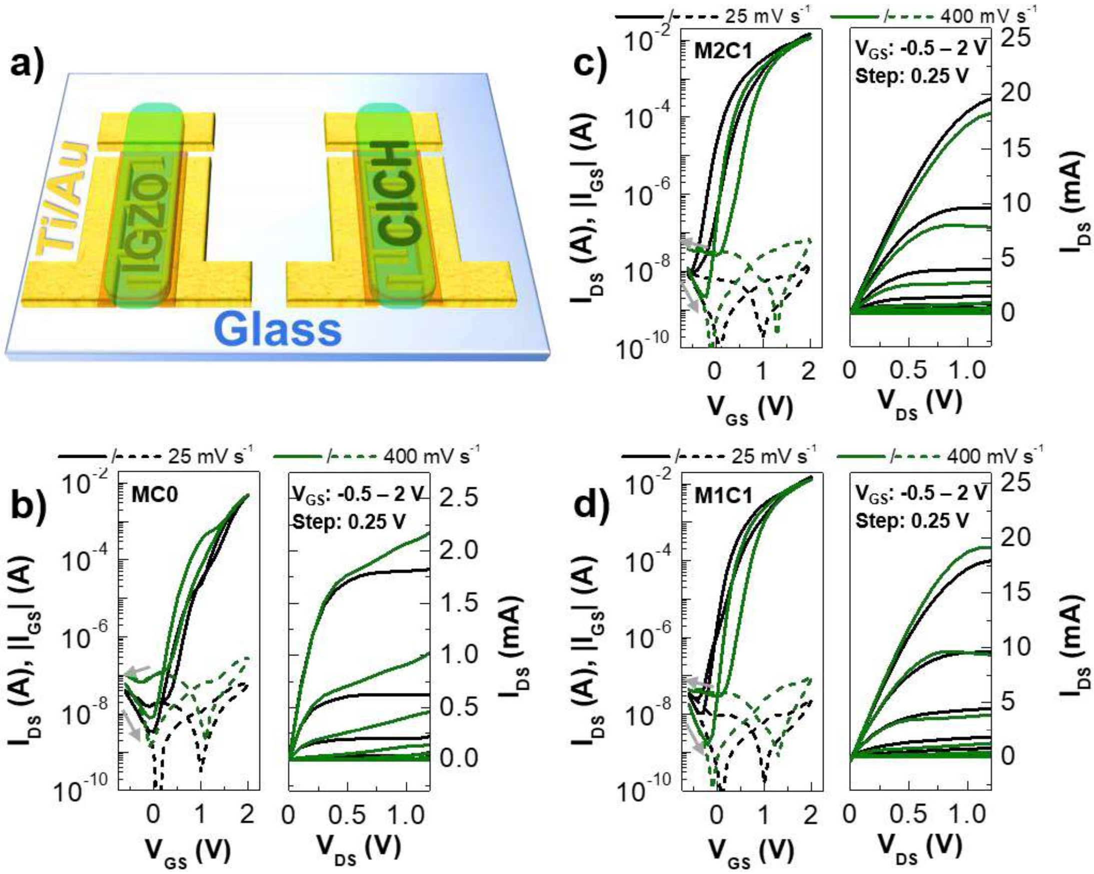

Figure 5.2. Electrical performance of IGZO transistors on glass gated by Li-CICHs. **a)** Schematic illustration of two planar CICH-gated IGZO EGTs fabricated on glass. Influence of V_{GS} scan rate on cyclic I_{DS}–V_{GS} curves of EGTs on glass gated by **b)** MC0, **c)** M2C1, and **d)** M1C1 for saturation regime (V_{DS} = 1.2 V), and respective I_{DS}–V_{DS} curves for a V_{GS} step of 0.25 V, from -0.5 to 2 V. Arrows represent the sweep direction, whereas continuous and dashed lines correspond to drain (I_{DS}) and leakage ($|I_{GS}|$) currents, respectively.

The fabricated EGTs exhibit a typical n-type behavior, low operating voltage (<2 V), high $I_{ON/OFF}$ ranging from five up to almost seven orders of magnitude, gate leakage currents ($|I_{GS}|$) varying between 10^{-7} and 10^{-8} A and a large I_{DS} of up to 10 mA at a V_{GS} of 2 V. The maximum S_S is lower than 0.2 V dec^{-1}, and such a small value usually indicates that the transistor can modulate more current with a lower V_{GS}. Moreover, the EGTs are in the ON state at V_{GS} <0 V (normally on characteristics).

The differences visible in the electrical performance of the devices are mainly influenced by Li-CICHs' formulation and the applied V_{GS} scan rate. The latter parameter has great influence on the hysteresis and transition to a predominantly electrochemical doping regime, as will be discussed further below. The EGTs gated by Li-CICHs with CMC in their composition exhibit higher

$I_{ON/OFF}$ (>10^6), enhanced μ_{Sat} (close to 21 cm^2 V^{-1} s^{-1}), lower S_S (<0.13 V dec^{-1}), and smaller $|I_{GS}|$ values (<100 nA at V_{GS} = 2 V and V_{GS} scan rate = 400 mV s^{-1}), when comparing with those gated by MC0 membrane. Concerning the amount of CMC, a superior modulation of I_{DS} is observed for the EGTs gated by M1C1 membrane, which translates into smaller values of S_S around 0.1 V dec^{-1}, as well as improved mobility reaching a μ_{Sat} of 21 cm^2 V^{-1} s^{-1} for a V_{GS} scan rate of 25 mV s^{-1}. Furthermore, faster scan rates considerably improve electrical modulation between ON and OFF states at the cost of smaller mobility and higher $|I_{GS}|$ with a difference of one order of magnitude.

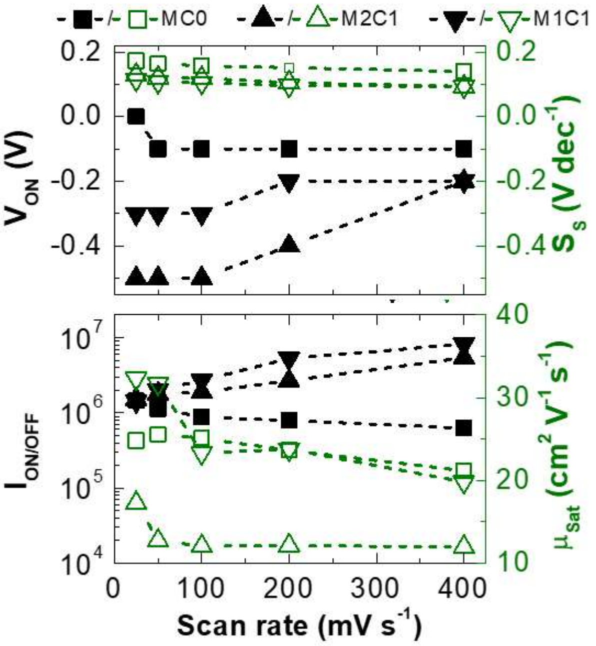

Figure 5.3. Comparison of electrical parameters obtained for the developed IGZO EGTs on glass gated by Li-ClCHs (MC0, M2C1, and M1C1) using distinct V_{GS} scan rates.

As mentioned before, the addition of CMC improves the mechanical and electrochemical properties of Li-ClCHs. CMC was already reported in some works as an efficient material to be used as a host of gel polymer electrolytes for application in electrochemical devices, including electrochromic devices,[82] and lithium ion batteries.[323,324] Thus, the enhancement of the electrical performance observed on the EGTs gated by Li-ClCHs composed of CMC (M2C1 and M1C1 membranes) can be due to the suitable use of CMC as a hosting material of regenerated cellulose. Thus, the smooth, sticky, and flexible surface of the Li-ClCHs composed of CMC provides a better conformity to the semiconductor, leading to an improved interface between the dielectric and the surface of amorphous IGZO.

According to the output characteristics, the EGTs can reach saturation regime, showing high I_{DS} values at very low V_{GS} (2 V) and V_{DS} (1.2 V), which are significantly higher for the laminated M2C1 and M1C1 hydrogels (≈20 mA).

Working mechanism of IGZO EGTs

The understanding of the working principle of the EGTs is also of important matter.[47] Depending on the applied range of V_{GS}, V_{GS} scan rate, and ionic permeability of the semiconductor, distinct operation mechanisms can occur in the developed EGTs. As previously shown in **Figure 4.7**c, owing to the presence of faradaic currents associated to reversible redox reactions in the range of voltages under study, the EGTs are expected to reach the electrochemical regime, depending on the V_{GS} used. Moreover, there is the possibility that the electrochemical reactions also take place at the IGZO/electrolyte interface. Therefore, CV measurements were also performed under identical experimental conditions, including the IGZO layer in the capacitor structure (**Figure 5.4**). Although the same peaks are visible in the CV curves, the possibility of electrochemical reactions occurring at the IGZO/electrolyte interface cannot be entirely put away. Therefore, we can expect the devices working under mixed operating mechanisms (field-effect and electrochemical doping).

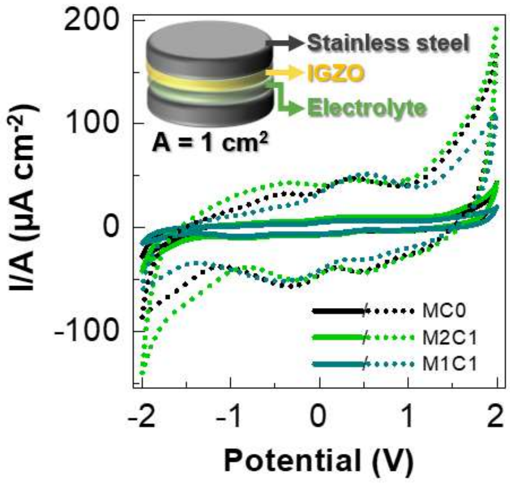

Figure 5.4. Electrochemical stability of IGZO/electrolyte interface. CV measurements of the developed Li-ClCHs combined with IGZO from -2 to 2 V at different scan rates, whereas continuous and dashed lines correspond to 25 and 400 mV s^{-1}, respectively (inset: schematic illustration of the electrochemical cell structure, including the IGZO layer).

The coexistence of two working mechanisms is clear on the transfer curves for higher V_{GS} (>1 V), and it is less evident on the EGTs gated by Li-ClCHs with CMC, where the transition to a predominant electrochemical doping regime seems more continuous. A closer look in this range of V_{GS} (**Figure 5.5**) reveals a smooth decrease on I_{DS} and $|I_{GS}|$ for a narrow range of V_{GS} followed by a new rise of current, which suggests that a different operation mechanism becomes dominant. Transfer characteristics do not exhibit a constant value, which could be explained by redox reactions occurring in the IGZO/electrolyte interface, and consequently doping of the semiconductor, which require charge compensating ions as well as electrons.

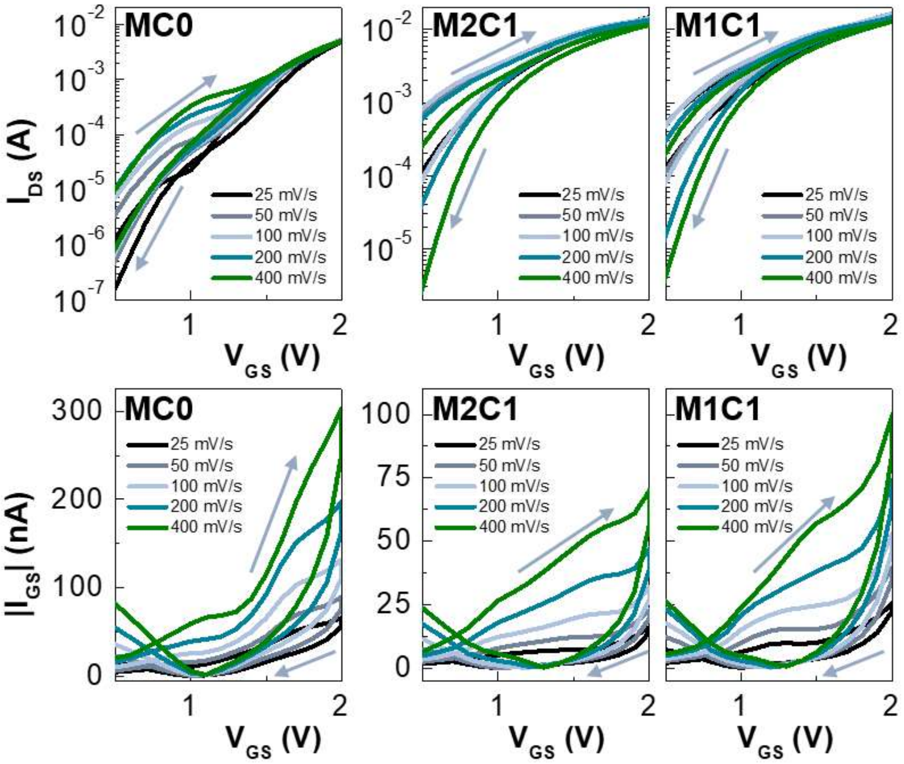

Figure 5.5. Influence of V_{GS} scan rate on I_{DS} and $|I_{GS}|$ of IGZO EGTs on glass gated by Li-CICHs, for saturation regime (V_{DS} = 1.2 V), on a narrow range of applied gate voltage from 0.5 to 2 V, where it is visible a bump suggesting a redox reaction and consequently doping of the semiconductor. Arrows represent the sweep direction.

Santos et al.[325] reported EGTs using IGZO nanoparticles gated by a composite solid polymer electrolyte and has demonstrated that ions from the electrolyte can penetrate or be adsorbed into the IGZO layer, and for a certain range of applied V_{GS} the channel formation is an electrochemical process. In a similar way, by controlling the applied V_{GS}, the operation mechanism of the EGTs can switch from EDL to electrochemical doping. Hence, the restriction of applied V_{GS} for smaller values (<1 V) can ensure that electrostatic field-effect dominates rather than chemical reactions at the IGZO/Li-CICH interface that are responsible for lower device switching speeds. Additionally, undesired hysteresis effects during transfer characteristics can also be avoided.[52]

The transition to electrochemical doping also shifts depending on the V_{GS} scan rate used, as this ultimately determines the ionic relaxation in the electrolyte. For slower V_{GS} scan rates, the ions have enough time to diffuse into the semiconductor, promoting electrochemical doping even for low V_{GS}. Thus, an earlier hump of the I_{DS} and a more pronounced field-effect to electrochemical doping transition is visible in the transfer characteristics. In parallel, a higher S_S value is obtained, leading to a slower transition between the ON and OFF states.

Considering the narrow range of operating gate voltage (<2 V), the EGTs show a small difference in the current value during forward and backward sweeps of the V_{GS}. Although, hysteresis in the current–voltage characteristics has potential applications in nonvolatile memory devices, this phenomenon is unwanted in standard integrated circuits, and as a result it must be avoided.[326] In agreement with previous results with IGZO as semiconductor in EGTs,[325] the direction of the hysteresis is always clockwise, which is attributed to charge carrier trapping effects close to the IGZO/electrolyte interface. Moreover, hysteresis magnitude is heavily dependent on the sweep rate that plays a key role for distinguishing different hysteresis mechanisms.[326] A larger hysteresis is observed for higher scan rates, pointing to entrapment of charge carriers rather than species with low mobility (ions) in the semiconductor.

Air-stability overtime

We have also examined the environmental stability of EGTs stored and operated in air. Just slight changes in the transfer characteristics were observed for the devices exposed to ambient conditions for more than one month (**Figure 5.6**). This demonstrates that these electrolytes have superior environmental stability, which represents a huge advantage on EGTs application since there is no need of specific device encapsulation.

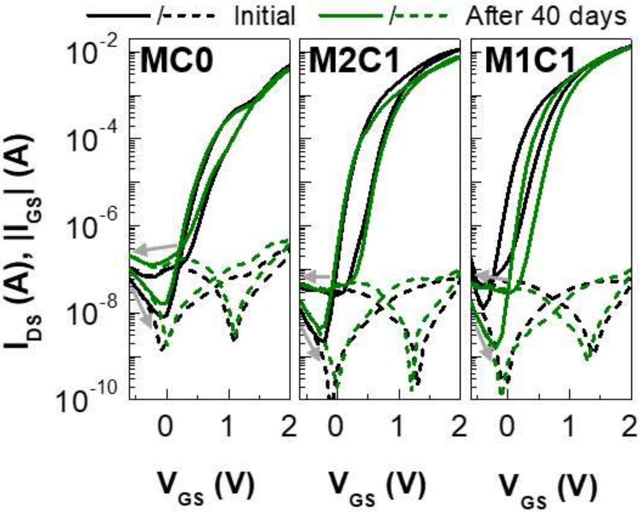

Figure 5.6. Electrical performance of IGZO EGTs on glass overtime. Cyclic I_{DS}–V_{GS} curves of EGTs gated by Li-ClCHs for saturation regime (V_{DS} = 1.2 V) at a fixed V_{GS} scan rate of 400 mV s^{-1}. Arrows represent the sweep direction, whereas continuous and dashed lines correspond to I_{DS} and $|I_{GS}|$, respectively.

5.1.2.2. Li-ClCHs as electrolyte-gate in flexible IGZO EGTs

Taking advantage of the low processing temperature of the laminated Li-ClCHs, EGTs were also fabricated on a multilayer-coated paper substrate adopting the design illustrated in **Figure 5.1** (see also **Figure 5.7**a). For this purpose, the M1C1 electrolyte was chosen for further studies owing to the impressive electrical performance of the IGZO EGTs when applied as gate dielectric, and due to its flexibility, superior robustness, and ability to be easily shaped, peeled-off, transferred, and attached to other substrates.

Electrical performance: flat state

Figure 5.7b presents cyclic transfer characteristics of IGZO EGTs on paper and a comparison of the electrical parameters depending on the V_{GS} scan rate is displayed in **Table 5.1**. Compared to devices on glass, the main differences are higher V_{ON} (0.1 V) for the lowest scan rate (25 mV s^{-1}), lower $I_{ON/OFF}$ (near two orders of magnitude inferior), and smaller μ_{Sat}. Even so, the EGT in its flat state shows good electrical performance, with an $I_{ON/OFF}$ higher than 10^4, large saturation I_{DS} of near 1 mA, and small S_S around 0.2 V dec^{-1}. A still impressive μ_{Sat} of 7.5 cm^2 V^{-1} s^{-1} was achieved at a fixed scan rate of 25 mV s^{-1}. The output characteristic curves reveal an excellent linear behavior at low V_{DS}, and a high current saturation is reached (>1 mA) for increasing V_{DS}, making the flexible EGTs suitable for ultralow-voltage applications.

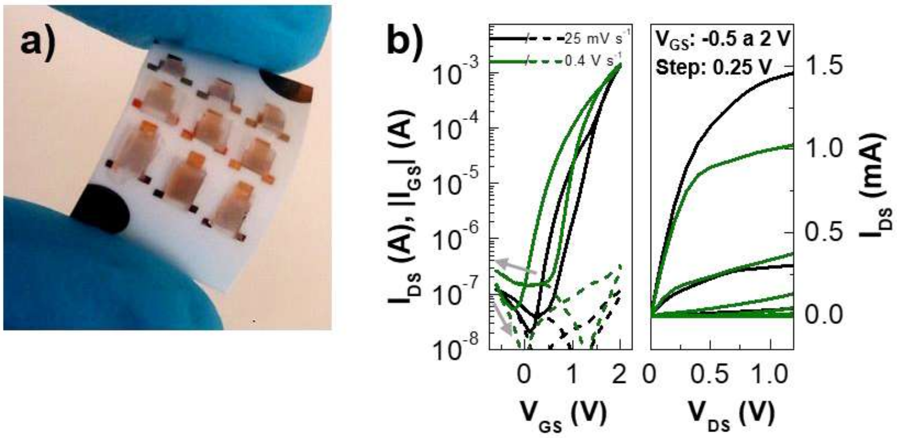

Figure 5.7. Electrical performance of IGZO EGTs on multilayer-coated paper. **a)** Photography of the developed flexible IGZO EGT on multilayer-coated paper gated by M1C1 electrolyte. **b)** Cyclic I_{DS}–V_{GS} curves of the bendable device on its flat state at different V_{GS} scan rates for saturation regime (V_{DS} = 1.2 V) and respective I_{DS}–V_{DS} curves (the step for the V_{GS} was 0.25 V, from −0.5 up to 2 V). Arrows represent the sweep direction, whereas continuous and dashed lines correspond to I_{DS} and $|I_{GS}|$ currents, respectively.

Table 5.1. Results of the electrical characterization of the IGZO EGT on paper gated by M1C1 electrolyte (V_{DS} = 1.2 V).

Scan rate [mV s^{-1}]	$I_{ON/OFF}$	V_{ON} [V]	g_m [mS]	S_S [V dec^{-1}]	μ_{Sat} [cm^2 V^{-1} s^{-1}][a)]
25	6.8×10^4	0.1	3.9	0.19	7.5
200	2.8×10^4	-0.2	3.4	0.22	5.1
400	2.6×10^4	-0.2	3.0	0.23	4.2

[a)] Mobility calculated using the C_{DL} value determined from the data fitting of the EIS measurements using Dasgupta's ECM.

A possible explanation for the loss of electrical performance relies on the poorer quality of the IGZO films deposited on the paper substrate. As shown in **Figure 5.8**, the removal of the paper substrate from the glass holder used during deposition of IGZO and Ti/Au contacts promotes the discharge of the accumulated strain on the substrate and, therefore, cracking of the Ti/Au brittle film. Also, the surface of the nanoporous polymeric coating layer of the thick raw paper is slightly cracked due to the thermal annealing performed on IGZO, which in turn affects the subsequent deposited layers.

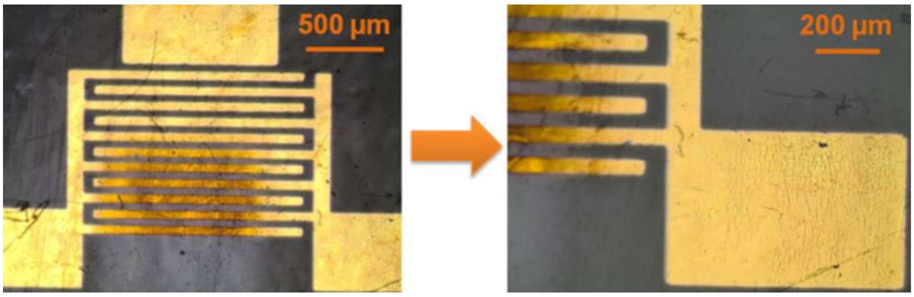

Figure 5.8. Optical microscope images showing the IGZO and Ti/Au layers deposited on multilayer-coated paper, where are visible cracks on Ti/Au electrodes and a misalignment of the patterned IGZO with the source and drain contacts.

Bending measurements

To demonstrate the flexibility of the IGZO EGTs on paper, a device was tested under different bending strain along the channel axis using substrate holders with several bending radii (from 45 down to 5 mm). **Figure 5.9**a compares the cyclic transfer curves of the EGT in its flat state, during inward and outward bending strains for a bending radius of 5 mm, and after back in its flat state (recovery). **Figure 5.9**b shows the most relevant transistor performance parameters for different bending radii.

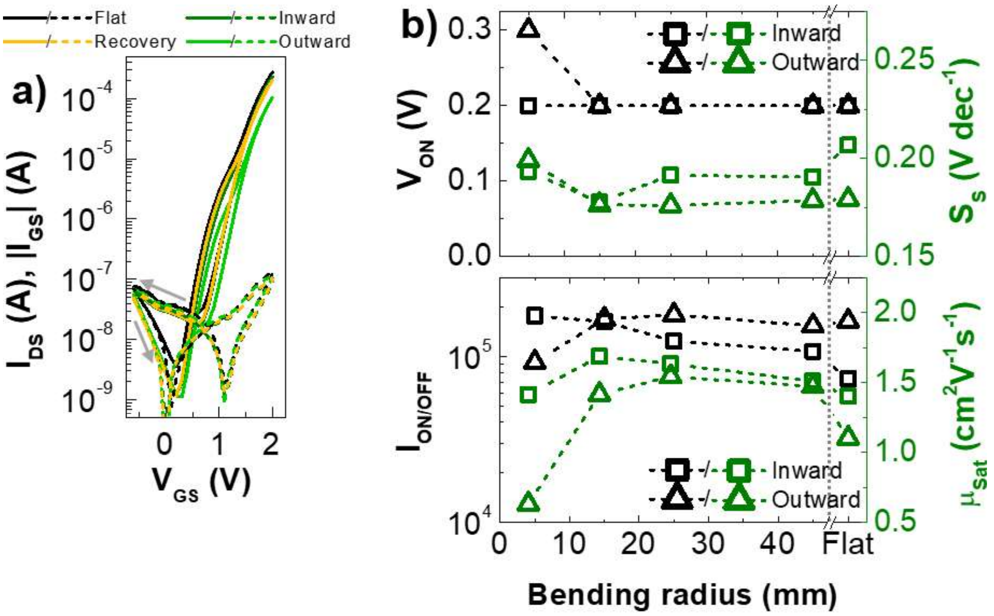

Figure 5.9. Electrical performance of IGZO EGTs on multilayer-coated paper under bending. **a)** Cyclic I_{DS}–V_{GS} curves of the IGZO EGT on paper gated by M1C1 electrolyte for saturation regime (V_{DS} = 1.2 V) at a fixed scan rate of 25 mV s^{-1} measured before bending, under inward (radius 5 mm) or outward (radius 5 mm) bending, and after removal of bending deformation (recovery to the flat state). Arrows represent the sweep direction, whereas continuous and dashed lines correspond to I_{DS} and $|I_{GS}|$, respectively. **b)** Comparison of electrical parameters before and after deformation for increasing bending radii.

In general, inward bending induces compressive strain on the EGT, which in turn contributes to slight improvements of the electrical performance of the device with decreasing bending radius down to 5 mm. The formation of additional cracks in the deposited Ti/Au film can be induced owing to the bending deformation, turning the surface of the film irregular and rough. Still, the contact at the IGZO/electrolyte interface can be at the same time enhanced due to the conformable and smooth surface of the electrolyte that allows its easy adaptation to the irregular surface of the films. Also, the compressive strain promotes an artificial channel shortening, thus an increase of $I_{ON/OFF}$ and μ_{Sat} can be observed. After inward bending, the direction of deformation was inverted. Therefore, a tensile strain deformation is displayed by outward bending and the performance loss of the EGT is observed for the smallest bending radius (5 mm), due to the delamination of the electrolyte from the semiconductor in its extremities and the cracked surface of the Ti/Au thin films.

Regardless the induced deformation, the bendable EGT exhibits similar electrical properties to the ones obtained when the device is in the flat state, with some variations in $I_{ON/OFF}$ and μ_{Sat}. The return to the flat state of the bended device occurs without changing or damaging the electrolyte and the device remains functional, exhibiting an electrical modulation slightly above 10^5, a S_S of 0.2 V dec^{-1} and μ_{Sat} near 2 cm^2 V^{-1} s^{-1}.

Electrical stress: static and dynamic measurements

To assess the electrical stress of the flexible IGZO EGTs on paper, static and dynamic measurements were performed. Regarding the static measurements, the EGTs on paper were studied under electrical stress in air by performing 100 successive cycles with a delay of 5 min between each scan. As shown in **Figure 5.10**a-b, the device exhibits a highly stable electrical performance even after 100 cycles. Although there are some electrical variations during the first two cycles, the $I_{ON/OFF}$ decreases almost insignificantly for increasing number of cycles, keeping an electrical modulation above five orders of magnitude, whereas V_{ON} remains constant at 0.2 V. Thus, the device demonstrates high stability under severe electrical stress measurements.

Concerning dynamic operation of EGTs, the switching times (between OFF and ON states) and operating frequencies should also be considered. These parameters are highly influenced by the transistor's dimensions, the mobility of the carriers, the polarization response time, that is, the EDL formation time of the electrolyte, and the ion permeability of the semiconductor.[47] In general, electrolytes with higher ionic conductivities can achieve high capacitances and fast polarization speeds in response to the applied gate electric fields, which in turn contributes considerably to the enhancement of dynamic behavior of the EGTs. Higher operating frequencies, even in the kHz range, have been reported for EGTs/circuits with ionic liquids or ionic liquid-based gels used as high capacitance gate dielectrics.[263,267,268]

Dynamic electrical characterization of the flexible IGZO EGTs on paper was undertaken through the application of a square-wave gate signal (between -0.6 until 2 V) for a fixed V_{DS} (1.2 V) and at different frequencies (1–200 Hz) (**Figure S1**), to determine the cut-off frequency and switching response. The former parameter is here determined considering the frequency at which the $I_{ON/OFF}$ becomes equal to 10,[327] whereas the latter is defined as the time required to reach from 10 to 90 % of the maximum current. These times will be addressed as off (t_{off}) and on (t_{on}) times, respectively.[327] Ten consecutive cycles of gate voltage pulses were performed, providing information about the transistor's stability during dynamic switching.

As shown in **Figure 5.10**c-d, the evolution of $I_{ON/OFF}$ with increasing cycles for a fixed frequency and the variations of I_{ON} and I_{OFF} with increasing frequencies was plotted, evidencing that the device can be switched frequently with stable $I_{ON/OFF}$ within a few milliseconds.

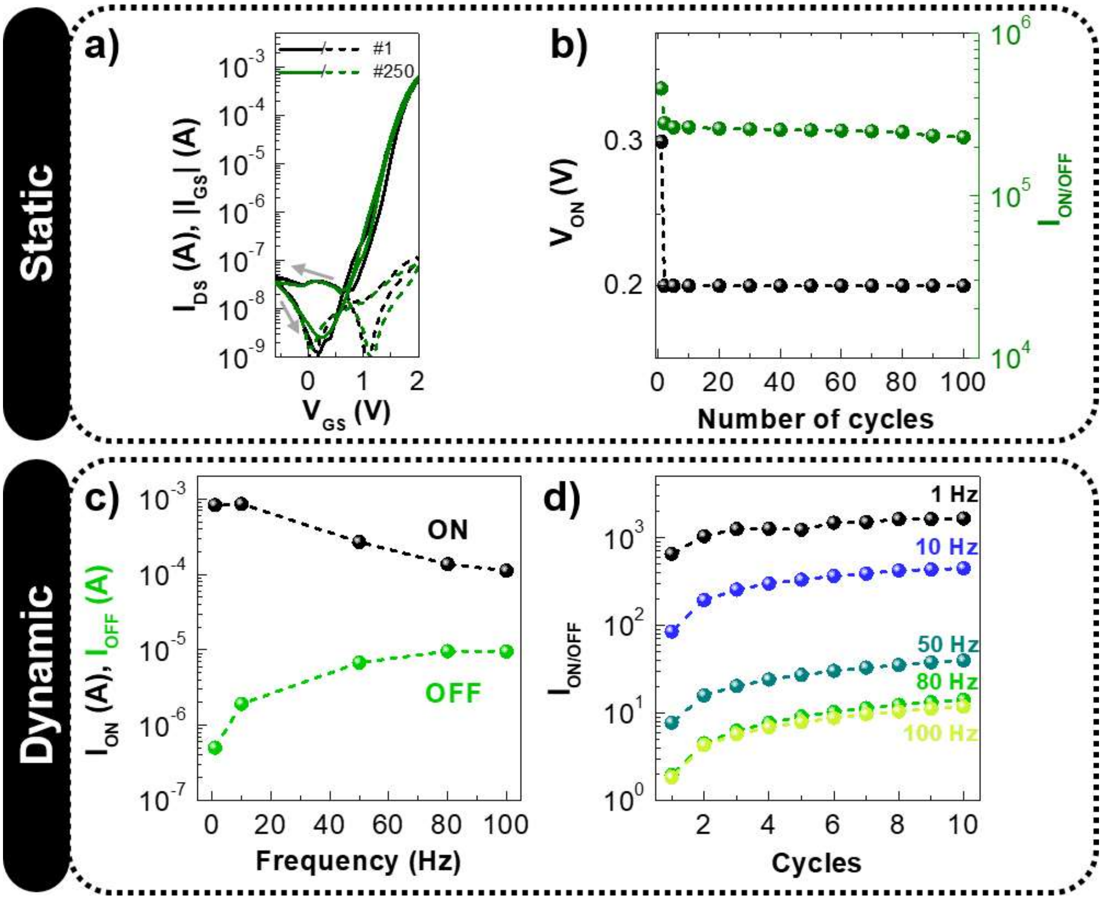

Figure 5.10. Electrical performance stability of IGZO EGTs on paper gated by M1C1 electrolyte under electrical stress. Static measurements: **a)** cyclic I_{DS}–V_{GS} curves after 1 and 100 cycles (delay of 5 min between each cycle) for saturation regime (V_{DS} = 1.2 V) at a fixed scan rate of 25 mV s^{-1}. Arrows represent the sweep direction, whereas continuous and dashed lines correspond to I_{DS} and $|I_{GS}|$, respectively. **b)** Variation of V_{ON} and $I_{ON/OFF}$ after 100 cycles. Dynamic measurements: **c)** variation of $I_{ON/OFF}$ with increasing cycles for a square-wave gate signal between -0.6 until 2 V for a fixed V_{DS} of 1.2 V and at different frequencies; **d)** evolution of I_{ON} and I_{OFF} with frequency for the tenth cycle.

Owing to the parasitic capacitance effect, spikes are observed during dynamic switching, which are more evident for faster switching frequencies.[266] A significant variation of I_{DS} between Off and On states up to three orders of magnitude is observed on a very short time scale for the lowest frequency (1 Hz), and the response times were determined around t_{on} = 85 ms and t_{off} = 3 ms. As already reported in some work,[327,328] the value calculated for t_{on} is largely superior than t_{off}, as a result of the longer time required for electrochemical charging than discharging. The fast polarization response is a demonstration of the large concentration and mobility of ionic species in the electrolyte. Although, faster electrical response is obtained for higher frequencies (for instance,

t_{on} = 6 ms and t_{off} = 2 ms at 50 Hz), this is directly related with the shrink of the $I_{ON/OFF}$ due to the increase in I_{OFF} with increasing frequency. For a frequency of 50 Hz, an $I_{ON/OFF}$ slightly above 10 is obtained. Although there is some electrical switching at 100 Hz, where $I_{ON/OFF}$ is close to 10, further increase in the working frequencies toward the cut-off frequency will lead to a fast decreasing of $I_{ON/OFF}$ until unity. Current modulation is already below 10 at frequency of 200 Hz (**Figure S1**f), which means cut-off frequency was already achieved, in accordance with the EIS results (**Figure 4.7**a). Therefore, the potential of using the developed Li-ClCH as gate dielectric in EGTs that can operate up to, at least, 100 Hz under a narrow range of V_{GS} (<2 V) was demonstrated.

The fast switching speed verified by the developed flexible IGZO EGTs on paper is substantially superior when compared with other reported solid polymer electrolytes used for electrolyte gating, since they suffer from slow polarization response, limiting transistor's switching frequency to less than 1 Hz.[327] The flexible and low-cost devices reported here are not limited to low operation speed application and fits the requirements needed for circuit applications, as further discussed in **section 5.1.3**.[47] Additional improvements in speed and cut-off frequency may be possible to achieve by proper optimization of both transistor's design and fabrication process.

Besides, regarding the electrolyte's composition, the high demand and the limited abundance of lithium salts trigger the search for sustainable alternatives. In this regard, the most suitable alternative to replace LiOH in the electrolyte's formulation, without compromising the dissolution of cellulose, is NaOH, as mentioned earlier in this chapter in **section 4.1.1.2**.

5.1.2.3. LN-ClCHs and Na-ClCHs as electrolyte-gate in flexible IGZO EGTs

A more in-depth study of the influence of the alkali hydroxide used in the formulation of the different classes of ClCHs (Li-, Na-, and LN-ClCHs when using LiOH, NaOH, or mixtures of both alkali salts, respectively, for MCC dissolution) on the electrical performance of IGZO EGTs on paper is presented in the following section. To avoid misunderstandings among the different ClCHs' composition, the developed M1C1 electrolyte, referring to the optimized formulation of Li-ClCHs, will now be named L100 electrolyte.

Influence of the alkali hydroxide

Figure 5.11 shows typical cyclic transfer curves in saturation regime, and respective output curves of the flexible EGTs on paper. Important figures of merit are summarized in **Table S5** and plotted as a function of the amount of NaOH used for cellulose dissolution (**Figure 5.12**). The values shown represent a statistical average of measurements performed for five devices, and respective errors.

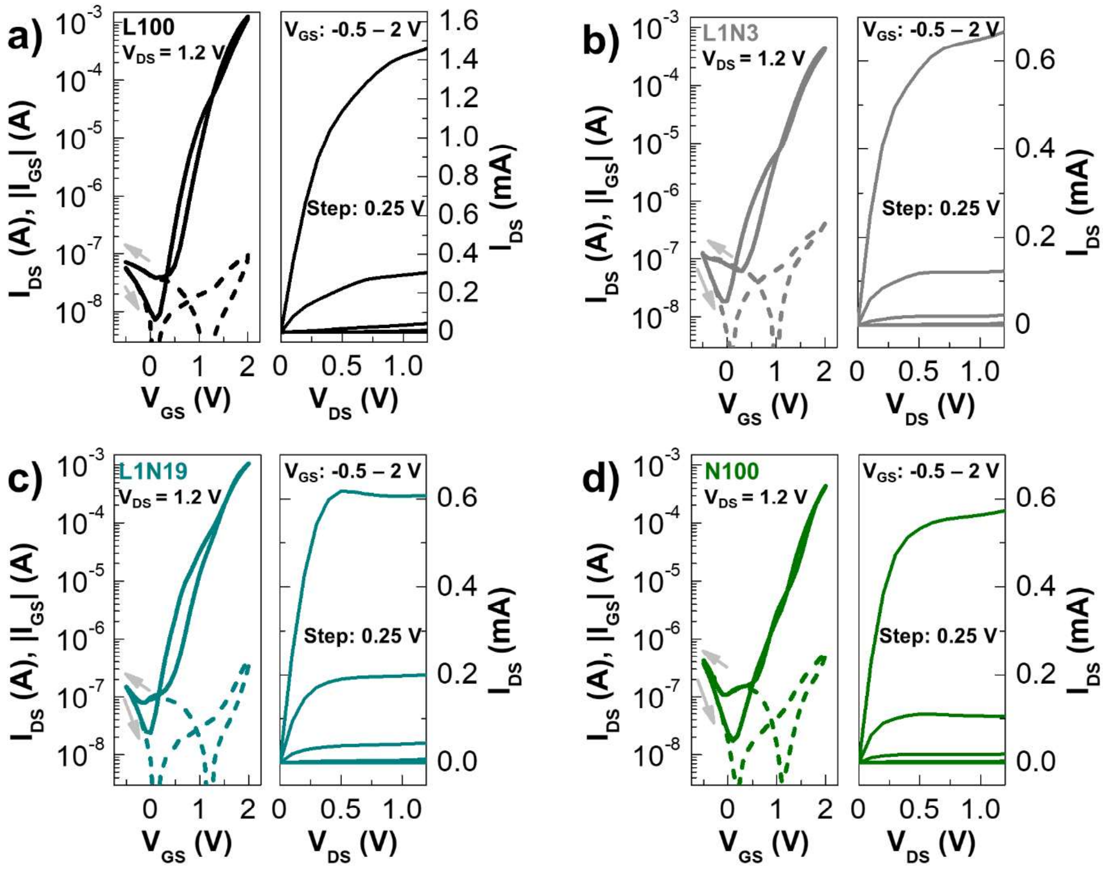

Figure 5.11. Electrical characteristics of the fabricated planar ClCH-gated IGZO EGTs on multilayer-coated paper. Cyclic I_{DS}–V_{GS} curves for saturation regime at V_{DS} = 1.2 V of IGZO EGTs gated by **a)** L100, **b)** L1N3, **c)** L1N19 or **d)** N100 membranes, and respective I_{DS}–V_{DS} curves obtained for a V_{GS} step of 0.25 V from -0.5 V until 2 V. For the transfer curves, arrows represent the sweep direction, whereas continuous and dashed lines correspond to I_{DS} and $|I_{GS}|$, respectively. All curves were acquired with a V_{GS} scan rate of 50 mV s^{-1}.

The fabricated flexible ClCH-gated EGTs are enhancement n-type transistors, which is confirmed by positive V_{ON} (0.04–0.18 V), and exhibit $I_{ON/OFF}$ ratio larger than 10^4, low S_S up to 0.26 V dec^{-1}, and the μ_{Sat} average values were calculated to be around 3.4 and 6.9 cm^2V^{-1} s^{-1}. The devices operate at low V_{GS} (<2 V) showing a small hysteresis window with clockwise direction related to charge carrier trapping effects close the IGZO/ClCH interface, indication that is not determined by ion relaxation in the electrolyte, as mentioned before.

It is clear from the results that the nature of cations has influence on the electrical performance of the different ClCH-gated transistors. The devices gated by L100 membrane achieve the highest performance reaching an $I_{ON/OFF}$ of 8.97×10^4 and a μ_{Sat} of 5.3 $cm^2V^{-1}s^{-1}$, comparing with EGTs gated by N100 electrolyte that reach 1.85×10^4 and 3.4 $cm^2V^{-1}s^{-1}$, respectively. As aforementioned in **sections 4.1.2** and **4.1.3.2** (see **Figure 4.5** and **Figure 4.8**), the slight differences observed are directly related with the quick and unstable formation of urea dendrites in the latter electrolyte that leads to lower values of σ_i. These "tree-like" structures affect negatively its optical, electrochemical, and mechanical properties, becoming opaquer and brittle as well as less conformable and adhesive to the active semiconducting surface, as expressed also by the slight increase of S_S for higher contents of NaOH. Even so, EGTs gated by LN-CICHs have an electrical performance comparable with those gated by Li-CICH.

The output characteristics of the flexible EGTs demonstrate a linear behavior at low V_{DS} values together with a clear pinch-off and saturation for higher V_{DS} values, while the current levels in the output characteristics decrease for increasing levels of Na^+ in the CICH composition.

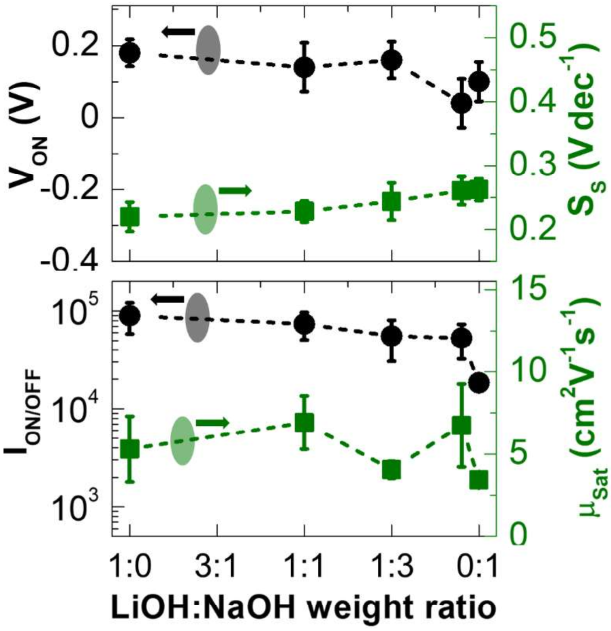

Figure 5.12. Statistical distribution of device metrics ($I_{ON/OFF}$, V_{ON}, μ_{Sat} and S_S) for flexible CICH-gated IGZO EGTs on multilayer-coated paper substrate, represented as a function of LiOH and NaOH contents used for cellulose dissolution. The electrical parameters were calculated from transfer characteristic curves in the forward sweep direction and in the saturation regime at V_{DS} = 1.2 V for a V_{GS} scan rate = 50 mV s^{-1}. The data points show the average and corresponding errors bars obtained from five samples.

Electrical stress: static measurements

IGZO EGTs on paper gated by LN-CICHs with the two highest concentrations of NaOH (L1N3 and L1N19 membranes) were subjected to 250 successive V_{GS} cycles with a delay of 5 min between each scan, and their performance was compared with L100 membrane (**Figure 5.13**). The devices gated by L100 or L1N3 membranes do not show significant signs of degradation, demonstrating their high stability under severe electrical stress measurements. On the other hand, it is clear a degradation of the EGT's performance using the L1N19 membrane after around 150 cycles, as the dendrites start appearing.

Still, their performance can also be highly dependent on the environmental conditions as the CICHs' composition confers a hydrogel-state. One way to have a glance of such effects consists of testing such devices under distinct environmental conditions, as further mentioned in the next section.

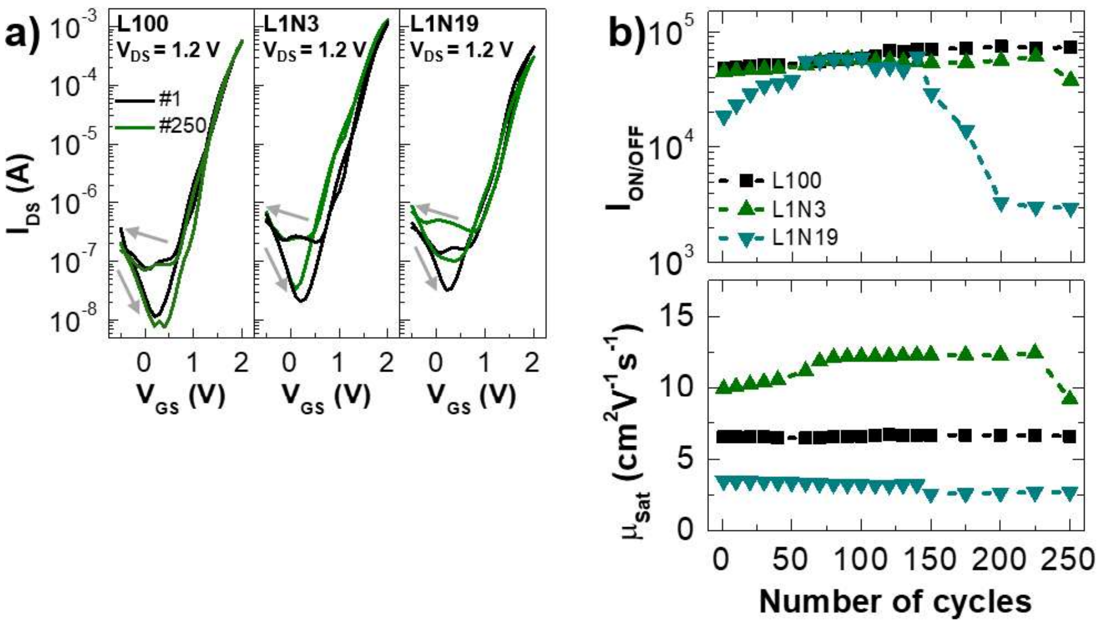

Figure 5.13. Electrical performance stability of the fabricated CICH-gated IGZO transistors on multilayer-coated paper under static electrical stress. **a)** Cyclic I_{DS}–V_{GS} curves of the fabricated EGTs gated by L100, L1N3 or L1N19 membranes for saturation regime (V_{DS} = 1.2 V) at a fixed V_{GS} scan rate of 50 mV s^{-1} before and after 250 cycles (delay of 5 min between each cycle). Arrows represent the sweep direction. **b)** Variation of the electrical parameters ($I_{ON/OFF}$ and μ_{Sat}) after sucessive cycles.

Environmental endurance: influence of temperature and humidity

Considering the hydrogel-nature of the CICHs, the environmental conditions affect the amount of water retained into their structure and, therefore, its swelling behavior. Thus, the role of temperature and RH on the electrical performance of the IGZO EGTs on paper was also undertaken (**Figure 5.15** and **Figure S2**). The L1N3 electrolyte was used for these measurements due to its superior environmental stability overtime in comparison with the CICHs with higher amounts of NaOH, as well as similar thermal behavior and electrochemical properties to the L100 membrane. The temperature range at which the devices were tested was limited to 100 ºC, as the electrolyte and paper substrate show some signs of degradation for higher temperatures (**Figure 5.14**). It is worth to mention that the layers deposited on paper are not expected to be significantly deformed with the swelling of the fibers, since it loses only a small amount of adsorbed water (4.2 % of its weight) on the cellulose fibers at 100 ºC.

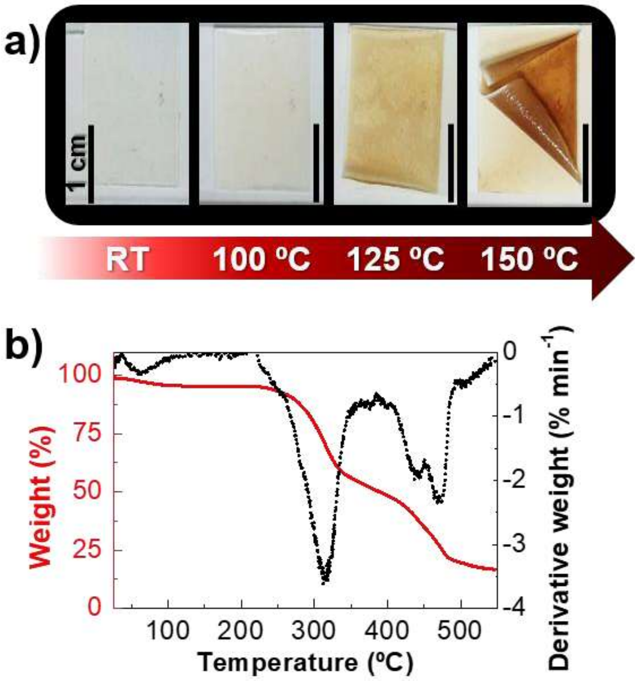

Figure 5.14. Thermal behavior of multilayer-coated paper substrate. **a)** Photographs of the L1N3 membrane attached to the paper substrate after heating at different temperatures. **b)** TGA and respective derivative of the TGA curve.

There is a clear change of the electrical parameters with heating, demonstrating a steep degradation of the electrical performance for temperatures higher than 50 ºC due to water release, resulting in the loss of ionic conductivity and adhesion to the semiconductor surface.[102] As temperature increases until 100 ºC, $I_{ON/OFF}$ is substantially affected decreasing to one order of magnitude as a result of the increase of I_{OFF} and considerable decrease of I_{ON}. During heating, V_{ON} shifts in direction to negative V_{GS} values due to thermal activation of the intrinsic conductivity of the semiconductor, that also explains the increase of I_{OFF} (**Table S6**).[329]

A very similar behavior was observed after testing a device overtime under vacuum conditions to study the influence of the RH (**Table S7**). In this case, it is remarkable the stability of the device as pressure drops inside the chamber down to 4.2×10^{-3} mbar, showing still some electrical modulation (inferior to one order of magnitude) at very low-pressure levels ($\approx 7.4 \times 10^{-4}$ mbar). The presence of hygroscopic alkali metal ionic species in the hydrogels aids in water retention even in environments with low RH.[330]

Also, important to mention is the fast recovery of the electrical performance of the EGTs within a few minutes when exposed again to ambient conditions (24 ± 2 °C, 43 ± 4 %RH). In both cases, during cooling or after exposing the devices to atmospheric pressure conditions, $I_{ON/OFF}$ reaches the same range of values obtained for pristine devices, despite both I_{OFF} and I_{ON} shift to higher values. This behavior demonstrates that this shift is determined by the IGZO rather than the electrolyte. These results also demonstrate that the electrolyte can spontaneously recover its performance overtime under ambient conditions without any external stimulus, due to the charged hydrophilic functional groups on cellulose chains that are able to attract the ions within the network, whereas large amounts of water are reversibly adsorbed.[102]

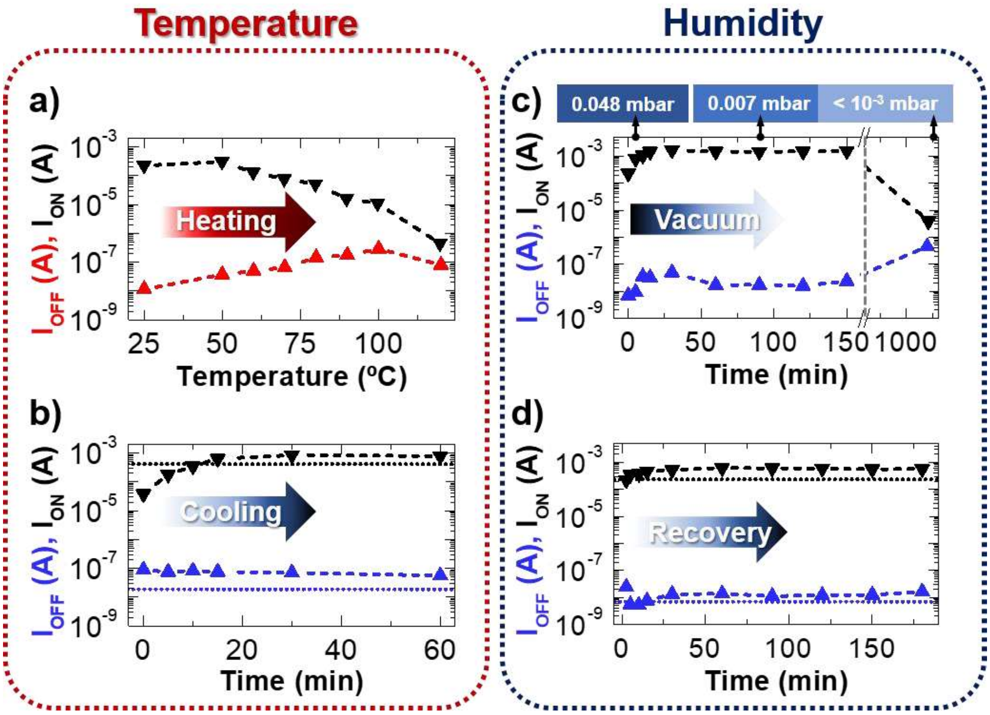

Figure 5.15. Influence of temperature and humidity on the electrical performance of the fabricated L1N3 hydrogel-gated IGZO transistors on multilayer-coated paper. Variation of the electrical parameters I_{ON} and I_{OFF} **a)** during heating directly on the probe station at different temperatures from RT to 120 ºC (20 min of stabilization at each temperature before measuring), and **b)** while cooling at ambient conditions a device previously heated at 80 ºC for 20 min. Variation of the electrical parameters I_{ON} and I_{OFF} **c)** under vacuum conditions, and **d)** during recovery at atmospheric pressure. All curves were acquired with a V_{GS} scan rate of 50 mV s^{-1} for saturation regime (V_{DS} = 1.2 V). Short dotted lines correspond to the original performance of the EGTs before heating or vacuum.

This behavior is further explored in the **chapter 7**, as the reversible swelling ability of the electrolytes offers additional benefits in healing and recycling the membranes that can be reused in new iontronic devices, triggering the introduction of environmentally responsible behaviors towards sustainability.

5.1.3. Electrical performance of CICH-gated IGZO circuits on paper

Figure 5.16a shows four resistive-load inverters with planar sputtered IGZO EGTs on multilayer-coated paper gated by N100 membrane, and its respective circuit schematic. The circuit VTC curves (output voltage V_{OUT} vs. input voltage V_{IN} and |gain| vs. V_{IN}) are plotted in **Figure 5.16**b-c. A good signal inverting behavior is observed when switching V_{IN} from the “0” state (V_{IN} = 0 V) to the “1” state (V_{IN} = 2.5 V) for a supply voltage (V_{DD}) of 1 V, meaning that if the applied input is low then the output becomes high and close to $V_{DD} – R_L I_{DS}$, and vice versa. The V_{OUT} fully swept from near 1 V to almost 0 V with a relatively small output hysteresis. When increasing the R_L from 36 to 230 kΩ, the logic gate reaches a maximum |gain| ($-\partial V_{OUT}/\partial V_{IN}$) of 1.8 and 2.4, respectively.

Owing to their low-voltage operation, thin-film batteries, supercapacitors, external radio frequency fields or energy-harvesting systems can be used to power these logic gate circuits.[47,263,269]

Regarding the dynamic response of the inverter (**Figure 5.16**d-g), the operation speed is highly limited and degraded by the contribution of the parasitic capacitance from the probing (≈160 pF) and the oscilloscope cabling (≈15 pF). Although the test setup, consisting of a semiconductor parameter analyzer, an oscilloscope, and a wave generator, does not accurately simulate the dynamic behavior of the circuit, we can get at least a sense of the magnitude of the switching time.

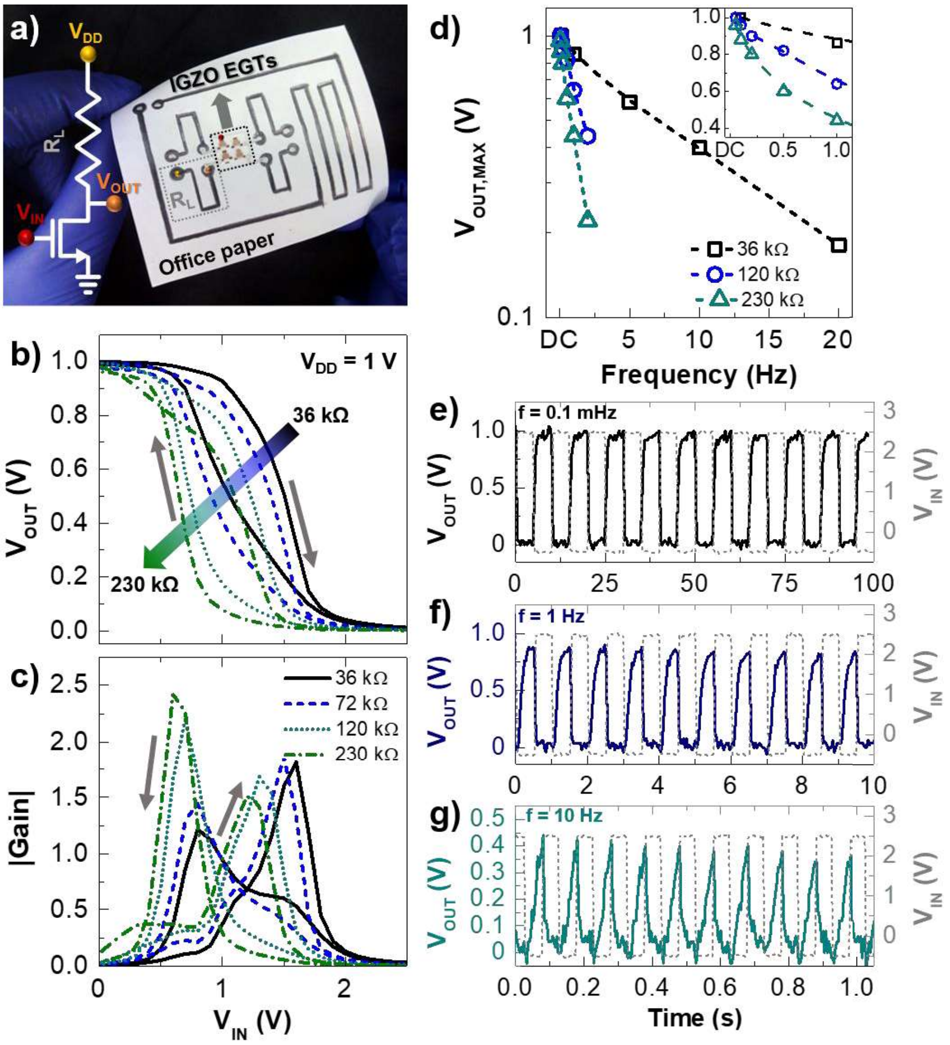

Figure 5.16. Electrical characterization of planar NOT gates on paper. **a)** Photograph of the fabricated flexible planar NOT-gates with IGZO transistors gated by N100 membrane and pencil-drawn resistive tracks (inset: circuit schematic). VTC curves for different load resistances along a pencil-drawn graphitic line (arrows represent the sweep direction): **b)** V_{OUT} vs. V_{IN}, and **c)** |gain| vs. V_{IN}. **d)** Variation of maximum V_{OUT} ($V_{OUT,\ Max.}$) with frequency for different resistances along a pencil-drawn graphitic line to an input square-wave pulse from V_{IN} = -0.5 V to 2.5 V and V_{DD} = 1 V after five cycles. Dynamic response of the flexible planar NOT gate with a pencil-drawn R_L of 36 kΩ to an input square-wave pulse from V_{IN} = -0.5 to 2.5 V and V_{DD} = 1 V for **e)** 0.1 Hz, **f)** 1 Hz, and **g)** 10 Hz.

Figure 5.16d demonstrates that the inverter can switch at rates in the 1–20 Hz range depending on the R_L. As shown in **Figure 5.16**e-g (see also **Figure S3**), a better dynamic response is observed for lower values of R_L around of 36 kΩ. Higher operating frequencies, in kHz range, have already been reported in literature for EGTs and circuits.[208,260,328,331,332]

The dynamic performance can be further improved by adopting a vertical top-gate architecture, shortening transistors' channel length, getting a better control of the overlap between source-drain electrodes and the thick electrolyte, and reducing the gate-channel distance. Less capacitive probing or isolation of the output note with a buffer circuit can considerably improve the frequency of operation.

5.2. "Interstrate" ACICC-gated IGZO transistors

Throughout this thesis, it was heavily emphasized the importance of depositing compatible functional materials that can establish smooth interfaces among the different layers that compose the transistors towards enhanced electrical performance. Moreover, the patterning of electrodes with shorter channel lengths and the design of EGTs with a vertical architecture were pointed out as key factors when looking for transistors with fast switching speed. In line with these considerations, the paper substrate and the hydrogel electrolyte-gate are replaced by a single material, an intrinsically ionic conductive cellulose-based substrate, which combines the advantages of both materials, thus allowing the manufacturing of EGTs with simpler designs.

As displayed in **Figure 5.17**a, sputtered amorphous IGZO EGTs were fabricated onto the ACICC membrane with a "interstrate" staggered-bottom gate structure, consisting of Al source-drain electrodes and IZO gate electrode. The channel length and width were 230 μm and 2.3 mm, respectively, resulting in a W/L ratio of 10 (**Figure 5.17**b).

As demonstrated in **Figure 5.17**c (see **Table 5.2**), a considerable improvement on the electrical performance of the "interstrate" nanopaper composite gated transistors (NCGTs) is observed in comparison with the fabricated flexible in-plane CICH-gated IGZO transistors. Despite the superior conformability of CICH membranes compared to the ACICC substrate, the direct lamination of these hydrogels on the channel region can create local interface defects from trapped air bubbles. On the other hand, the controlled deposition of uniform stacked inorganic layers with nanometric dimensions alongside the smooth surface of ACICC membrane can avoid such issue.

The devices show a good electrical performance, where the hysteresis is almost inexistent and exhibit anti-clockwise direction, related to the accumulation of ionic charges on the interfaces that the ACICC membrane establishes with the IGZO and IZO electrode. An electrical modulation of more than four orders of magnitude is achieved at lower operating voltages (<2 V), reaching the saturation regime for V_{DS} values lower than 1.5 V. The devices work in the depletion mode (normally-on), achieving a maximum I_{ON} of nearly 1 mA for a V_{GS} of 2 V, whereas the $|I_{GS}|$ values are within the 0.2 μA scale, and S_S is substantially decreased down to just about 0.14 V dec^{-1}.

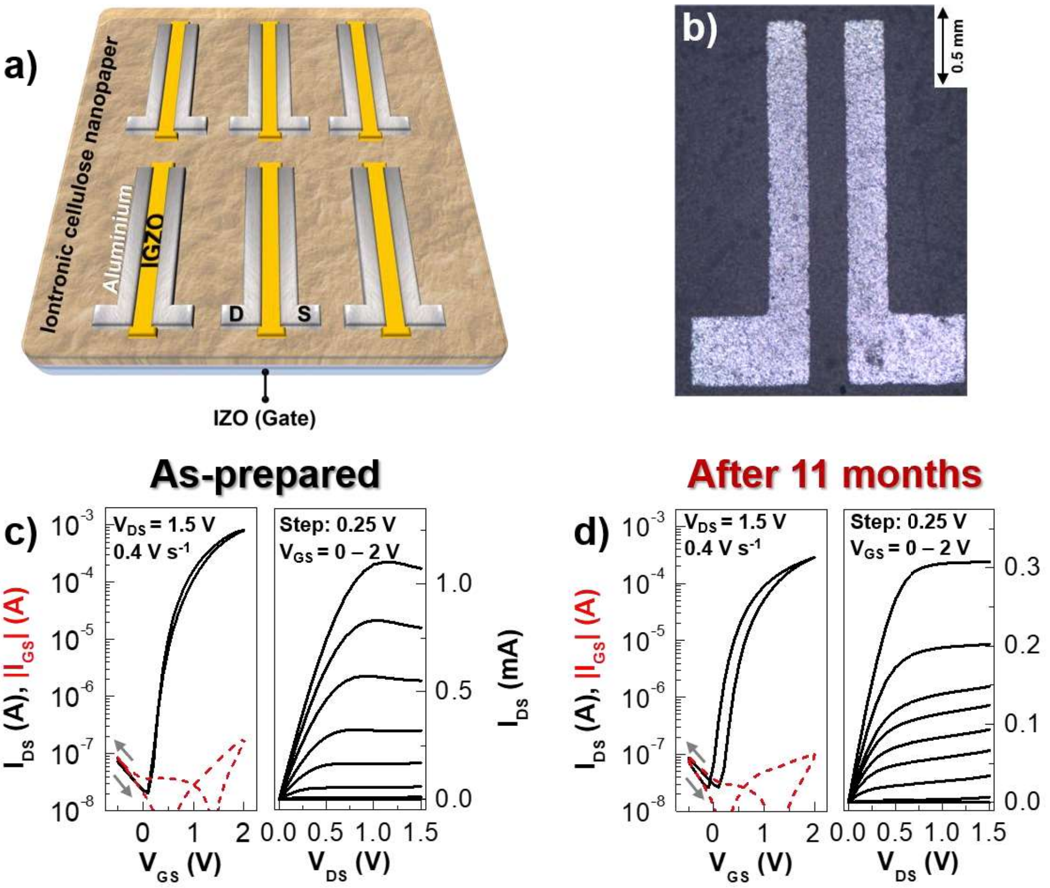

Figure 5.17. Design and electrical characterization of the fabricated ACICC-gated IGZO transistors. **a)** Schematic illustration of the structure of the sputtered IGZO EGTs using the ACICC membrane as ionic conductive substrate. **b)** Optical micrograph image of a single device fabricated on the ACICC membrane, showing the source and drain contacts. I_{DS}–V_{GS} curves and respective I_{DS}–V_{DS} curves (the step for the V_{GS} was 0.25 V, starting from -0.5 up to 2 V), collected with a V_{DS} = 1.5 V and V_{GS} scan rate of 0.4 V s^{-1}: **c)** as-prepared, and **d)** after almost eleven months of storage under ambient conditions. Arrows represent the sweep direction, whereas continuous and dashed lines correspond to I_{DS} and $|I_{GS}|$, respectively.

Table 5.2. Resume of the electrical performance stability of ACICC-gated IGZO transistors overtime. The values show the average and respective standard error of the mean obtained from six samples (V_{DS} = 1.5 V, V_{GS} scan rate: 0.4 V s^{-1}).

Electrical parameters	As-deposited	11 months
V_{ON} [V]	0.00 ± 0.03	-0.12 ± 0.02
I_{OFF} [nA]	22.7 ± 2.49	20.8 ± 1.68
I_{ON} [mA]	0.63 ± 0.09	0.25 ± 0.03
$\|I_{GS}\|$ [nA]	192 ± 11.5	102 ± 2.00
$I_{ON/OFF}$ [×10^4]	2.78 ± 0.28	1.22 ± 0.10
S_S [V dec^{-1}]	0.141 ± 0.003	0.144 ± 0.003
μ_{Sat} [cm^2 V^{-1} s^{-1}]$^{a)}$	11.4 ± 1.07	4.02 ± 0.60

$^{a)}$ Mobility calculated using the capacitance values extracted directly from the EIS data at 0.1 Hz.

Considering the materials that establish an interface with the ACICC membrane, the capacitance of the electrolyte-gate was determined from EIS measurements, using a capacitor structure consisting of stacked layers of Al/ACICC/IZO that constitute the source-drain electrodes, gate dielectric, and gate electrode, respectively (**Figure S4a-c**). The μ_{Sat} value is around 11.4 ± 1.07 cm^2 V$^-$

^{1} s^{-1} for a capacitance value of 6.93 ± 0.68 μF cm^{-2}, extracted from EIS data at 0.1 Hz (EDL formation regime). Furthermore, the ECM proposed by Dasgupta et al.[52] was used to estimate σ_i for such capacitor structure, which is around 0.16 ± 0.03 mS cm^{-1}. Both capacitance and σ_i are much superior to that previously calculated in **section 4.2.2**, when using carbon electrodes. A plausible explanation for the differences observed in the electrochemical behavior of the ACICC for distinct conductive materials relies on a possible electrochemical doping mechanism that occurs in the contact regions of the electrolyte with Al and IZO contacts, thus leading to much larger capacitances.[261]

For the ACICC-gated IGZO transistors under discussion, the composition of the source-drain electrodes can generate some drawbacks because Al is an electropositive metal, meaning that under positive bias the metal electrode can be dissolved in the electrolyte, and Al has also a strong affinity for oxygen that promotes its oxidation.[263] Furthermore, electrochemical doping of IGZO has already been reported.[31,32,265] Therefore, the electrochemical stability of the devices was also undertaken, using a capacitor structure that includes the semiconducting material IZO/ACICC/IGZO/Al (**Figure S4**a). A capacitor structure without IGZO was used as reference to ensure where the electrochemical reactions take place.

Contrarily to the electrochemically stable screen-printed carbon electrodes, electrochemical reactions are visible in both electrochemical systems composed of Al and IZO electrodes (**Figure S4**d). Additional faradaic redox currents are visible when IGZO is integrated into the electrochemical cell, which evidences its permeability to ions, as already verified in this work in **section 5.1.2**. Nevertheless, the sputtered IGZO NCGTs show exceptional environmental stability, remaining functional after ageing for almost 11 months under ambient conditions, showing some changes in their performance, namely on μ_{Sat} and I_{ON} parameters (**Figure 5.17**d and **Table 5.2**). For longer storage periods, the Al contacts show some signs of deterioration probably due to the ionic composition of ACICC membrane.

Despite the considerably larger channel length of the electrochemically-gated sputtered IGZO EGTs fabricated on the ACICC membrane in comparison with the flexible CICH-gated IGZO transistors, the prior devices exhibit a faster dynamic response, being able to operate for superior frequencies up to 250 Hz with a proper electrical modulation above one order of magnitude (**Figure 5.18** and **Figure S5**). The considerable enhancement in the dynamic response can be justified by the adopted vertical configuration and better conformability of the active layers to the electrolyte-gate.

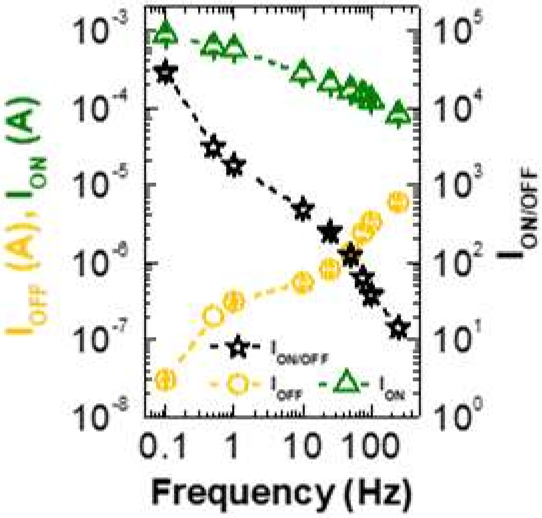

Figure 5.18. Dynamic electrical characterization of the fabricated sputtered amorphous IGZO NCGTs. Evolution of I_{ON}, I_{OFF} and $I_{ON/OFF}$ with frequency for gate voltage pulses from -1 until 2 V (the data points show the average and corresponding errors bars obtained from five devices).

Chapter 6

Ion-controlled screen-printed ZnO transistors and circuits

6. Ion-controlled screen-printed ZnO transistors and circuits 101

6.1. Screen-printed ZnO EGTs and integrated circuits on paper 102

6.1.1. Design and architecture 102

6.1.1.1. Pencil-drawn resistive-load logic gates with screen-printed ZnO EGTs 102

6.1.1.2. Tunable optoelectrical resistor switch as load resistance for NOT logic gates 105

6.1.2. Electrical performance of screen-printed ZnO EGTs on office paper 106

6.1.2.1. Performance of as-printed devices.. 106

6.1.2.2. Air-stability overtime 108

6.1.2.3. Bending measurements 109

6.1.2.4. Environmental endurance: influence of temperature and humidity........ 111

6.1.2.5. Electrical stress: static and dynamic measurements 113

6.1.2.6. Optimization of EGTs' performance with porous ZnO nanoplates......... 114

6.1.3. Electrical performance of screen-printed ZnO circuits on office paper 116

6.1.3.1. Handwritten logic gates with screen-printed ZnO EGTs 116

6.1.3.2. UV-responsive inverters 118

6.2. Fully screen-printed ZnO nanopaper composite gated transistors and logic gates 122

6.2.1. Design and architecture 122

6.2.2. Electrical performance of fully screen-printed ZnO nanopaper composite gated transistors 124

6.2.2.1. Performance of as-printed devices.. 124

6.2.2.2. Air-stability overtime 126

6.2.2.3. Bending measurements 127

6.2.2.4. Electrical stress: static and dynamic measurements 130

6.2.3. Logic gate operations with fully printed ZnO nanopaper composite gated transistors 131

The substitution of time-consuming, sophisticated, energy-intensive, and highly expensive conventional microfabrication techniques, such as those addressed in the previous chapter, by solution-processed functional materials compatible with printing techniques is an important strategy towards flexible electronics, where cellulose-based paper substrates fit in, decreasing drastically the cost of the devices.[15,139] Therefore, an important objective of this PhD plan was to integrate the developed cellulose-based composites (electrolyte membranes and semiconducting inks) in fully printed/written transistors and circuits able to operate with only a few volts (<3 V).

Within this context, devices were also fabricated using the formulated screen-printable ZnO-based inks to pattern the channel layer either on paper-based substrates, where the Li-CICH works as gate dielectric, or directly on the developed ACICC membrane. Both strategies reduce considerably the time and degree of complexity of the manufacturing process of the EGTs, while ensuring additional features, such as low-voltage operation, flexibility, and recyclability.

Logic gate operations either on paper or on the developed “paper-like” active substrate are demonstrated by adopting a user-friendly hybrid manufacturing process that combines screen-printing with handwriting techniques to easily draw conductive/resistive paths. Having in mind the huge potential demonstrated by ZnO nanostructures for UV photodetection, which has been extensively explored in our research group,[58,254,276,284,333,334] low-voltage photo-electronic ZnO-based logic circuits are also demonstrated on paper, which brings a new light to the field of flexible smart sensing applications through UV illumination stimuli.

6.1. Screen-printed ZnO EGTs and integrated circuits on paper

The formulated CMC/ZnO inks are further explored in this section as they yield screen-printed films composed of densely percolated functional particles on paper that display good adhesion, superior smoothness and homogeneity compared to the heavily cracked and non-uniform EC/ZnO films. Several measurements were performed on the screen-printed ZnO EGTs and integrated circuits (NOT, NAND, and NOR logic gates) fabricated on office paper to assess their electrical endurance under mechanical bending, static and dynamic electrical stress as well as resilience under extreme environmental conditions (temperature vs. humidity), and air-stability overtime. The influence of particles morphology on the electrical performance of the devices is also studied. Moreover, due to the ability of tuning the electrical properties of ZnO upon UV light exposure, photoelectronic ZnO circuits on paper were also fabricated by combining UV switchable light sensors, working as tunable load resistances controlled by UV light, with ZnO EGTs.

6.1.1. Design and architecture

6.1.1.1. Pencil-drawn resistive-load logic gates with screen-printed ZnO EGTs

As depicted in **Figure 6.1**, handwritten logic gates with CICH-gated screen-printed ZnO transistors with a channel length (L) and width (W) of 200 and 500 µm (W/L ≈ 2.5), respectively, were produced on standard office paper using a conventional source and drain electrodes architecture with an in-plane-gate configuration. Contrarily to the previous approach (**section 5.1.1**), the manufacturing/assembling processes involved are exclusively devoted to printing and handwriting techniques, including a film-transfer lamination process, which were strategically selected to offer freedom of design.

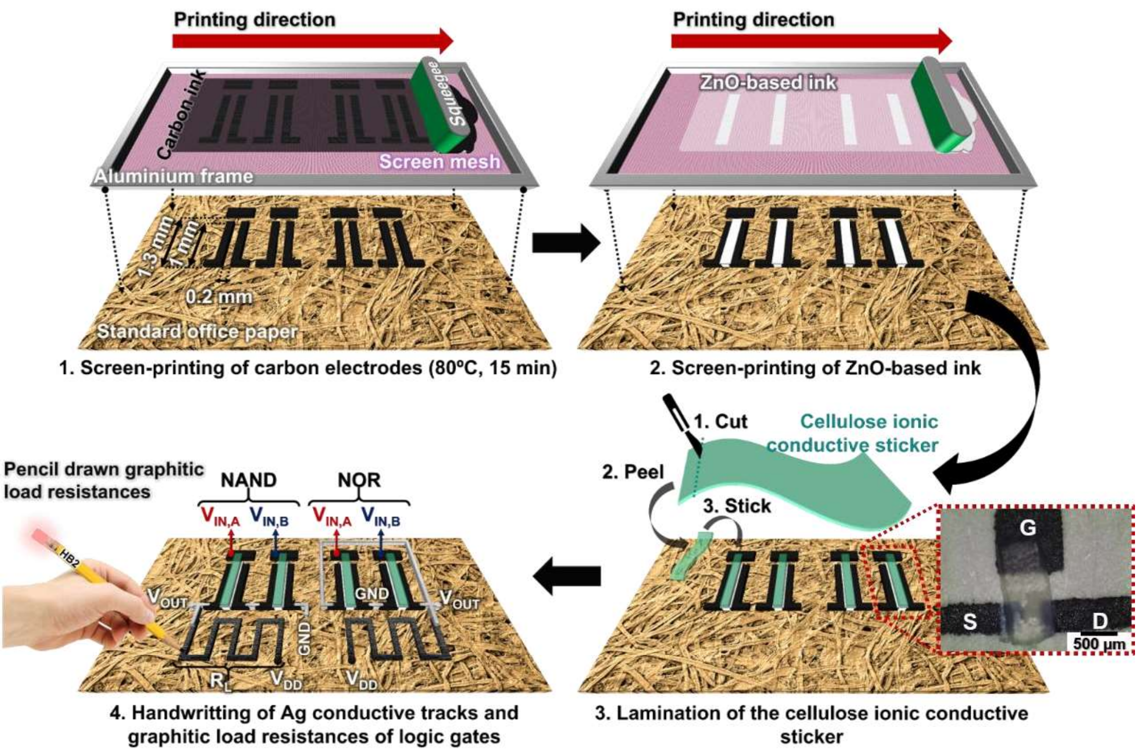

Figure 6.1. Schematic representation of the fabrication steps of handwritten logic gates with screen-printed ZnO EGTs on office paper gated by the Li-CICH (inset: optical microscope image of a printed ZnO EGT on office paper). S, D, G, R_L, V_{DD}, V_{OUT}, GND, $V_{IN,A}$ and $V_{IN,B}$ are referred to source, drain, gate, load resistance, supply voltage, output voltage, ground, and input voltages for EGTs A and B, respectively.

Sheets of ordinary office paper, where are already patterned the carbon electrodes and the inorganic semiconducting layer of the transistors, are provided in the form of a portable kit that includes calligraphy acessories (HB-2 pencil and commercial conductive silver ink rollerball pen) and the Li-CICH sticker.

The unique features of the healable and recyclable CICH stickers, which offer portability, flexibility and conformability, together with the developed water-based cellulose composite semiconducting ink that does not require sintering processes after printing, have a significant role in this demonstration of portable, disposable and low-cost circuits fabricated on-the-spot. Both functional materials can withstand large periods of storage under ambient conditions without loosing performance.

A commercial carbon-based electroconductive ink was selected as the material for the electrodes, since it is electrochemically stable and a less expensive alternative material to inert and costly noble metals, such as gold and platinum.[47] With only one screen-printing pass, it is possible to deposit a continuous carbon electroconductive layer (**Figure 6.2**a-c). Pinholes and pores are visible on the surface of the electrodes, which were likely formed during evaporation of residue from the ink. Despite these surface imperfections, the carbon layer smooths paper's surface roughness from nearly 3 μm[58,129] down to 161 nm RMS (**Figure 6.2**d). Screen-printed carbon films with a square shape (area of 1 cm^2) reach a R_s of 160 ± 6.96 $\Omega\ \square^{-1}$ (determined from four-point probe measurements, using **Equation S6**) after curing at 100 ºC for 30 min.

As the dynamic response of the printed transistors is improved for shorter channel lengths, the device dimensions were downscaled towards the maximum resolution achieved for the carbon electrodes on office paper.[11] Well-defined lines can be printed with the commercial carbon ink on office paper with a width resolution of 162 ± 2.80 μm and 211 ± 5.15 μm for line openings of 150 and 200 μm, respectively (**Figure 6.2**e).[172] Since for line widths of 150 μm the printed lines still tend to occasionally merge on office paper along a single fiber coated with conductive carbon, the channel of the transistors was designed with screen masks with minimum openings of 200 μm to avoid unintentional short circuits between the electrodes, thus ensuring a better yield of functional devices.

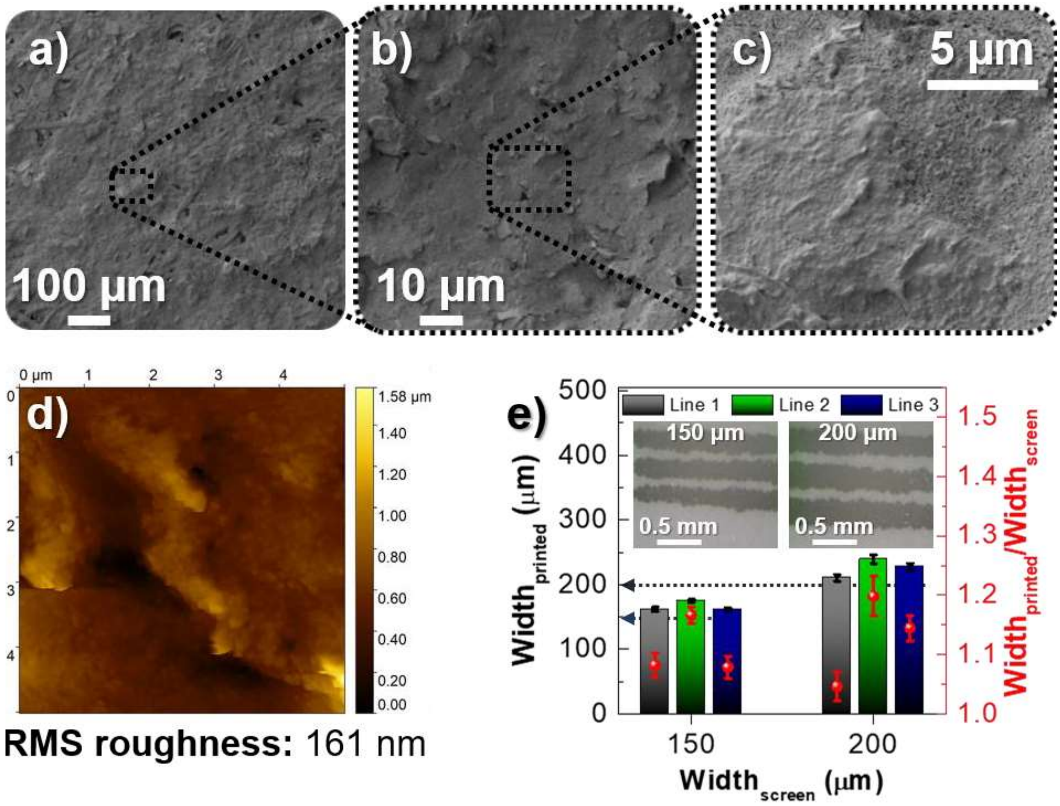

Figure 6.2. Printability and electrical characteristics of screen-printed carbon electrodes on office paper. **a-c)** SEM images for different magnifications of screen-printed carbon films dried at 100 ºC for 30 min, and respective **d)** AFM image. **e)** Printing resolution of the carbon ink on office: width$_{printed}$ vs. width$_{screen}$, and respective width$_{printed}$/width$_{screen}$ ratio (inset: optical microscope image of screen-printed lines on office paper). The values show the average and respective standard error of the mean obtained from ten measurements for each line.

Then, the developed cellulose composite inks based on ZnO nanostructures were printed in the channel region, and the printed film is dried at RT in a short period of time (<10 min). To complete the printed EGTs' fabrication, the developed freestanding cellulose electrolyte-gate sticker is cut from the glass substrate, transferred with a tweezer, and laminated directly on the device to bridge the channel region and gate electrode.

Considering the simplicity of all the tasks involved in the printing and assembling of the active materials, the whole process of manufacturing takes less than 1 h. As demonstrated in **section 6.2.1**, this time can be even shortened by using a substrate with ionic conductivity, thus eradicating the subsequent task related with the deposition of the gate dielectric.

The fabricated screen-printed EGTs can be easily integrated in logic gates (NOT, NAND, and NOR gates) by using basic ubiquitous calligraphy accessories, such as a commercial conductive silver-based ink rollerball pen and a pencil, for easy patterning of conducting tracks and graphitic load resistances, respectively. The logic circuits were constructed by connecting in series a pencil drawn R_L with one drive ZnO EGT (EGT_D) for the NOT logic gate. The NAND logic gate is designed by a series connection of a pencil drawn load resistance and two identical driving printed ZnO transistors, while a NOR logic gate is formed by two parallel driving transistors instead.

6.1.1.2. Tunable optoelectrical resistor switch as load resistance for NOT logic gates

Flexible broadband photosensing devices, that combine electrical signal amplification with light detection, can be used for detecting, processing, and control information when integrated in logic circuits controlled by incident light, answering to the emerging demand for applications in the field of optical imaging, health monitoring and diagnosis, flame detection, security control, and environmental monitoring.[335–338]

From a broad list of optoelectronic materials, ZnO nanostructures stands out as one of the most preferred materials for UV photodetection by virtue of its wide bandgap in the UV range and high photosensitivity due to a higher aspect ratio of length to diameter and higher surface area of nanostructures.[58,254,276,333,335,339–343]

In this work, UV photo-switchable circuits were fabricated by connecting the fabricated screen-printed ZnO PNPs EGTs with UV sensors with a conductive silver ink rollerball pen (**Figure 6.3**), being both components based on porous ZnO nanostructures as the inorganic photosensitive material. A porous morphology in combination with a high surface area is advantageous to create additional active adsorption sites, thereby improving photosensing properties of ZnO.[257,344] In this case, the photo-electrical modulation of the circuit is promoted by exposing the UV sensor directly to a UV light source, thus working as an optoelectrical load resistor that shifts from a high resistive state to a more conductive state. A piece of office paper was laminated on top of the sticky electrolyte-gate to protect the photosensitive ZnO channel layer of the transistors from the effects of UV radiation, thus being possible to control the electrical performance of the circuit through the OER switch.

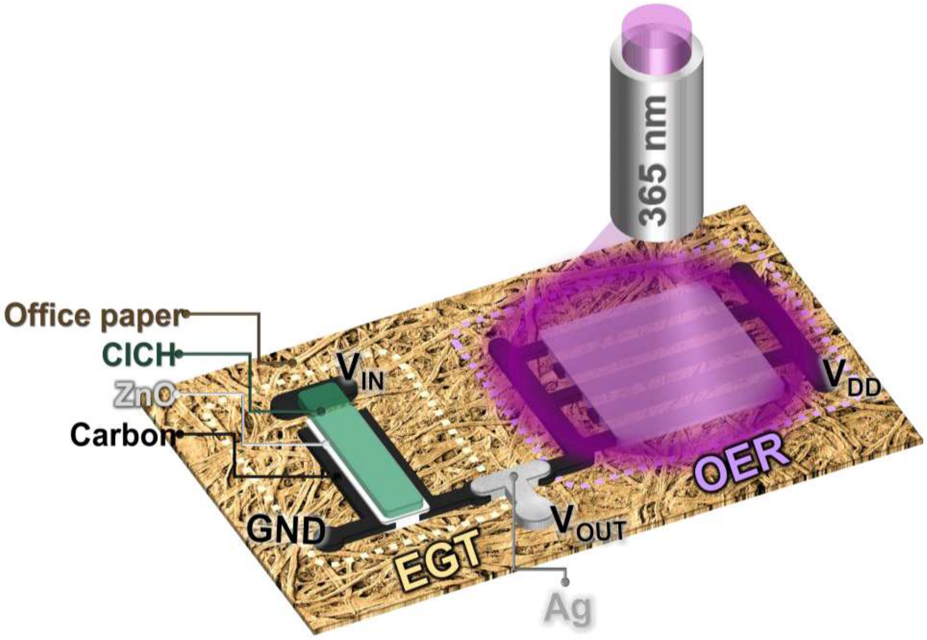

Figure 6.3. Schematic representation of the fabricated photoelectronic ZnO inverter on office paper, composed of a single screen-printed ZnO EGT gated by the Li-ClCH connected to a switchable opto-load resistance that is controlled by UV light (365 nm).

6.1.2. Electrical performance of screen-printed ZnO EGTs on office paper

6.1.2.1. Performance of as-printed devices

Figure 6.4 shows cyclic transfer and respective output curves of the fabricated ClCH-gated printed CMC/ZnO transistors prepared from C3Z40 ink on standard office paper. As already discussed in **section 3.3.2.1.**, inks with lower concentrations of commercial ZnO NPs (≤ 30 wt.%) were also tested, however such inks were not further studied as the fabricated printed EGTs did not show appealing electrical modulation.

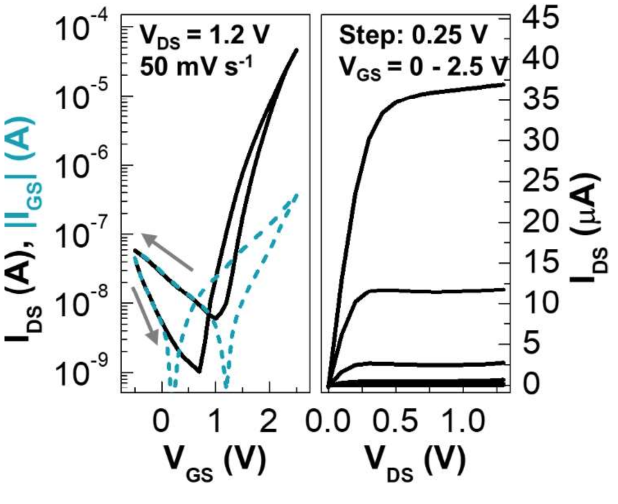

Figure 6.4. Electrical performance of screen-printed C3Z40 EGTs on office paper. Cyclic I_{DS}–V_{GS} curves of screen-printed C3Z40 EGTs for saturation regime (V_{DS} = 1.2 V) at a fixed V_{GS} scan rate of 50 mV s^{-1}, and respective I_{DS}–V_{DS} curves (the step for the V_{GS} was 0.25 V, from -0.5 up to 2.5 V). Arrows represent the sweep direction, whereas continuous and dashed lines correspond to I_{DS} and $|I_{GS}|$ currents, respectively.

Table 6.1. Results of the electrical characterization of CICH-gated screen-printed CMC/ZnO NPs EGTs on office paper. The values show the average and respective standard error of the mean obtained from twenty samples (V_{DS} = 1.2 V, V_{GS} scan rate: 0.05 V s^{-1}).

Electrical parameters	Values
V_{ON} [V]	0.75 ± 0.07
I_{OFF} [nA]	1.40 ± 0.26
I_{ON} [μA]	36.8 ± 6.46
$\lvert I_{GS} \rvert$ [μA]	0.56 ± 0.06
$I_{ON/OFF}$ [$\times 10^4$]	3.31 ± 0.50
S_S [V dec^{-1}]	0.19 ± 0.02
μ_{Sat} [cm^2 V^{-1} s^{-1}]$^{a)}$	21.7 ± 2.70

$^{a)}$ Mobility calculated using the C_{DL} value determined from the data fitting of the EIS measurements using Dasgupta's ECM.

The screen-printed EGTs exhibit n-type behavior and operate in the enhancement mode (normally-off), which is confirmed by positive V_{ON} (≈0.8 V), thus, leading to more stable operation. When V_{GS} is varied within a narrow range of values from -0.5 to 2.5 V, the channel conductance shifts sharply more than four orders of magnitude recording a maximum value of 8.2×10^4. The devices can reach a maximum I_{ON} of tens of μA, whereas the $\lvert I_{GS} \rvert$ values range from 0.1 to 1 μA, which are comparable with typical reported values for electrolyte-gates.[47] The calculated μ_{Sat} is also found to be notably large around 21.7 ± 2.70 cm^2 V^{-1} s^{-1}, whereas the S_S is low (0.19 ± 0.01 V dec^{-1}). Despite such remarkable results, there are still some variations in the devices' performance that can be attributed to the rough and non-uniform surface of the untreated office paper.

The devices display small current hysteresis with clockwise direction, which is associated to charge carrier trapping effects close to the semiconductor/CICH interface rather than species with low mobility (ions) in the semiconductor. According to the output characteristics, the printed devices show hard saturation behavior at very low V_{GS} (<2.5 V) and V_{DS} (<1 V).

Compared to the current state-of-the-art in the field of printed TMOS transistors, this work demonstrates screen-printed ZnO transistors using a suitable strategy that enables RT processing of the oxide semiconductor in combination with ease of fabrication, while ensuring outstanding devices characteristics at low operating voltages on challenging and heavily texturized paper substrates. As far as we know, the superb mobility achieved for the fabricated devices, when using CMC/ZnO ink (**Table S1** and **Table S2**), is the highest ever reported for printed ZnO transistors (precursor and/or nanoparticulate route) or other printed TMOS materials using nanoparticulate approach.[52,53,57,58,132,190,203–209,230] High mobility is desirable to display fast dynamic response when integrated in circuits comprising several interconnected transistors.[141]

As verified by a cross-sectional SEM image depicting the distinct layers that compose the EGTs (**Figure 6.5**a), the sticky, soft, and highly conformable surface of the Li-CICHs provides a good interface quality with the screen-printed CMC/ZnO semiconductor layer, mitigating the adverse effects of rough surfaces. All the screen-printed layers can be clearly distinguished and confirmed through an EDS element analysis (**Figure 6.5**b-d). The thick screen-printed films do not exhibit cracks alongside their thickness, which was estimated around 9.20 ± 0.89 μm and 8.65 ± 0.21 μm for carbon electrode and semiconductor layer, respectively.

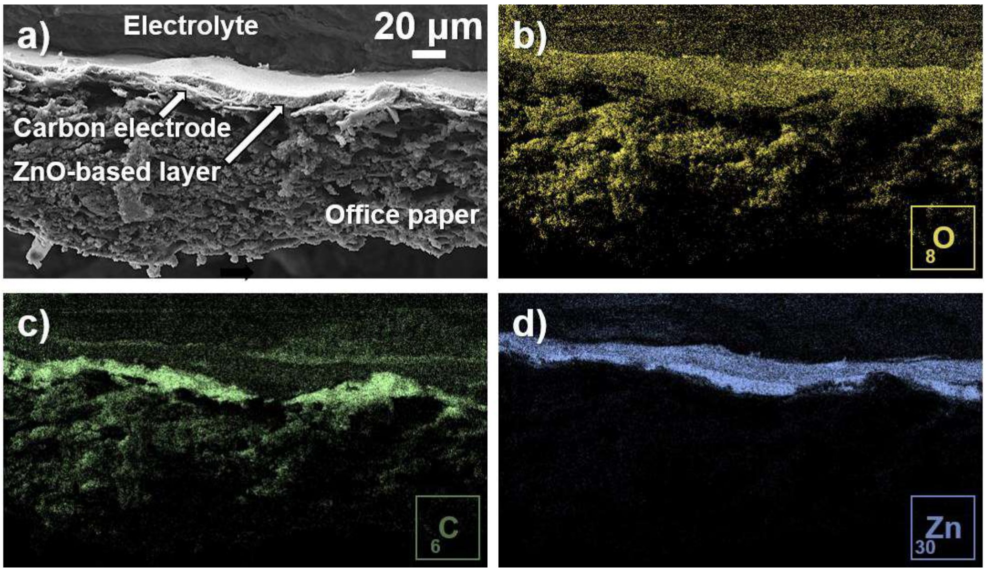

Figure 6.5. Quality of the interfaces between the different layers that compose the printed EGTs, including the office paper substrate, screen-printed carbon electrode, screen-printed C3Z40 ink, and the electrolyte. **a)** Cross-section SEM image depicting the EGT's layers. EDS mapping of **b)** O, **c)** C, and **d)** Zn.

6.1.2.2. *Air-stability overtime*

Regarding the environmental stability of the devices, a steep degradation of the electrical properties of the C3Z40 EGTs is observed after one week of storage in air, decreasing significantly the electrical modulation from four to two orders of magnitude, due to a considerable decrease of I_{ON}, while μ_{Sat} decays almost 98 % (**Figure 6.6** and **Table 6.2**). The increase of $|I_{GS}|$ and decrease of I_{ON} over the weeks can be associated to the reactivity of the ZnO particles with protons and hydroxyl ions from the electrolyte, leading to the formation of zinc complexes under potential biases and/or UV light illumination.[319,345,346]

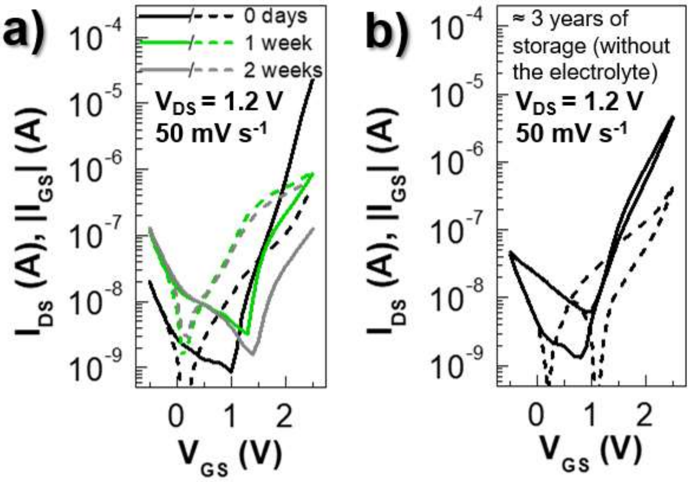

Figure 6.6. Electrical performance stability of screen-printed C3Z40 EGTs on standard office paper overtime under ambient conditions. I_{DS}–V_{GS} curves: **a)** obtained after storing a device up to 2 weeks under ambient conditions; b) obtained after storing separately the electrolyte and the office paper with the printed layers for nearly 3 years under ambient conditions (V_{DS} = 1.2 V, V_{GS} scan rate of 50 mV s^{-1}). Continuous and dashed lines correspond to I_{DS} and $|I_{GS}|$ currents, respectively.

Table 6.2. Variation of the electrical performance of CICH-gated screen-printed CMC/ZnO EGTs on office paper overtime. The values show the average and respective standard error of the mean obtained from three samples (V_{DS} = 1.2 V, V_{GS} scan rate: 0.05 V s^{-1}).

Electrical parameters	As-deposited	1 week	2 weeks	≈3 years of storage[b)]
V_{ON} [V]	0.93 ± 0.03	1.30 ± 0.06	1.17 ± 0.09	1.03 ± 0.12
I_{OFF} [nA]	1.04 ± 0.09	2.46 ± 0.45	3.72 ± 2.20	1.11 ± 0.13
I_{ON} [µA]	13.1 ± 4.74	0.92 ± 0.18	1.06 ± 0.63	5.95 ± 1.43
$\|I_{GS}\|$ [µA]	0.75 ± 0.11	1.16 ± 0.15	0.78 ± 0.27	0.59 ± 0.18
$I_{ON/OFF}$ [$\times 10^3$]	13.6 ±6.14	0.39 ± 0.07	0.34 ± 0.18	5.83 ± 2.12
S_S [V dec^{-1}]	0.23 ± 0.01	0.19 ± 0.01	0.20 ± 0.05	0.22 ± 0.03
μ_{Sat} [cm^2 V^{-1} s^{-1}][a)]	22.6 ± 7.42	0.52 ± 0.35	0.26 ± 0.05	4.38 ± 2.23

[a)] Mobility calculated using the C_{DL} value determined from the data fitting of the EIS measurements using Dasgupta's ECM.

[b)] Electrolyte and office paper with the printed layers of the transistors were stored separately for nearly 3 years under ambient conditions.

It is also important to mention that the electrolyte and the office paper platform that hosts the printed layers can be stored separately for long periods of time (tested after nearly 3 years of storage under ambient conditions) without significative degradation of performance. Since electrical degradation occurs after lamination of the electrolyte, the as-prepared devices are best suited for low-cost, portable, and disposable applications on-the-spot.

6.1.2.3. *Bending measurements*

The mechanical flexibility and robustness of the printed C3Z40 EGTs on office paper was investigated under inward (**Figure 6.7**a) and outward (**Figure 6.7**b) bending strains along the channel axis, while varying the bending radius. The mechanical deformation of the devices promotes the cracking of the CMC/ZnO layer, which in turn leads to a slight loss of performance (**Figure 6.7**c-h). Bending deformation promotes a decrease of I_{ON} and μ_{Sat}, which negatively affects the I_{ON}/I_{OFF} ratio, while V_{ON} shifts to increasing values. For a bending radius of 15 mm, which corresponds to an equivalent strain (ε) of 0.36% (calculated according to **Equation S7**),[347] I_{ON} decreased almost 72 % (21 to 6 µA) and 82 % (17 to 3 µA) when inducing a tensile and compressive strain, respectively. In a similar way, μ_{Sat} was reduced by 80 % (18 to 3.5 $cm^2V^{-1}s^{-1}$) and 83 % (17 to 2.8 $cm^2V^{-1}s^{-1}$) after outward and inward bending, respectively.

Considering the slightly better mechanical endurance of the devices under outward bending deformation, the paper transistors were also tested for a smaller bending radius of 5 mm (ε = 1.09 %). Such bending conditions promote an even greater decline in the electrical characteristics of the devices, due to the decrease of I_{ON} down to 2 µA, while the electrical modulation decreases one order of magnitude (≈ 10^3), and the same trend is observed for μ_{Sat}, which is estimated around 1 $cm^2V^{-1}s^{-1}$. Still, the devices can keep working with lower performance when returning to the flat state without damaging the electrolyte, due to its conformable and robust nature.

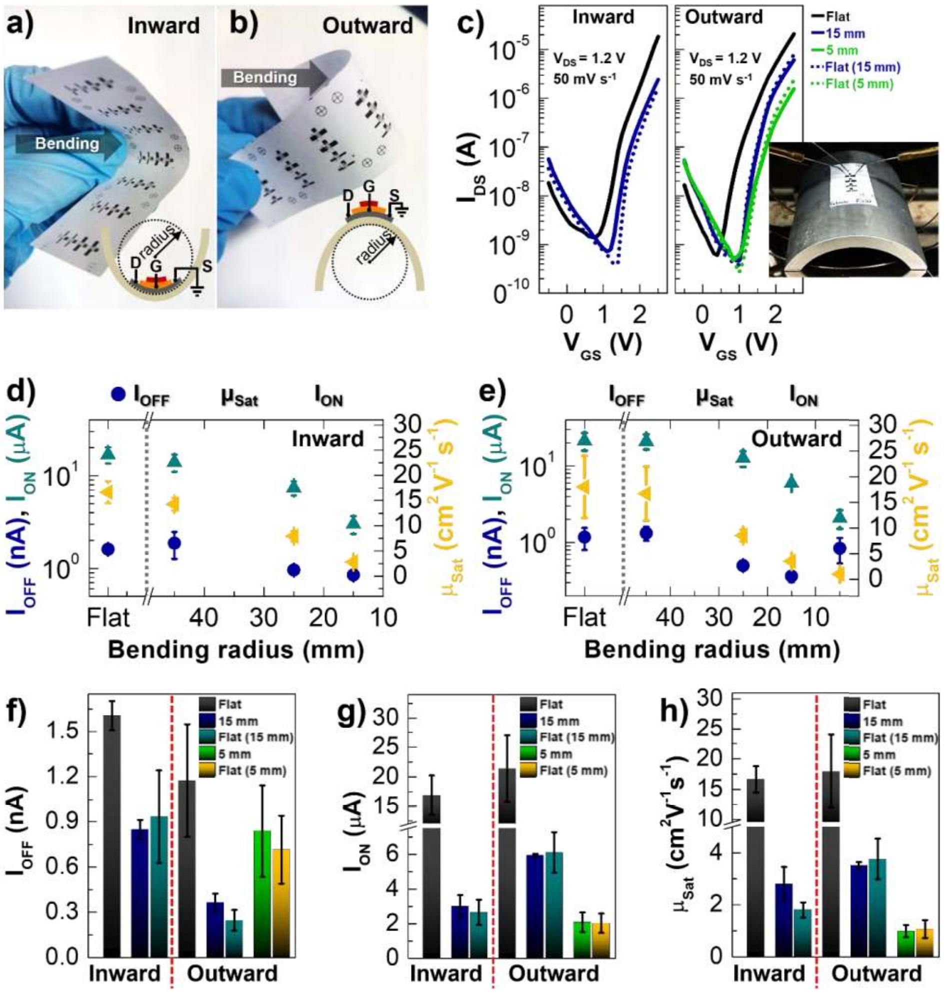

Figure 6.7. Mechanical flexibility of screen-printed C3Z40 EGTs of office paper. Photos of the devices during **a)** inward and **b)** outward bending deformation. **c)** I_{DS}–V_{GS} curves of the devices obtained before bending (flat), during inward or outward bending, and after removal of bending deformation for V_{DS} = 1.2 V and V_{GS} scan rate = 50 mV s^{-1} (inset: photo of the flexible paper devices under outward bending). Respective electrical performance variation during **d)** inward, and **e)** outward bending stress. Comparison of the electrical parameters before bending (flat), during inward (bending radius of 15 mm) or outward bending (bending radii of 5 and 15 mm), and after removal of bending deformation: **f)** I_{OFF}, **g)** I_{ON}, **h)** μ_{Sat}. All the data points show the average and corresponding errors bars obtained from three devices for each bending condition.

While for outward bending the device can still recover a small share of its performance, the same is not observed when bending is performed in the opposite direction (**Figure 6.7**f-h). The reason relies on the large thickness of the semiconducting film that leads to a lower mechanical resistance under compressive strain rather than tensile strain. This behavior is evident when folding the device (**Figure 6.8**). The fractures along the surface of the printed channel layer grew considerably under folding leading to device's performance breakdown. During inward bending, the ZnO particles crash with each other in the folding region and are peeled-off from the device, destroying the channel layer. On the other hand, outward bending promotes the stretching of the active layers printed on the paper substrate, creating smaller fissures along the fold line. The cellulosic matrix that hosts the ZnO NPs can follow the stretching, avoiding the creation of macrofissures at the cost of increasing the distance between ZnO NPs in the folding region, thus destroying some percolation paths that can be restored when returning to the flat state.

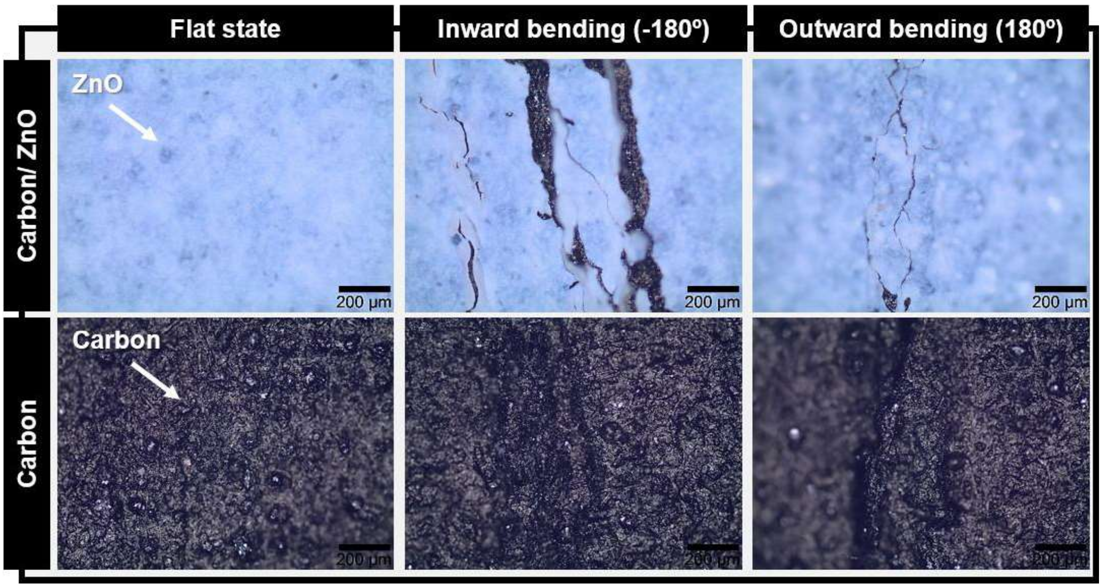

Figure 6.8. Optical microscope images of the screen-printed layers on office paper before bending, and after extreme inward (-180º folding) and outward bending (180º folding).

6.1.2.4. *Environmental endurance: influence of temperature and humidity*

As the environmental conditions display a key role in the amount of water retained into cellulose structure, the role of temperature and RH was also undertaken on the electrical performance of flexible printed CMC/ZnO NPs EGTs.

Figure 6.9a,b show the transfer characteristics within a temperature range from RT to 100 ºC and corresponding variation of the electrical parameters with heating. The range of temperatures considered do not promote cracking of the printed layers (inset image in **Figure 6.9**d). The device was heated directly on the hotplate of the probe station and kept at each temperature for 20 min before measuring. As temperature increases, there is a larger concentration of free carriers available in the semiconductor. As a result, V_{ON} shifts towards negative values from 0.7 down to -0.4 V while I_{DS} increases, implying that the semiconductor and hence the device are becoming more conductive.[329,348]

As depicted in **Figure 6.9**c,d, in just a couple of minutes the device starts recovering its performance under cooling at ambient conditions after heating at 80 ºC. In less than 6 h, the device restores up to 28.5 % of its initial $I_{ON/OFF}$ value ($\approx 9.3 \times 10^3$). The reason relies on the reversible swelling of the cellulose-based matrix that is present in the composition of the electrolyte and inorganic semiconductor layers.

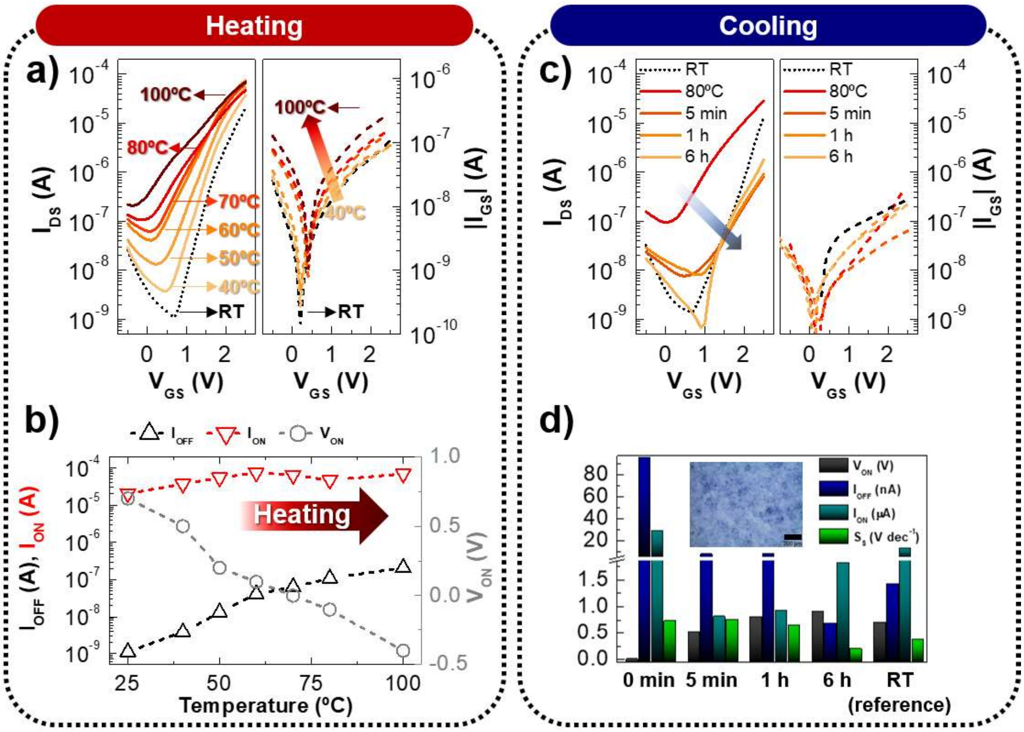

Figure 6.9. Thermal response of screen-printed C3Z40 EGTs on office paper. **a)** I_{DS}-V_{GS} curves for different temperatures (V_{DS} = 1.2 V, V_{GS} scan rate = 50 mV s^{-1}), and **b)** respective variation of the electrical parameters with heating. **c)** I_{DS}-V_{GS} curves of a device during cooling at RT after being heated at 80 ºC for 20 min (V_{DS} = 1.2 V, V_{GS} scan rate = 50 mV s^{-1}), and **d)** respective variation of the electrical parameters (inset: optical microscope image of the CMC/ZnO layer after heating at 80 ºC for 20 min).

Figure 6.10 shows the effect of the RH on the electrical properties of the printed EGTs acquired during pressure dropping for various time intervals and then its recovery at atmospheric pressure overtime. As pressure drops inside the chamber, the water desorption occurs, and the device exhibits a variation of the electrical characteristics in a similar way as observed during heating. The device still exhibits current modulation after 20 h under vacuum conditions (pressure inside the chamber reaches 9.7 × 10^{-4} mbar). When the device is brought again to atmospheric pressure, it restores very quickly a big share of its original performance in less than 10 min at the cost of smaller $I_{ON/OFF}$ (≈2.2 × 10^3), which decreases more than one order of magnitude in comparison with the initial performance (≈1.5 × 10^4). There is not a significant improvement of its performance even after 4 h of storage at atmospheric pressure conditions.

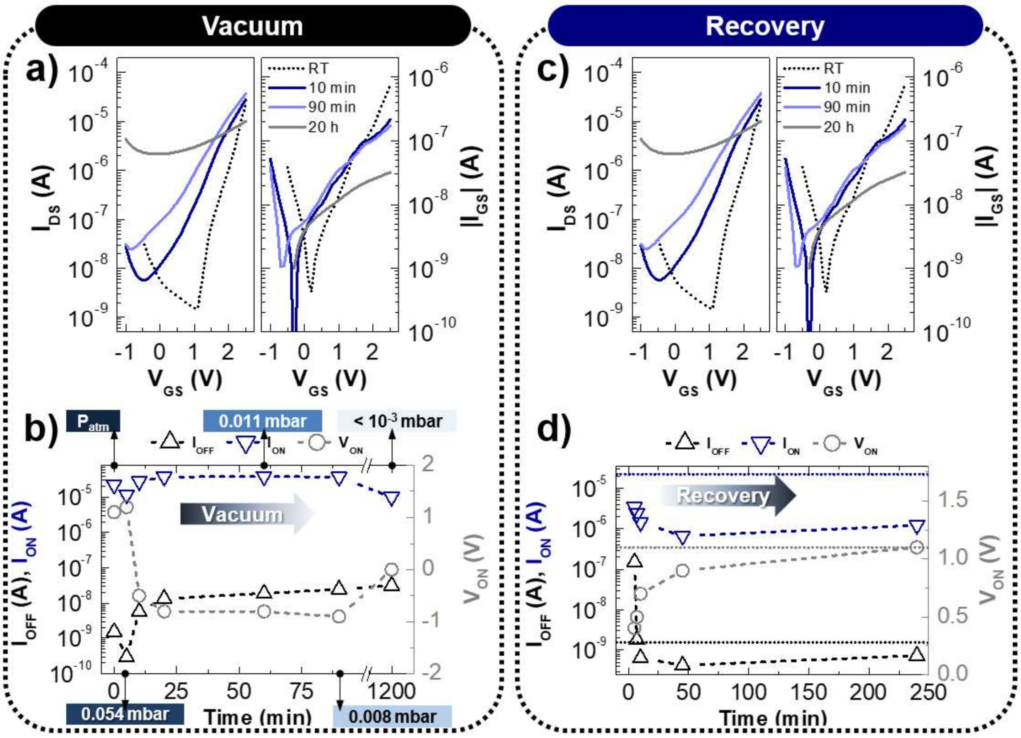

Figure 6.10. Humidity response of screen-printed C3Z40 EGTs on office paper. I_{DS}-V_{GS} curves **a)** under vaccum, and **b)** during recovery at atmospheric pressure (V_{DS} = 1.2 V, V_{GS} scan rate = 50 mV s^{-1}). Respective variation of the electrical parameters curves **b)** under vaccum, and **d)** during recovery at atmospheric pressure. Dotted horizontal lines correspond to the initial electrical performance of the device before depressurisation.

6.1.2.5. Electrical stress: static and dynamic measurements

Static electrical stress measurements were performed to get a better estimation of how quickly the devices deteriorate (**Figure 6.11**a,b). Immediately after laminating the electrolyte on the device, the device starts showing changes in the transfer characteristics during the first ten cycles. An increase of V_{ON} from 0.8 to 1.2 V is observed, due to electron trapping in the electrolyte/semiconductor interface trap-sites,[349,350] while both I_{OFF} and I_{ON} shift for lower values, decreasing the $I_{ON/OFF}$ nearly 58 % of its initial value, and μ_{Sat} decreases from 37 to 6.3 cm^{2}V^{-1}s^{-1} (-83 %). %). Despite the changes observed in the first few cycles, the device then maintains a reasonable stable performance for four days under successive cycling. After 800 cycles, the devices exhibit a good electrical performance, operating with a current modulation above three orders of magnitude and reasonable high μ_{Sat} around 6 cm^{2}V^{-1}s^{-1}, which is still high considering the current state-of-the-art in the field of printed TMOS as channel layer in transistors (see **Table S1** and **Table S2**).

The dynamic response of the EGTs was assessed by applying a square-wave gate signal at different frequencies (1–10 Hz), between -0.5 and 2.5 V for a V_{DS} fixed at 1.2 V (**Figure 6.11**c-f). It can be estimated that an $I_{ON/OFF}$ above 10, required for proper integration in digital circuits, is achieved for frequencies lower than 10 Hz.

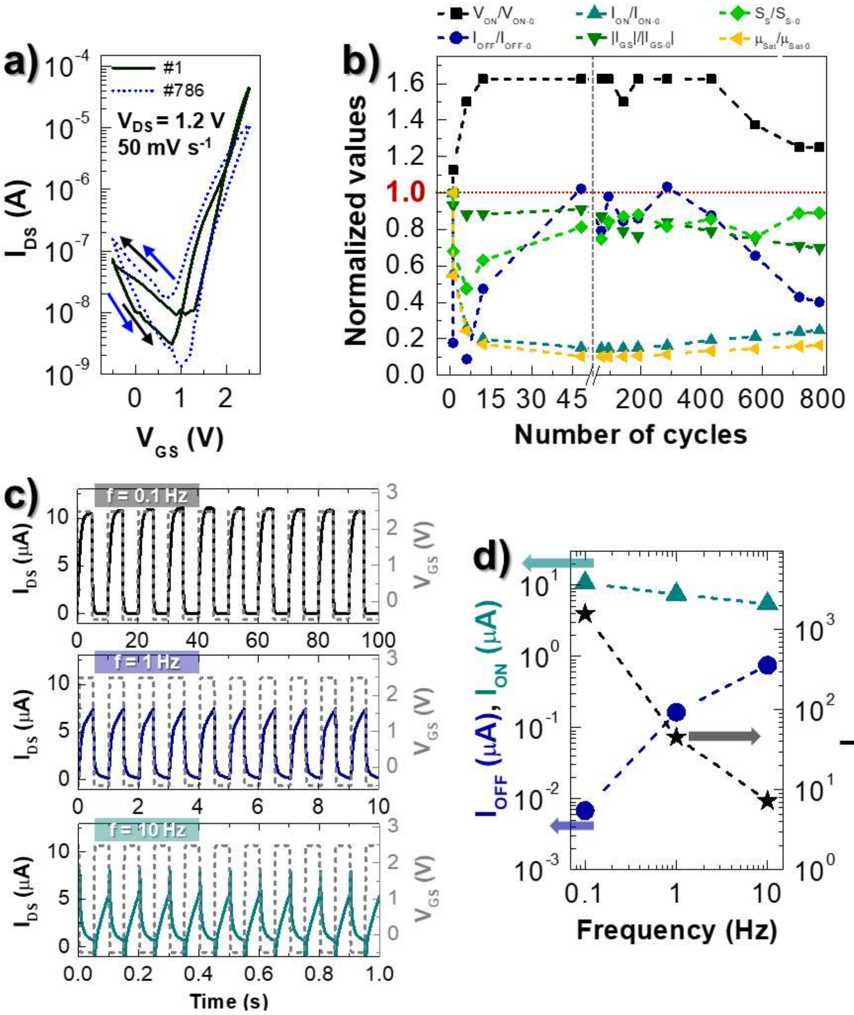

Figure 6.11. Static and dynamic electrical characterization of screen-printed CMC/ZnO EGTs on standard office paper. **a)** I_{DS}–V_{GS} curves after performing consecutive cycles (delay of 5 min between each cycle, V_{DS} = 1.2 V, V_{GS} scan rate of 50 mV s^{-1}). Arrows represent the sweep direction for each curve. **b)** Respective variation of the electrical parameters with increasing number of cycles. **c)** Dynamic response for different frequencies: 0.1, 1, and 10 Hz. **f)** Evolution of $I_{ON(VGS = 2.5\ V)}$, $I_{OFF(VGS = -0.5\ V)}$, and respective $I_{ON/OFF}$ with frequency for the tenth cycle of the square-shaped V_{GS} signal.

6.1.2.6. *Optimization of EGTs' performance with porous ZnO nanoplates*

Throughout this work, commercial ZnO NPs were successfully used to formulate screen-printable water-based inks suitable for patterning reasonably smooth semiconducting layers with RT functionality in flexible EGTs on paper-based substrates. The devices exhibit appealing electrical performance without performing additional post-printing treatments that could compromise the integrity of the paper substrate, while adding complexity to the manufacturing process. However, a high loading content of functional material (40 wt.%) is needed to create enough percolation paths between the particles and achieve a satisfactory electrical modulation of the fabricated screen-printed EGTs on rough and fibrous standard office paper. Besides, although such devices show some mechanical flexibility under bending, the thick channel layer is destroyed under folding due to the formation of large fissures along the fold line.

To address these issues, percolative pathways for conduction can be improved by using particles with higher aspect ratio, while enhancing the mechanical endurance of the functional layer.[33,351]

Therefore, the small sized commercial ZnO NPs were replaced by ZnO PNPs, which exhibit higher aspect ratio and larger active area for interaction with ionic species from the electrolyte. **Figure 6.12** shows the impact of the loading content of ZnO PNPs in the electrical performance of the fabricated EGTs. Despite the significantly rougher surface of screen-printed ZnO PNPs on paper compared to commercial ZnO NPs, the conformable nature of the hydrogel electrolyte can easily follow the surface roughness of the printed composite films, thus reducing charge trapping effects that hinder charge transfer from drain to source.[52] It is possible to decrease nearly 50 % the amount of functional material to yield devices with almost comparable electrical performance to those composed of commercial ZnO NPs. Besides, the electrical performance is considerably improved for superior amounts of ZnO PNPs (≥ 30 wt.%), showing a notorious increase of I_{ON} (43 ± 0.4 μA), $I_{ON/OFF}$ ((8.6 ± 3.5) × 10^4), and μ_{Sat} (35 ± 3.0 $cm^2V^{-1}s^{-1}$). There are not significant improvements in the electrical performance for loading contents of 40 wt.%.

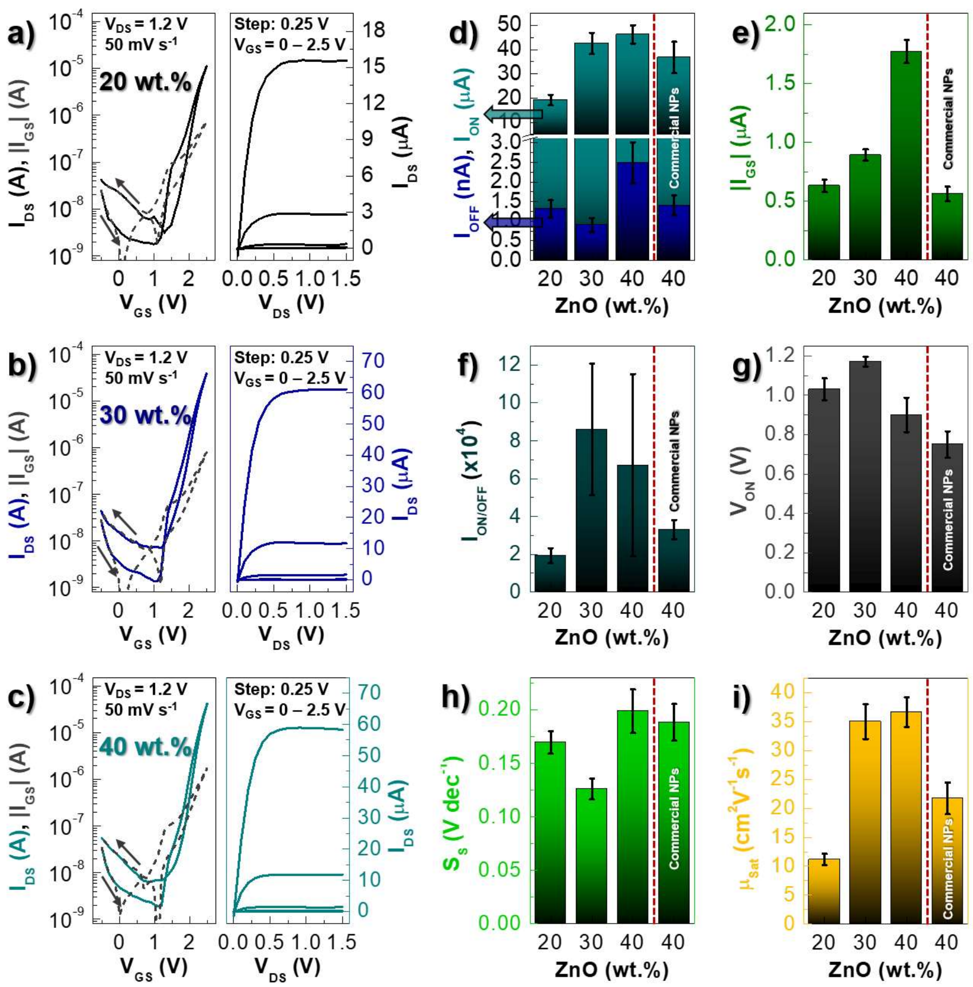

Figure 6.12. Electrical performance of screen-printed ZnO PNPs EGTs on office paper. Cyclic I_{DS}–V_{GS} curves of screen-printed ZnO PNPs EGTs with different contents of ZnO PNPs **a)** 20 wt.%, **b)** 30 wt.%, and **c)** 40 wt.%) for saturation regime (V_{DS} = 1.2 V) at a fixed V_{GS} scan rate of 50 mV s^{-1}, and respective I_{DS}–V_{DS} curves (the step for the V_{GS} was 0.25 V, from -0.5 up to 2.5 V). Arrows represent the sweep direction, whereas continuous and dashed lines correspond to I_{DS} and $|I_{GS}|$ currents, respectively. Respective electrical parameters obtained for screen-printed ZnO PNPs EGTs fabricated on office paper (the data points show the average and corresponding errors bars obtained from ten devices), and comparison with screen-printed commercial ZnO NPs (C3Z40 ink) EGTs (the data points show the average and corresponding errors bars obtained from twenty devices): **d)** I_{OFF} and I_{ON}, **e)** $|I_{GS}|$, **f)** $I_{ON/OFF}$, **g)** V_{ON}, **h)** S_S, and **i)** μ_{Sat}.

The exceptional performance displayed by the devices prepared with C3ZPN30 ink is further explored in **sections 6.1.3.2** and **6.2**.

6.1.3. Electrical performance of screen-printed ZnO circuits on office paper

6.1.3.1. Handwritten logic gates with screen-printed ZnO EGTs

A user-friendly strategy designed for early-stage learners to produce low-voltage,fully recyclable and flexible circuitry on ordinary paper targeting on-the-spot applications was demonstrated (**Figure 6.13**a).

Figure 6.13b-d displays the circuit diagrams and respective VTC curves of the handwritten digital electronic circuits with printed C3Z40 EGTs on office paper. As shown in **Figure 6.13**b, it is clear that the inverter circuit outputs a voltage representing the opposite logic-level to its input, when V_{IN} is swept from 0 V (logic input signal “0”) to 3.5 V (logic input signal “1”) for a low V_{DD} of 1.5 V. Therefore, V_{OUT} becomes “HIGH” and close to V_{DD} – R_LI_{DS} when the applied V_{IN} is “LOW”. On the other hand, when V_{IN} is “HIGH”, the driving EGT starts conducting and there is a finite voltage drop across the R_L, which results in low V_{OUT}. For R_L = 150 kΩ, V_{OUT} shows logic output “1” of 1.44 V close to V_{DD}, and output logic “0” of almost zero, demonstrating a maximum |gain| of 2.4. The inverter exhibits low output hysteresis between the forward (V_{IN} switched to “1” state) and reverse (V_{IN} switched to “0” state) V_{IN} sweeps, which is a good indicative of reliable switching behavior. A detailed study of the resistive-load inverter is presented in **Figure S6**, which demonstrates that almost full swing of the V_{OUT} to near ≈0 V is observed when increasing the R_L along the same graphitic line from 50 to 150 kΩ. The maximum |gain| is considerably improved from 2 to 3.4 for a R_L of 50 kΩ by increasing the V_{DD} values from 1 to 2 V, respectively.

Figure 6.13c,d show good NAND and NOR logic gates responses to a V_{DD} of 1.5 V and two input signals $V_{IN,A}$ and $V_{IN,B}$ for a R_L of 150 kΩ. The fabricated NAND gate only produces a “LOW” V_{OUT} (≈0.12 V) when both input signals are “HIGH” ($V_{IN,A}$ = $V_{IN,B}$ = 3.5 V). Otherwise, a “HIGH” V_{OUT} and close to V_{DD} – R_LI_{DS} (≈1.48 V) is obtained. The opposite behavior is observed for the NOR gate, in which a “HIGH” V_{OUT} (≈1.38 V) is obtained if both of the inputs to the gate are held at “0” state ($V_{IN,A}$ = $V_{IN,B}$ = 0 V), whereas a low V_{OUT} (≈0.04 V) results only if one or both input signals $V_{IN,A}$ (= 3.5 V) and/or $V_{IN,B}$ (= 3.5 V) are at “1” state, due to a high voltage drop across R_L. The maximum |gain| reaches 2.4 and 3.2 for NAND and NOR logic gates, respectively.

NAND and NOR gates are considered the “universal gates”, meaning that they can be used to make all the other gates. The low-voltage operation of these circuits enables the use of portable thin-film batteries, external radio frequency fields, or energy harvesting schemes as power supply, which is essential for the development of the IoT concept.[132,263,269]

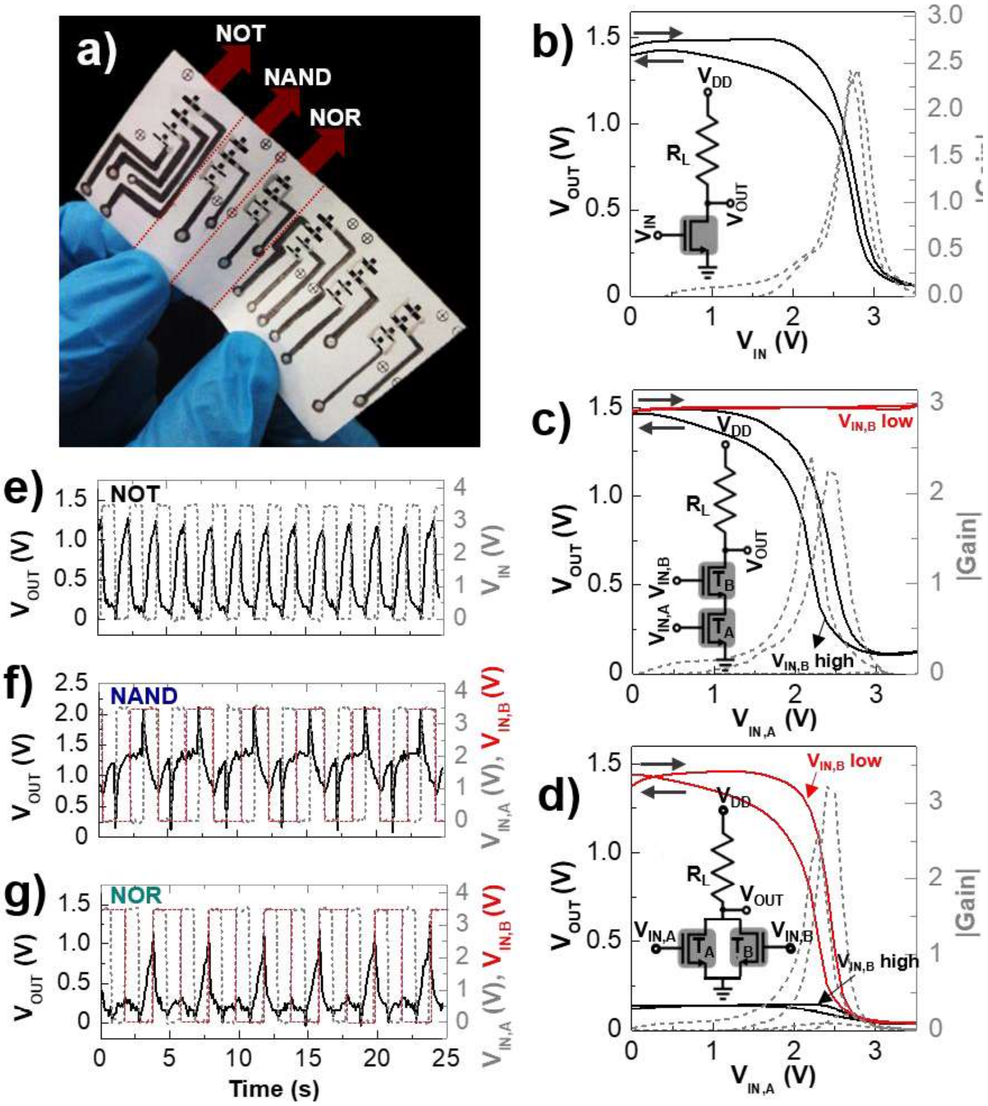

Figure 6.13. Electrical performance of planar pencil-drawn resistor-loaded logic gates with driving screen-printed C3Z40 EGTs on office paper. **a)** Photograph of the fabricated handritten/printed paper-based circuits. Schematic and VTC curves (V_{OUT} vs. V_{IN}) of the printed EGTs with a pencil-drawn resistance of 150 kΩ: **b)** NOT gate; **c)** NAND gate and **d)** NOR gate for a V_{DD} = 1.5 V and voltage scan rate of 50 mV s^{-1}. Arrows represent the sweep direction. Dynamic response (V_{OUT}, V_{IN} vs. time) of the logic gates with a pencil-drawn resistance of 50 kΩ for a V_{DD} = 1.5 V at 500 mHz: **e)** NOT, **f)** NAND, and **g)** NOR gates.

Figure 6.13e-g show that the V_{OUT} of the logic gates responded well to a 500 mHz square-wave V_{IN} signal at V_{DD} of 1.5 V for a R_L of 50 kΩ (see also **Figure 6.14**). The small spikes observed at this frequency result from the contribution of the parasitic capacitance effect, which may limit the operation frequency.[263,352] The logic gates are still able to exhibit desired functionality, though degradation in the output is noticed for relative higher frequencies around 1 Hz.

As already mentioned in **section 5.1.3**, some strategies can be implemented to improve the frequency of operation of the circuits, but some of them can be limited by the materials, processing and manufacturing methods used. Although the reduction of the channel's length towards submicrometric dimensions can contribute positively for the enhancement of the dynamic performance of these devices, this strategy is challenging when using printing techniques.[243,248] Some efforts have been made to overcome this issue whether using SAP technique or adopting a new transistor design, where the semiconductor is printed between source-drain electrodes.[240] Furthermore, the planarization of fibrous standard office paper, without compromising its recyclability nor low-cost, or the use of highly smooth nanocellulose or RCF substrates can also display a key role to reduce its surface defects, enhancing interface interaction with the oxide semiconductor targeting maximum operating frequencies.[5,15,129]

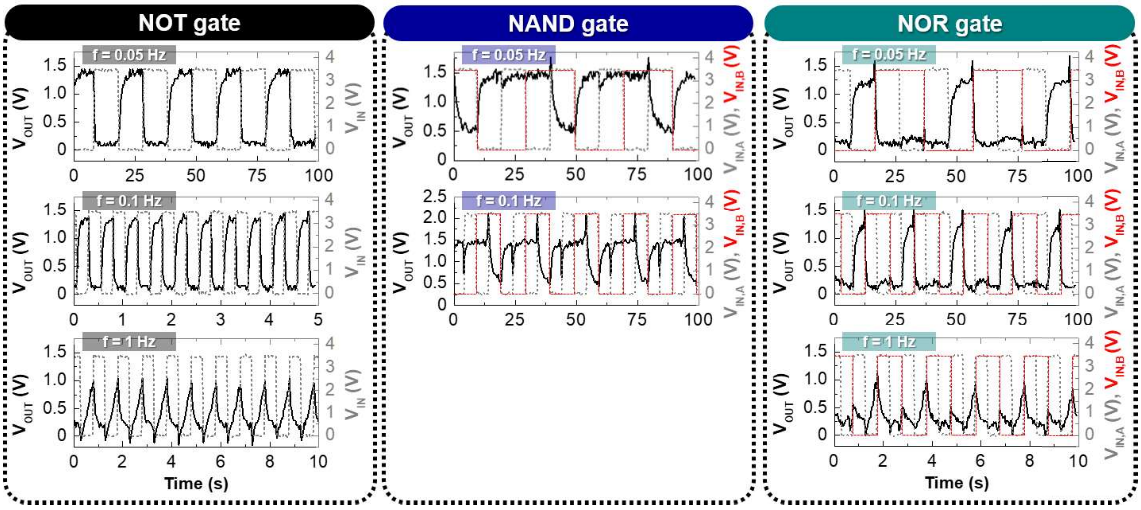

Figure 6.14. Dynamic response of the logic gates with a pencil-drawn resistance of 50 kΩ for a V_{DD} = 1.5 V at different frequencies (50 mHz, 100 mHz and 1 Hz).

6.1.3.2. UV-responsive inverters

Figure 6.15 shows the UV sensing performance of the photonic devices for different UV light intensities, under a fixed bias voltage of 1.5 V, which value is identical to the applied V_{DD} to operate the previous logic gate circuits with pencil-drawn load resistances. Regarding the photosensing layer of the UV sensor, the C3ZPN10 ink was used to pattern this layer as it enables the local functionalization of the paper's surface with a reasonably good percolation of ZnO particles (see **Figure 3.9**). Since the UV sensors are intended to be used as R_L for logic operations, the obtained photocurrent values were converted to resistance.

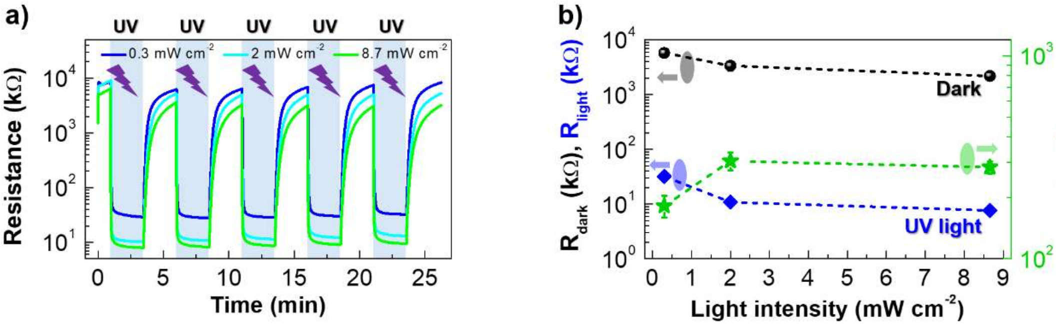

Figure 6.15. Photoswitching characteristics of the screen-printed ZnO PNPs OERs on office paper under different UV light intensities: **a)** variation of the resistance overtime for a bias voltage of 1.5 V, during five consecutive ON/OFF cyles (LED ON: 150 s; LED OFF: 150 s), and **b)** respective dark resistance (R_{dark}), resistance under UV light (R_{light}), and OFF/ON ratio (R_{dark}/R_{light}) for the last ON/OFF cycle. The data points show the average and corresponding errors bars obtained from 4 samples.

By exposing the sensor to UV light, electron-hole pairs are created by absorbing photons with energy larger than the band-gap energy of ZnO. The adsorption and desorption of oxygen molecules on the ZnO's surface from ambient atmosphere also play a crucial role in the photoconduction. Under UV light illumination, the photogenerated holes recombine with negatively charged oxygen ions and release the adsorbed oxygen molecules from ZnO surface back to atmosphere, decreasing the depletion region. The unpaired photogenerated electrons in the conduction band of the ZnO together with the available holes contribute for photoconduction, and consequently an increase in current is observed. When returning to the dark state, oxygen molecules are again adsorbed onto the particles' surface, capturing free electrons and depleting the channel region, which will promote the decrease of the electrical conductivity.[353–355]

The sensors exhibit a stable performance under consecutive ON/OFF cycling, shifting exponentially from ≈10 MΩ to less than few tens of kΩ under UV light illumination, which represents a decrease of more than two orders of magnitude in the resistance, thus being possible to work as a UV-tunable load resistance. Regarding the influence of the UV light intensity, lower resistance values are achieved for increasing intensities, as a consequence of the increase of the number of photogenerated carriers with the increase of the incident photons, reaching an average resistance value of 32, 11, and 8 kΩ for a UV light intensity of 0.3, 2.0, and 8.7 mW cm^{-2}, respectively. There are not significant differences between the two highest UV light intensities, possibly due to the balance between recombination and the generation of electron-hole pairs during exposure to UV light radiation.[337]

The switching response kinetics of the photonic sensors was evaluated to understand how quickly they shift the optoelectrical properties when exposed to UV light (rise time) and when turning back to the dark state (fall time). Both parameters were calculated in the range between 10 and 90 % of the total electrical modulation. The reasonably long-time response in both states is related to slow adsorption/desorption of oxygen molecules from the nanostructures' surface, which is typical for ZnO-based UV photodetectors.[340,356] The rising time increases with UV illumination intensity, and it was determined to be around 24.2, 45.8, and 45.7 s for UV light intensities of 0.3, 2.0, and 8.7 mW cm^{-2}, respectively. On the other hand, the fall time does not change much with the UV light intensity, being around 11 s. The shorter fall time response lies on the faster oxygen adsorption kinetics, while the longer rise time is related to the decreasing rate of the adsorbed oxygen ions.[355]

The integration of EGTs with the optoelectronic sensing system enables photo-stimulated logic functionality on a single platform, where the electrical performance switches actively under UV light stimulus. The optically triggered NOT logic gate circuits were investigated by acquiring successive VTC curves overtime during an ON/OFF UV illumination, under different light intensities, while applying a fixed V_{DD} of 1.5 V and sweeping V_{IN} from 0 to 3 V.(**Figure 6.16**).

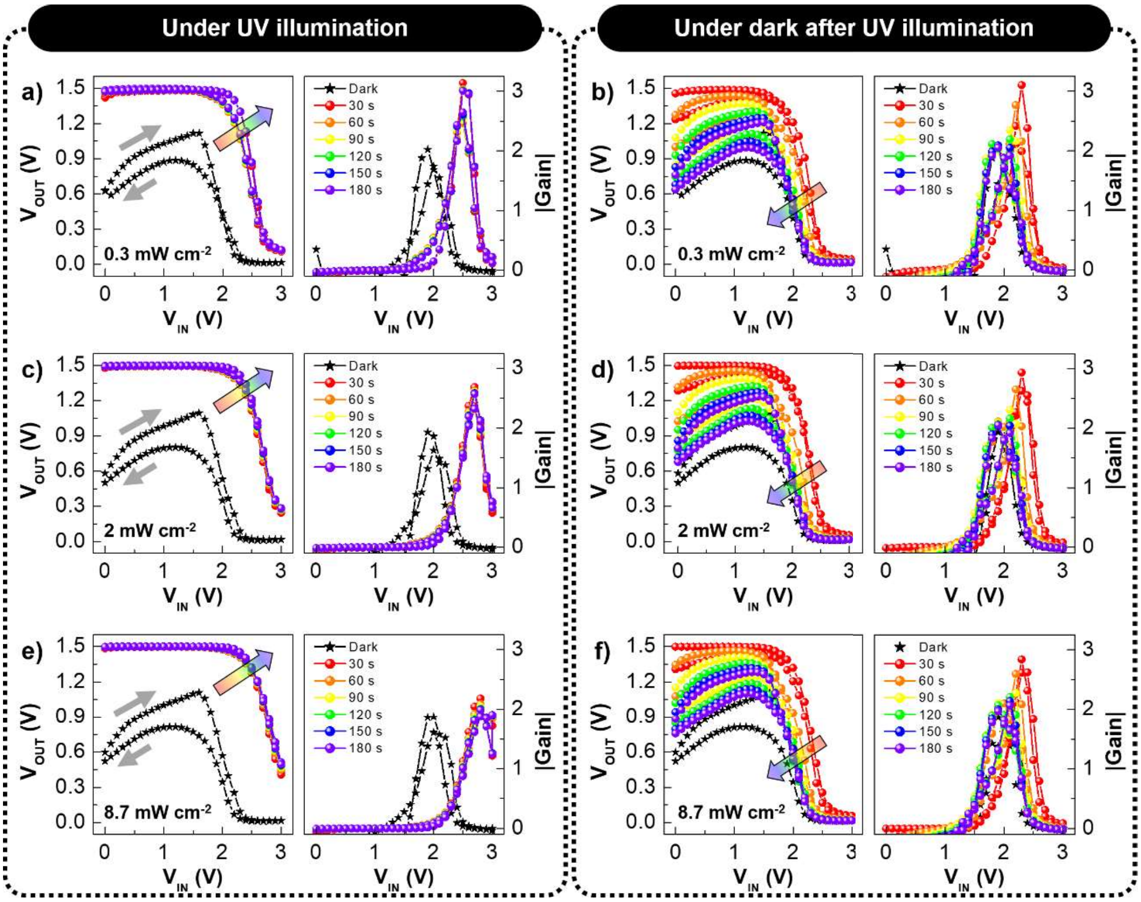

Figure 6.16. Photoswitching characteristics of the fabricated planar OER-loaded opto-NOT gates under cyclic UV illumination. VTC curves acquired overtime during (**a, c, e**) and after (**b, d, f**) UV light exposure for a UV light intensity of 0.3, 2.0, and 8.7 mW cm^{-2}, respectively (LED ON: 3 min, LED OFF: 3 min, V_{DD} = 1.5 V, voltage scan rate = 400 mV s^{-1}). Grey arrows represent the sweep direction.

The variation of the electrical parameters of the inverters were plotted in **Figure 6.17**. In the pristine state (before UV illumination), the opto-logic gates exhibit an inverter behavior that alternates from 1.1 V to ≈0 V for increasing V_{IN} values, when sweeping from 0 to 3 V, respectively. Under such conditions, the inverter reaches a maximum gain of 2.2, and shows a reasonably small clockwise hysteresis.

Immediately after turning on the UV light, the VTC curves quickly shift towards superior V_{IN} values, which is more prominent for increasing UV light intensities, and the hysteresis becomes negligible. As the UV light promotes the decrease of the R_L of the OER, output high level (V_{OH}) increases rapidly towards the applied V_{DD} (≈1.5 V), whereas output low level (V_{OL}) is also pulled up with the increase of UV light intensity, shifting to 0.1, 0.3, and 0.5 V for 0.3, 2.0, and 8.7 mW cm^{-2}, respectively. Although an increase of the gain up to 2.9 is observed for the lowest UV light intensity, where the R_L is around 32 kΩ, this trend is reversed with the further decrease of the R_L as the UV light intensity increases, reaching a gain value of 2.1 for the highest UV light intensity. When returning to the dark state, the VTC curves show a very slow transition towards the initial inverter characteristics obtained before UV light exposure.

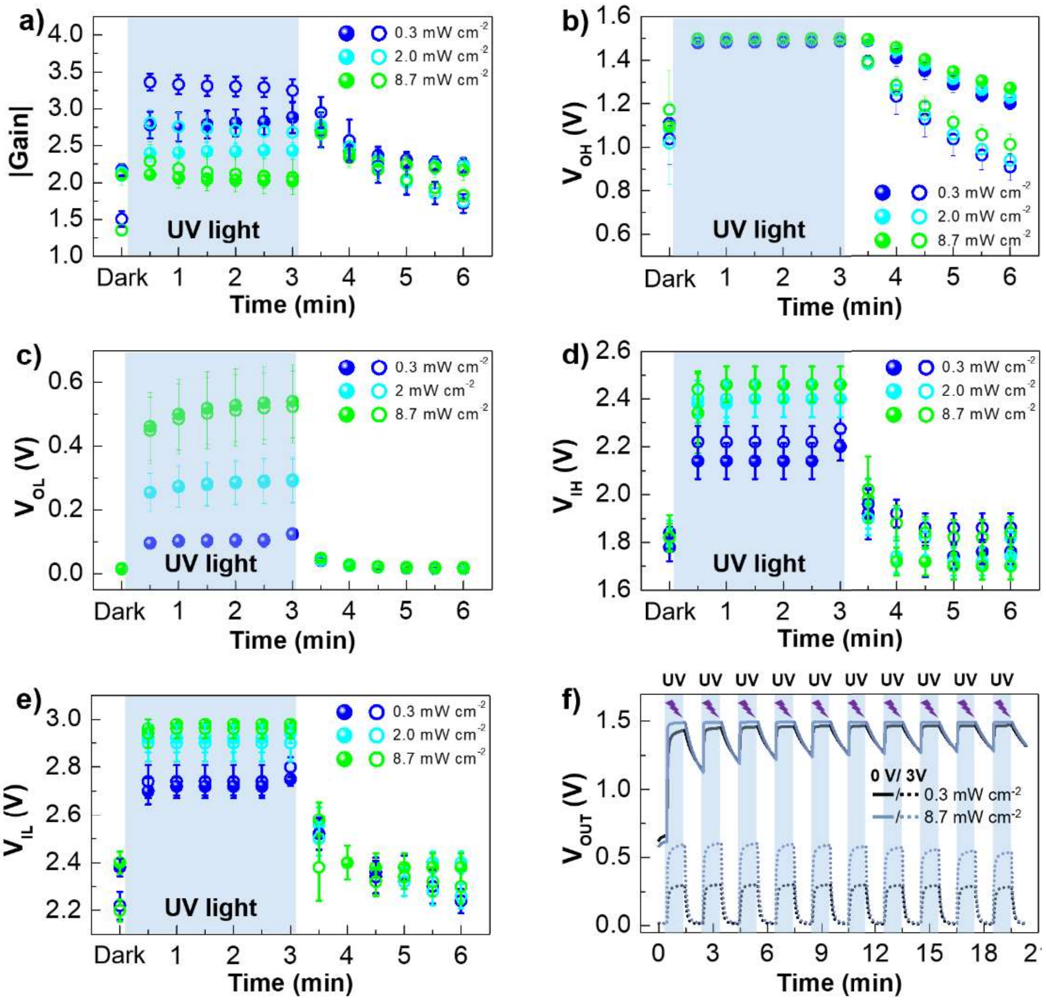

Figure 6.17. Electrical characterization of planar opto-NOT gates on office paper composed of screen-printed ZnO PNPs EGTs and OER as photoswitchable load resistance. Respective variation of the main figures of merit of the inverters during an ON/OFF cycle (3 min ON, and 3 min OFF) for increasing light intensities from 0.3 to 8.7 mW cm^{-2} (V_{DD} = 1.5 V, voltage scan rate = 400 mV s^{-1}): **a)** |gain|, **b)** output high level (V_{OH}), **c)** output low level (V_{OL}), **d)** maximum value of input interpreted by the inverter as a logic "0" (V_{IL}), and **e)** minimum value of input interpreted by the inverter as a logic "1" (V_{IH}). The data points show the average and corresponding errors bars obtained from 5 samples. **f)** Variation of V_{OUT} for successive ON/OFF UV illumination cycles (60 s ON, and 60 s OFF) at a fixed light intensity (0.3 or 8.7 mW cm^{-2}) and V_{IN} (0 or 3 V).

Dynamic electrical characterization of the inverters was assessed by measuring the change of V_{OUT} during consecutive ON/OFF switching of UV light, under a constant light intensity, while applying a fixed V_{IN} (0 or 3 V) and V_{DD} (1.5 V) (**Figure 6.17**f). The photo-inverter exhibits a reasonably stable and reversible electric-switching behavior for repeated ON/OFF UV light cycles. As the UV light is turned on, V_{OUT} increases rapidly to 1.5 V for a V_{IN} of 0 V with a rise time of 4.8 and 0.4 s for an UV light intensity of 0.3 and 8.7 mW cm^{-2}, respectively, while the fall time is very slow and does not reach the initial value due to a persistent photoconductivity.[357] The inverter operating at a V_{IN} of 3 V, corresponding to output logic level "0", exhibits a faster photoresponse with a rise time of 12 and 9.7 s for a UV light intensity of 0.3 and 8.7 mW cm^{-2}, respectively, and a fall time of 16 and 13 s for the same UV light intensities.

6.2. Fully screen-printed ZnO nanopaper composite gated transistors and logic gates

To further simplify the manufacturing process, the developed ACICC membrane was used as a robust ionic conductive material to support the printed devices, while displaying electrochemical features favorable to achieve low-operating voltages. For such purpose, the optimized screen-printable water-based CMC/ZnO PNPs ink was used to pattern the semiconducting layer of the NCGTs, since, as previously observed in **section 6.1.2.6**, it yields printed ZnO EGTs on office paper with the best electrical performance.

The operation of the NCGTs under mechanical deformation or electrical stress will be presented and discussed, and their integration in low-voltage cellulose-based microelectronic circuits will be addressed. Furthermore, a comparison between the two types of electrolyte-gating (deformable hydrogel sticker vs. robust ionic conductive substrate), and the impact of the interface between the electrolyte and the semiconductor layer will be studied.

6.2.1. Design and architecture

As illustrated in **Figure 6.18**, fully screen-printed, in-plane, ZnO NCGTs were fabricated on the smoothest side of the ACICC membrane, used as support and high capacitance gate dielectric. Only two printing steps are needed to fabricate fully functional NCGTs by patterning the planar carbon electrodes (R_s = 253 ± 10.2 Ω □$^{-1}$, determined from four-point probe measurements using **Equation S6**), and then the semiconducting layer onto the ionic conductive substrate.

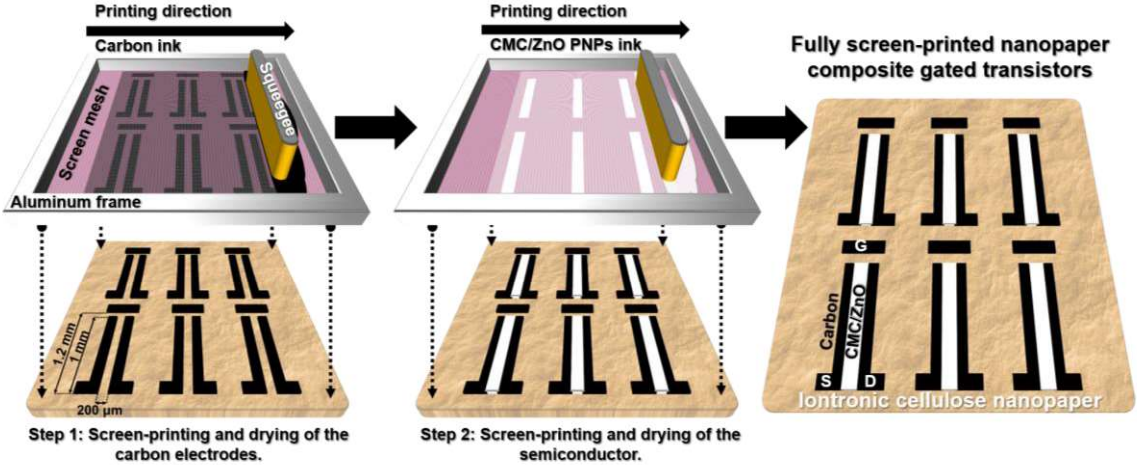

Figure 6.18. Schematic illustration of the fabrication process of the fully screen-printed ZnO NCGTs.

As previously discussed in **section 6.1**, we demonstrated screen-printed ZnO EGTs and logic gates using a suitable strategy that enables RT processing of oxide semiconductors in combination with ease of fabrication, while ensuring outstanding devices' characteristics at low-operating voltages on ubiquitous office paper substrates. The substitution of nanosized commercial ZnO NPs by ZnO PNPs revealed advantageous to form percolative pathways for conduction at lower contents, thus leading to devices with enhanced electrical performance.[33,351] The C3ZPN30 ink was used to pattern the channel layer as it yields devices with superior electrical performance.

Figure 6.19 show SEM images focused on the semiconducting layer printed onto the ACICC membrane, which reveal a very similar topography as the one observed on office paper substrate (see **Figure 3.9**). The nanoplate-shape provides a more direct percolation path for electron transport and a larger interface between the particles and the ACICC substrate. This morphology assists in the interaction with ionic species of the electrolyte that can also interact with the porous surface defects, working as electrochemically active sites. No signs of cracks along its surface nor peeling are visible, although micro-sized voids are observed among the particles for higher magnifications, which also contributes for the large surface roughness of the printed CMC/ZnO PNPs film.

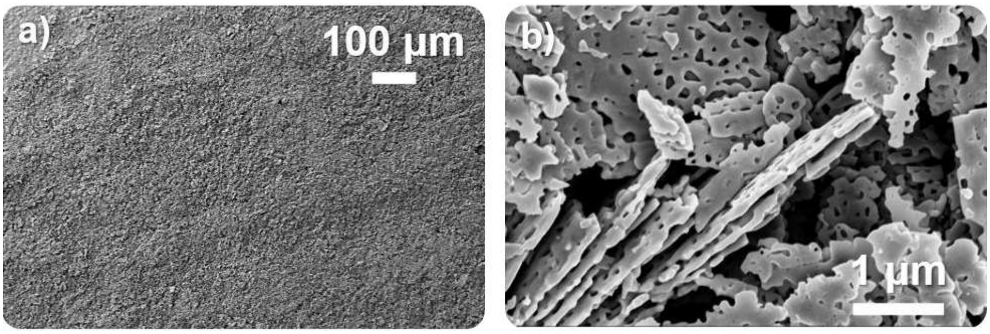

Figure 6.19. a-b) SEM images of the printed CMC/ZnO PNPs channel layer on ACICC membrane for different magnifications.

To further develop applications based on the fabricated planar, fully screen-printed NCGTs, these devices were integrated into digital logic circuits (**Figure 6.20**), using a similar strategy as the pencil-drawn logic gates fabricated onto office paper. Yet, since the ACICC membrane is not compatible with pencil drawing, a sheet of office paper was used instead to pattern resistive graphitic tracks that will in turn establish the R_L. The ACICC membrane was glued with a double-sided tape to the office paper, and the transistors were printed onto its smooth surface. After printing the carbon electrodes, a pencil brush was used to handwrite thick carbon conductive tracks. The drawn electrical connections and the screen-printed electrodes were dried simultaneously at 70 ºC for 15 min, and stored at ambient conditions for 1 h to let the ACICC membrane restore its moisture, before printing the CMC/ZnO PNPs channel. By doing so, it is possible to easily bridge the intended electrodes from the hosting cellulose-based materials (office paper and ACICC membrane).

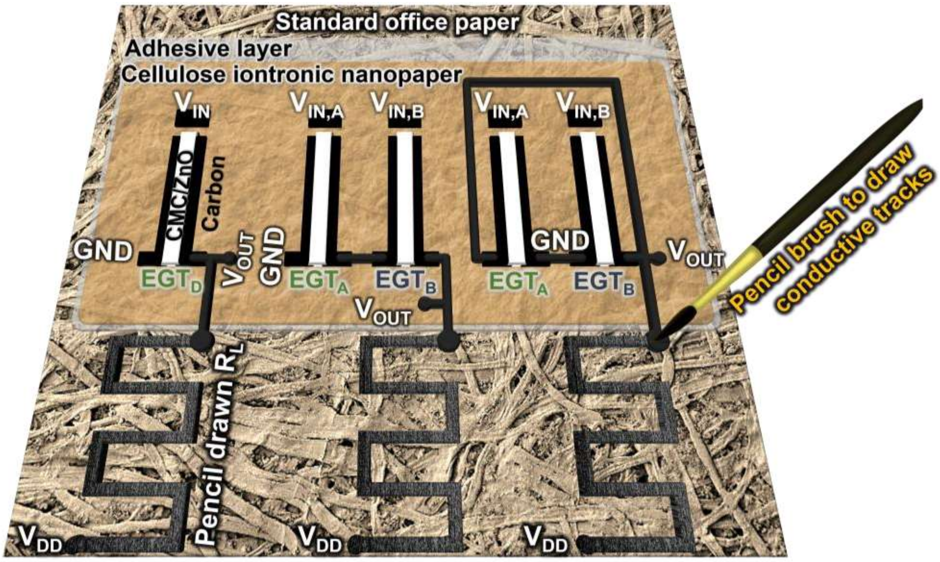

Figure 6.20. Schematics of the fabricated logic gates (from left to right – NOT, NAND, and NOR gates) with planar fully screen-printed NCGTs.

6.2.2. Electrical performance of fully screen-printed ZnO nanopaper composite gated transistors

6.2.2.1. Performance of as-printed devices

Figure 6.21c shows typical cyclic transfer and respective output curves of the fabricated fully screen-printed ZnO NCGTs depicted in **Figure 6.21**a-b. The devices were tested one hour after printing de semiconducting layer, under ambient conditions (≈40 % RH). Statistical variations of twenty-five devices are displayed in the histograms of **Figure 6.21**d-i, corresponding to the vital figure of merits of transistors, which strongly depend on the capacitance of ACICC membrane and its surface defects. The electrical parameters were calculated in the forward sweep direction and in the saturation regime (V_{DS} = 1.2 V). The corresponding mean values and their standard error of the mean are also mentioned.

The parameters S_S and μ_{Sat} were calculated according to **Equation S4** and **Equation S5**, respectively. Regarding the latter parameter, contrarily to the previously studied CICHs, the less conformable nature of the ACICC membrane to the deposited functional materials can lead to additional interfacial defects that can make the estimation of C_{DL} more complex, despite the good fitting of the ECM chosen for data interpretation. Thus, the capacitance value used to determine the NCGTs' mobility was the one obtained at the lowest value of frequency (0.1 Hz) from previous EIS measurements (**section 4.2.2**), within the EDL formation regime, which corresponds to 0.8 μF cm^{-2}.

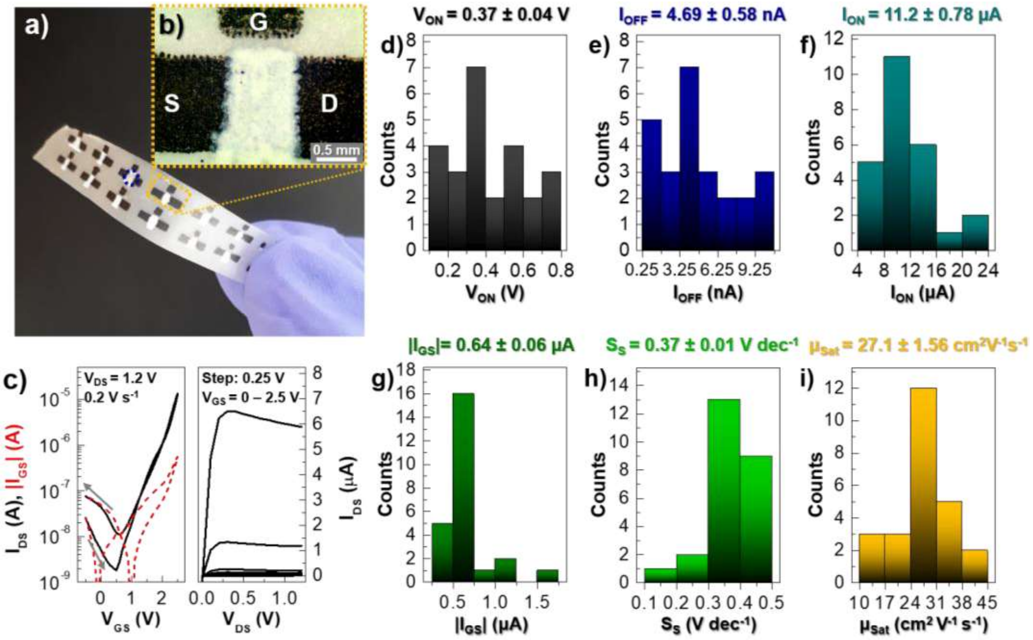

Figure 6.21. Electrical characterization of the fabricated fully screen-printed ZnO NCGTs. **a)** Photograph of the fabricated fully screen-printed "intertrates" EGTs on the ACICC membrane. **b)** Optical micrograph image of a single NCGT (S, G and D stand for source, gate and drain electrodes). **c)** Cyclic I_{DS}–V_{GS} curve, and respective I_{DS}–V_{DS} curve (the V_{GS} step was 0.25 V, starting from -0.5 up to 2.5 V) for saturation regime (V_{DS} = 1.2 V) at a fixed V_{GS} scan rate of 0.2 V s^{-1}. Arrows represent the sweep direction, whereas continuous and dashed lines correspond to I_{DS} and $|I_{GS}|$, respectively. Histograms of device metrics for 25 devices: **d)** V_{ON}, **e)** I_{OFF}, **f)** I_{ON}, **g)** $|I_{GS}|$, **h)** S_S, and **i)** μ_{Sat}.

The fabricated NCGTs operate with negligible hysteresis (anti-clockwise direction) in the enhancement mode (normally-off) with a V_{GS} of less than 2.5 V, which is much lower than conventional cellulose-based paper transistors, typically reported in the order of tens of volts. The channel conductance varies more than three orders of magnitude (3.5 × 10^3), reaching an I_{OFF}, I_{ON} and $|I_{GS}|$ of 4.69 ± 0.58 nA, 11.2 ± 0.78 µA and 0.64 ± 0.06 µA, respectively.

The large $|I_{GS}|$ observed is strictly related to the faradaic redox currents (as previously confirmed by CV measurements in **Figure 4.14**, since small ions, such as H^+ and Li^+ ions, tend to diffuse into the highly permeable semiconducting layer. Its porous morphology works as electrochemically active sites that promote electrochemical reactions, inducing a 3D conduction channel. Both I_{DS} and $|I_{GS}|$ curves exhibit distinct behaviors depending on the applied V_{GS}, which evidence that a different operation mechanism becomes dominant, shifting from a field-effect to a predominant electrochemical doping regime for higher V_{GS} values. Furthermore, the devices exhibit large μ_{Sat} of 27.1 ± 1.56 cm^2 V^{-1} s^{-1}, and relatively small S_S of 0.37 ± 0.01 V dec^{-1}. According to the output characteristics, the printed devices show hard saturation behavior at very low V_{GS} (<2.5 V) and V_{DS} (<0.5 V).

Although the smooth surface of the ACICC membrane leads to lower variations in the electrical parameters in comparison with the ZnO PNPs EGTs printed on rough and non-uniform standard office paper, the electrical performance of the fully screen-printed NCGTs is not as good as the latter ones. The observed differences are due to the lower conformability of the ACICC membrane to the semiconducting layer that leads to a poorer dielectric/semiconductor interfacial quality in comparison with the Li-ClCH sticker. The adverse effects of the intrinsically rough and porous surface of the ZnO PNPs are easily mitigated when using the highly conformable, smooth, and sticky CICH stickers, as they enhance considerably the contact at the semiconductor/electrolyte interface.

The electrical performance of the NCGTs can be improved by sintering the particles to some extent to create a denser yet smoother structure,[15,177,178] or through the creation of a continuous and smooth ZnO dual-phase layer to address the large surface roughness issue.[58,351] Besides, the degree of alignment of the semiconducting particles also influence the devices' performance, being favorably affected for well-aligned particles along the transport direction.[351]

6.2.2.2. Air-stability overtime

The environmental stability of six printed ZnO NCGTs overtime was also assessed. The transfer curves are measured at as-prepared conditions and after three weeks in air (**Figure 6.22**). In a similar way as the screen-printed ZnO EGTs on office paper (**section 6.1.2.2)**, the electrical performance of the devices is also quickly degraded just after a few days, decreasing their electrical modulation almost one order of magnitude, due to a considerable decrease of I_{ON}, while μ_{Sat} decays almost 95 %. Their performance remains almost constant after one week, yet for longer periods of storage they no longer exhibit a satisfactory electrical modulation as the $|I_{GS}|$ surpasses the I_{ON}. Since the devices' performance is not maintained for long periods of time, they are more suitable for disposable applications.

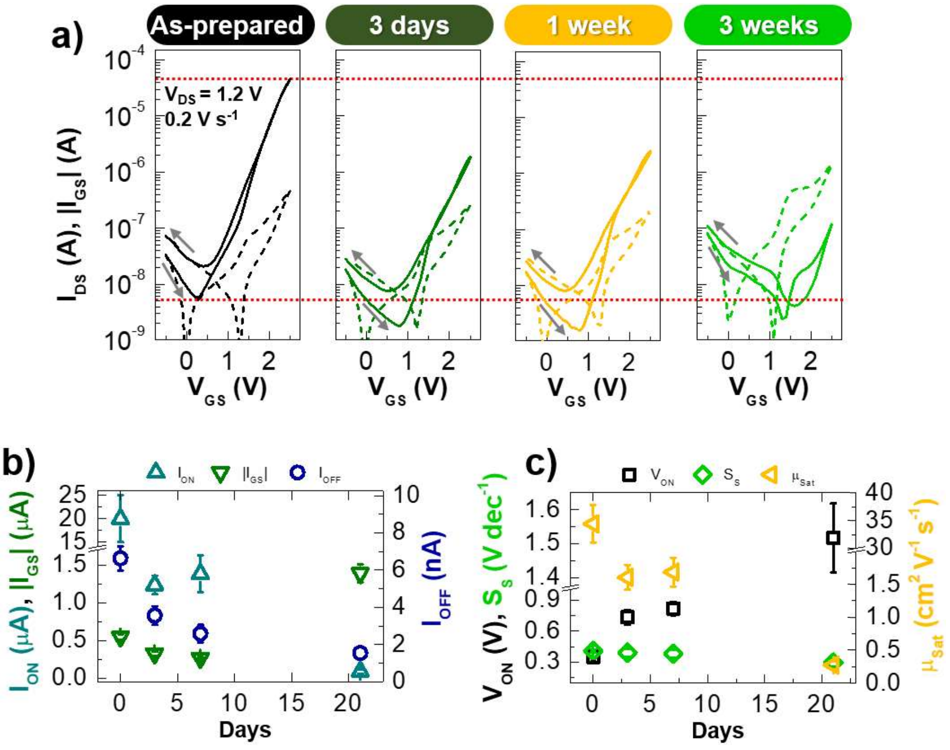

Figure 6.22. Ageing effect of the fabricated fully screen-printed ZnO NCGTs. **a)** I_{DS}–V_{GS} curves obtained after three days, one week, and three weeks of storage under ambient conditions and comparison with the as-prepared devices (V_{DS} = 1.2 V, V_{GS} scan rate = 0.2 V s^{-1}). Arrows represent the sweep direction, whereas continuous and dashed lines correspond to I_{DS} and $|I_{GS}|$, respectively. Variation of electrical parameters overtime: **b)** I_{ON}, $|I_{GS}|$, I_{OFF}, **c)** V_{ON}, S_S, and μ_{Sat} (the data points show the average and corresponding errors bars obtained from six samples).

6.2.2.3. *Bending measurements*

Although several reports have demonstrated the flexibility of oxide-based paper TFTs with proper operation under bending strains,[32,33,41,44,57] foldability has not been achieved. Up to date, organic semiconductors have demonstrated superior endurance to mechanical deformations.[129]

Figure 6.23 shows the influence of mechanical deformation on the transfer characteristic curves of the devices before and after inducing a bending deformation along the channel axis, using a substrate holder with a bending radius of 15 mm, as well as the recovery to the flat state of the folded devices. The ACICC membrane and printed carbon electrodes show mechanical resistance after bending or folding, which lead us to conclude that the differences observed in the devices' performance can be mainly attributed to the cracking, peeling or even alignment of the ZnO PNPs, depending on the type of induced mechanical deformation.

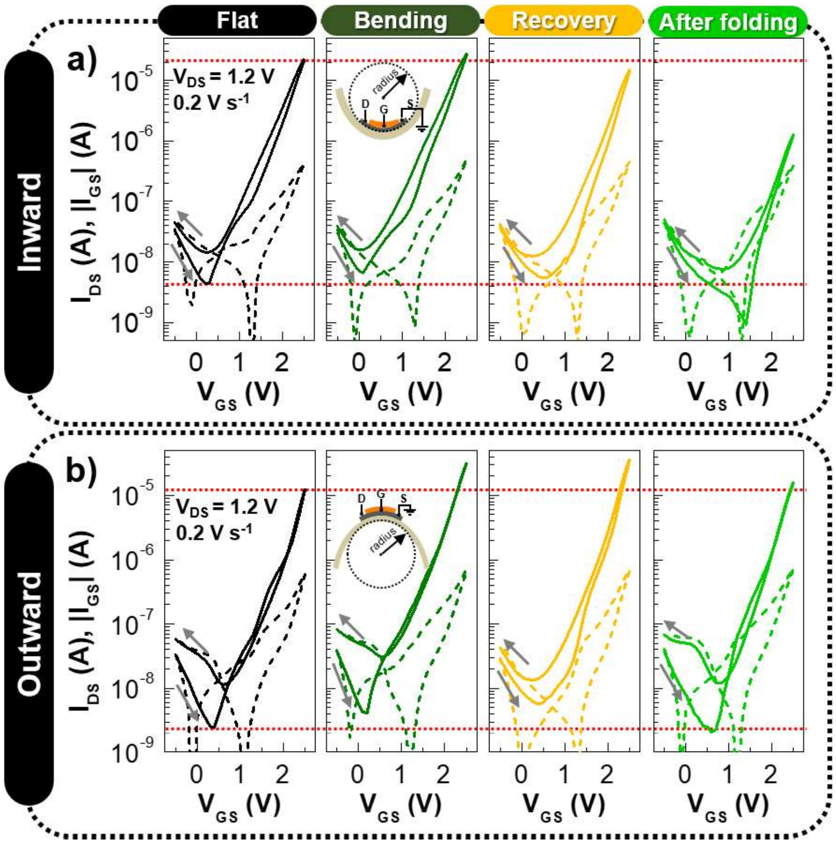

Figure 6.23. Electrical characterization of the fabricated fully screen-printed ZnO NCGTs before and after inducing a mechanical deformation. I_{DS}–V_{GS} curves obtained before and after performing **a)** inward or **b)** outward bending/folding (V_{GS} scan rate of 0.2 V s^{-1}). Arrows represent the sweep direction, whereas continuous and dashed lines correspond to I_{DS} and $|I_{GS}|$, respectively.

Figure 6.24a,d displays the respective variation on the electrical performance before and after performing bending or folding. For inward bending, a deterioration in the electrical properties is observed, where a small shift of V_{ON} for higher values is observed, while I_{ON} and μ_{Sat} reduces about 12 and 11 %, respectively, compared to its original performance in the flat state. These changes are due to the formation of some cracks throughout the thick CMC/ZnO layer. When returning to the flat state, the performance is further degraded due to the peeling of crashed particles. Despite the propagation of the fractures along the channel layer during folding, contrarily to ZnO NPs, the elongated size of the ZnO PNPs proves to be advantageous to guarantee enough percolation paths that ultimately avoid the total failure of the devices after folding, as confirmed by SEM (**Figure 6.24**b,c).

A quite different behavior is observed when inducing a tensile strain correspondent to outward bending. In this case, a considerable improvement of the devices' performance is observed since the outward bending promotes the local preferential orientation of the particles in the source-drain direction, which facilitates electron transport of the semiconducting film, and the local alignment of the nanopaper fibers, thus enhancing ion percolation within the ACICC membrane. This reason can explain the favorable increase of 47 and 14 % of I_{ON} and μ_{Sat}, respectively, resulting in an optimization of $I_{ON/OFF}$ of 4 %. The removal of the bending stress promotes a better accommodation of the locally oriented particles, restoring and creating new percolation paths, which in turn leads to a further improvement of the NCGTs' original performance. Comparing the performance before and after bending, the I_{ON} increases 61 %, whilst an increase of 46 % is achieved for the μ_{Sat}.

Regarding recovery after folding, the devices demonstrate a remarkable performance, almost comparable to that obtained before inducing a bending deformation, showing only a slight shift of V_{ON} from 0.3 to 0.7 V and a decrease in $I_{ON/OFF}$ of 24 %. As observed in **Figure 6.24**e,f, the device remains uninjured after folding, which clearly demonstrates the good quality of the semiconductor/ACICC membrane interface.

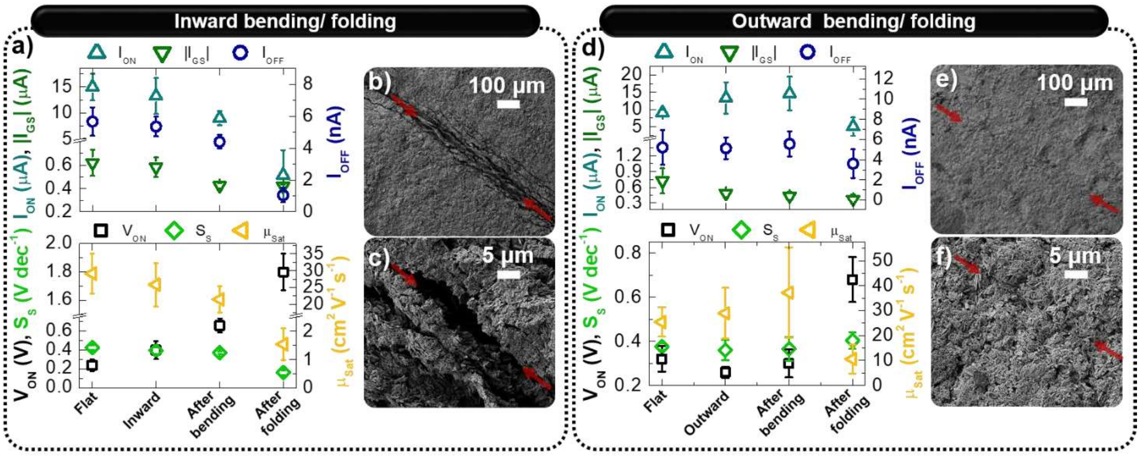

Figure 6.24. Electrical characterization of the fabricated fully screen-printed ZnO NCGTs before and after inducing mechanical deformation. Variation of the electrical parameters before and after performing **a)** inward or **d)** outward bending/folding (V_{DS} = 1.2 V, V_{GS} scan rate = 0.2 V s^{-1}). The data points show the average and corresponding errors bars obtained from five samples. SEM images of the devices in the flat state after performing **(b,c)** inward or **(e,f)** outward folding.

As depicted in **Figure 6.25**, the folding stability of three screen-printed ZnO NCGTs was assessed over 100 outward folding/unfolding cycles. The most significant changes occur during the first five cycles in a similar way as previously described, showing a decrease in I_{ON} and mobility, as well as a displacement of the V_{ON} to higher values. Their performance remains stable with the increase in folding/unfolding cycles, which demonstrates that these devices have satisfactory mechanical tolerance, serving the purpose of flexible electronics.

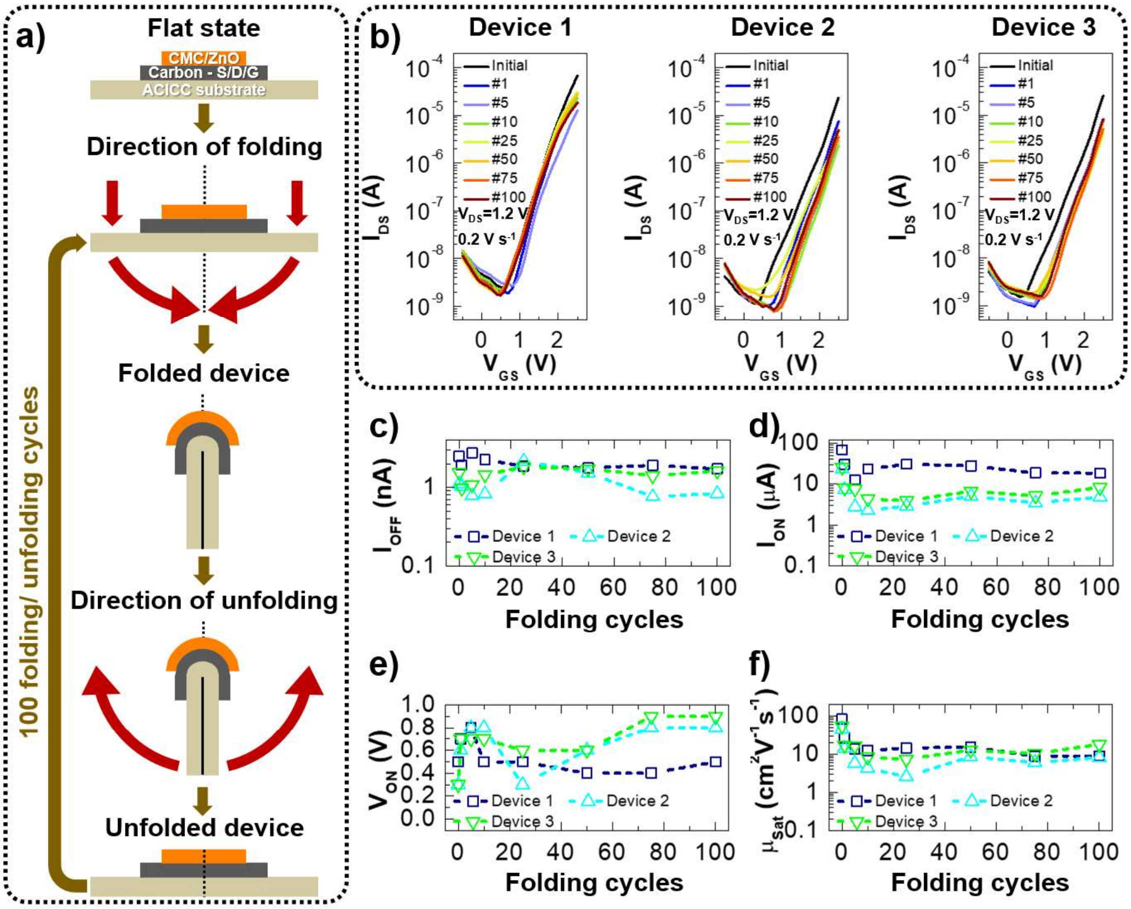

Figure 6.25. Mechanical electrical stress measurements of the fully screen-printed ZnO NCGTs on the flat state after consecutive 100 outward folding/unfolding cycles. **a)** Schematic representation of successive folding/unfolding cycles. **b)** I_{DS}–V_{GS} curves of three devices after successive folding/unfolding cycles (V_{DS} = 1.2 V, V_{GS} scan rate = 0.2 V s^{-1}), and respective evolution of the electrical parameters: **c)** I_{OFF}, **d)** I_{ON}, **e)** V_{ON}, and **f)** μ_{Sat}.

Considering all these results, a fair comparison was performed with the current state-of-the-art in the field of transistors gated by cellulose-based paper substrates, starting with the works of CENIMAT group, which established the foundations of paper as an active material in electronics, and the follow up from several research groups (**Table S3**). Although most of these works are devoted to conventional vacuum-based deposition techniques to deposit inorganic semiconductors materials on several types of engineered cellulose-based paper substrates, their operating voltage is still in the range of tens of volts to enable the creation of electric double layers. More recently, Dai and co-workers[51,358] produced flexible transistors and CMOS inverters with low-voltage operation on TEMPO-oxidized NFC membranes using thermally evaporated n- and p-type organic semiconductors.

In comparison, this work reports for the first time fully printed devices on ACICC membrane, successfully using ZnO nanostructures as the channel layer, showing remarkable mechanical endurance under folding deformations, while operating with merely a few volts with appealing electrical characteristics. Therefore, the possibility to build extremely low-power flexible transistors based on TMOS materials is no longer limited to low-mobile organic semiconductors, despite their undeniable superior processability.

6.2.2.4. Electrical stress: static and dynamic measurements

Static and dynamic measurements were performed to assess the electrical stress of printed ZnO NCGTs. For the static measurements, one device was subjected to 1000 consecutive cycles between -0.5 a 2.5 V (forward and backward sweep), without delay between each measurement (**Figure 6.26**a,b). The device exhibits a satisfactory electrical endurance after 1000 cycles. For increasing number of cycles, I_{OFF} and S_S decrease, whereas the remaining electrical parameters show some fluctuations over cycling. In a first stage until 100 cycles, the V_{ON} shifts from 0.6 to 1.1 V, and an increase on I_{ON} (37 %), $|I_{GS}|$ (2.4 %) and μ_{Sat} (28 %) is observed. Then this trend is reversed as the same parameters start to decrease successively, and an enlargement of the hysteresis occurs. Despite the shift of both I_{DS} and $|I_{GS}|$ for lower values, an improvement of the device's modulation is observed. This trend can be associated with a side effect that can occur after successive cycling, which is the Joule heating, as it can promote water desorption, thus hindering the ionic conduction of the ACICC.

The dynamic characterization was carried out by applying a square-wave gate signal at different frequencies (1–25 Hz), between -0.5 until 2.5 V for a V_{DS} fixed at 1.2 V (**Figure 6.26**c-h). The devices show an electrical modulation above two orders of magnitude at 0.1 Hz, and a steep decrease of $I_{ON/OFF}$ towards one order of magnitude is observed for frequencies between 5 and 10 Hz, this being the maximum frequency at which the fabricated logic gates are expected to operate. Although it is still possible to distinguish between the OFF and ON states at 25 Hz, the $I_{ON/OFF}$ does not reach one order of magnitude. Despite the ionic response of the ACICC membrane points to a capacitive behavior for superior frequencies (≈1.9 kHz) (according to previous EIS results in **Figure 4.13**), the rough ZnO PNPs particles can limit the device's switching.

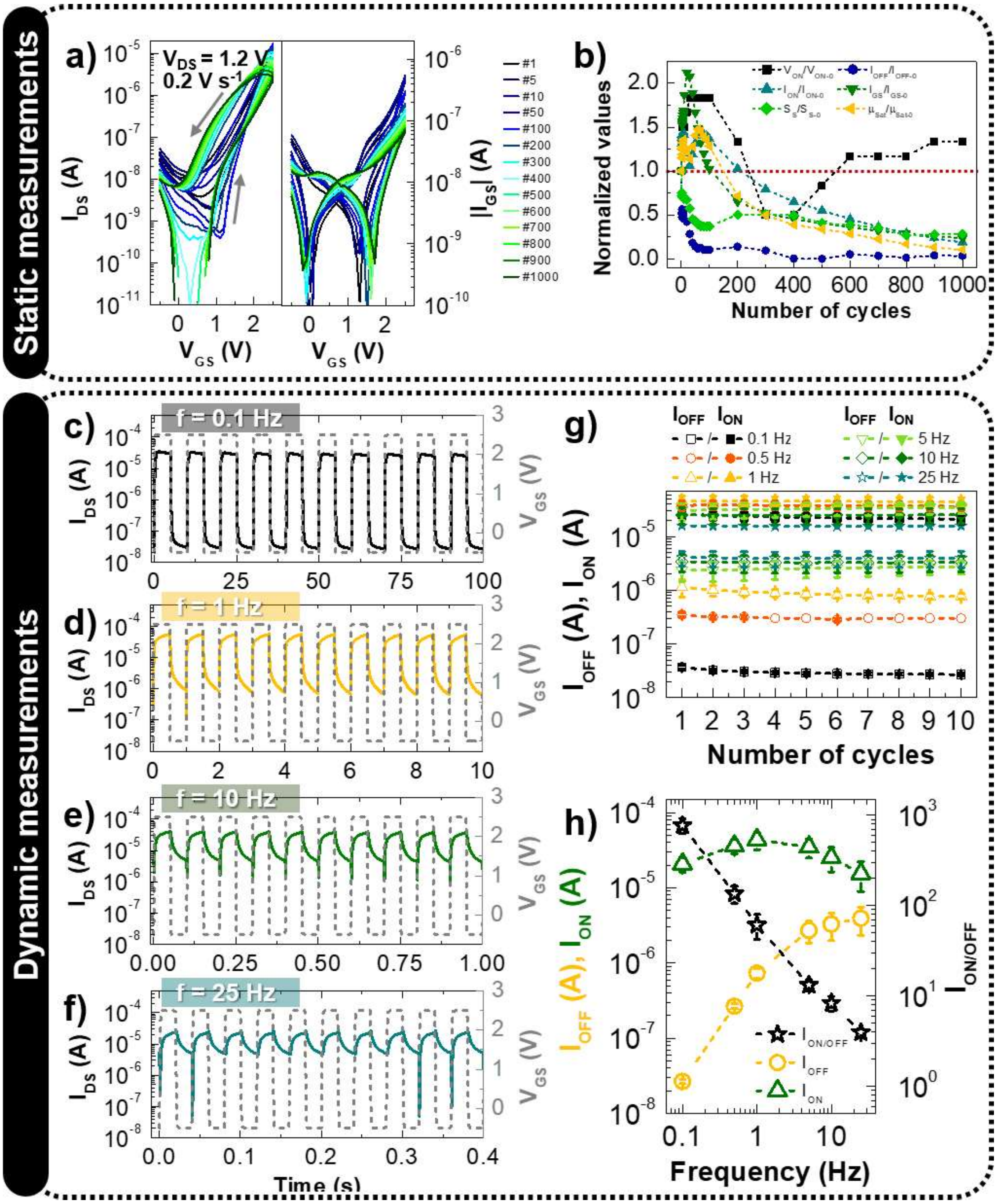

Figure 6.26. Static and dynamic electrical characterization of the fabricated fully screen-printed ZnO NCGTs. **a)** I_{DS}–V_{GS} curves obtained after consecutive cycling without delay between each cycle (V_{DS} = 1.2 V, V_{GS} scan rate = 0.2 V s^{-1}). Arrows represent the sweep direction. **b)** Normalized electrical parameters for increasing cycles. Variation of I_{DS} with increasing cycles of V_{GS} pulses from -0.5 until 2.5 V for different frequencies: **c)** 0.1, **d)** 1, **e)** 10, and **f)** 25 Hz. **g)** Variation of I_{ON} and I_{OFF} with increasing cycles for a square-wave gate signal between -0.5 until 2.5 V for a fixed V_{DS} of 1.2 V and at different frequencies (open symbols correspond to I_{ON}, while closed symbols correspond to I_{OFF}). **h)** Evolution of I_{ON}, I_{OFF} and $I_{ON/OFF}$ with frequency for the tenth cycle (the data points show the average and corresponding errors bars obtained from four devices).

6.2.3. Logic gate operations with fully printed ZnO nanopaper composite gated transistors

Figure 6.27a show VTC curves of the NOT gate with a pencil-drawn R_L of 300 kΩ and a EGT$_D$ with L = 200 µm and W = 1 mm. The circuit shows a clear steep inverting behavior with low output hysteresis when V_{IN} is swept from -0.5 (logic input signal “0”) to 3 V (logic input signal “1”) for a low V_{DD} of 1.5 V. The V_{OUT} at logic input signal “0” is close to the V_{DD} (≈1.43 V), which is determined by $V_{OUT} = V_{DD} – R_L.I_{DS}$. When the transistor shifts to the ON state with the increase of V_{IN}, V_{OUT} drops almost to zero (≈0.05 V). The inverter exhibits a maximum |gain| of 2.9.

The output characteristics of NAND and NOR logic gates are shown in **Figure 6.27**b,c, respectively, showing also low hysteresis. In the case of the NAND gate, when either one or both of the input gate voltages ($V_{IN,A}$ and $V_{IN,B}$) are logic “0” ($V_{IN,A} = V_{IN,B} = 0$ V), the V_{OUT} is “HIGH” (1.34 V), corresponding to output logic “1”. Only when both input gate voltages are logic “1” ($V_{IN,A} = V_{IN,B} = 3$ V), the transistors turn to ON state and the V_{OUT} becomes “LOW”, corresponding to output logic “0” (0.09 V), reaching a |gain| of 1.6.

In contrast, for the NOR gate, output signal “1” is obtained only when all the transistors are in the OFF state. The maximum value to define output signal “1” corresponds to 1.33 V, reaching a |gain| of 1.1. The output logical “0” can be defined when applying input signals $V_{IN,A} = 3$ V and $V_{IN,B} = 0$ V, reaching a minimum value for V_{OUT} of 0.09 V. Nevertheless, V_{OUT} is slightly high when $V_{IN,B} = 3$ V and low input signals $V_{IN,A}$ are applied, since either the EGT_A is not entirely in the OFF state or $|I_{GS}|$ have increased. In this case, when $V_{IN,B} = 3$ V and $V_{IN,A} = 0$ V the V_{OUT} records a value of 0.83 V.

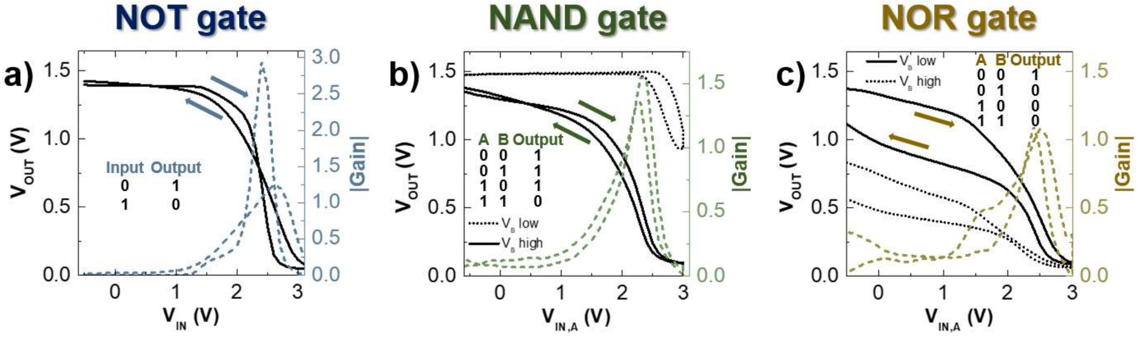

Figure 6.27. Logic gate applications of the planar fully screen-printed ZnO NCGTs with pencil-drawn load resistances. VTC curves of **a)** the NOT gate; **b)** NAND gate, and **c)** NOR gate, and respective |gain| for different $V_{DD} = 1.5$ V at a fixed voltage scan rate of 0.2 V s^{-1}. Truth tables of the fabricated logic gates are summarized as insets in the respective plots.

Chapter 7

Environmental responsible strategies

7. Environmental responsible strategies 133
7.1. Reuse, repair, and recyclability of cellulose iontronic stickers 135
7.2. Biodegradability and recyclability assessment of all-cellulose ionic conductive substrates 139
7.3. Adding value to cork wastes 144

Beyond the need of ecofriendly materials as well as compatible economically efficient and scalable processing, manufacturing, and assembling methods, a convenient end-of-life management of electronic/electrochemical systems is imperative in a current world that assists to a more and more use of these systems integrated into commodity items, and now the upcoming trend of IoT devices that threatens to increase E-waste in the future.[359]

The arise of IoT is also in line with the benefits offered by scalable printing/handwriting manufacturing technologies that enable the fabrication of multiple devices in a short-time and at extremely low-cost, thus making the resulting product affordable to the final end-user. Nevertheless, the criteria regarding their properties and stability overtime are usually more relaxed, when compared to similar devices prepared from sophisticated vacuum-deposition techniques, being sometimes meant to endure from a single to just a few life cycles, and then discarded, as in the case of health monitoring or diagnosis applications. Therefore, a path must be drawn to ensure an entirely sustainable system, where the entire product or a share of its materials/components, whether partially or totally damaged due to either extreme or overtime usage or even contamination from toxic materials (e.g. heavy metals, and biological hazards), are easily recovered and repaired to minimize as much as possible the harmful effects to the environment resulting from improper waste management.

When looking into environmental sustainability, current end-of-life management has focused primarily on recycling. Nonetheless, depending on the degree of complexity of the products, recycling can be an energy consuming process since a large amount of energy can be dispended to transport, process and reassemble recyclable materials. Instead, repair or reuse are far kinder strategies compared with recycling for a proper implementation of the circular economy concept. In this section, although the use of cellulose-based materials in electronics is usually linked with the concept of disposability due to its biodegradable nature,[137,360] sustainable concepts from reusing, repairing to recycling are demonstrated to reduce the generation of waste and extend the lifetime of the devices, as illustrated in **Figure 7.1**. Furthermore, the possibility to apply these sustainable strategies in the recover and processing of biocomposite wastes, such as those obtained from cork industry that can not find appealing commercial use, was also investigated.

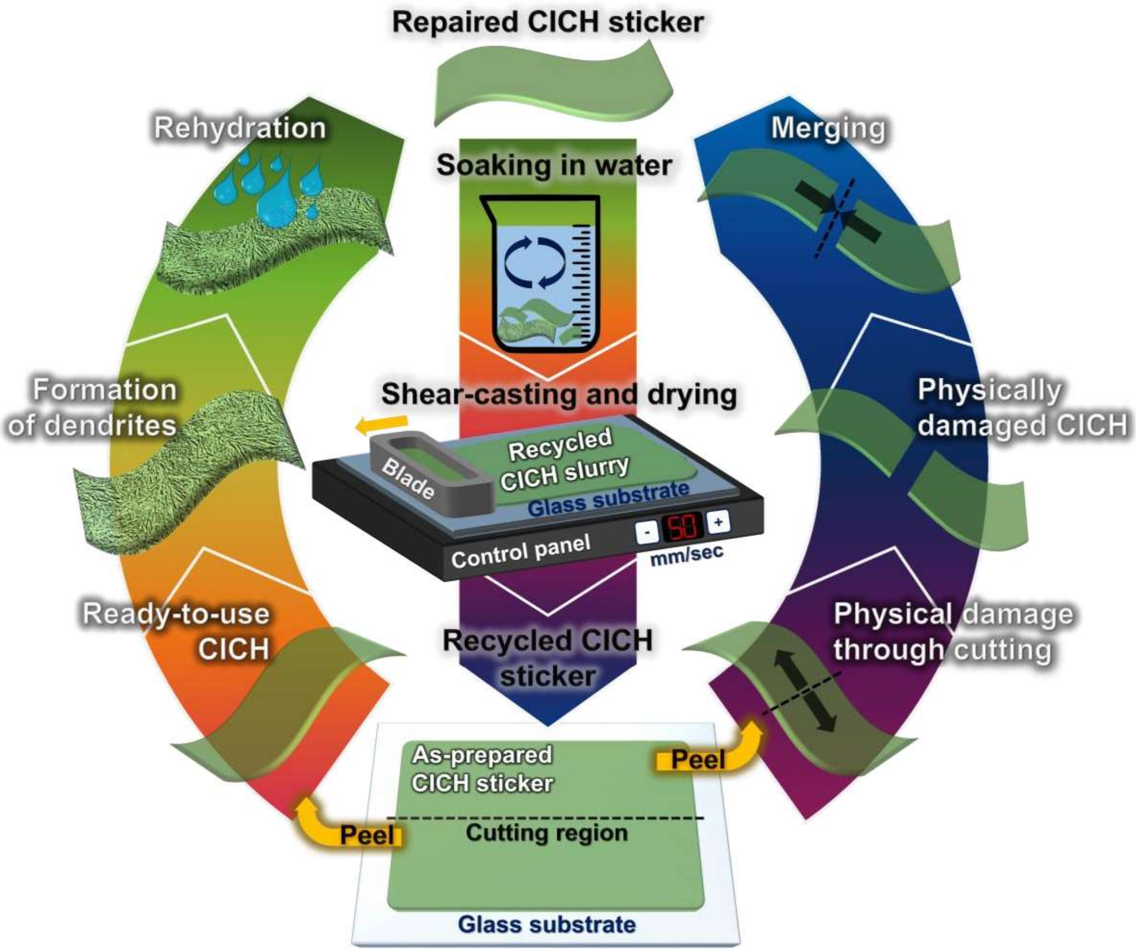

Figure 7.1. Circular sustainability loop for cellulose-based ionic conductors using repairing and recycling strategies that enable the endless reuse of the obtained ionic conductive membranes.

7.1. Reuse, repair, and recyclability of cellulose iontronic stickers

Due to the superior performance and stability of the L100 electrolyte demonstrated throughout this work, further tests were performed to assess its reusability. For this purpose, a single membrane used as gate dielectric in an IGZO EGT on paper was carefully removed with a blade and reused successive times in different flexible IGZO EGTs. As shown in **Figure 7.2**, the results demonstrate the efficient reuse of the recovered membrane in five additional flexible EGTs, since no electrical degradation of the devices was observed after its repeated use. However, for such tests, the reused membrane is not damage during the transfer process. Thus, the possibility to repair damaged materials due to improper or overtime usage arises substantial interest, as such strategy extends their lifetime and durability.

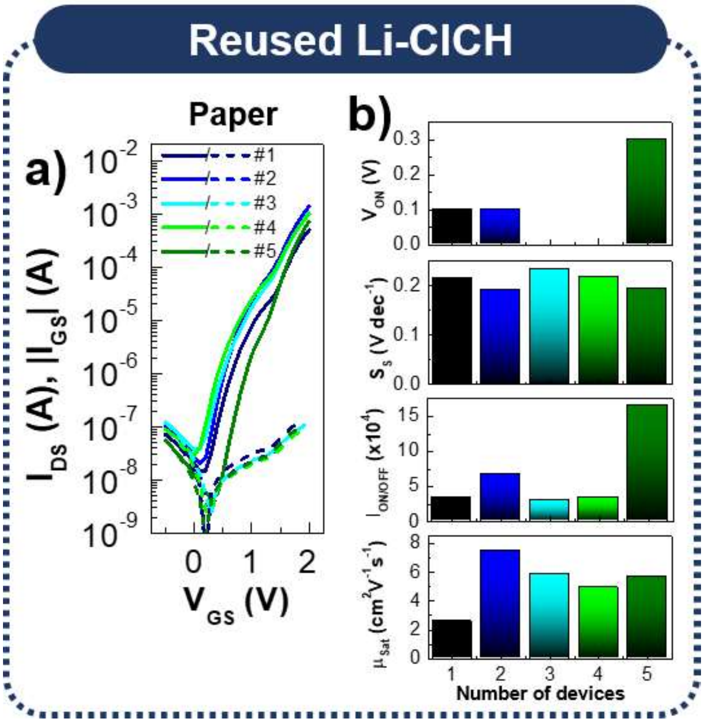

Figure 7.2. Electrical performance of IGZO EGTs gated by repeatedly reused L100 hydrogel. **a)** I_{DS}–V_{GS} curves, and **b)** respective electrical parameters obtained for five additional IGZO EGTs on multilayer-coated paper substrate gated by reused L100 membrane (V_{DS} = 1.2 V; V_{GS} scan rate = 25 mV s^{-1}).

Considering the presence of hydrogen bonds in the developed CICHs (see **Figure 4.3**e), cut/healing tests were performed under ambient conditions to assess the healing capability of the CICHs. For these tests, the L100, L1N3 and N100 electrolytes were cut into two parts with a razor blade, and then the fragments were instantly merged into one by pressing them back together in the cutting region for 10 s (see **Figure 7.3**a). **Figure 7.3**b shows the σ_i of the electrolytes after repeated cutting-off and contact healing (see also **Figure S7**). The results suggest that the two fragments, after being brought back into contact, can rapidly reestablish the network at the interface through the formation of physically cross-linked domains by hydrogen bonding, mediated by either hydroxyl or amide groups.[102,104–106,109,111,113,314] As a result, the CICHs can restore their electrochemical properties by combining pressure with their self-healing characteristic, keeping the σ_i in the same range of values. By doing so, waste membranes can be recombined, reshaped, and reused.

Another important point is that the reversible swelling ability of the electrolytes prepared from solutions with high levels of NaOH can delay or even reverse the formation of dendrites. The self-healing ability through a hydration process, under distinct environmental conditions, were further explored in the N100 membrane, which is more prone to dendrite formation (**Figure 7.3**c-f).

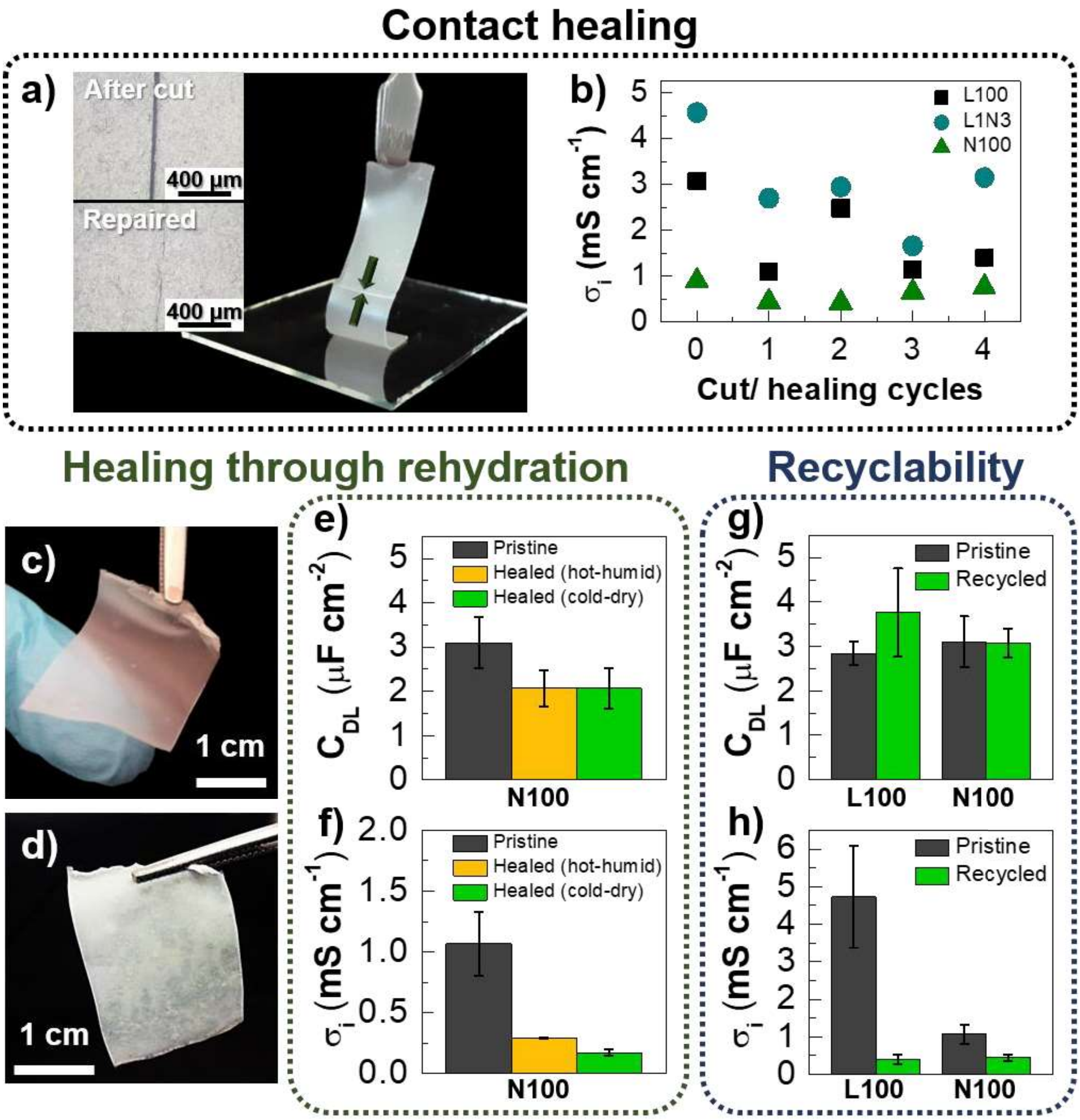

Figure 7.3. Self-healing ability and recyclability of the freestanding CICHs. **a)** Photograph of the repaired N100 membrane after being cut into two pieces with a razor blade and then restored by gently pressing the pieces back into contact in the cutting region for 10 s (inset: optical microscope images of the N100 membrane in the cutting region after cut and repair). **b)** Ionic conductivity of the L100, L1N3 and N100 membranes after multiple cutting/healing cycles in the same position at RT. Photographs of the freestanding N100 ionic hydrogel **c)** before, and **d)** after formation of dendrites. Comparison of (**e, g**) C_{DL} and (**f, h**) σ_i for the different N100 membranes (pristine, recycled, healed – "hot-humid" environment, healed – "cold-dry" environment). The data points show the average and corresponding errors bars obtained from 4 samples.

To investigate the influence of environmental conditions on the self-healing ability of the N100 electrolyte, the membrane was cut into two fragments and stored in a closed box with controlled environment (T = 24 ± 2 ºC, 33 ± 2 %RH) until both were completely covered by dendrites (≈1 day). One of the fragments was exposed for 2 hours to water vapor, mimicking a "hot-humid" environment. The other fragment was kept inside a freezer at -25 ºC overnight, simulating a "cold-dry" environment. The membranes obtained from both experiments were then kept in a controlled environment at 24 ± 2 ºC and 33 ± 2 %RH for one day and tested right after exposing them to ambient conditions (≈45–50 %RH).

In both cases, the rehydration of the membranes promotes the solubilization of the urea dendrites in water, thus promoting their healing. Yet, the electrochemical performance of the healed hydrogel membranes is very distinct in comparison with the pristine membranes, as the performed hydration treatments influence the water content retained in the membrane that aid the healing process.

Figure 7.3e,f (see also **Figure S8** and **Table 7.1**) confirms that both approaches are suitable to recover the electrolyte after occurring the unwanted formation of dendrites at the cost of smaller σ_i with a difference of almost one order of magnitude. The membranes repaired in a “hot-humid” environment exhibit a better electrochemical performance ($\sigma_i \approx 0.29$ mS cm^{-1}), as the rehydration occurs faster when compared with those exposed to a “cold-dry” environment ($\sigma_i \approx 0.17$ mS cm^{-1}). In the latter case, the rehydration only starts when the membrane is stored inside the closed box in a relatively dry environment. This leads to a slower but not complete recovery of the membrane, as only a limited number of hydrophilic groups of cellulose are in an active state to promote self-healing.[314]

At the end of the products lifespan, recycling is a very attractive and sustainable strategy to address the negative impact of waste on the natural environment (**Figure 7.3**g,h, **Figure S8**, and **Table 7.1**). The CICHs can be easily disassembled from sputtered IGZO EGTs, and then efficiently recycled by soaking the recovered membranes in water under stirring to obtain a homogeneous solution, and new recycled membranes were prepared in the same way as the pristine ones. In a similar way as the healed membranes, a loss of electrochemical performance is observed in the recycled membranes that is more pronounced in the recycled L100 electrolyte, where σ_i decreased almost 91 % (4.73 to 0.41 mS cm^{-1}) in contrast with 58 % (1.07 to 0.45 mS cm^{-1}) in the case of recycled N100 membrane.

Considering the electrochemical performance displayed by the healed and the recycled membranes, they can be successfully reused as gate dielectric in IGZO EGTs and lead to devices that display satisfactory electrical performance with an electrical modulation in the range of five orders of magnitude (**Figure 7.4**). The electrical parameters obtained for each device are also displayed in **Table 7.1.**

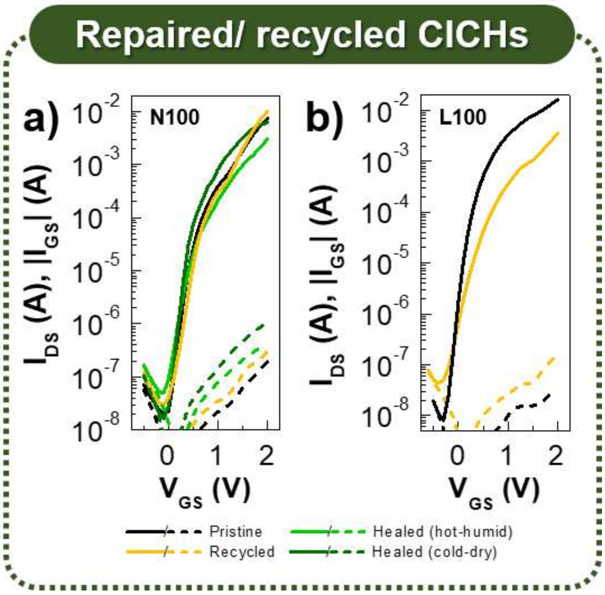

Figure 7.4. Electrical performance of IGZO EGTs gated by pristine, healed, or recycled ClCHs**.** Comparison between I_{DS}–V_{GS} curves of IGZO EGTs on glass gated by: **a)** pristine, recycled or healed N100 membranes recovered from exposure to hot-humid or cold-dry environment; **b)** pristine or recycled L100 membranes (V_{DS} = 1.2 V; V_{GS} scan rate = 50 mV s^{-1}).

Table 7.1. Comparison of the electrochemical parameters for the different N100 membranes (pristine, healed, and recycled) and recycled L100, and their influence on the electrical performance of the fabricated IGZO transistors on glass (V_{DS} = 1.2 V, V_{GS} scan rate: 0.05 V s^{-1}).

Parameters	Pristine	Healed (“hot-humid”)	Healed (“cold-dry”)	Recycled	L100 recycled
$C_{f=1\ Hz}$ [μF cm^{-2}]a)	8.2 ± 0.6	7.9 ± 1.2	7.1 ± 1.3	9.8 ± 0.6	9.9 ± 0.7
C_{DL} [μF cm^{-2}]b)	3.1 ± 0.6	2.1 ± 0.4	2.1 ± 0.5	3.1 ± 0.3	3.8 ± 1.0
σ_i [mS cm^{-1}]b)	1.07 ± 0.26	0.29 ± 0.01	0.17 ± 0.03	0.45 ± 0.08	0.41 ± 0.13
V_{ON} [V]	-0.1	-0.1	-0.1	-0.1	-0.3
I_{OFF} [nA]	19.5	50.4	16.3	29.9	30.2
I_{ON} [mA]	7.40	3.04	6.27	10.1	4.72
$I_{ON/OFF}$ [×10^5]	3.80	0.60	3.84	3.37	1.56
S_S [V dec^{-1}]	0.13	0.18	0.12	0.17	0.21
μ_{Sat} [cm^{2}V^{-1}s^{-1}]c)	30.3	22.7	24.9	54.8	18.5

a) Values obtained directly from the EIS data. The values show the average and respective standard error of the mean obtained from four samples.
b) Electrochemical parameters calculated from the data fitting of EIS measurements using Dasgupta’s ECM.The values show the average and respective standard error of the mean obtained from four samples.
c) Mobility calculated using the capacitance values determined from the data fitting of the EIS measurements using Dasgupta’s ECM.

7.2. Biodegradability and recyclability assessment of all-cellulose ionic conductive substrates

Considering the short lifetime of the fabricated screen-printed ZnO NCGTs and circuits related to the reactivity of the ZnO PNPs when in contact with the ACICC membrane, we explored a non-toxic, low-cost process to efficiently recycle the devices.

Taking advantage of the water-based formulation of both electrolyte and semiconductor layers, the pristine ACICC membranes that host the iontronic devices were soaked in water, and then stirred to obtain a homogeneous pulp of fibers, which is used as raw material for the preparation of recycled membranes by performing solvent-casting in polystyrene Petri dishes. During stirring, the transistors array disintegrate into individual devices, and then gradually disappears depending on the dispersion or dissolution rate of the various constituent materials.[361] As observed in previous reports.[362–364], ZnO can be easily dispersed and partially dissolved in water to form zinc hydroxide. On the other hand, the carbon material, coming from the electrodes and conductive tracks, has different dimensions and is randomly dispersed in the composite pulp that can be partially sieved before preparing the recycled membrane.

The clear biodegradability of ACICC membrane and CMC/ZnO layer arises concepts such as biodegradable electronics (or “transient electronics”), in which the materials completely or partially dissolve, resorb, or physically disappear after functioning in environmental or physiological conditions at controlled rates.[364] Therefore, such devices can be used as environmentally friendly alternatives to existing electronics that disintegrate when exposed to water, thus solving the problem of E-waste management.

Also, the composite pulp can have a greater use when recycled. **Figure 7.6**a shows a photograph of the resulting recycled ACICC membrane, which is clearly less transparent, and more fragile than the pristine one due to the present of carbon conductive material and ZnO particles from the devices, as demonstrated by EDS (**Figure 7.5**d). Although the sieving of the carbon material minimizes the creation of irregularities on the surface and avoids unintentional conducting paths in some regions of the recycled membrane that might occur if not properly filtered, the recycled membrane still exhibits a quite irregular fibrous surface covered by waste material from the devices (**Figure 7.5**a-c). Thus, its surface is substantially rougher compared to the pristine one, reaching a large RMS roughness in the range of a few hundred nanometers (**Figure 7.5**e).

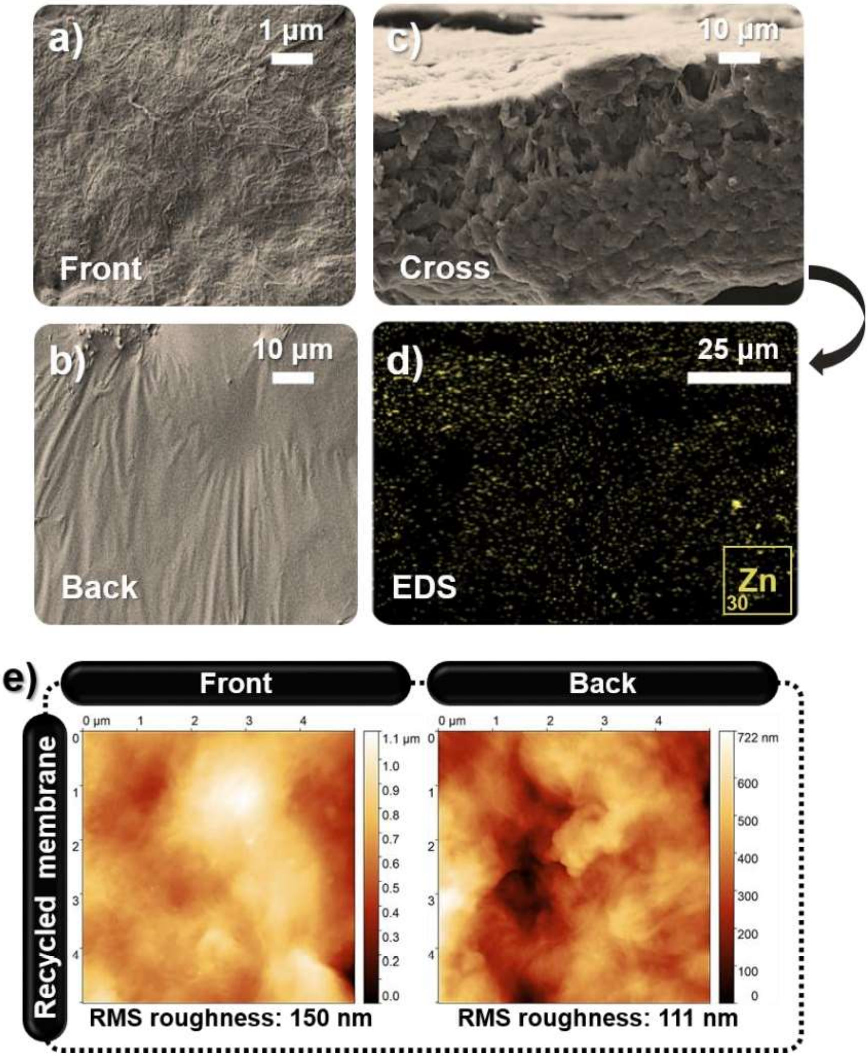

Figure 7.5. SEM images of the recycled ACICC membrane, and EDS mapping of Zn. SEM images of the **a)** front side (surface in contact with air), **b)** back side (surface in contact with the container during the drying stage), and **c)** cross-section. **d)** EDS element identification of Zn. **e)** AFM characterization of the front and back side of the recycled ACICC membrane.

The electrochemical behavior is also very distinct compared to pristine membrane (**Figure 7.6**). We need to take into consideration the contribution of carbon and porous ZnO particles trapped within the membrane, as they create new interfaces. In particular, the ZnO PNPs exhibit a high surface reactivity, due to their large active surface area and porous morphology that is filled with electrolytic species, working as electrochemically active sites, where EDLs form and electrochemical reactions take place. These observations led us to the proposed ECM depicted in **Figure 7.6**b, which produced a good fitting to the experimental data. This ECM has already been reported in the literature.[31]

As shown in **Figure 7.6**c,e, although the capacitance of the recycled membrane is slightly lower compared to the pristine one, the σ_i and maximum frequency at which the EDL formation occurs are substantially higher, reaching average values in the order of 15 kHz and 0.25 mS cm^{-1}, respectively. The incorporation of inorganic fillers, such as ZnO particles, into gel electrolytes has been reported to be a promising way to enhance the ionic conductivity by developing additional conductive pathways.[365]

CV measurements reveal redox reaction peaks in the same range of voltages applied to operate the printed transistors on the recycled membrane under study, meaning that the devices can operate in mixed operating mode (field-effect and electrochemical doping mode) (**Figure 7.6**f).

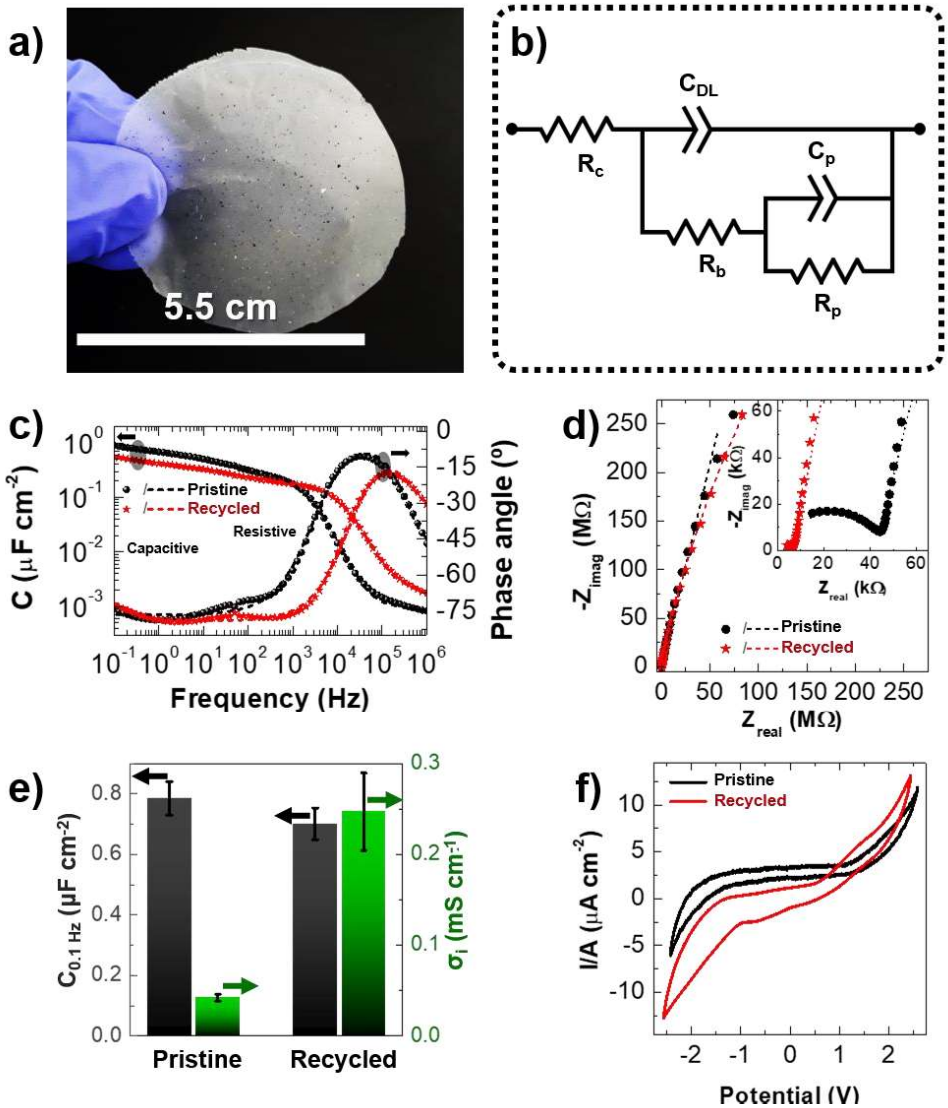

Figure 7.6. Electrochemical characterization of the recycled ACICC membrane. **a)** Photograph of the recycled ACICC membrane. **b)** ECM used for data fitting, where R_c, R_b, R_p, C_p, C_{DL} correspond to contact resistance, bulk resistance, pore resistance, pore capacitance, and interface double layer capacitance, respectively. **c)** Capacitance and phase angle as a function of frequency, and respective **d)** nyquist plots for the pristine and recycled ACICC membrane, using carbon/membrane/carbon structure with an active area of 1 mm^2. The symbols and the dashed lines denote the experimental and the fitted data, respectively. **e)** Comparison of capacitance and σ_i for the pristine and recycled ACICC membranes (the data points show the average and corresponding errors bars obtained from five samples). **f)** Comparison of the CV curves of the pristine and recycled membrane for electrochemical cell with carbon/membrane/carbon layered structure.

The recycled ACICC membrane was successfully reused as gate dielectric in printed ZnO transistors, working at low-voltages with higher hysteresis and slightly lower performance compared to the pristine one (**Figure 7.7**). The large counterclockwise current hysteresis behavior indicates the existence of a memory effect, being capable of storing electrical information.[36,273] This feature can be exploited in neuromorphic systems capable of mimicking human brain activity as they can realize artificial neurons and synapses.[366]

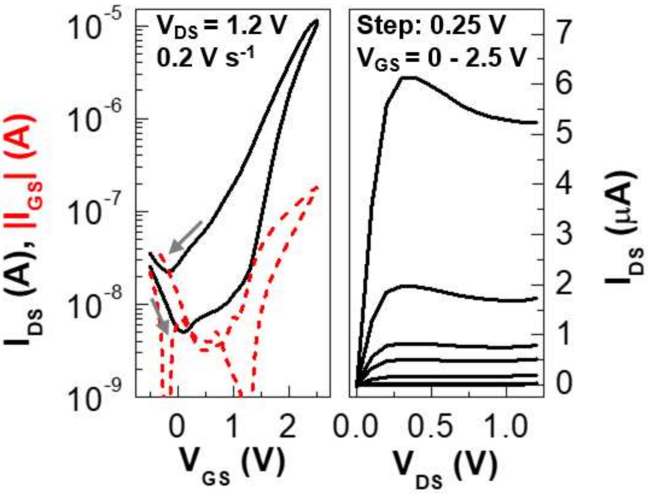

Figure 7.7. Electrical performance of screen-printed ZnO transistors fabricated on the recycled membrane. I_{DS}–V_{GS} curve and respective I_{DS}–V_{DS} curve (the step for the V_{GS} was 0.25 V, starting from -0.5 up to 2.5 V), collected with a V_{GS} scan rate of 0.2 V s^{-1}. Arrows represent the sweep direction, whereas continuous and dashed lines correspond to I_{DS} and $|I_{GS}|$, respectively.

As summarized in **Table 7.2**, the devices exhibited a more significant variation in the electrical performance, compared to those printed on pristine ACICC membrane, which can be attributed to the large surface roughness. The performance of such devices can be significantly improved by performing better filtration of the remaining conductive carbon material. Despite this deviation in the device metrics, they exhibit an electrical modulation of almost three orders of magniture with μ_{Sat} of 4 cm^2 V^{-1} s^{-1} and S_S of 0.5 V dec^{-1}, demonstrating that sustainability and performance can go hand-in-hand.

Table 7.2. Comparison of the electrical parameters of the printed ZnO NCGTs using pristine or recycled ACICC membranes. The values show the average and corresponding standard error of the mean obtained from twenty-five and ten devices gated by pristine and recycled membranes, respectively (V_{DS} = 1.2 V, V_{GS} scan rate: 0.2 V s^{-1}).

ACICC membrane	V_{ON} [V]	I_{OFF} [nA]	I_{ON} [µA]	$I_{ON/OFF}$ [×10^3]	S_S [V dec^{-1}]	μ_{Sat} [cm^2 V^{-1} s^{-1}]$^{a)}$
Pristine	0.37 ± 0.04	4.69 ± 0.58	11.2 ± 0.78	3.48 ± 0.47	0.37 ± 0.01	27.1 ± 1.56
Recycled	0.31 ± 0.10	4.34 ± 0.59	3.49 ± 0.82	0.88 ± 0.19	0.45 ± 0.03	4.04 ± 0.91

[a)] Mobility calculated using the capacitance values extracted directly from the EIS data at 0.1 Hz.

7.3. Adding value to cork wastes

Throughout this chapter, we demonstrated the remarkable synergy between cellulose and sustainability. Interestingly, these concepts are not limited to cellulose and can be further extended to other naturally occurring materials, using similar processing strategies, as further demonstrated.

When selecting raw materials intended to be reengineered into an innovative and sustainable class of materials with appealing functionalities, beyond the criteria that they must fulfill regarding abundancy and renewability, an additional interest arises concerning the possibility of reinventing already processed raw materials that did not find applicability. Therefore, a paradigm shift of reusing and recycling wastes from industry, especially those derived from nature, can fuel a new source of raw materials towards a more circular economy.[1] A proper waste management through reusing and reengineering reduces the stress on the environment as it eradicates the activities related to resource exploitation, thus minimizing chemical and energy consumption.

In this regard, an important issue that cork industry is currently dealing is the huge amounts of industrial waste materials, such as cork powder, scraps, and granulates, that are obtained from cork processing stage or during the quality control phase. These residues are mostly generated from cork stoppers industry, representing 20–30% of the total annual cork production in Portugal that is estimated around 100000 tons (≈50% of the world's total cork production).[367–371] The final use of these residues are mainly as burning fuel for energy production, finding no other commercial value.

Hence, valorization of cork byproducts is of high interest, and can be achieved by either exploring them in their natural form, without further modification, as reinforcement or filler agents for the development of cork-based composites or through the development of suitable processing methodologies to extract valuable chemical components.[368] Regarding the latter strategy, the one-of-a-kind chemical composition of cork deserves especial focus as it gives unique properties, that if explored individually can have a better use for certain applications. Yet, a better understanding of the interest behind cork, which is strictly related to its origin, composition, and morphological arrangement, and how it can be a perfect ally for the purpose of sustainability, must be addressed.

Cork is a natural, biodegradable, renewable and sustainable biocomposite raw material that can be 100% reused and recycled, constituting one of the most important economic sectors in Portugal.[372] It is stripped from the outer bark of the cork oak tree (*Quercus Suber* L.) that grows mostly in Mediterranean climates, where Portugal covers the world's largest cork oak forest area (one third of the total cork oak forest area of 2.1 million hectares).[373] The harvesting of cork is performed periodically every 9 years without felling nor damaging the tree, unlike wood, whose bark undergoes a self-regeneration process.[368] Furthermore, cork offers additional environmental benefits, including its capability of capture and retain carbon dioxide that is improved with the harvesting process (carbon dioxide sequestration is up to five times more efficient in harvested cork oak tree than unharvested), making it a formidable ally against climate change with the help of mankind's invervention.[373,374]

Microscopically, cork consists of suberin, a natural aliphatic-aromatic cross-linked polyester, as a major cell wall structural component (30–50 %) with a porous alveolar microstructure composed of closed, hollow, and thin-walled pentagonal or hexagonal honeycomb cells (**Figure 7.8**c), with a few micrometers wide, that contain in their interior an air-like gas (≈80 % of its volume).[368,374–376] Other compounds are identified in its chemical composition, such as lignin (15–30 %), polysaccharides, including cellulose and hemicelluloses (6–25 %), and extractives (8–20 %).[368,372,375,377,378]

The unique composition and cellulose structure of cork endows several fascinating properties, such as good thermal, electrical and acoustic insulation, low density (120–240 kg m^{-3}), impermeability to liquids and gases, resistance to fire and high temperatures, high-friction resistance, elasticity, compressibility, and significant chemical and microbial resistance.[372,373,378–381] This set of properties are the reason for the numerous applications of cork ranging from wine stoppers, textiles, packaging, flooring, absorption of pollutants, heat shields of spacecrafts to construction structures and automobile components.[373,382,383] Yet, cork is far to be limited to such applications and new approaches have been developed to take advantage of cork and its valuable components, such as suberin.

Suberin is exceptionally interesting as it is very abundant in cork, it is responsible for the majority of the properties of cork, and it plays the role of a protective hydrophobic barrier.[384] Several methods have been reported in the literature to promote its depolymerization and simultaneous isolation from cork, which involves extensive ester bond cleavage through alkaline methanolysis with sodium methoxide, calcium oxide methanolysis, aqueous alkaline hydrolysis, or ionic liquids (cholinium hexanoate) that release monomeric and/or small oligomeric constituent.[370,379,382,384,385] This hydrophophobic polyester component can serve as building block for new macromolecules and materials with interesting properties.[368,370,385] Recently, Garcia and co-authors[386] demonstrated a suitable application for suberin films obtained from ionic liquid cholinium hexanoate depolymerization method, which are moderately hydrophobic, waterproof, and biocompatible and show bactericidal and anti-biofouling properties, making them suitable for clinical usage.

Contrarily to this trend of understanding the structure and complex chemical composition of suberin, little efforts have been done to find suitable applications for this material. This served as motivation for two Master Thesis entitled "Iontronics with cork" and "Cork as a raw material for antibacterial membranes and fibers", developed by António Além, and Hélder Alves, respectively, under my co-supervision. Both works were focused on finding alternative ways to give a second life to wine cork stoppers, while bringing new insights to advanced functional materials based on cork components and their application in the field of electronics or as antibacterial agents.

Learning from the previous results obtained in this PhD work using the aqueous alkali salt/urea dissolution system of cellulose that is suitable for the preparation of ionic conductive materials, this approach shares some resemblances with the alkaline hydrolysis process used for cork depolymerization.[382] Therefore, this method was adapted to develop electrolytes based on cork components, as it assists in the depolymerization of suberin structures, by breaking ester linkage between carboxylic and hydroxyl groups existing in the aliphatic and aromatic chains, while affecting the hydrogen-bonded structure of the polysaccharides.

To do so, cork stoppers, collected from different wine brands (**Figure 7.8**a), were recycled by grinding with a domestic mixer grinder, and the recycled granulates resulting from this process were sieved down to a powder with approximately 500 μm in size (**Figure 7.8**b). The obtained cork powder was sequentially washed in boiled ethanol, and then boiling deionized water to expand and collapse the honeycomb-like morphology of cork, while removing its impurities, and finally dried at 100 ºC.

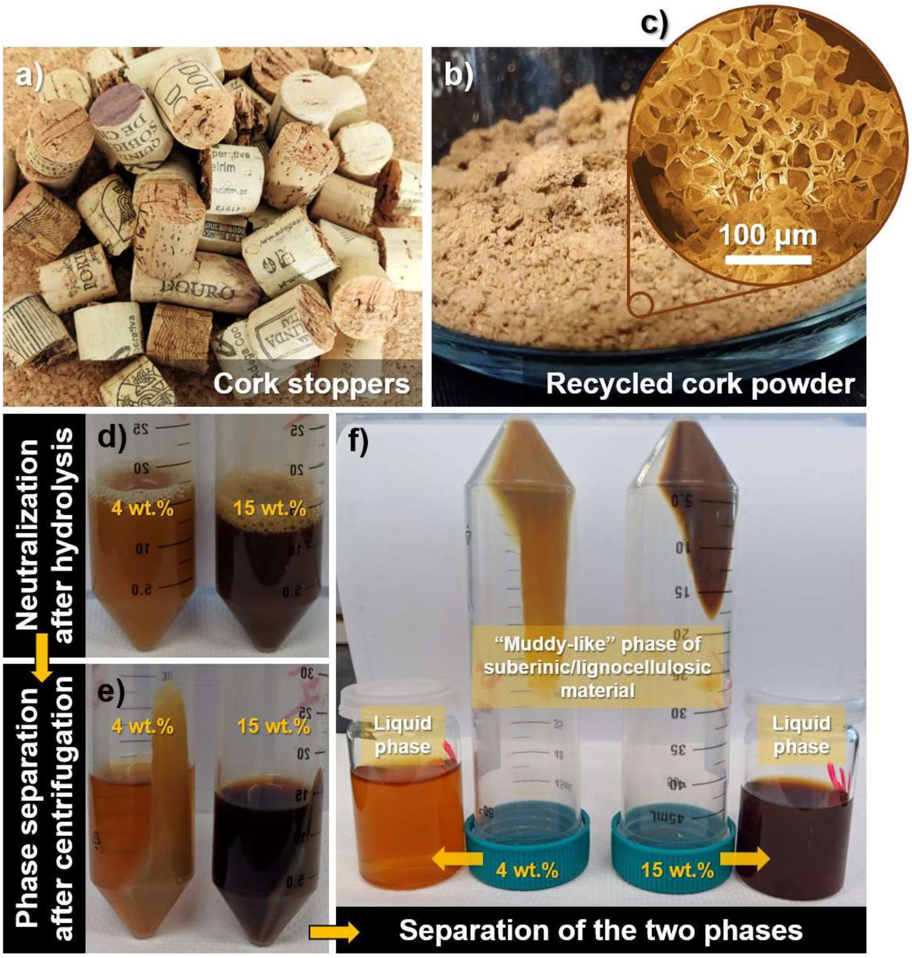

Figure 7.8. Schematic representation of the depolymerisation process used for cork. **a)** Photograph of the collected cork stoppers. **b)** Cork powder obtained after sieving the recycled cork stoppers granulates with a 500 μm mesh. **c)** SEM image of the obtained cork powder. **d)** Resulting solutions after hydrolysis of cork for a starting amount of 4 or 15 wt.% in aqueous LiOH/urea solvent system and neutralization with acetic acid. **e)** Precipitation of a "muddy-like" phase after performing a centrifugation step. **f)** Separation of the "muddy-like" material from the liquid phase.

Contrarily to the low-temperature dissolution method of cellulose explored in this work, the cork powder was fully processed at RT conditions as it yields a faster solubilization of cork. As illustrated in **Figure 7.8**d-f, the processing strategy consists of mixing a certain amount of cork powder with the previously prepared LiOH/urea/water solvent system (4.6/15/80.4 weight ratio) under vigorous stirring at RT, until its complete solubilization in a homogeneous brownish solution (≈ 1 day). A neutralization step was performed with the addition of acetic acid under stirring, and shortly after concluding this step and stopping the stirring process an insoluble “muddy-like” by-product started accumulating at the bottom of the flask. A centrifugation step was performed to optimize and accelerate the phase separation between the clear brownish liquid and the deposited “muddy” phase, which were then collected to further study.

Looking at the FTIR spectra in **Figure 7.9**, the pre-treatment performed on the recycled cork powder does not affect its composition, showing the typical characteristic peaks of cork associated to suberin (2915, 2850, 1733, 1260, 1153 and 719 cm^{-1}), lignin (1508, 848, and 817 cm^{-1}), and polysaccharides (1089 and 1029 cm^{-1}).[370,379,381,382,384,387] Furthermore, the spectra display the broad band between 3000 and 3700 cm^{-1} that is associated with the stretching vibration of hydroxyl groups and can be attributed to carboxylic acids and alcohol groups.[370,382,384]

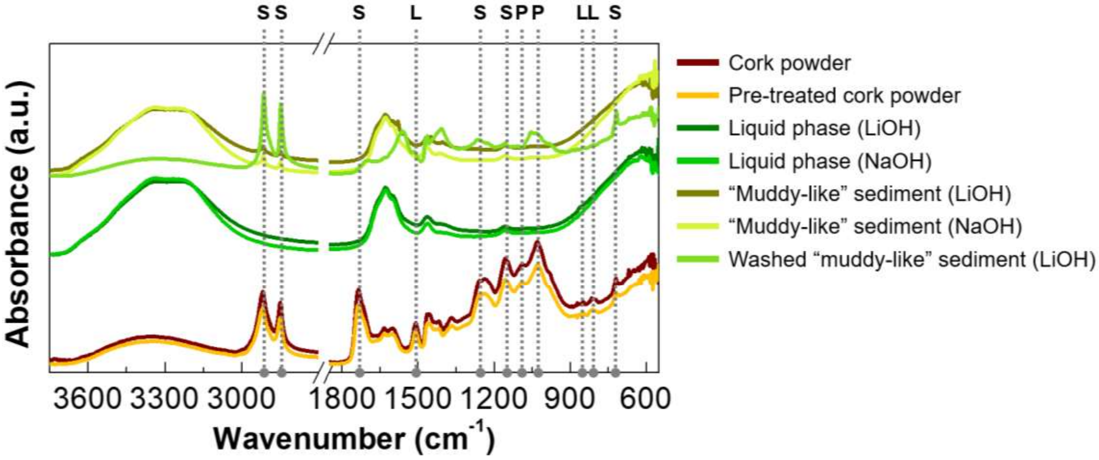

Figure 7.9. FTIR spectra of the cork raw materials (before and after perfoming the pre-treatment in ethanol and water and extracted materials from the depolymerization process of cork powder (15 wt.%) in aqueous alkali salt (LiOH or NaOH)/urea solvent system. The peaks assigned for suberin (S), lignin (L), and polysaccharides (P) are represented by dotted vertical lines.

Comparing the characteristic peaks of cork with the spectrum of the filtered liquid phase, obtained after performing dissolution/depolymerization in the aqueous LiOH/urea solvent system and neutralization with acetic acid, it is clear that all the peaks associated with the cork components disappeared, except the one at 1153 cm^{-1} that can be related to suberin, corresponding to asymmetric C–O stretching vibration.[370] Thus, this suberinic liquid material is mainly composed of a “soap” of monomers obtained from the several components that constitute the cork raw material. However, as also observed in the FTIR spectra of the developed CICHs (**Figure 4.3**e), the visible suberinic peak can be overlapped with a band assigned for rocking vibration of amino group, and this theory is reinforced due to the presence of a band between 1800 and 1400 cm^{-1}, which can be attributed to Amide I, Amide II, and Amide III of urea molecules.[308,309]

On the other hand, the “muddy-like” sediment, collected from the bottom of the flask, is richer in suberinic material, as evidenced by the smalls peaks at 1153, 2848 and 2915 and cm^{-1}, being the latter two attributed to the long aliphatic chains of suberin, accounting for symmetric and asymmetric C–H stretching vibrations, respectively.[370,376,379] The disappearance of the band at 3000–3700 cm^{-1}, and a remarkable increase of the peak intensity attributed to suberin at 2915 and 2850 cm^{-1} is observed in the sample obtained after washing the “muddy” material with water to remove remnants of the liquid phase and reagents. Furthermore, there is a resurgence of other suberinic peaks at 1733, 1260, and 719 cm^{-1}, corresponding to the vibration of carbonyl groups typical of esters, symmetric C–O stretching, and C–H bend associated with vinyl groups, respectively, as well as those associated to lignin at 1508 cm^{-1} and polysaccharides at 1029 cm^{-1}.[370,379,382]

A comparison was also carried out between LiOH and NaOH to address the influence of alkali ionic species in the depolymerization of suberin. The overall spectra obtained for the samples prepared from hydrolysis with NaOH, which is a “greener” and less expensive alkali salt, are very similar to those prepared with LiOH, thus being also a suitable approach to exploit suberin depolymerization.

To fully explore the materials extracted from cork, the ionic properties of the extracted liquid phase were explored to develop a freestanding electrolyte membrane suitable to be used as electrolyte-gate in printed EGTs. Considering the suberinic-based composition of both extracted materials, they were also investigated for antibacterial applications.

Regarding the first set of applications, the suberinic liquid phase was left to dry at RT in a glass container yielding a highly adhesive, brownish “resin-like” material (**Figure 7.10**a). Still, to make it robust enough, CMC was added to the solution prior the neutralization step aiming to obtain freestanding membranes, similarly to what was done in the preparation of the ClCH stickers (**section 4.1**). For an amount of 5 wt.% of CMC (relative to the total amount of solution), stretchable, moldable and sticky membranes are obtained (**Figure 7.10**b), which can be conveniently shaped according to the need as the developed cellulose-based electrolyte stickers.

As shown in **Figure 7.10**c, the obtained composite membrane exhibits interesting electrochemical properties to be used as electrolyte-gate material in transistors, displaying large EDL capacitance (≈8 $\mu F\ cm^{-2}$) and high ionic conductivity (≈10^{-4} $S\ cm^{-1}$), being both electrochemical parameters estimated from the fitting of the experimental data with the Dasgupta’s ECM (**Figure 4.7**a).

As a proof-of-concept, EGTs were screen-printed on a commercial sheet of cork textile from Corticeira Viking Lda to investigate the potential use of this material also as substrate for electronic applications, while using the developed composite membrane as electrolyte layer. This type of substrate was already reported in our research group by Figueira and co-authors,[284] who demonstrated for the first time its successful application, without any previous surface treatment, for the fabrication of fully screen-printed ZnO UV photodetectors.

Screen-printed EGTs with a channel width of 890 µm and length of 319 µm were fabricated in the same conditions as mentioned in **section 2.3.3**, using the C3Z40 ink to pattern the semiconducting layer. However, considering the non-regular surface of cork, the semiconductor layer was printed before the carbon electrodes. For comparison purposes, the electrical performance of the EGTs was compared with a device gated by Li-ClCH sticker (L100 hydrogel membrane).

Figure 7.10d shows the electrical performance of the printed transistors on cork, disclosing a fully functional low-voltage device mostly composed of cork-based materials in its composition. As verified in **Table 7.3**, preliminary results point to an inferior performance when using cork as a substrate in comparison with office paper, which can be attributed to the defective and slight hydrophobic behavior of cork's surface. Besides, the suberinic composite electrolyte revealed to lead to devices with poorer performance in comparison with the cellulose-based electrolyte, yielding devices with an electrical modulation that does not exceeds the three orders of magnitude.

Apart from this application, the antibacterial effect of the suberinic materials obtained after alkaline hydrolysis of cork (suberinic liquid phase and suberinic/lignocellulosic “muddy-like” paste) was investigated against gram-positive *Staphylococcus aureus* (ATCC® 6538 ™) and gram-negative *Escherichia coli* (ATCC® 8739™) using the agar well diffusion method. The inhibition zone diameters formed around each well were measured with a ruler to evaluate the antibacterial activity.

Figure 7.10e-g demonstrate that the extracted materials from cork exhibit antibacterial activity, which is in accordance to literature.[386,388] The inhibition of bacteria growth is improved by increasing the amount of cork used for suberin depolymerization, as evidenced by the enlargement in the blurred zones formed around the wells. Yet, different behaviors in the antibacterial activity were observed in the suberinic materials. While the suberinic liquid phase displays antibacterial activity against both types of bacterias, showing antibacterial effect even for low amounts of cork (≤10 wt.%) against *Escherichia coli*, the suberinic/lignocellulose paste showed a poor intervention in the inhibition of bacteria growth, especially to *Escherichia coli*. On the other hand, the washed suberinic/lignocellulose paste did not exhibit any antibacterial activity, despite being the sample that revealed the presence of several suberinic functional groups. Therefore, alternative assays for screening and/or quantifying the antibacterial response must considered.[389]

For comparison, the influence of the addition of ZnO in the antibacterial activity was investigated, as it is well-known its antibacterial features against the bacterias under study.[390–392] For such purpose, suberinic materials were also extracted from alkaline hydrolysis depolymerization process assisted by ZnO, using a small amount of commercial ZnO NPs that was mixed with the solvent system (ZnO/LiOH/urea/waster: 0.5/4.6/15/79.9 wt.%) prior suberin depolymerization. The results show the beneficial contribution of ZnO in the antibacterial activity against both bacterias, creating a clear inhibition zone.

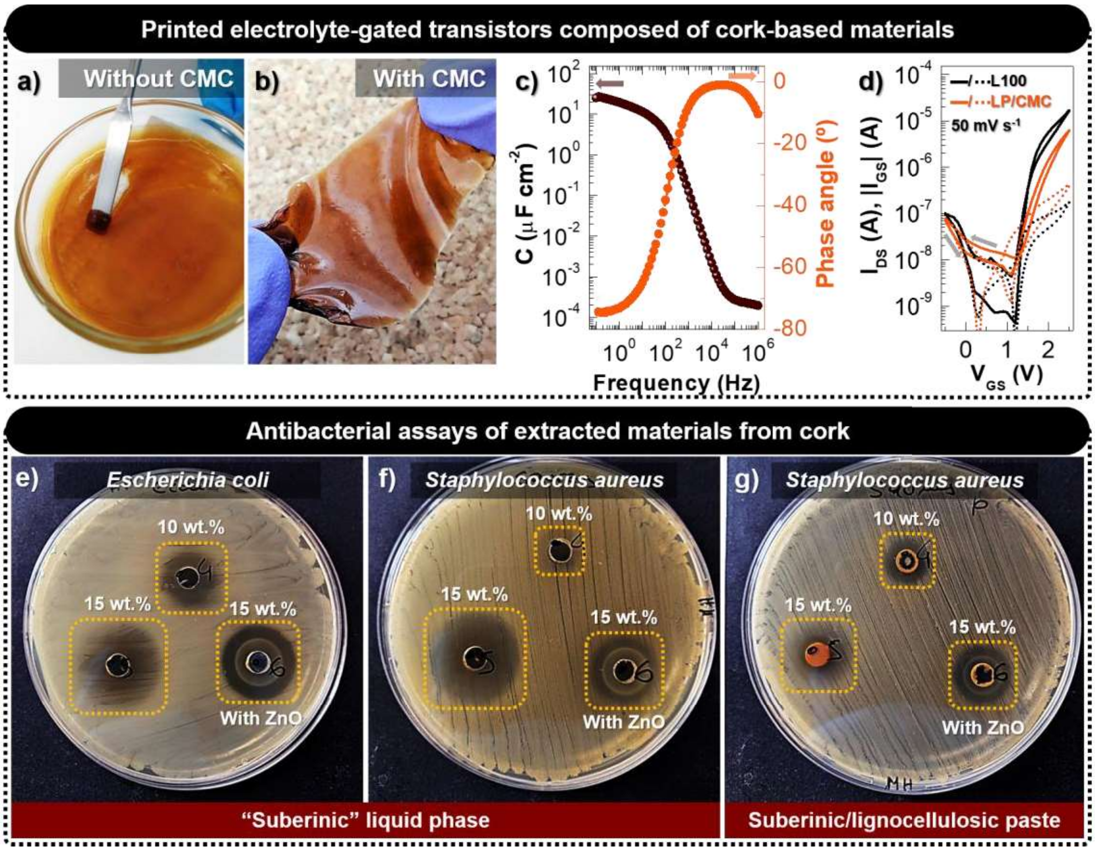

Figure 7.10. Features of the extracted materials from cork raw material and their potential applications. Photographs of the **a)** "resin-like" material obtained after drying the suberinic liquid phase extracted from cork, and of the **b)** developed composite membrane composed of a mixture of liquid phase and CMC (LP/CMC). **c)** Capacitance and phase angle as a function of frequency for LP/CMC membrane using stainless-steel discs with an active area of 1 cm^2. **d)** Comparison of the cyclic I_{DS}–V_{GS} curves of the fabricated screen-printed CMC/ZnO NPs EGTs fabricated on cork textile substrate, using LP/CMC membrane or ClCH membrane (L100 hydrogel) as electrolyte-gate, collected at a fixed V_{DS} of 1.2 V and V_{GS} scan rate of 50 mV s^{-1}. Arrows represent the sweep direction, whereas continuous and dashed lines correspond to I_{DS} and $|I_{GS}|$, respectively. Antibacterial assays: suberinic liquid phase against **e)** Escherichia coli, and **f)** Staphylococcus aureus, and also **g)** "suberinic/lignocellulosic" paste against Staphylococcus aureus. The extracted suberinic materials were obtained from alkaline hydrolysis depolymerization process, with or without ZnO, using different amounts of cork powder (10 or 15 wt.).

Table 7.3. Comparison of the electrical parameters of the printed ZnO EGTs gated by the developed suberinic-based composite with those gated by Li-ClCH electrolyte (V_{GS} scan rate: 50 mV s^{-1}).

Electrolyte	V_{DS} [V]	V_{ON} [V]	$I_{ON/OFF}$	S_S [V dec^{-1}]	μ_{Sat} [cm^2 V^{-1} s^{-1}]$^{a)}$
LP/CMC	0.8	1.0	1.41 × 10^3	0.27	0.41
L100	1.1	1.2	9.52 × 10^3	0.09	2.23

$^{a)}$ Mobility calculated using the capacitance values determined from the data fitting of the EIS measurements using Dasgupta's ECM.

The preliminary results obtained for the extracted suberinic materials, using recycled cork stoppers as raw material, bring a new light for novel fields of research by exploring their application in packaging with antibacterial capacity, which provides an interesting solution to prolong the lifetime of perishable food, while respecting current environmental concerns.

Chapter 8

General conclusions and new directions

8. General conclusions and new directions 151

8.1. Main achievements 152

8.1.1. Screen-printed ZnO semiconducting films with RT functionality 152

8.1.2. Cellulose-based ionic conductors: from stickers to substrates 153

8.1.3. Iontronic devices on paper or "paper-like" substrates 153

8.1.4. Sustainable end-of-life management 156

8.2. Future perspectives 157

8.2.1. Smoother cellulose-based (nano)paper substrates 157

8.2.2. Submicrometric channel lengths 158

8.2.3. Environmental stability 158

8.2.4. Low-temperature sintering of TMOS materials on paper 158

8.2.5. From personal fabrication to upscaling printed electronics based on cellulose materials 159

8.2.6. Printed cellulose-based ring oscillators with multi-responsiveness 160

8.2.7. Future prospects for suberinic-based composites 160

8.1. Main achievements

In summary, several strategies were addressed in line to a sustainable design thinking concept focused on drawing a path for electronics to go “green”. The methodology adopted considers the exponential growth of new technologies in the field of electronics, which are affordable and readily accessible to individuals, together with a consumerist mentality, fed mostly by mass media and advertisements that encourages consumers to replace existing products with new ones.

To avoid the negative outcome for the environment and human health in a long term, from an overexploitation of resources as well as unproper management of e-waste, the development of novel nature-based engineered functional materials combined with sustainable and economically efficient processes are among the great challenges for the future of mankind. Furthermore, sustainability, flexibility, and low-power consumption are key features to meet the growing requirements of increasing simplicity and multifunctionality of low-cost, disposable/recyclable smart electronic systems in the emerging area of the IoT.

Within this context, cellulose was chosen as the key natural raw material in this PhD project to integrate a new class of “green” electronic devices to impact the upcoming generations, while fulfilling the sustainability concept. Yet, far more than technological advances, a societal evolution by means of an environmental conscious mindset, focused on reusing, repairing, and recycling, will ultimately define the course of our future.

As summarized in the following sections, the main achievements of this work rely on the development of cellulose composite materials with different functionalities (semiconductor or ionic conduction), using scalable solution-based procedures compatible with R2R principle, which were successfully integrated in recyclable, fully printed, flexible iontronic circuits with low-voltage operation.

8.1.1. Screen-printed ZnO semiconducting films with RT functionality

Printing of TMOS materials to integrate into flexible, fully printed transistors and circuits is far to be a simple process, as these materials usually require high annealing temperatures that are not compatible with conventional paper substrates.

In this work, screen-printable highly loaded inks based on ZnO commercial NPs (40 wt.%) were formulated. With only one printing step, it is possible to pattern relatively smooth, continuous, thick, and densely percolated films on the heavily rough and porous surface of non-coated standard office paper, that display semiconducting functionality at RT. Due to the better film-forming ability of CMC compared with EC, water-based inks composed of ZnO PNPs were also formulated. By replacing the small-sized ZnO NPs with ZnO PNPs, their elongated size forms a percolation network at considerably lower amounts at the cost of the resulting films exhibit rougher surfaces.

To put the attributes of the formulated inks in perspective, these inks were used to pattern the active semiconducting channel in flexible screen-printed transistors and integrated circuits.

8.1.2. Cellulose-based ionic conductors: from stickers to substrates

A new generation of versatile flexible, adhesive, and highly conformable regenerated cellulose hydrogel electrolytes with high ionic conductivity (≈10^{-4}–10^{-3} S cm^{-1}), large specific capacitances (>1 μF cm^{-2}), and reasonable transparency (>80 %) were successfully demonstrated. The reported CICHs were designed and engineered through a simple, fast, low-cost, and environmental-friendly dissolution method of MCC at low temperature using aqueous alkali hydroxide (LiOH and/or NaOH)/urea solvent system. The cellulose solution was combined with CMC, as a mechanical strengthener, followed by the regeneration with acetic acid and simultaneous ion incorporation into the cellulose matrix. Freestanding membranes were prepared by shear-casting.

Due to their robustness and sticky surface, as well as appealing electrochemical performance, the developed CICH membranes can be supplied in the form of conformable stickers, easily molded as plasticine, and thus applied “on-the-fly”, through a “cut, transfer and stick” process, making them suitable for integration in low-power flexible iontronics.

Although the use of NaOH is a more environmentally friendly and less expensive alternative compared with LiOH, the hydrogels prepared from NaOH approach exhibit a rougher surface, retain less water, and inferior electrochemical performance compared to those prepared with LiOH or mixtures of both alkali hydroxides. Beyond the lower dissolution efficiency of cellulose in solvent systems mostly composed of NaOH, which requires an additional freeze-thawing step to enhance cellulose solubility, one additional side back is the poorer air-stability overtime of the resulting membranes. This is due to the formation of urea dendrites that lead to a gradual loss of transparency, conformability, and adhesion of the membranes, while becoming more brittle.

Despite the appealing features demonstrated by the CICHs, their soft, sticky, and easy deformable surface, which is influenced by the environmental conditions that affect the amount of water retained into their structure, is not suitable to host electronic systems. To address this issue, an all-cellulose nanopaper composite was developed.

The underlying science of the engineered nanopaper composite is based on the merging of the intrinsic mechanical robustness, thermal resistance, and optical transparency of micro/nano-fibrous cellulose nanopaper, used as reinforcing agent, with the superior electrochemical performance and environmental stability of the Li-CICHs. These materials yield an ionic conductive nanopaper composite with tailored properties, including robustness, smooth surface, high-capacitance, and acceptable transparency (>80 %), which are not possible to achieve when used solely. Thus, the “dual-functionality” (support and dielectric) of the engineered nanopaper composite has revived a compelling concept of low-power paper electronics.

8.1.3. Iontronic devices on paper or “paper-like” substrates

The appealing electrochemical properties demonstrated by the developed ionic conductive membranes make them suitable for application as electrolyte-gate in transistors and circuits. Two types of electrolyte-gating strategies were adopted, either based on the developed CICH stickers, which are directly applied on the devices using a transfer-lamination procedure, or the developed "paper-like" active substrate (ACICC membrane) that works not only as the support but also as an "active" constituent of the devices themselves.

Conventional high-vacuum deposition techniques were used in the first place to fabricate the EGTs, through the deposition and patterning of pure, thin, and high-quality evaporated electrodes and sputtered benchmark amorphous IGZO channel layer, either on glass or on cellulose-based substrates (multilayer-coated paper or the developed ACICC membrane). A planar configuration was adopted to simplify the devices' fabrication and integration in circuits.

The produced planar IGZO EGTs on glass gated by the Li-CICHs, with an optimal proportion of MCC:CMC (1:1 weight ratio), displayed excellent electrical performance at low operating voltages (<2 V), showing mixed operating mode (field-effect and electrochemical doping mode), and good environmental stability after one month of storage at ambient conditions, reaching an $I_{ON/OFF}$ of 10^6, a S_S lower than 0.2 V dec^{-1} and large μ_{Sat} of 26 $cm^2\ V^{-1}\ s^{-1}$. A slight loss of electrical performance was observed in the EGTs fabricated on the reasonably smooth, flexible, and impermeable multilayer-coated paper substrate, due to the poorer quality of the deposited films. Still, these devices exhibit a good performance ($I_{ON/OFF}$ >10^4, μ_{Sat} >3.4 $cm^2\ V^{-1}\ s^{-1}$, and S_S <0.26 V dec^{-1}) under operating voltage below 2 V, and under electrical stress. Furthermore, they can operate at a bending radius down to 5 mm, and their maximum operation frequency is up to 100 Hz.

Basic low-voltage (<2.5 V) NOT gates were demonstrated by combining the manufacturing procedures used for the fabrication of the planar CICH-gated IGZO EGTs on paper with ubiquitous and portable calligraphy accessories. The use of handwriting techniques allows the easy and fast patterning "on-the-fly" of conductive paths and graphitic load resistances of the circuits on a sheet of office paper, where the EGTs are attached. The inverters can reach a maximum |gain| of 2.4 for low V_{DD} values of 1 V, while the dynamic performance does not exceed 20 Hz.

In alternative, both paper substrate and hydrogel electrolyte can be replaced by a single intrinsically ionic conductive cellulose-based substrate. The fabricated sputtered IGZO NCGTs with staggered-bottom gate structure showed lower hysteresis, superior mobility values, remained functional after ageing nearly one year, although showing some signs of deterioration of the electrical contacts, and exhibited a faster switching speed around 250 Hz in comparison with the previous CICH-gated IGZO EGTs on paper. The overall improvement in the electrical characteristics is due to the adopted vertical configuration and better interface established between the thin inorganic layers and the smooth surface of the ACICC membrane.

To substantially decrease the manufacturing complexity and cost of the devices, solution-phase printing or handwriting techniques, compatible with R2R principle, offer competing advantages over conventional microfabrication techniques, towards flexible electronics, where cellulose-based composites and paper fit in. Within this context, the manufacturing/assembling processes involved in the fabrication of the printed EGTs and integrated circuits, which includes screen-printing technique, calligraphy tools and a transfer-lamination process, were strategically selected to offer freedom of design. Furthermore, the materials chosen for the different layers of the digital electronic circuits were fully processed and functional at temperatures near ambient conditions, and fit the compromise of low-cost, abundancy and environmental awareness.

The printed EGTs were fabricated with a planar configuration, using the formulated screen-printable ZnO-based inks to pattern the channel layer either on office paper, where the Li-ClCH works as gate dielectric, or directly on the developed AClCC membrane.

Despite the extremely rough and fibrous surface of standard office paper, the electrolyte-sticker has a key role in the performance of the fabricated planar screen-printed ZnO NPs EGTs, enabling their low-voltage operation (<2.5 V) with satisfactory electrical performance ($I_{ON/OFF} < 10^5$ and $\mu_{Sat} \approx 22$ cm^{2}V^{-1}s^{-1}), and under mechanical deformation (bending radius down to 15 mm). Still, this performance is only achieved for high amounts of small-sized ZnO NPs (40 wt.%), and the thick channel layer is destroyed under folding.

On the other hand, the elongated nanoplate-shape of the porous ZnO nanostructures, which exhibit higher aspect ratio and a larger active area for interaction with the ionic species from the electrolyte, results not only in a more direct percolation path for electron transport, due to the reduced nanoplates' thickness (<100 nm), but also in plane-to-plane contacts between the particles. Although the screen-printed CMC/ZnO PNPs films exhibit a considerably rougher surface compared with those with ZnO NPs, the electrical performance is almost comparable with the CMC/ZnO NPs films for half the amount of functional material in the ink (20 wt.% ZnO PNPs), which can be improved for higher contents of ZnO PNPs (≥30 wt.%). Such results demonstrate the benefits of using the developed electrolyte-sticker, since its highly conformable, smooth, and sticky behavior can overcome the undesirable surface roughness of the printed CMC/ZnO PNPs films, thus reducing charge trapping effects.

Considering the exceptional performance displayed by the devices prepared with C3ZPN30 ink, this ink was further explored in the successful fabrication of the first planar, fully screen-printed NCGTs with low-voltage operation and exceptional mechanical endurance. Compared to the electrolyte-sticker, the poorer conformability of the AClCC membrane to the intrinsically rough and porous surface of the ZnO PNPs creates additional interfacial defects, which in combination with the larger overlap between the AClCC membrane and electrodes, yield devices with inferior electrical performance. Still, the smooth surface of the AClCC membrane led to lower variation in the devices' performance, and the devices displayed a remarkable mechanical endurance upon folding stress that competes with the current state-of-the-art in the field of transistors gated by cellulose-based substrates, serving the purpose of flexible electronics.

A negative aspect of the use of ZnO as the channel layer of the fabricated printed EGTs concerns its lack of stability overtime (≈1 week), thus making these devices more suitable for disposable applications on-the-spot.

Regarding the dynamic performance of the printed ZnO EGTs, they can operate at switching speeds up to 10 Hz, which is mostly limited by the large dimensions of the channel length and planar configuration.

Flexible cellulose-based ZnO iontronic circuits, from simple inverters to “universal” logic gates (NOR and NAND gates), were also demonstrated for both types of electrolyte-gating strategy. In a similar way as the previous flexible IGZO inverters, the printed ZnO circuits were fabricated “on-demand” by connecting pencil-drawn load resistances and driving printed ZnO EGTs, using suitable printing tools. Although the fabrication of the printed NCGTs is simpler in comparison with the CICH-gated EGTs on paper, their integration in circuits using pencil-drawn load resistances is slightly more complex, as the ACICC membrane, unlike office paper, is not compatible with pencil drawing. Thus, the ACICC membrane is previously attached to an office paper platform, and thick carbon conductive tracks are draw with a pencil brush to establish the electrical connections between the NCGTs and the pencil-drawn resistive tracks on office paper. On the other hand, the screen-printed CICH-gated EGTs on office paper are readily integrated into circuits using pen-on-paper and pencil-on-paper approaches to establish the proper electrical connections and pattern the graphitic tracks, respectively.

Furthermore, additional functionalities can be incorporated into the circuits, by exploring the photo-electronic properties of ZnO under UV light exposure. Thus, photoswitchable ZnO circuits on paper were also demonstrated by connecting the fabricated drive ZnO EGTs with optoelectronic ZnO load resistances, capable to actively tune their electrical performance under UV light stimulus.

All the fabricated screen-printed ZnO circuits operate at low V_{IN} inferior to 3.5 V and reach gains suitable for signal amplification. Thus, they can serve as building blocks for more complex functions, while being powered by portable energy storage and/or harvesting systems, which makes them attractive for smart sensing applications and concepts such as the IoT.

8.1.4. Sustainable end-of-life management

The environmental impact of the developed composites and integrated devices was evaluated.

The CICHs can be reused and easily repaired if mechanically damaged. Interestingly, those prepared from NaOH approach, that are susceptible to the formation of urea dendrites, can be repaired through a rehydration process in humid environments. Such sustainable strategies avoid the full replacement of the devices in case of damage and overtime usage, thus extending their lifetime and durability. Besides, the hydrogels can be recycled by soaking them in water and a similar recycling strategy can also be applied to the ionic conductive substrates.

Due to the short lifetime of the printed ACICC-gated devices, they can be easily disintegrated in water to form a composite pulp that can be recycled and reused to produce new membranes to host iontronic devices, thus ensuring a resource-conscious mentality that fits into a circular economy model, where waste is treated as a resource.

These exciting results may usher in a new era of sustainable, low-power, foldable, printed biopolymer-based iontronic devices with simplified designs that combined with user-friendly, safe, low-cost, and non-complex manufacturing approaches and proper management of end-of-life devices, paves the way for the concept of DIY electronics without generating waste, as the materials involved in the whole process can be reused, healed, or recycled.

Furthermore, the possibility of using these strategies with other naturally occurring raw materials, such as cork, was successfully addressed. Motivated by the excessive waste of the cork industry along with the poor applicability found for cork materials besides the traditional applications, cork stoppers were reused and recycled to obtain a powder that was used as starting material for suberin depolymerization through alkaline hydrolysis. This process is identical to the one used for cellulose dissolution, but it is performed at RT conditions, thus being less energy demanding and simpler.

The extracted suberinic materials can be combined with CMC to yield stretchable and conformable membranes with suitable electrochemical properties to be used as electrolyte layer in printed EGTs, using a sheet of cork textile as substrate. The applications of suberin goes beyond electronics, finding also potential as antibacterial material for safe and hygienic packaging. Like cellulose, cork can be foreseen as an exceptional raw material with plentiful of potential for applications that will surpass its conventionality.

8.2. Future perspectives

Considering the results obtained throughout this work, there are still several challenges that remain to be addressed regarding the operation lifetime, interfacial surface roughness, dynamic response, as well as reliability and yield of the fabricated printed ionic-responsive transistors under focus to fabricate circuits that display more complex functions. Thus, this list of issues fuels another explosion of research activity focused on these optimizations.

Following all the proposed suggestions and contemplating the further advances in cellulose engineering, paper electronics and printed electronics, it is possible to predict a faster progress of these technologies way out of the laboratory towards their maturity, while keeping in mind the conquest of the market and be part of people's routine. This will in turn open new avenues to obtain flexible, low-cost, and disposable/recyclable printed transistors and circuits on cellulose-based substrates, either based on n-type or p-type semiconductors with high-mobility, able to operate at low-voltages with faster switching frequencies.

8.2.1. Smoother cellulose-based (nano)paper substrates

The first consideration is regarding the well-known challenges related to the surface of office paper when looking to more ambitious applications, as the ones demonstrated in this work, far away from its common use as a simple tool for taking notes. Planarization of fibrous standard office paper, without compromising its recyclability nor low-cost, or the use of highly smooth and less permeable nanocellulose-based paper or RCFs can display a key role to reduce its surface defects.[5,15,61,66,77,78,129,130,135–137,393] Such strategy is expected to enhance interface interaction with the oxide semiconductor, while the electrodes can be patterned with a better definition and superior resolution targeting maximum operating frequencies.

8.2.2. Submicrometric channel lengths

More importantly, there is a plenty of room to optimize the operation speed of the circuits towards GHz, by adopting transistors with vertical architecture instead of side-gate geometry, and by shortening the channel length dimensions to submicron scale. However, the latter strategy is one of the major challenges in printed electronics, thus limiting the switching speed to just some tens of Hz, as observed in this work.

Accordingly to what has already been reported in literature, two distinct approaches can be explored in future works focused on reducing the channel length, whether using SAP manufacturing technique,[203,248,249] which is based on chemical gapping processes, or by fabricating transistors with vertical source-drain configuration,[394,395] where the channel length corresponds to the thickness of the semiconducting layer.

8.2.3. Environmental stability

An easy approach to overcome the reasonably short lifetime of the fabricated TMOS devices consists of depositing a passivation layer (e.g. self-assembled monolayers, parylene-based polymers, poly(methyl methacrylate, photoresists, etc) to protect the TMOS material against the external reactive molecules in ambient atmosphere, block light exposure, and eliminate uncoordinated oxygen species from TMOS material, thus enhancing its stability.[319,346]

8.2.4. Low-temperature sintering of TMOS materials on paper

The intrinsic morphology of nanostructures and their propensity to agglomerate lead to surface roughness issues that can hinder the devices' electrical performance, even when using intrinsically smooth yet non-conformable ionic conductive substrates, such as the developed ACICC membrane. Therefore, low-temperature sintering can be an appealing approach that deserves special attention to address this issue, through the optimization of the percolation pathways between the ZnO particles, while creating a denser and smoother film, without compromising the integrity of the remaining functional layers nor the substrate.[15,177,178]

As mentioned in **section 1.2.3.2**, there is a boom of recent works that trigger different directions to follow when looking for low-temperature methods to aid in the sintering of TMOS materials, including microwaves, plasma, electrical voltages, and/or RT sintering using chemical agents.[15,148,158,177–179] The proposed low-temperature sintering techniques can certainly be extended to p-type TMOS materials to optimize their mobility values towards those typically obtained for high-performance n-type counterparts, envisioning their further application in integrated CMOS circuits that require both type of semiconductors.

8.2.5. From personal fabrication to upscaling printed electronics based on cellulose materials

The satisfactory results obtained at a lab-scale for the printed EGTs and integrated circuits, using solely user-friendly, low-temperature, sheet-to-sheet (S2S) manufacturing processes suitable to be used by non-skilled individuals, without requiring sophisticated facilities, raised a realistic introduction to the concept of DIY while booming creativity. In fact, we demonstrate how fun it can be, since an amateur in electronics can participate in all the fabrication stages of the developed iontronic devices by following basic instructions. Thus, the idea of designing, training, prototyping, or even developing personal electronic gadgets at home ("lab-at-home") is far to be farfetched, being only necessary for that purpose a compartment where we can find room to trigger our imagination, but also to accommodate and store the materials and tools needed to accomplish such ideas.

Despite the vision behind DIY idea, towards easy customization of electronic systems, this concept is limited to small volume of manufacturing and the process is mostly handmade. However, when looking for a complex level of integration of materials, components, and devices, we need to move to a fully automated production by large-scale R2R principle, where manual handling from printing to completion is avoided, to speed up the process, minimize error, and obtain a high volume of products, which in turn leads to extensive cost reductions.

Thus, considering the extreme importance of ensuring a reliable process with high yield, before transferring the developed technology from S2S to industrial R2R manufacturing environments, we need to implement a strategy that envision the optimization and upscaling of the EGTs' manufacturing process. To do so, the custom-made flatbed screen-printing station can be replaced by a semi-automatic screen-printer machine. Although this approach still relies on S2S principle, this is a significant step to take as it opens an opportunity to start distancing from lab-scale prototyping and get closer to pilot-scale manufacturing process using rotary screen printing, by having a better control over the printing parameters.

Furthermore, to ensure the patterning of high-resolution features using screen-printing technique, the polymeric mesh made of twisted yarns can be replaced by a non-woven, flexible, and highly defined metal plate that exhibit superior durability and endurance to hard conditions, although being more expensive.[172,396]

Regarding the step related to the deposition of electrolyte-gate stickers, instead of laminating individual hydrogel membranes one-by-one for each device, a single hydrogel membrane can be directly laminated to fit multiple devices alongside a row of an array of EGTs to make the manufacturing process easier and faster. Although such strategy minimizes the number of lamination steps to activate the partially manufactured EGTs, this approach can have a negative impact in the devices' electrical performance. This is due to the overlap between the electrodes and the electrolyte that is substantially increased when using such strategy, thus leading to an increase in off and leakage currents.

In line with these issues, a transfer/stamping process[11,141,153,397] can be an efficient and fast procedure to easily transfer multiple patterned thick membranes into individual EGTs in a single move. To do so, a macroscopic membrane formed on a donor substrate (glass) can be patterned through a mechanical cutting process. The excess of membrane is removed and reused/recycled, whereas the patterned membranes can be transferred to a reusable, conformable elastomer stamp with compatible adhesion. An alignment step is required between the stamp, where the individualized electrolyte-gate membranes are attached, and the receiving substrate that hosts the fabricated screen-printed devices. This ensures that in a single move the multiple patterned membranes are transferred during the stamping step to the devices in their precise positions. For faster and precise integration, a “pick-and-place” machine can be used to align, arrange, and transfer the stamp with the electrolyte membranes towards the desired place.

8.2.6. Printed cellulose-based ring oscillators with multi-responsiveness

The accomplishment of these suggestions will establish the road for the easy integration of several transistors into more complex circuitry, such as ring oscillators that can be realized by connecting in series an odd number of inverters, where the output of the last inverter is fed back into the input of the first one.[259]

To minimize circuits dimensions, the pencil-drawn graphitic load resistances can be replaced by a single transistor or a sensing component capable of tuning its electrical properties upon an external stimulus. Although this latter strategy was successfully explored in this work using ZnO UV sensors as photoswitchable load resistances, additional features can be added to a single circuit by exploring the multi-responsiveness of ZnO, as it also exhibits pyro-, thermo- and piezoelectric properties,[253,353] while enhancing the performance of the sensing devices.

The integration of these properties into smart-signal responsive systems capable of processing optical illumination, mechanical strain, and/or thermal inputs into electronic controlling signals, affords a reconfigurable platform that performs multiple logic operations by tuning the input states.[336,340,342,353,355,398,399] Furthermore, the incorporation of switchable sensing components into circuits can generate internal built-in electrical field that is enough to power them without any external bias voltage, which is extremely appealing in terms of power consumption.

8.2.7. Future prospects for suberinic-based composites

The preliminary results obtained for recycled cork stoppers as a sustainable raw material to extract suberin were very promising, serving as foundation for new research paths in the field of electronics, as well as safe and hygienic packaging. Hence, there is a lot of room for further development and optimization in future works.

In the first place, the methodology used for processing cork must be deeply investigated looking for a better understating of the influence of each component in the chemical composition of the resulting suberinic-based materials. The role of urea, alkali salt, and the influence of the acid used during the neutralization process is still unclear as how they affect the features of the components extracted from cork as well as their antibacterial properties. The latter property assumes particular interest considering the need for materials composites, either in the form of membranes, fiber mats, patterned or coated films, that can protect human health from bacterial infections. Thus, the realization of complementary antibacterial assays must be performed in the developed materials.

Chapter 9

Outputs

9. Outputs 163
- 9.1. Publications.. 164
- 9.2. Scientific conferences 165
- 9.3. Workshops and courses 166
- 9.4. Projects 166
- 9.5. Recognitions 166

A proper selection of the most relevant results obtained during the execution of the PhD activities resulted in the preparation of brief reports that were immediately converted into scientific papers, developed in co-authorship research. Furthermore, these works were also presented in scientific meetings as a helpful tool to share and acquire knowledge related to new research trends, advanced materials, and techniques that might impact our work.

A summary of all the publications, oral and poster presentations in national and international conferences is provided as well as their recognition.

9.1. Publications

Published work during PhD activities (8, +2 ongoing):

- **I. Cunha**, J. Martins, P. Ganga Bahubalindruni, J. Tiago Carvalho, J. Rodrigues, S. Rubin, E. Fortunato, R. Martins, and L. Pereira. Handwritten and sustainable electronic logic circuits with fully printed paper transistors (under revision in Advanced Materials Technologies);
- M. João Oliveira, **I. Cunha**, M. P. de Almeida, T. Calmeiro, E. Fortunato, R. Martins, L. Pereira, E. Pereira, H. J. Byrne, R. Franco, and H. Águas. Reusable and highly sensitive SERS immunoassay utilizing gold nanostars and a cellulose hydrogel-based platform (under revision in Journal of Materials Chemistry B);
- S. H. Ferreira, **I. Cunha**, J. V. Pinto, J. P. Neto, L. Pereira, E. Fortunato, R. Martins. UV-responsive screen-printed porous ZnO nanostructures on office paper for foldable electronics. Chemosensors (2021). doi: 10.3390/chemosensors9080192;
- P. Claro, A. C. Marques, **I. Cunha**, R. Martins, L. Pereira, J. M. Marconcini, L. H. C. Mattoso, and E. Fortunato. Tuning the Electrical Properties of Cellulose Nanocrystals through Laser-Induced Graphitization for UV Photodetectors. *ACS Appl. Nano Mater.* (2021). doi: 10.1021/acsanm.1c01453;
- P. Claro, **I. Cunha**, R. Paschoalin, D. Gaspar; K. Miranda, O. N. Oliveira Jr., R. Martins; L. Pereira, J. Marconcini, E. Fortunato, L. Mattoso. Ionic conductive cellulose mat by solution blow spinning as substrate and dielectric interstrate layer for flexible electronics. *ACS Applied Materials & Interfaces.* (2021). doi: 10.1021/acsami.1c06274;
- S. Nandy, S. Goswami, A. Carolina Marques, D. Gaspar, P. Grey, **I. Cunha**, D. Nunes, A. Pimentel, R. Igreja, P. Barquinha, L. Pereira, E. Fortunato, R. Martins. Cellulose: A Contribution for the Zero e-Waste Challenge. *Adv. Mater. Technol.* (2021) doi: admt.202000994;
- **I. Cunha**, J. Martins, D. Gaspar, P. Ganga Bahubalindruni, E. Fortunato, R. Martins, and L. Pereira. Healable Cellulose Iontronic Hydrogel Stickers for Sustainable Electronics on Paper. *Adv. Electron. Mater.* (2021). doi: 10.1002/aelm.202001166;
- P. Duarte, S. Pereira, **I. Cunha,** A. Pimentel, M. Dionísio, E. Fortunato, R. Martins, and L. Pereira. Cellulose-Based Solid Electrolyte Membranes Through Microwave Assisted Regeneration and Application in Electrochromic Displays. *Front. Mater.* (2020). doi: 10.3389/fmats.2020.00269;
- J. Tiago Carvalho, V. Dubceac, P. Grey, **I. Cunha**, E. Fortunato, R. Martins, A. Clausner, E. Zschech, and L. Pereira. Fully Printed Zinc Oxide Electrolyte-Gated Transistors on Paper. *Nanomaterials* (2019). doi: 10.3390/nano9020169;
- E. Fortunato, D. Gaspar, **I. Cunha,** M. Mendes, A. Vicente, H. Águas, A. Carolina Marques, A. Pimentel, D. Nunes, L. Pereira and R. Martins. Paper electronics: a sustainable multifunctional platform. *2018 76th Device Research Conference (DRC)* (2018). doi: 10.1109/DRC.2018.8442238.

List of articles under preparation/submission (4):

- **I. Cunha**, S. H. Ferreira, J. Martins, E. Fortunato, R. Martins, and L. Pereira. Foldable, recyclable iontronic cellulose nanopaper for low-power printed electronics (ready for submission);
- J. T. Carvalho, **I. Cunha**, J. Coelho, E. Fortunato, R. Martins, and L. Pereira. Energy storing textiles based on carbon yarns coated with in-situ regenerated ionic conductive cellulose (under preparation);
- **I. Cunha**, S. H. Ferreira, P. Grey, J. Martins, J. Pinto, A. Kiazadeh, E. Fortunato, R. Martins, and L. Pereira. Sensing light on paper: UV-responsive screen printed ZnO circuits on paper (under preparation);
- S. H. Ferreira, R. Huertas, **I. Cunha**, L. Pereira, V. Pereira, E. Fortunato, R. Martins. Adding value to ZnO-rich industrial residue nanopowder for multifunctional and zero-waste applications (under preparation).

Previous scientific publications that boosted the proposed research activities of this PhD work (3):

- **I. Cunha**, R. Barras, P. Grey, D. Gaspar, E. Fortunato, R. Martins, and L. Pereira. Reusable Cellulose-Based Hydrogel Sticker Film Applied as Gate Dielectric in Paper Electrolyte-Gated Transistors. *Adv. Funct. Mater.* (2017). doi:10.1002/adfm.20160675;
- P. Grey, D. Gaspar, **I. Cunha**, R. Barras, J. Tiago Carvalho, J. Rafael Ribas, E. Fortunato, R. Martins, and L. Pereira. Handwritten Oxide Electronics on Paper. *Adv. Mater. Technol.* (2017). doi: 10.1002/admt.201700009;
- R. Barras, **I. Cunha**, D. Gaspar, E. Fortunato, R. Martins, and L. Pereira. Printable cellulose-based electroconductive composites for sensing elements in paper electronics. *Flex. Print. Electron.* (2017). doi: 10.1088/2058-8585/aa5ef9.

9.2. Scientific conferences

Oral communications (3):

- **I. Cunha**, S. Ferreira, J. Martins, E. Fortunato, R. Martins and L. Pereira, “Foldable, recyclable iontronic cellulose nanopaper composite for low-power applications”. E-MRS Spring Meeting 2021, May 31th – 4th June, 2021, Online conference.
- **I. Cunha.** J. Martins, J. Rodrigues, S. Rubin, J.T. Carvalho, P. G. Bahubalindruni, E. Fortunato, R. Martins, L. Pereira; “Handwritten logic gates with flexible printed zinc-oxide electrolyte-gated transistors on paper”. EUROMAT 2019, September 1st-5th, 2019, Stockholm, Sweden.
- **I. Cunha**, P. Grey, D. Gaspar, E. Fortunato, R. Martins, L. Pereira; “Dual-cation cellulose electrolytes for flexible iontronics on paper”. Symposium W: Hybrid materials: state of the art and new frontiers. E-MRS 2018 Spring Meeting, June 18th-22th, 2018, Strasbourg, France.

Poster communications (7):

- **I. Cunha.** J. Martins, D. Gaspar, P. G. Bahubalindruni, E. Fortunato, R. Martins, L. Pereira; “Healable cellulose iontronic hydrogel sticker for sustainable electronics”. Encontro Ciência 2020, November 2th-4th, 2020, Lisboa, Portugal.
- **I. Cunha.** J. Martins, J. Rodrigues, S. Rubin, J.T. Carvalho, P. G. Bahubalindruni, E. Fortunato, R. Martins, L. Pereira; “Printed and drawn flexible electronics based on cellulose nanocomposites”. Encontro Ciência 2019, July 8th-10th, 2019, Lisboa, Portugal.

- **I. Cunha.** J. Martins, J. Rodrigues, S. Rubin, J.T. Carvalho, P. G. Bahubalindruni, E. Fortunato, R. Martins, L. Pereira; "Handwritten digital electronics with printed paper transistors". XIX Congresso da SPM and X International Symposium on Materials, April 14th-17th , 2019, Lisboa, Portugal.
- **I. Cunha**, R. Barras, P. Grey, D. Gaspar, E. Fortunato, R. Martins, L. Pereira; "Reusable and recyclable cellulose electrolytes for paper electronics". Symposium R: Solid state ionics: advanced functional materials for solid state devices. E-MRS 2018 Spring Meeting, June 18th-22th, 2018, Strasbourg, France.
- **I. Cunha**, R. Barras, P. Grey, D. Gaspar, E. Fortunato, R. Martins, L. Pereira; "Cellulose Ion EcoSitcker applied as gate dielectric in paper electrolyte-gated transistors". VI World Materials Summit & Forum for next generation of researchers, November 18th-21th, 2017, Strasbourg, France.
- **I. Cunha**, R. Barras, P. Grey, D. Gaspar, E. Fortunato, R. Martins, L. Pereira; "Cellulose Ion EcoSitcker applied as gate dielectric in paper electrolyte-gated transistors". 5th DRESDEN Nanoanalysis Symposium, September 1st, 2017 Dresden, Germany.
- **I. Cunha**, R. Barras, P. Grey, D. Gaspar, E. Fortunato, R. Martins, L. Pereira; "Cellulose-based hydrogel stickers applied as gate dielectric in paper electrolyte-gated transistors". Encontro Ciência 2017, July 5th-7th, 2017, Lisboa, Portugal.

9.3. Workshops and courses

- Sciencepreneur Course, NOVA Doctoral School, January 12th-April 6th 2021, Lisbon, Portugal;
- HiseedTech training Program, March – July 2018, Lisbon, Portugal;
- VI World Materials Summit & FORUM FOR NEXT GENERATION OF RESEARCHERS – Materials Innovation for the Global Circular Economy and Sustainable Society, November 18th-21th, 2017, Strasbourg, France;
- ERASMUS-ELBYSIER Intensive Program in Graphene technologies & Nanoelectronics, FCT-UNL, CENIMAT, October 9th-13th, 2017, Caparica, Portugal.
- European Advanced Training Course - "Nanoscale Materials – Characterization Techniques and Applications", August 29th-31th, 2017, Dresden, Germany;
- Science Communication Course, NOVA Doctoral School, May 9th-11th, 2017 Lisbon, Portugal;
- International Doctoral School in Functional Materials: Research and Innovation, First Spring School –Life Cycle of Materials and Project & Risk Management, April 23th -29th, 2017, Lisbon, Portugal.

9.4. Projects

- GlassLink - Self-adhesive dynamic smart film (HiseedTech 2018), Lisbon, Portugal;
- International Physics Olympiad (IPhO 2018), Lisbon, Portugal.

9.5. Recognitions

- **1st place poster award: I. Cunha**, J. Martins, J. Rodrigues, S. Rubin, J.T. Carvalho, P. G. Bahubalindruni, E. Fortunato, R. Martins, L. Pereira; "Handwritten digital electronics with printed paper transistors". XIX Congresso da SPM and X International Symposium on Materials, April 14th-17th, 2019, Lisboa, Portugal;
- **3rd place poster award: I. Cunha**, R. Barras, P. Grey, D. Gaspar, E. Fortunato, R. Martins, L. Pereira; "Cellulose Ion EcoSitcker applied as gate dielectric in paper electrolyte-gated transistors". 5th DRESDEN Nanoanalysis Symposium, September 1st, 2017 Dresden, Germany.

References

1. Irimia-Vladu, M. “Green” electronics: biodegradable and biocompatible materials and devices for sustainable future. *Chem. Soc. Rev.* **43**, 588–610 (2014).
2. Danish, M., Ali, S., Ahmad, M. A. & Zahid, H. The Influencing Factors on Choice Behavior Regarding Green Electronic Products: Based on the Green Perceived Value Model. *Economies* **7**, 99 (2019).
3. Sahajwalla, V. & Gaikwad, V. The present and future of e-waste plastics recycling. *Curr. Opin. Green Sustain. Chem.* **13**, 102–107 (2018).
4. Martins, R. *et al.* Papertronics: Multigate paper transistor for multifunction applications. *Appl. Mater. Today* **12**, 402–414 (2018).
5. T. Vicente, A. *et al.* Multifunctional cellulose-paper for light harvesting and smart sensing applications. *J. Mater. Chem. C* **6**, 3143–3181 (2018).
6. Adila, A. S., Husam, A. & Husi, G. Towards the self-powered Internet of Things (IoT) by energy harvesting: Trends and technologies for green IoT. in *2018 2nd International Symposium on Small-scale Intelligent Manufacturing Systems (SIMS)* 1–5 (IEEE, 2018). doi:10.1109/SIMS.2018.8355305
7. Irimia-Vladu, M., Sariciftci, N. S. & Bauer, S. Exotic materials for bio-organic electronics. *J. Mater. Chem.* **21**, 1350–1361 (2011).
8. Ferreira, G. *et al.* Touch-Interactive Flexible Sustainable Energy Harvester and Self-Powered Smart Card. *Adv. Funct. Mater.* **30**, 1908994 (2020).
9. Copani, G. *et al.* Integrated Technological Solutions for Zero Waste Recycling of Printed Circuit Boards (PCBs). in *Factories of the Future* 149–169 (Springer International Publishing, 2019). doi:10.1007/978-3-319-94358-9_7
10. Zhao, D. *et al.* High-Strength and High-Toughness Double-Cross-Linked Cellulose Hydrogels: A New Strategy Using Sequential Chemical and Physical Cross-Linking. *Adv. Funct. Mater.* **26**, 6279–6287 (2016).
11. Garlapati, S. K. *et al.* Printed Electronics Based on Inorganic Semiconductors: From Processes and Materials to Devices. *Adv. Mater.* **30**, 1–55 (2018).
12. S. Dassanayake, R., Acharya, S. & Abidi, N. Biopolymer-Based Materials from Polysaccharides: Properties, Processing, Characterization and Sorption Applications. *Adv. Sorption Process Appl.* 1–24 (2019). doi:10.5772/intechopen.80898
13. Klemm, D. *et al.* Nanocellulose as a natural source for groundbreaking applications in materials science: Today’s state. *Mater. Today* **21**, 720–748 (2018).
14. Chang, C. & Zhang, L. Cellulose-based hydrogels: Present status and application prospects. *Carbohydr. Polym.* **84**, 40–53 (2011).
15. Tobjörk, D. & Österbacka, R. Paper Electronics. *Adv. Mater.* **23**, 1935–1961 (2011).
16. Moon, R. J., Martini, A., Nairn, J., Simonsen, J. & Youngblood, J. Cellulose nanomaterials review: structure, properties and nanocomposites. *Chem. Soc. Rev.* **40**, 3941 (2011).
17. Shi, Z., Phillips, G. O. & Yang, G. Nanocellulose electroconductive composites. *Nanoscale* **5**, 3194 (2013).
18. Shen, X., Shamshina, J. L., Berton, P., Gurau, G. & Rogers, R. D. Hydrogels based on cellulose and chitin: fabrication, properties, and applications. *Green Chem.* **18**, 53–75 (2016).
19. Fu, L.-H., Qi, C., Ma, M.-G. & Wan, P. Multifunctional cellulose-based hydrogels for biomedical applications. *J. Mater. Chem. B* **7**, 1541–1562 (2019).

20. Zhu, H. *et al.* Wood-Derived Materials for Green Electronics, Biological Devices, and Energy Applications. *Chem. Rev.* **116**, 9305–74 (2016).

21. Wan, C. J., Zhu, L. Q., Wan, X., Shi, Y. & Wan, Q. Organic/inorganic hybrid synaptic transistors gated by proton conducting methylcellulose films. *Appl. Phys. Lett.* **108**, (2016).

22. Wolfberger, A. *et al.* Photolithographic patterning of cellulose: a versatile dual-tone photoresist for advanced applications. *Cellulose* **22**, 717–727 (2015).

23. Petritz, A. *et al.* Ambipolar inverters with natural origin organic materials as gate dielectric and semiconducting layer. *Phys. status solidi - Rapid Res. Lett.* **9**, 358–361 (2015).

24. Petritz, A. *et al.* Cellulose as biodegradable high-k dielectric layer in organic complementary inverters. *Appl. Phys. Lett.* **103**, 153303 (2013).

25. Faraji, S., Danesh, E., Tate, D. J., Turner, M. L. & Majewski, L. A. Cyanoethyl cellulose-based nanocomposite dielectric for low-voltage, solution-processed organic field-effect transistors (OFETs). *J. Phys. D. Appl. Phys.* **49**, 185102 (2016).

26. Petritz, A. *et al.* Cellulose-Derivative-Based Gate Dielectric for High-Performance Organic Complementary Inverters. *Adv. Mater.* **27**, 7645–7656 (2015).

27. Bae, J. W., Jang, H. S., Park, W. H. & Kim, S. Y. Triacetate cellulose gate dielectric organic thin-film transistors. *Org. Electron. physics, Mater. Appl.* **41**, 186–189 (2017).

28. Nagashima, K. *et al.* Cellulose nanofiber paper as an ultra flexible nonvolatile memory. *Sci. Rep.* **4**, 5532 (2014).

29. Valentini, L., Bittolo Bon, S., Cardinali, M., Fortunati, E. & Kenny, J. M. Cellulose nanocrystals thin films as gate dielectric for flexible organic field-effect transistors. *Mater. Lett.* **126**, 55–58 (2014).

30. Grey, P. *et al.* Field-Effect Transistors on Photonic Cellulose Nanocrystal Solid Electrolyte for Circular Polarized Light Sensing. *Adv. Funct. Mater.* **1805279**, 1–8 (2018).

31. Grey, P. *et al.* Ionically Modified Cellulose Nanocrystal Self-Assembled Films with a Mesoporous Twisted Superstructure: Polarizability and Application in Ion-Gated Transistors. *ACS Appl. Electron. Mater.* **2**, 426–436 (2020).

32. Cunha, I. *et al.* Reusable Cellulose-Based Hydrogel Sticker Film Applied as Gate Dielectric in Paper Electrolyte-Gated Transistors. *Adv. Funct. Mater.* **27**, 1606755 (2017).

33. Thiemann, S. *et al.* Cellulose-Based Ionogels for Paper Electronics. *Adv. Funct. Mater.* **24**, 625–634 (2014).

34. Gaspar, D. *et al.* Engineered cellulose fibers as dielectric for oxide field effect transistors. *Phys. Status Solidi Curr. Top. Solid State Phys.* **12**, 1421–1426 (2015).

35. Fortunato, E. *et al.* High-Performance Flexible Hybrid Field-Effect Transistors Based on Cellulose Fiber Paper. *IEEE Electron Device Lett.* **29**, 988–990 (2008).

36. Martins, R. *et al.* Write-erase and read paper memory transistor. *Appl. Phys. Lett.* **93**, 203501 (2008).

37. Martins, R. *et al.* Complementary Metal Oxide Semiconductor Technology With and On Paper. *Adv. Mater.* **23**, 4491–4496 (2011).

38. Ferreira, I. *et al.* Solid-state paper batteries for controlling paper transistors. *Electrochim. Acta* **56**, 1099–1105 (2011).

39. Martins, R. F. P. *et al.* Recyclable, Flexible, Low-Power Oxide Electronics. *Adv. Funct. Mater.* **23**, 2153–2161 (2013).

40. Gaspar, D. *et al.* Nanocrystalline cellulose applied simultaneously as the gate dielectric and the substrate in flexible field effect transistors. *Nanotechnology* **25**, 094008 (2014).

41. Pereira, L. *et al.* The influence of fibril composition and dimension on the performance of paper gated oxide transistors. *Nanotechnology* **25**, 094007 (2014).

42. Marques, A. C. *et al.* Office Paper Platform for Bioelectrochromic Detection of Electrochemically Active Bacteria using Tungsten Trioxide Nanoprobes. *Sci. Rep.* **5**, 9910 (2015).

43. Zschieschang, U. & Klauk, H. Organic transistors on paper: a brief review. *J. Mater. Chem. C* **7**, 5522–5533 (2019).

44. Gaspar, D. *et al.* Planar Dual-Gate Paper/Oxide Field Effect Transistors as Universal Logic Gates. *Adv. Electron. Mater.* **4**, 1800423 (2018).

45. Russo, A. *et al.* Pen-on-Paper Flexible Electronics. *Adv. Mater.* **23**, 3426–3430 (2011).

46. Kurra, N. & Kulkarni, G. U. Pencil-on-paper: electronic devices. *Lab Chip* **13**, 2866 (2013).

47. Kim, S. H. *et al.* Electrolyte-Gated Transistors for Organic and Printed Electronics. *Adv. Mater.* **25**, 1822–1846 (2013).

48. Kang, B., Lee, W. H. & Cho, K. Recent Advances in Organic Transistor Printing Processes. *ACS Appl. Mater. Interfaces* **5**, 2302–2315 (2013).

49. Baeg, K.-J., Caironi, M. & Noh, Y.-Y. Toward Printed Integrated Circuits based on Unipolar or Ambipolar Polymer Semiconductors. *Adv. Mater.* **25**, 4210–4244 (2013).

50. Zhang, L., Di, C., Yu, G. & Liu, Y. Solution processed organic field-effect transistors and their application in printed logic circuits. *J. Mater. Chem.* **20**, 7059 (2010).

51. Dai, S. *et al.* Intrinsically ionic conductive cellulose nanopapers applied as all solid dielectrics for low voltage organic transistors. *Nat. Commun.* **9**, 2737 (2018).

52. Dasgupta, S. *et al.* Printed and Electrochemically Gated, High-Mobility, Inorganic Oxide Nanoparticle FETs and Their Suitability for High-Frequency Applications. *Adv. Funct. Mater.* **22**, 4909–4919 (2012).

53. Dasgupta, S., Kruk, R., Mechau, N. & Hahn, H. Inkjet Printed, High Mobility Inorganic-Oxide Field Effect Transistors Processed at Room Temperature. *ACS Nano* **5**, 9628–9638 (2011).

54. Garlapati, S. K. *et al.* Ink-Jet Printed CMOS Electronics from Oxide Semiconductors. *Small* **11**, 3591–3596 (2015).

55. Perelaer, J. *et al.* Printed electronics: the challenges involved in printing devices, interconnects, and contacts based on inorganic materials. *J. Mater. Chem.* **20**, 8446 (2010).

56. Torres Sevilla, G. A. & Hussain, M. M. Printed Organic and Inorganic Electronics: Devices To Systems. *IEEE J. Emerg. Sel. Top. Circuits Syst.* **7**, 147–160 (2017).

57. Carvalho, J. *et al.* Fully Printed Zinc Oxide Electrolyte-Gated Transistors on Paper. *Nanomaterials* **9**, 169 (2019).

58. Grey, P. *et al.* Handwritten Oxide Electronics on Paper. *Adv. Mater. Technol.* **2**, 1700009 (2017).

59. Rosa, P., Câmara, A. & Gouveia, C. The Potential of Printed Electronics and Personal Fabrication in Driving the Internet of Things. *Open J. Internet Things* **1**, 16–36 (2015).

60. de Amorim, J. D. P. *et al.* Plant and bacterial nanocellulose: production, properties and applications in medicine, food, cosmetics, electronics and engineering. A review. *Environ. Chem. Lett.* **18**, 851–869 (2020).

61. Zhang, Y. *et al.* Flexible Electronics Based on Micro/Nanostructured Paper. *Adv. Mater.* **30**, 1801588 (2018).

62. Qiu, X. & Hu, S. "Smart" Materials Based on Cellulose: A Review of the Preparations, Properties, and Applications. *Materials (Basel).* **6**, 738–781 (2013).

63. Tayeb, A. H., Amini, E., Ghasemi, S. & Tajvidi, M. Cellulose nanomaterials-binding properties and applications: A review. *Molecules* **23**, 1–24 (2018).

64. Nechyporchuk, O., Belgacem, M. N. & Bras, J. Production of cellulose nanofibrils: A review of recent advances. *Ind. Crops Prod.* **93**, 2–25 (2016).

65. Rongpipi, S., Ye, D., Gomez, E. D. & Gomez, E. W. Progress and Opportunities in the Characterization of Cellulose – An Important Regulator of Cell Wall Growth and Mechanics. *Front. Plant Sci.* **9**, 1–28 (2019).

66. Zhu, H., Fang, Z., Preston, C., Li, Y. & Hu, L. Transparent paper: Fabrications, properties, and device applications. *Energy Environ. Sci.* **7**, 269–287 (2014).

67. Olsson, C. & Westm, G. Direct Dissolution of Cellulose: Background, Means and Applications. *Cellul. - Fundam. Asp.* (2013). doi:10.5772/52144

68. Pinkert, A., Marsh, K. N., Pang, S. & Staiger, M. P. Ionic liquids and their interaction with cellulose. *Chem. Rev.* **109**, 6712–6728 (2009).

69. Singh, P. *et al.* From Cellulose Dissolution and Regeneration to Added Value Applications — Synergism Between Molecular Understanding and Material Development. *Cellul. - Fundam. Asp. Curr. Trends* 1–44 (2015). doi:10.5772/61402

70. Ho, T. T. T., Zimmermann, T., Hauert, R. & Caseri, W. Preparation and characterization of cationic nanofibrillated cellulose from etherification and high-shear disintegration processes. *Cellulose* **18**, 1391–1406 (2011).

71. Jiang, F. *et al.* Wood-Based Nanotechnologies toward Sustainability. *Adv. Mater.* **30**, 1703453 (2018).

72. Paajanen, A., Ceccherini, S., Maloney, T. & Ketoja, J. A. Chirality and bound water in the hierarchical cellulose structure. *Cellulose* **26**, 5877–5892 (2019).

73. Eichhorn, S. J. Cellulose nanowhiskers: Promising materials for advanced applications. *Soft Matter* **7**, 303–315 (2011).

74. Kabir, S. M. F. *et al.* Cellulose-based hydrogel materials: chemistry, properties and their prospective applications. *Prog. Biomater.* **7**, 153–174 (2018).

75. Miyashiro, D., Hamano, R. & Umemura, K. A review of applications using mixed materials of cellulose, nanocellulose and carbon nanotubes. *Nanomaterials* **10**, 1–23 (2020).

76. Hoeng, F., Denneulin, A. & Bras, J. Use of nanocellulose in printed electronics: A review. *Nanoscale* **8**, 13131–13154 (2016).

77. Fang, Z., Zhu, H., Preston, C. & Hu, L. Development, application and commercialization of transparent paper. *Transl. Mater. Res.* **1**, 015004 (2014).

78. Agate, S., Joyce, M., Lucia, L. & Pal, L. Cellulose and nanocellulose-based flexible-hybrid printed electronics and conductive composites – A review. *Carbohydr. Polym.* **198**, 249–260 (2018).

79. Lindman, B., Karlström, G. & Stigsson, L. On the mechanism of dissolution of cellulose. *J. Mol. Liq.* **156**, 76–81 (2010).

80. Wang, S., Lu, A. & Zhang, L. Recent advances in regenerated cellulose materials. *Prog. Polym. Sci.* **53**, 169–206 (2016).

81. Medronho, B. & Lindman, B. Brief overview on cellulose dissolution/regeneration interactions and mechanisms. *Adv. Colloid Interface Sci.* **222**, 502–508 (2015).

82. Ramos, A. M. *et al.* Preparation and characterization of cellulose nanocomposite hydrogels as functional electrolytes. *Solid State Ionics* **242**, 26–32 (2013).

83. Zhang, S., Li, F., Yu, J. & Hsieh, Y. Dissolution behaviour and solubility of cellulose in NaOH complex solution. *Carbohydr. Polym.* **81**, 668–674 (2010).

84. Luo, X. & Zhang, L. New solvents and functional materials prepared from cellulose solutions in alkali/urea aqueous system. *Food Res. Int.* **52**, 387–400 (2013).

85. Cai, J., Kimura, S., Wada, M., Kuga, S. & Zhang, L. Cellulose Aerogels from Aqueous

Alkali Hydroxide–Urea Solution. *ChemSusChem* **1**, 149–154 (2008).

86. Cai, J., Wang, L. & Zhang, L. Influence of coagulation temperature on pore size and properties of cellulose membranes prepared from NaOH–urea aqueous solution. *Cellulose* **14**, 205–215 (2007).

87. Cai, J. & Zhang, L. Rapid Dissolution of Cellulose in LiOH/Urea and NaOH/Urea Aqueous Solutions. *Macromol. Biosci.* **5**, 539–548 (2005).

88. Yang, Q., Fukuzumi, H., Saito, T., Isogai, A. & Zhang, L. Transparent Cellulose Films with High Gas Barrier Properties Fabricated from Aqueous Alkali/Urea Solutions. *Biomacromolecules* **12**, 2766–2771 (2011).

89. He, M. *et al.* Fast Contact of Solid–Liquid Interface Created High Strength Multi-Layered Cellulose Hydrogels with Controllable Size. *ACS Appl. Mater. Interfaces* **6**, 1872–1878 (2014).

90. Han, D. & Yan, L. Preparation of all-cellulose composite by selective dissolving of cellulose surface in PEG/NaOH aqueous solution. *Carbohydr. Polym.* **79**, 614–619 (2010).

91. Kamal Mohamed, S. M., Ganesan, K., Milow, B. & Ratke, L. The effect of zinc oxide (ZnO) addition on the physical and morphological properties of cellulose aerogel beads. *RSC Adv.* **5**, 90193–90201 (2015).

92. Wang, S., Yang, Y., Lu, A. & Zhang, L. Construction of cellulose/ZnO composite microspheres in NaOH/zinc nitrate aqueous solution via one-step method. *Cellulose* **26**, 557–568 (2019).

93. Budtova, T. & Navard, P. Cellulose in NaOH–water based solvents: a review. *Cellulose* **23**, 5–55 (2016).

94. Jiao, L., Ma, J. & Dai, H. Preparation and characterization of self-reinforced antibacterial and oil-resistant paper using a NaOH/Urea/ZnO solution. *PLoS One* **10**, 1–16 (2015).

95. Yang, Q., Qin, X. & Zhang, L. Properties of cellulose films prepared from NaOH/urea/zincate aqueous solution at low temperature. *Cellulose* **18**, 681–688 (2011).

96. Yang, Q. *et al.* Role of sodium zincate on cellulose dissolution in NaOH/urea aqueous solution at low temperature. *Carbohydr. Polym.* **83**, 1185–1191 (2011).

97. Cai, J. *et al.* Hydrogen-Bond-Induced Inclusion Complex in Aqueous Cellulose/LiOH/Urea Solution at Low Temperature. *ChemPhysChem* **8**, 1572–1579 (2007).

98. Cai, J. *et al.* Dynamic Self-Assembly Induced Rapid Dissolution of Cellulose at Low Temperatures. *Macromolecules* **41**, 9345–9351 (2008).

99. Yaksic, A. & Tilton, J. E. Using the cumulative availability curve to assess the threat of mineral depletion: The case of lithium. *Resour. Policy* **34**, 185–194 (2009).

100. Vignarooban, K. *et al.* Current trends and future challenges of electrolytes for sodium-ion batteries. *Int. J. Hydrogen Energy* **41**, 2829–2846 (2016).

101. Eshetu, G. G. *et al.* Electrolytes and Interphases in Sodium-Based Rechargeable Batteries: Recent Advances and Perspectives. *Adv. Energy Mater.* **10**, 2000093 (2020).

102. Wang, Z. *et al.* Hydrogel Electrolytes for Flexible Aqueous Energy Storage Devices. *Adv. Funct. Mater.* **1804560**, 1–30 (2018).

103. Caló, E. & Khutoryanskiy, V. V. Biomedical applications of hydrogels: A review of patents and commercial products. *Eur. Polym. J.* **65**, 252–267 (2015).

104. Kang, J., Tok, J. B. H. & Bao, Z. Self-healing soft electronics. *Nat. Electron.* **2**, 144–150 (2019).

105. Taylor, D. L. & in het Panhuis, M. Self-Healing Hydrogels. *Adv. Mater.* **28**, 9060–9093 (2016).

106. Talebian, S. *et al.* Self-Healing Hydrogels: The Next Paradigm Shift in Tissue

Engineering? *Adv. Sci.* **6**, 1801664 (2019).

107. Liu, Y. & Hsu, S. Synthesis and Biomedical Applications of Self-healing Hydrogels. *Front. Chem.* **6**, 1–10 (2018).

108. Li, Q. *et al.* The design, mechanism and biomedical application of self-healing hydrogels. *Chinese Chem. Lett.* **28**, 1857–1874 (2017).

109. Tamate, R. & Watanabe, M. Recent progress in self-healable ion gels. *Sci. Technol. Adv. Mater.* **21**, 388–401 (2020).

110. Liu, Y. J., Cao, W. T., Ma, M. G. & Wan, P. Ultrasensitive Wearable Soft Strain Sensors of Conductive, Self-healing, and Elastic Hydrogels with Synergistic 'soft and Hard' Hybrid Networks. *ACS Appl. Mater. Interfaces* **9**, 25559–25570 (2017).

111. Deng, Z., Wang, H., Ma, P. X. & Guo, B. Self-healing conductive hydrogels: preparation, properties and applications. *Nanoscale* **12**, 1224–1246 (2020).

112. Khatib, M. *et al.* A Freestanding Stretchable and Multifunctional Transistor with Intrinsic Self-Healing Properties of all Device Components. *Small* **15**, 1803939 (2018).

113. Wei, Z. *et al.* Self-healing gels based on constitutional dynamic chemistry and their potential applications. *Chem. Soc. Rev.* **43**, 8114–8131 (2014).

114. Tao, F., Qin, L., Wang, Z. & Pan, Q. Self-Healable and Cold-Resistant Supercapacitor Based on a Multifunctional Hydrogel Electrolyte. *ACS Appl. Mater. Interfaces* **9**, 15541–15548 (2017).

115. Jia, H., Tao, X. & Wang, Y. Flexible and Self-Healing Thermoelectric Converters Based on Thermosensitive Liquids at Low Temperature Gradient. *Adv. Electron. Mater.* **2**, 1600136 (2016).

116. Parida, K. *et al.* Highly Transparent, Stretchable, and Self-Healing Ionic-Skin Triboelectric Nanogenerators for Energy Harvesting and Touch Applications. *Adv. Mater.* **29**, 1702181 (2017).

117. Jeon, I., Cui, J., Illeperuma, W. R. K., Aizenberg, J. & Vlassak, J. J. Extremely Stretchable and Fast Self-Healing Hydrogels. *Adv. Mater.* **28**, 4678–4683 (2016).

118. Ko, J., Kim, Y. J. & Kim, Y. S. Self-Healing Polymer Dielectric for a High Capacitance Gate Insulator. *ACS Appl. Mater. Interfaces* **8**, 23854–23861 (2016).

119. Cao, Y. *et al.* Self-healing electronic skins for aquatic environments. *Nat. Electron.* **2**, 75–82 (2019).

120. Bubel, S., Menyo, M. S., Mates, T. E., Waite, J. H. & Chabinyc, M. L. Schmitt Trigger Using a Self-Healing Ionic Liquid Gated Transistor. *Adv. Mater.* **27**, 3331–3335 (2015).

121. Shin, S. H. *et al.* Ion-conductive self-healing hydrogels based on an interpenetrating polymer network for a multimodal sensor. *Chem. Eng. J.* **371**, 452–460 (2019).

122. Zhang, Q. *et al.* An Elastic Autonomous Self-Healing Capacitive Sensor Based on a Dynamic Dual Crosslinked Chemical System. *Adv. Mater.* **30**, 1–8 (2018).

123. Jing, X. *et al.* Highly transparent, stretchable, and rapid self-healing polyvinyl alcohol/cellulose nanofibril hydrogel sensors for sensitive pressure sensing and human motion detection. *Sensors Actuators B Chem.* **295**, 159–167 (2019).

124. Lien, D.-H. *et al.* All-Printed Paper Memory. *ACS Nano* **8**, 7613–7619 (2014).

125. Sia, S. Cutting edge: Thin, lightweight, foldable thermochromic displays on paper. *Lab Chip* **9**, 2763 (2009).

126. Tehrani, P., Hennerdal, L.-O., Dyer, A. L., Reynolds, J. R. & Berggren, M. Improving the contrast of all-printed electrochromic polymer on paper displays. *J. Mater. Chem.* **19**, 1799 (2009).

127. Yoon, B. *et al.* Inkjet Printing of Conjugated Polymer Precursors on Paper Substrates for

Colorimetric Sensing and Flexible Electrothermochromic Display. *Adv. Mater.* **23**, 5492–5497 (2011).

128. Nuchtavorn, N. & Macka, M. A novel highly flexible, simple, rapid and low-cost fabrication tool for paper-based microfluidic devices (µPADs) using technical drawing pens and in-house formulated aqueous inks. *Anal. Chim. Acta* **919**, 70–77 (2016).

129. Hyun, W. J. *et al.* All-Printed, Foldable Organic Thin-Film Transistors on Glassine Paper. *Adv. Mater.* **27**, 7058–7064 (2015).

130. Ihalainen, P. *et al.* Influence of Surface Properties of Coated Papers on Printed Electronics. *Ind. Eng. Chem. Res.* **51**, 6025–6036 (2012).

131. Grau, G., Kitsomboonloha, R., Swisher, S. L., Kang, H. & Subramanian, V. Printed Transistors on Paper: Towards Smart Consumer Product Packaging. *Adv. Funct. Mater.* **24**, 5067–5074 (2014).

132. Hong, K., Kim, S. H., Lee, K. H. & Frisbie, C. D. Printed, sub-2V ZnO Electrolyte Gated Transistors and Inverters on Plastic. *Adv. Mater.* **25**, 3413–3418 (2013).

133. Zheng, Y., He, Z., Gao, Y. & Liu, J. Direct Desktop Printed-Circuits-on-Paper Flexible Electronics. *Sci. Rep.* **3**, 1786 (2013).

134. Brus, V. V. *et al.* Fine Art of Thermoelectricity. *ACS Appl. Mater. Interfaces* **10**, 4737–4742 (2018).

135. Bollström, R. *et al.* Printability of functional inks on multilayer curtain coated paper. *Chem. Eng. Process. Process Intensif.* **68**, 13–20 (2013).

136. Huang, J. *et al.* Highly Transparent and Flexible Nanopaper Transistors. *ACS Nano* **7**, 2106–2113 (2013).

137. Zhu, H. *et al.* Biodegradable transparent substrates for flexible organic-light-emitting diodes. *Energy Environ. Sci.* **6**, 2105 (2013).

138. Spence, K. L., Venditti, R. a., Habibi, Y., Rojas, O. J. & Pawlak, J. J. The effect of chemical composition on microfibrillar cellulose films from wood pulps: Mechanical processing and physical properties. *Bioresour. Technol.* **101**, 5961–5968 (2010).

139. Khan, S., Lorenzelli, L. & Dahiya, R. S. Technologies for Printing Sensors and Electronics Over Large Flexible Substrates: A Review. *IEEE Sens. J.* **15**, 3164–3185 (2015).

140. Moonen, P. F., Yakimets, I. & Huskens, J. Fabrication of Transistors on Flexible Substrates: from Mass-Printing to High-Resolution Alternative Lithography Strategies. *Adv. Mater.* **24**, 5526–5541 (2012).

141. Fukuda, K. & Someya, T. Recent Progress in the Development of Printed Thin-Film Transistors and Circuits with High-Resolution Printing Technology. *Adv. Mater.* **29**, 1602736 (2017).

142. Khan, Y. *et al.* A New Frontier of Printed Electronics: Flexible Hybrid Electronics. *Adv. Mater.* **32**, 1–29 (2020).

143. Hu, G. *et al.* Functional inks and printing of two-dimensional materials. *Chem. Soc. Rev.* **47**, 3265–3300 (2018).

144. Wu, W. Inorganic nanomaterials for printed electronics: A review. *Nanoscale* **9**, 7342–7372 (2017).

145. Huang, Q. & Zhu, Y. Printing Conductive Nanomaterials for Flexible and Stretchable Electronics: A Review of Materials, Processes, and Applications. *Adv. Mater. Technol.* **4**, 1–41 (2019).

146. Mandal, S. & Noh, Y.-Y. Printed organic thin-film transistor-based integrated circuits. *Semicond. Sci. Technol.* **30**, 064003 (2015).

147. Fernandes, D. F., Majidi, C. & Tavakoli, M. Digitally printed stretchable electronics: A

review. *J. Mater. Chem. C* **7**, 14035–14068 (2019).

148. Chu, Y., Qian, C., Chahal, P. & Cao, C. Printed Diodes: Materials Processing, Fabrication, and Applications. *Adv. Sci.* **6**, (2019).

149. Sousa, R. E., Costa, C. M. & Lanceros-Méndez, S. Advances and Future Challenges in Printed Batteries. *ChemSusChem* **8**, 3539–3555 (2015).

150. Chung, S., Cho, K. & Lee, T. Recent Progress in Inkjet-Printed Thin-Film Transistors. *Adv. Sci.* **6**, 1801445 (2019).

151. Ng, L. W. T. *et al. Printing of Graphene and Related 2D Materials*. *Printing of Graphene and Related 2D Materials: Technology, Formulation and Applications* (Springer International Publishing, 2019). doi:10.1007/978-3-319-91572-2

152. Wang, G., Adil, M. A., Zhang, J. & Wei, Z. Large-Area Organic Solar Cells: Material Requirements, Modular Designs, and Printing Methods. *Adv. Mater.* **31**, 1–34 (2019).

153. Carlson, A., Bowen, A. M., Huang, Y., Nuzzo, R. G. & Rogers, J. A. Transfer printing techniques for materials assembly and micro/nanodevice fabrication. *Adv. Mater.* **24**, 5284–5318 (2012).

154. Liu, A., Zhu, H., Sun, H., Xu, Y. & Noh, Y.-Y. Solution Processed Metal Oxide High-κ Dielectrics for Emerging Transistors and Circuits. *Adv. Mater.* **30**, 1706364 (2018).

155. Subramanian, V. *et al.* Printed electronics for low-cost electronic systems: Technology status and application development. in *ESSCIRC 2008 - 34th European Solid-State Circuits Conference* 17–24 (IEEE, 2008). doi:10.1109/ESSCIRC.2008.4681785

156. Kamyshny, A. & Magdassi, S. Conductive Nanomaterials for Printed Electronics. *Small* **10**, 3515–3535 (2014).

157. Krebs, F. C. Fabrication and processing of polymer solar cells: A review of printing and coating techniques. *Sol. Energy Mater. Sol. Cells* **93**, 394–412 (2009).

158. Rim, Y. S. *et al.* Interface Engineering of Metal Oxide Semiconductors for Biosensing Applications. *Adv. Mater. Interfaces* **4**, 1700020 (2017).

159. Mattana, G. & Briand, D. Recent advances in printed sensors on foil. *Mater. Today* **19**, 88–99 (2016).

160. Perinot, A., Passarella, B., Giorgio, M. & Caironi, M. Walking the Route to GHz Solution-Processed Organic Electronics: A HEROIC Exploration. *Adv. Funct. Mater.* **30**, 1907641 (2020).

161. Andersson Ersman, P. *et al.* Monolithic integration of display driver circuits and displays manufactured by screen printing. *Flex. Print. Electron.* **5**, 024001 (2020).

162. Sowade, E. *et al.* All-inkjet-printed thin-film transistors: manufacturing process reliability by root cause analysis. *Sci. Rep.* **6**, 33490 (2016).

163. Honda, W., Harada, S., Arie, T., Akita, S. & Takei, K. Wearable, Human-Interactive, Health-Monitoring, Wireless Devices Fabricated by Macroscale Printing Techniques. *Adv. Funct. Mater.* **24**, 3299–3304 (2014).

164. Hu, L., Wu, H. & Cui, Y. Printed energy storage devices by integration of electrodes and separators into single sheets of paper. *Appl. Phys. Lett.* **96**, 94–97 (2010).

165. Gertsen, A. S., Castro, M. F., Søndergaard, R. R. & Andreasen, J. W. Scalable fabrication of organic solar cells based on non-fullerene acceptors. *Flex. Print. Electron.* **5**, (2020).

166. Magdassi, S., Grouchko, M. & Kamyshny, A. Copper nanoparticles for printed electronics: Routes towards achieving oxidation stability. *Materials (Basel).* **3**, 4626–4638 (2010).

167. Yu, X., Marks, T. J. & Facchetti, A. Metal oxides for optoelectronic applications. *Nat. Mater.* **15**, 383–396 (2016).

168. Cruz, S. M. F., Rocha, L. A. & Viana, J. C. Printing Technologies on Flexible Substrates

for Printed Electronics. *Flex. Electron.* (2018). doi:10.5772/intechopen.76161

169. Andersson Ersman, P. *et al.* All-printed large-scale integrated circuits based on organic electrochemical transistors. *Nat. Commun.* **10**, 5053 (2019).

170. Andersson Ersman, P. *et al.* Screen printed digital circuits based on vertical organic electrochemical transistors. *Flex. Print. Electron.* **2**, 045008 (2017).

171. Contat-Rodrigo, L., Pérez-Fuster, C., Lidón-Roger, J. V., Bonfiglio, A. & García-Breijo, E. Screen-printed Organic Electrochemical Transistors for the detection of ascorbic acid in food. *Org. Electron.* **45**, 89–96 (2017).

172. Hyun, W. J., Secor, E. B., Hersam, M. C., Frisbie, C. D. & Francis, L. F. High-Resolution Patterning of Graphene by Screen Printing with a Silicon Stencil for Highly Flexible Printed Electronics. *Adv. Mater.* **27**, 109–115 (2015).

173. Hyun, W. J. *et al.* Screen Printing of Highly Loaded Silver Inks on Plastic Substrates Using Silicon Stencils. *ACS Appl. Mater. Interfaces* **7**, 12619–12624 (2015).

174. Inukai, K., Takahashi, Y., Ri, K. & Shin, W. Rheological analysis of ceramic pastes with ethyl cellulose for screen-printing. *Ceram. Int.* **41**, 5959–5966 (2015).

175. Faddoul, R., Reverdy-Bruas, N. & Blayo, A. Formulation and screen printing of water based conductive flake silver pastes onto green ceramic tapes for electronic applications. *Mater. Sci. Eng. B* **177**, 1053–1066 (2012).

176. Lin, H. W., Chang, C. P., Hwu, W. H. & Ger, M. D. The rheological behaviors of screen-printing pastes. *J. Mater. Process. Technol.* **197**, 284–291 (2008).

177. Carlos, E. *et al.* Boosting Electrical Performance of High-κ Nanomultilayer Dielectrics and Electronic Devices by Combining Solution Combustion Synthesis and UV Irradiation. *ACS Appl. Mater. Interfaces* **9**, 40428–40437 (2017).

178. Carlos, E. *et al.* Printed, Highly Stable Metal Oxide Thin-Film Transistors with Ultra-Thin High-κ Oxide Dielectric. *Adv. Electron. Mater.* **6**, 1901071 (2020).

179. Yarali, E. *et al.* Recent Progress in Photonic Processing of Metal-Oxide Transistors. *Adv. Funct. Mater.* **30**, 1906022 (2020).

180. Zschieschang, U. *et al.* Roadmap to Gigahertz Organic Transistors. *Adv. Funct. Mater.* **30**, 1903812 (2020).

181. Matsui, H., Takeda, Y. & Tokito, S. Flexible and printed organic transistors: From materials to integrated circuits. *Org. Electron.* **75**, 105432 (2019).

182. Gao, X. & Zhao, Z. High mobility organic semiconductors for field-effect transistors. *Sci. China Chem.* **58**, 947–968 (2015).

183. Quinn, J. T. E., Zhu, J., Li, X., Wang, J. & Li, Y. Recent progress in the development of n-type organic semiconductors for organic field effect transistors. *J. Mater. Chem. C* **5**, 8654–8681 (2017).

184. Yoon, S., Kim, S. J., Tak, Y. J. & Kim, H. J. A solution-processed quaternary oxide system obtained at low-temperature using a vertical diffusion technique. *Sci. Rep.* **7**, 1–7 (2017).

185. Wang, Z., Nayak, P. K., Caraveo-Frescas, J. A. & Alshareef, H. N. Recent Developments in p-Type Oxide Semiconductor Materials and Devices. *Adv. Mater.* **28**, 3831–3892 (2016).

186. Shang, Z.-W., Hsu, H.-H., Zheng, Z.-W. & Cheng, C.-H. Progress and challenges in p-type oxide-based thin film transistors. *Nanotechnol. Rev.* **8**, 422–443 (2019).

187. Huang, H., Hu, H., Zhu, J. & Guo, T. Inkjet-Printed In-Ga-Zn Oxide Thin-Film Transistors with Laser Spike Annealing. *J. Electron. Mater.* **46**, 4497–4502 (2017).

188. Chen, C. *et al.* Low-temperature solution-processed flexible metal oxide thin-film transistors via laser annealing. *J. Phys. D. Appl. Phys.* **52**, 0–11 (2019).

189. Leppäniemi, J., Eiroma, K., Majumdar, H. & Alastalo, A. Far-UV Annealed Inkjet-Printed In2O3 Semiconductor Layers for Thin-Film Transistors on a Flexible Polyethylene Naphthalate Substrate. *ACS Appl. Mater. Interfaces* **9**, 8774–8782 (2017).

190. Vaseem, M., Hong, A. R., Kim, R. T. & Hahn, Y. B. Copper oxide quantum dot ink for inkjet-driven digitally controlled high mobility field effect transistors. *J. Mater. Chem. C* **1**, 2112–2120 (2013).

191. Jung, Y., Yang, W., Koo, C. Y., Song, K. & Moon, J. High performance and high stability low temperature aqueous solution-derived Li-Zr co-doped ZnO thin film transistors. *J. Mater. Chem.* **22**, 5390–5397 (2012).

192. Lin, Y. H. *et al.* Al-Doped ZnO Transistors Processed from Solution at 120 °C. *Adv. Electron. Mater.* **2**, 1–11 (2016).

193. Kumar, M., Jeong, H. & Lee, D. Sol-gel derived Hf- and Mg-doped high-performance ZnO thin film transistors. *J. Alloys Compd.* **720**, 230–238 (2017).

194. Chang, J. *et al.* Solution processed F doped ZnO (ZnO:F) for thin film transistors and improved stability through co-doping with alkali metals. *J. Mater. Chem. C* **3**, 1787–1793 (2015).

195. Yoon, J. Y. *et al.* A high-temperature resistant polyimide gate insulator surface-modified with a YOx interlayer for high-performance, solution-processed Li-doped ZnO thin-film transistors. *J. Mater. Chem. C* **2**, 2191–2197 (2014).

196. Park, S. Y. *et al.* Low-temperature, solution-processed and alkali metal doped zno for high-performance thin-film transistors. *Adv. Mater.* **24**, 834–838 (2012).

197. Jun, T., Jung, Y., Song, K. & Moon, J. Influences of pH and Ligand Type on the Performance of Inorganic Aqueous Precursor-Derived ZnO Thin Film Transistors. *ACS Appl. Mater. Interfaces* **3**, 774–781 (2011).

198. Nketia-yawson, B. & Noh, Y. Recent Progress on High-Capacitance Polymer Gate Dielectrics for Flexible Low-Voltage Transistors. **1802201**, 1–27 (2018).

199. Ortiz, R. P., Facchetti, A. & Marks, T. J. High- k Organic, Inorganic, and Hybrid Dielectrics for Low-Voltage Organic Field-Effect Transistors. *Chem. Rev.* **110**, 205–239 (2010).

200. Lenz, T. *et al.* Charge transport in nanoparticular thin films of zinc oxide and aluminum-doped zinc oxide. *J. Mater. Chem. C* **3**, 1468–1472 (2015).

201. Cho, S. Y. *et al.* Novel Zinc Oxide Inks with Zinc Oxide Nanoparticles for Low-Temperature, Solution-Processed Thin-Film Transistors. *Chem. Mater.* **24**, 3517–3524 (2012).

202. Park, J. W., Kang, B. H. & Kim, H. J. A Review of Low-Temperature Solution-Processed Metal Oxide Thin-Film Transistors for Flexible Electronics. *Adv. Funct. Mater.* **30**, 1904632 (2020).

203. Noh, Y. Y. *et al.* Ink-jet printed ZnO nanowire field effect transistors. *Appl. Phys. Lett.* **91**, (2007).

204. Liu, X. *et al.* Materials Integration for Printed Zinc Oxide Thin-Film Transistors: Engineering of a Fully-Printed Semiconductor/Contact Scheme. *J. Disp. Technol.* **12**, 214–218 (2016).

205. Lim, S. C. *et al.* Device characteristics of inkjet-printed ZnO TFTs by solution process. *Jpn. J. Appl. Phys.* **53**, (2014).

206. Meyers, S. T. *et al.* Aqueous inorganic inks for low-temperature fabrication of ZnO TFTs. *J. Am. Chem. Soc.* **130**, 17603–17609 (2008).

207. Wang, Y., Khan, M. Y., Lee, S. K., Park, Y. K. & Hahn, Y. B. Parametric study of nozzle-jet printing for directly drawn ZnO field-effect transistors. *Sci. Adv. Mater.* **8**, 148–155 (2016).

208. Hong, K. *et al.* Aerosol jet printed, Sub-2 v complementary circuits constructed from P- and N-type electrolyte gated transistors. *Adv. Mater.* **26**, 7032–7037 (2014).

209. Hong, K., Kim, S. H., Mahajan, A. & Frisbie, C. D. Aerosol jet printed p- and n-type electrolyte-gated transistors with a variety of electrode materials: Exploring practical routes to printed electronics. *ACS Appl. Mater. Interfaces* **6**, 18704–18711 (2014).

210. Yong-Hoon Kim *et al.* Ink-Jet-Printed Zinc–Tin–Oxide Thin-Film Transistors and Circuits With Rapid Thermal Annealing Process. *IEEE Electron Device Lett.* **31**, 836–838 (2010).

211. Kim, D. *et al.* Inkjet-printed zinc tin oxide thin-film transistor. *Langmuir* **25**, 11149–11154 (2009).

212. Lee, Y. G. & Choi, W. S. Electrohydrodynamic jet-printed zinc-tin oxide TFTs and their bias stability. *ACS Appl. Mater. Interfaces* **6**, 11167–11172 (2014).

213. Avis, C. & Jang, J. High-performance solution processed oxide TFT with aluminum oxide gate dielectric fabricated by a sol-gel method. *J. Mater. Chem.* **21**, 10649–10652 (2011).

214. Kwack, Y. J. & Choi, W. S. Electrohydrodynamic jet spraying technique for oxide thin-film transistor. *IEEE Electron Device Lett.* **34**, 78–80 (2013).

215. Hennek, J. W. *et al.* Reduced Contact Resistance in Inkjet Printed High-Performance Amorphous Indium Gallium Zinc Oxide Transistors. *ACS Appl. Mater. Interfaces* **4**, 1614–1619 (2012).

216. Everaerts, K. *et al.* Printed Indium Gallium Zinc Oxide Transistors. Self-Assembled Nanodielectric Effects on Low-Temperature Combustion Growth and Carrier Mobility. *ACS Appl. Mater. Interfaces* **5**, 11884–11893 (2013).

217. Kim, G. H. *et al.* Inkjet-printed InGaZnO thin film transistor. *Thin Solid Films* **517**, 4007–4010 (2009).

218. Secor, E. B., Smith, J., Marks, T. J. & Hersam, M. C. High-Performance Inkjet-Printed Indium-Gallium-Zinc-Oxide Transistors Enabled by Embedded, Chemically Stable Graphene Electrodes. *ACS Appl. Mater. Interfaces* **8**, 17428–17434 (2016).

219. Jeong, S. *et al.* Metal salt-derived In-Ga-Zn-O semiconductors incorporating formamide as a novel co-solvent for producing solution-processed, electrohydrodynamic-jet printed, high performance oxide transistors. *J. Mater. Chem. C* **1**, 4236–4243 (2013).

220. Choi, Y. *et al.* Characteristics of gravure printed InGaZnO thin films as an active channel layer in thin film transistors. *Thin Solid Films* **518**, 6249–6252 (2010).

221. Lee, D. H., Han, S. Y., Herman, G. S. & Chang, C. H. Inkjet printed high-mobility indium zinc tin oxide thin film transistors. *J. Mater. Chem.* **19**, 3135–3137 (2009).

222. Avis, C., Hwang, H. R. & Jang, J. Effect of channel layer thickness on the performance of indium-zinc-tin oxide thin film transistors manufactured by inkjet printing. *ACS Appl. Mater. Interfaces* **6**, 10941–10945 (2014).

223. Lee, S. *et al.* Patterned oxide semiconductor by electrohydrodynamic jet printing for transparent thin film transistors. *Appl. Phys. Lett.* **100**, (2012).

224. Spiehl, D., Haming, M., Sauer, H. M., Bonrad, K. & Dorsam, E. Engineering of Flexo- and Gravure-Printed Indium–Zinc-Oxide Semiconductor Layers for High-Performance Thin-Film Transistors. *IEEE Trans. Electron Devices* **62**, 2871–2877 (2015).

225. Dilfer, S., Hoffmann, R. C. & Dörsam, E. Characteristics of flexographic printed indium-zinc-oxide thin films as an active semiconductor layer in thin film field-effect transistors. *Appl. Surf. Sci.* **320**, 634–642 (2014).

226. Lee, D. H., Chang, Y. J., Herman, G. S. & Chang, C. H. A general route to printable high-mobility transparent amorphous oxide semiconductors. *Adv. Mater.* **19**, 843–847 (2007).

227. Li, Y. *et al.* All Inkjet-Printed Metal-Oxide Thin-Film Transistor Array with Good Stability and Uniformity Using Surface-Energy Patterns. *ACS Appl. Mater. Interfaces* **9**, 8194–8200

(2017).

228. Meyer, S. *et al.* Soluble metal oxo alkoxide inks with advanced rheological properties for inkjet-printed thin-film transistors. *ACS Appl. Mater. Interfaces* **9**, 2625–2633 (2017).

229. Von Seggern, F. *et al.* Temperature-dependent performance of printed field-effect transistors with solid polymer electrolyte gating. *ACS Appl. Mater. Interfaces* **8**, 31757–31763 (2016).

230. Baby, T. T. *et al.* A General Route toward Complete Room Temperature Processing of Printed and High Performance Oxide Electronics. *ACS Nano* **9**, 3075–3083 (2015).

231. Li, Y. *et al.* Coffee-Ring Defined Short Channels for Inkjet-Printed Metal Oxide Thin-Film Transistors. *ACS Appl. Mater. Interfaces* **8**, 19643–19648 (2016).

232. Scheideler, W. J., Kumar, R., Zeumault, A. R. & Subramanian, V. Low-Temperature-Processed Printed Metal Oxide Transistors Based on Pure Aqueous Inks. *Adv. Funct. Mater.* **27**, (2017).

233. Garlapati, S. K. *et al.* High performance printed oxide field-effect transistors processed using photonic curing. *Nanotechnology* **29**, 235205 (2018).

234. Leppäniemi, J., Huttunen, O.-H., Majumdar, H. & Alastalo, A. Flexography-Printed In 2 O 3 Semiconductor Layers for High-Mobility Thin-Film Transistors on Flexible Plastic Substrate. *Adv. Mater.* **27**, 7168–7175 (2015).

235. Xie, W., Zhang, X., Leighton, C. & Frisbie, C. D. 2D Insulator–Metal Transition in Aerosol-Jet-Printed Electrolyte-Gated Indium Oxide Thin Film Transistors. *Adv. Electron. Mater.* **3**, 1–6 (2017).

236. Lee, J. S., Kwack, Y.-J. & Choi, W.-S. Inkjet-Printed In_2O_3 Thin-Film Transistor below 200 °C. *ACS Appl. Mater. Interfaces* **5**, 11578–11583 (2013).

237. Sun, D. *et al.* High performance inkjet-printed metal oxide thin film transistors via addition of insulating polymer with proper molecular weight. *Appl. Phys. Lett.* **112**, (2018).

238. Kim, S. Y. *et al.* High-resolution electrohydrodynamic inkjet printing of stretchable metal oxide semiconductor transistors with high performance. *Nanoscale* **8**, 17113–17121 (2016).

239. Garlapati, S. K. *et al.* Electrolyte-Gated, High Mobility Inorganic Oxide Transistors from Printed Metal Halides. *ACS Appl. Mater. Interfaces* **5**, 11498–11502 (2013).

240. Baby, T. T. *et al.* Sub-50 nm Channel Vertical Field-Effect Transistors using Conventional Ink-Jet Printing. *Adv. Mater.* **29**, 1–6 (2017).

241. Hu, H., Zhu, J., Chen, M., Guo, T. & Li, F. Inkjet-printed p-type nickel oxide thin-film transistor. *Appl. Surf. Sci.* **441**, 295–302 (2018).

242. Choi, C. H. *et al.* Low-temperature, inkjet printed p-type copper(i) iodide thin film transistors. *J. Mater. Chem. C* **4**, 10309–10314 (2016).

243. Singh, M., Haverinen, H. M., Dhagat, P. & Jabbour, G. E. Inkjet printing-process and its applications. *Adv. Mater.* **22**, 673–685 (2010).

244. Mattana, G. *et al.* Inkjet-Printing: A New Fabrication Technology for Organic Transistors. *Adv. Mater. Technol.* **2**, 1700063 (2017).

245. Bollström, R. *et al.* A multilayer coated fiber-based substrate suitable for printed functionality. *Org. Electron.* **10**, 1020–1023 (2009).

246. Mitra, K. Y. *et al.* Fully Inkjet-Printed Thin-Film Transistor Array Manufactured on Paper Substrate for Cheap Electronic Applications. *Adv. Electron. Mater.* **3**, 1700275 (2017).

247. Härting, M., Zhang, J., Gamota, D. R. & Britton, D. T. Fully printed silicon field effect transistors. *Appl. Phys. Lett.* **94**, 193509 (2009).

248. Grubb, P. M., Subbaraman, H., Park, S., Akinwande, D. & Chen, R. T. Inkjet printing of

high performance transistors with micron order chemically set gaps. *Sci. Rep.* **7**, 1–8 (2017).

249. Sele, C. W., von Werne, T., Friend, R. H. & Sirringhaus, H. Lithography-Free, Self-Aligned Inkjet Printing with Sub-Hundred-Nanometer Resolution. *Adv. Mater.* **17**, 997–1001 (2005).

250. Naveed Ul Haq, A. *et al.* Synthesis Approaches of Zinc Oxide Nanoparticles: The Dilemma of Ecotoxicity. *J. Nanomater.* **2017**, 1–14 (2017).

251. Nassar, M. Y., Moustafa, M. M. & Taha, M. M. Hydrothermal tuning of the morphology and particle size of hydrozincite nanoparticles using different counterions to produce nanosized ZnO as an efficient adsorbent for textile dye removal. *RSC Adv.* **6**, 42180–42195 (2016).

252. Dac Dien, N. Preparation of various morphologies of ZnO nanostructure through wet chemical methods. *Adv. Mater. Sci.* **4**, 67 (2019).

253. Kołodziejczak-Radzimska, A. & Jesionowski, T. Zinc Oxide—From Synthesis to Application: A Review. *Materials (Basel).* **7**, 2833–2881 (2014).

254. Nunes, D. *et al.* Metal oxide nanostructures for sensor applications. *Semicond. Sci. Technol.* **34**, (2019).

255. Arrabito, G. *et al.* Printing ZnO Inks: From Principles to Devices. *Crystals* **10**, 449 (2020).

256. Agarwal, H., Venkat Kumar, S. & Rajeshkumar, S. A review on green synthesis of zinc oxide nanoparticles – An eco-friendly approach. *Resour. Technol.* **3**, 406–413 (2017).

257. Laurenti, M. & Cauda, V. Porous zinc oxide thin films: Synthesis approaches and applications. *Coatings* **8**, (2018).

258. Mishra, Y. K. & Adelung, R. ZnO tetrapod materials for functional applications. *Mater. Today* **21**, 631–651 (2018).

259. Fortunato, E., Barquinha, P. & Martins, R. Oxide Semiconductor Thin-Film Transistors: A Review of Recent Advances. *Adv. Mater.* **24**, 2945–2986 (2012).

260. Cadilha Marques, G. *et al.* Digital power and performance analysis of inkjet printed ring oscillators based on electrolyte-gated oxide electronics. *Appl. Phys. Lett.* **111**, (2017).

261. Bu, X. *et al.* Ion-Gated Transistor: An Enabler for Sensing and Computing Integration. *Adv. Intell. Syst.* **2**, 2000156 (2020).

262. Cadilha Marques, G. *et al.* Progress Report on “From Printed Electrolyte-Gated Metal-Oxide Devices to Circuits”. *Adv. Mater.* **31**, 1806483 (2019).

263. Xia, Y. *et al.* Printed Sub-2 V Gel-Electrolyte-Gated Polymer Transistors and Circuits. *Adv. Funct. Mater.* **20**, 587–594 (2010).

264. Bisri, S. Z., Shimizu, S., Nakano, M. & Iwasa, Y. Endeavor of Iontronics: From Fundamentals to Applications of Ion-Controlled Electronics. *Adv. Mater.* **29**, 1–48 (2017).

265. Santos, L. *et al.* Solvothermal synthesis of gallium-indium-zinc-oxide nanoparticles for electrolyte-gated transistors. *ACS Appl. Mater. Interfaces* **7**, 638–646 (2015).

266. Ledwon, P., Andrade, J. R., Lapkowski, M. & Pawlicka, A. Hydroxypropyl cellulose-based gel electrolyte for electrochromic devices. *Electrochim. Acta* **159**, 227–233 (2015).

267. Lee, J. *et al.* Ion Gel-Gated Polymer Thin-Film Transistors: Operating Mechanism and Characterization of Gate Dielectric Capacitance, Switching Speed, and Stability. *J. Phys. Chem. C* **113**, 8972–8981 (2009).

268. Cho, J. H. *et al.* Printable ion-gel gate dielectrics for low-voltage polymer thin-film transistors on plastic. *Nat. Mater.* **7**, 900–906 (2008).

269. Gundlach, D. J. Low power, high impact. *Nat. Mater.* **6**, 173–174 (2007).

270. Martins, R. *et al.* Selective floating gate non-volatile paper memory transistor. *Phys. Status Solidi - Rapid Res. Lett.* **3**, 308–310 (2009).

271. Gherendi, F., Nistor, M. & Mandache, N. B. In2O3 thin film paper transistors. *IEEE/OSA J. Disp. Technol.* **9**, 760–763 (2013).

272. Fortunato, E. *et al. Optoelectronic Devices from Bacterial NanoCellulose*. *Bacterial Nanocellulose: From Biotechnology to Bio-Economy* (Elsevier B.V., 2016). doi:10.1016/B978-0-444-63458-0.00011-1

273. Martins, R. *et al.* Self-sustained n-type memory transistor devices based on natural cellulose paper fibers. *J. Inf. Disp.* **10**, 149–157 (2009).

274. Martins, R., Ferreira, I. & Fortunato, E. Electronics with and on paper. *Phys. status solidi - Rapid Res. Lett.* **5**, 332–335 (2011).

275. Lim, W. *et al.* High mobility InGaZnO4 thin-film transistors on paper. *Appl. Phys. Lett.* **94**, (2009).

276. Pimentel, A. *et al.* Synthesis of Long ZnO Nanorods under Microwave Irradiation or Conventional Heating. (2014).

277. Liang, J., Tong, K. & Pei, Q. A Water-Based Silver-Nanowire Screen-Print Ink for the Fabrication of Stretchable Conductors and Wearable Thin-Film Transistors. *Adv. Mater.* **28**, 5986–5996 (2016).

278. Barras, R. *et al.* Printable cellulose-based electroconductive composites for sensing elements in paper electronics. *Flex. Print. Electron.* **2**, (2017).

279. Manjunath, G., Pujari, S., Patil, D. R. & Mandal, S. A scalable screen-printed high performance ZnO-UV and Gas Sensor: Effect of solution combustion. *Mater. Sci. Semicond. Process.* **107**, 104828 (2020).

280. Murakami, S. *et al.* Effects of ethyl cellulose polymers on rheological properties of (La,Sr)(Ti,Fe)O3-terpineol pastes for screen printing. *Ceram. Int.* **40**, 1661–1666 (2014).

281. Lee, S., Paik, U., Yoon, S.-M. & Choi, J.-Y. Dispersant-Ethyl Cellulose Binder Interactions at the Ni Particle-Dihydroterpineol Interface. *J. Am. Ceram. Soc.* **89**, 3050–3055 (2006).

282. Phair, J. W. Rheological Analysis of Concentrated Zirconia Pastes with Ethyl Cellulose for Screen Printing SOFC Electrolyte Films. *J. Am. Ceram. Soc.* **91**, 2130–2137 (2008).

283. Marani, D. *et al.* Influence of hydroxyl content of binders on rheological properties of cerium–gadolinium oxide (CGO) screen printing inks. *J. Eur. Ceram. Soc.* **35**, 1495–1504 (2015).

284. Figueira, J. *et al.* Sustainable fully printed UV sensors on cork using zinc oxide/ethylcellulose inks. *Micromachines* **10**, (2019).

285. Wen, M. J., Subramani, S., Devarajan, M. & Sulaiman, F. Effect of ethyl cellulose on thermal resistivity of thixotropic ZnO nano-particle paste for thermal interface material in light emitting diode application. *Mater. Sci. Semicond. Process.* **58**, 61–67 (2017).

286. Li, H., Xie, Z., Zhang, Y. & Wang, J. The effects of ethyl cellulose on PV performance of DSSC made of nanostructured ZnO pastes. *Thin Solid Films* **518**, e68–e71 (2010).

287. Hayes, B. L. *Microwave Synthesis: Chemistry at the Speed of Light*. (CEM Publishing, 2002).

288. Mirzaei, A. & Neri, G. Microwave-assisted synthesis of metal oxide nanostructures for gas sensing application: A review. *Sensors Actuators, B Chem.* **237**, 749–775 (2016).

289. Bitenc, M. *et al.* The growth mechanism of zinc oxide and hydrozincite: a study using electron microscopies and in situ SAXS. *CrystEngComm* **14**, 3080 (2012).

290. Bitenc, M. *et al.* In and Ex Situ Studies of the Formation of Layered Microspherical Hydrozincite as Precursor for ZnO. *Chem. - A Eur. J.* **16**, 11481–11488 (2010).

291. Nagaraju, G. *et al.* Electrochemical heavy metal detection, photocatalytic, photoluminescence, biodiesel production and antibacterial activities of Ag–ZnO nanomaterial. *Mater. Res. Bull.* **94**, 54–63 (2017).

292. Segal, L., Creely, J. J., Martin, A. E. & Conrad, C. M. An Empirical Method for Estimating the Degree of Crystallinity of Native Cellulose Using the X-Ray Diffractometer. *Text. Res. J.* **29**, 786–794 (1959).

293. Somalu, M. R. & Brandon, N. P. Rheological Studies of Nickel/Scandia-Stabilized-Zirconia Screen Printing Inks for Solid Oxide Fuel Cell Anode Fabrication. *J. Am. Ceram. Soc.* **95**, 1220–1228 (2012).

294. Łojewska, J., Miśkowiec, P., Łojewski, T. & Proniewicz, L. M. Cellulose oxidative and hydrolytic degradation: In situ FTIR approach. *Polym. Degrad. Stab.* **88**, 512–520 (2005).

295. Abutalib, M. M. Effect of zinc oxide nanorods on the structural, thermal, dielectric and electrical properties of polyvinyl alcohol/carboxymethyle cellulose composites. *Phys. B Condens. Matter* **557**, 108–116 (2019).

296. Upadhyaya, L. *et al.* In situ grafted nanostructured ZnO/carboxymethyl cellulose nanocomposites for efficient delivery of curcumin to cancer. *J. Polym. Res.* **21**, (2014).

297. Lungu, M. V. *et al.* Investigation of optical, structural, morphological and antimicrobial properties of carboxymethyl cellulose capped Ag-ZnO nanocomposites prepared by chemical and mechanical methods. *Mater. Charact.* **120**, 69–81 (2016).

298. Zong, Y. *et al.* Facile synthesis of potassium copper ferrocyanide composite particles for selective cesium removal from wastewater in the batch and continuous processes. *RSC Adv.* **7**, 31352–31364 (2017).

299. Dong, H. *et al.* Aging study on carboxymethyl cellulose-coated zero-valent iron nanoparticles in water: Chemical transformation and structural evolution. *J. Hazard. Mater.* **312**, 234–242 (2016).

300. Gutul, T. *et al.* Preparation of poly(N-vinylpyrrolidone)-stabilized zno colloid nanoparticles. *Beilstein J. Nanotechnol.* **5**, 402–406 (2014).

301. Yang, H., Ni, S.-Q., Jiang, X., Jiang, W. & Zhan, J. In situ fabrication of single-crystalline porous ZnO nanoplates on zinc foil to support silver nanoparticles as a stable SERS substrate. *CrystEngComm* **14**, 6023 (2012).

302. Lopez, C. G., Colby, R. H. & Cabral, J. T. Electrostatic and Hydrophobic Interactions in NaCMC Aqueous Solutions: Effect of Degree of Substitution. *Macromolecules* **51**, 3165–3175 (2018).

303. Pettignano, A., Charlot, A. & Fleury, E. Carboxyl-functionalized derivatives of carboxymethyl cellulose: towards advanced biomedical applications. *Polym. Rev.* **59**, 510–560 (2019).

304. Oh, S. Y. *et al.* Crystalline structure analysis of cellulose treated with sodium hydroxide and carbon dioxide by means of X-ray diffraction and FTIR spectroscopy. *Carbohydr. Res.* **340**, 2376–2391 (2005).

305. Olsson, A. M. & Salmén, L. The association of water to cellulose and hemicellulose in paper examined by FTIR spectroscopy. *Carbohydr. Res.* **339**, 813–818 (2004).

306. Maréchal, Y. & Chanzy, H. The hydrogen bond network in I(β) cellulose as observed by infrared spectrometry. *J. Mol. Struct.* **523**, 183–196 (2000).

307. Sun, J. X., Sun, X. F., Zhao, H. & Sun, R. C. Isolation and characterization of cellulose from sugarcane bagasse. *Polym. Degrad. Stab.* **84**, 331–339 (2004).

308. Dong, Y., Hou, L. & Wu, P. Exploring the diffusion behavior of urea aqueous solution in the viscose film by ATR-FTIR spectroscopy. *Cellulose* **27**, 2403–2415 (2020).

309. Mafy, N. N., Afrin, T., Rahman, M. M., Mollah, M. Y. A. & Susan, M. A. B. H. Effect of temperature perturbation on hydrogen bonding in aqueous solutions of different urea

concentrations. *RSC Adv.* **5**, 59263–59272 (2015).

310. Mähler, J. & Persson, I. A Study of the Hydration of the Alkali Metal Ions in Aqueous Solution. *Inorg. Chem.* **51**, 425–438 (2012).

311. Hussain, I. *et al.* Enhancing the mechanical properties and self-healing efficiency of hydroxyethyl cellulose-based conductive hydrogels via supramolecular interactions. *Eur. Polym. J.* **105**, 85–94 (2018).

312. Brug, G. J., van den Eeden, A. L. G., Sluyters-Rehbach, M. & Sluyters, J. H. The analysis of electrode impedances complicated by the presence of a constant phase element. *J. Electroanal. Chem. Interfacial Electrochem.* **176**, 275–295 (1984).

313. Jović, V. D. & Jović, B. M. EIS and differential capacitance measurements onto single crystal faces in different solutions. *J. Electroanal. Chem.* **541**, 1–11 (2003).

314. Zhao, D. *et al.* A Dynamic Gel with Reversible and Tunable Topological Networks and Performances. *Matter* **2**, 390–403 (2020).

315. Zhong, C. *et al.* A review of electrolyte materials and compositions for electrochemical supercapacitors. *Chem. Soc. Rev.* **44**, 7484–7539 (2015).

316. Zhong, C. *et al. Electrolytes for Electrochemical Supercapacitors*. *Electrolytes for Electrochemical Supercapacitors* (CRC Press, 2016). doi:10.1201/b21497

317. Park, S., Baker, J. O., Himmel, M. E., Parilla, P. A. & Johnson, D. K. Cellulose crystallinity index: measurement techniques and their impact on interpreting cellulase performance. *Biotechnol. Biofuels* **3**, 10 (2010).

318. Shao, F. *et al.* Multifunctional Logic Demonstrated in a Flexible Multigate Oxide-Based Electric-Double-Layer Transistor on Paper Substrate. *Adv. Electron. Mater.* **3**, 1–7 (2017).

319. Ho, D., Jeong, H., Choi, S. & Kim, C. Organic materials as a passivation layer for metal oxide semiconductors. *J. Mater. Chem. C* **8**, 14983–14995 (2020).

320. Nomura, K. *et al.* Room-temperature fabrication of transparent flexible thin-film transistors using amorphous oxide semiconductors. *Nature* **432**, 488–492 (2004).

321. Olziersky, A. *et al.* Role of Ga2O3–In2O3–ZnO channel composition on the electrical performance of thin-film transistors. *Mater. Chem. Phys.* **131**, 512–518 (2011).

322. Barquinha, P., Pereira, L., Gonçalves, G., Martins, R. & Fortunato, E. Toward High-Performance Amorphous GIZO TFTs. *J. Electrochem. Soc.* **156**, H161 (2009).

323. Zhu, Y. S. *et al.* Natural macromolecule based carboxymethyl cellulose as a gel polymer electrolyte with adjustable porosity for lithium ion batteries. *J. Power Sources* **288**, 368–375 (2015).

324. Ahmad, N. H. B. & Isa, M. I. N. B. M. Proton conducting solid polymer electrolytes based carboxymethyl cellulose doped ammonium chloride: ionic conductivity and transport studies. *Int. J. Plast. Technol.* **19**, 47–55 (2015).

325. Santos, L. *et al.* Solvothermal Synthesis of Gallium–Indium-Zinc-Oxide Nanoparticles for Electrolyte-Gated Transistors. *ACS Appl. Mater. Interfaces* **7**, 638–646 (2015).

326. Egginger, M., Bauer, S., Schwödiauer, R., Neugebauer, H. & Sariciftci, N. S. Current versus gate voltage hysteresis in organic field effect transistors. *Monatshefte für Chemie - Chem. Mon.* **140**, 735–750 (2009).

327. Barquinha, P. *et al.* Flexible and Transparent WO 3 Transistor with Electrical and Optical Modulation. *Adv. Electron. Mater.* **1**, 1500030 (2015).

328. Nasr, B. *et al.* High-Speed, Low-Voltage, and Environmentally Stable Operation of Electrochemically Gated Zinc Oxide Nanowire Field-Effect Transistors. *Adv. Funct. Mater.* **23**, 1750–1758 (2013).

329. Martins, J. *et al.* Bias Stress and Temperature Impact on InGaZnO TFTs and Circuits.

Materials (Basel). **10**, 680 (2017).

330. Cao, Y. *et al.* A Transparent, Self-Healing, Highly Stretchable Ionic Conductor. *Adv. Mater.* **29**, 1605099 (2017).
331. Ha, M. *et al.* Aerosol Jet Printed, Low Voltage, Electrolyte Gated Carbon Nanotube Ring Oscillators with Sub-5 μs Stage Delays. *Nano Lett.* **13**, 954–960 (2013).
332. Herlogsson, L. *et al.* Low-Voltage Polymer Field-Effect Transistors Gated via a Proton Conductor. *Adv. Mater.* **19**, 97–101 (2007).
333. Pimentel, A. *et al.* Ultra-fast microwave synthesis of ZnO nanorods on cellulose substrates for UV sensor applications. *Materials (Basel).* **10**, No. 1308 (2017).
334. Pimentel, A. *et al.* Microwave synthesized ZnO nanorod arrays for UV sensors: A seed layer annealing temperature study. *Materials (Basel).* **9**, (2016).
335. Khokhra, R., Bharti, B., Lee, H.-N. & Kumar, R. Visible and UV photo-detection in ZnO nanostructured thin films via simple tuning of solution method. *Sci. Rep.* **7**, 15032 (2017).
336. Yu, R. *et al.* Piezo-phototronic Boolean Logic and Computation Using Photon and Strain Dual-Gated Nanowire Transistors. *Adv. Mater.* **27**, 940–947 (2015).
337. Dang, V. Q. *et al.* High-Performance Flexible Ultraviolet (UV) Phototransistor Using Hybrid Channel of Vertical ZnO Nanorods and Graphene. *ACS Appl. Mater. Interfaces* **7**, 11032–11040 (2015).
338. Rim, Y. S. *et al.* Ultrahigh and Broad Spectral Photodetectivity of an Organic-Inorganic Hybrid Phototransistor for Flexible Electronics. *Adv. Mater.* **27**, 6885–6891 (2015).
339. Kim, D. *et al.* High performance stretchable UV sensor arrays of SnO 2 nanowires. *Nanotechnology* **24**, 315502 (2013).
340. Wang, Z. *et al.* Light-induced pyroelectric effect as an effective approach for ultrafast ultraviolet nanosensing. *Nat. Commun.* **6**, 1–7 (2015).
341. Gupta, A. A., Arunachalam, S., Cloutier, S. G. & Izquierdo, R. Fully Aerosol-Jet Printed, High-Performance Nanoporous ZnO Ultraviolet Photodetectors. *ACS Photonics* **5**, 3923–3929 (2018).
342. Gao, T., Ji, Y. & Yang, Y. Thermo-Phototronic-Effect-Enhanced Photodetectors Based on Porous ZnO Materials. *Adv. Electron. Mater.* **5**, 1–10 (2019).
343. Pimentel, A. *et al.* Microwave Synthesized ZnO Nanorods Arrays for UV Sensors : a Seed Layer Annealing Temperature Study. *Materials (Basel).* **9**, No. 299 (2016).
344. Li, Z. *et al.* Ultra-sensitive UV and H2S dual functional sensors based on porous In2O3 nanoparticles operated at room temperature. *J. Alloys Compd.* **770**, 721–731 (2019).
345. Liu, C.-F., Lu, Y.-J. & Hu, C.-C. Effects of Anions and pH on the Stability of ZnO Nanorods for Photoelectrochemical Water Splitting. *ACS Omega* **3**, 3429–3439 (2018).
346. Tak, Y. J. *et al.* Multifunctional, Room-Temperature Processable, Heterogeneous Organic Passivation Layer for Oxide Semiconductor Thin-Film Transistors. *ACS Appl. Mater. Interfaces* **12**, 2615–2624 (2020).
347. Saleh, R., Barth, M., Eberhardt, W. & Zimmermann, A. Bending Setups for Reliability Investigation of Flexible Electronics. *Micromachines* **12**, 78 (2021).
348. Takechi, K., Nakata, M., Eguchi, T., Yamaguchi, H. & Kaneko, S. Temperature-Dependent Transfer Characteristics of Amorphous InGaZnO 4 Thin-Film Transistors. *Jpn. J. Appl. Phys.* **48**, 011301 (2009).
349. Barquinha, P. *et al.* Low-temperature sputtered mixtures of high-κ and high bandgap dielectrics for GIZO TFTs. *J. Soc. Inf. Disp.* **18**, 762 (2010).
350. Barquinha, P. *et al.* Performance and Stability of Low Temperature Transparent Thin-Film Transistors Using Amorphous Multicomponent Dielectrics. *J. Electrochem. Soc.* **156**,

H824 (2009).

351. Thiemann, S. *et al.* High-Mobility ZnO Nanorod Field-Effect Transistors by Self-Alignment and Electrolyte-Gating. *ACS Appl. Mater. Interfaces* **5**, 1656–1662 (2013).

352. Ha, M. *et al.* Printed, Sub-3V Digital Circuits on Plastic from Aqueous Carbon Nanotube Inks. *ACS Nano* **4**, 4388–4395 (2010).

353. Deka Boruah, B. Zinc oxide ultraviolet photodetectors: Rapid progress from conventional to self-powered photodetectors. *Nanoscale Adv.* **1**, 2059–2085 (2019).

354. Charipar, K., Kim, H., Piqué, A. & Charipar, N. ZnO Nanoparticle/Graphene Hybrid Photodetectors via Laser Fragmentation in Liquid. *Nanomaterials* **10**, 1648 (2020).

355. Xu, Q. *et al.* Flexible Self-Powered ZnO Film UV Sensor with a High Response. *ACS Appl. Mater. Interfaces* **11**, 26127–26133 (2019).

356. Al-Hardan, N. H., Hamid, M. A. A., Shamsudin, R. & Othman, N. K. Ultraviolet Sensors Based on Two-Dimensional Zinc Oxide Structures. *Optoelectron. - Adv. Device Struct.* (2017). doi:10.5772/67311

357. Gao, Y. *et al.* A Novel Hybrid-Layered Organic Phototransistor Enables Efficient Intermolecular Charge Transfer and Carrier Transport for Ultrasensitive Photodetection. *Adv. Mater.* **31**, 1–9 (2019).

358. Dai, S. *et al.* Wood-Derived Nanopaper Dielectrics for Organic Synaptic Transistors. *ACS Appl. Mater. Interfaces* **10**, 39983–39991 (2018).

359. Pietsch, M. *et al.* Biodegradable inkjet-printed electrochromic display for sustainable short-lifecycle electronics. *J. Mater. Chem. C* **8**, 16716–16724 (2020).

360. Cao, Y. & Uhrich, K. E. Biodegradable and biocompatible polymers for electronic applications: A review. *J. Bioact. Compat. Polym.* **34**, 3–15 (2019).

361. Hwang, S. W. *et al.* Materials and fabrication processes for transient and bioresorbable high-performance electronics. *Adv. Funct. Mater.* **23**, 4087–4093 (2013).

362. Dagdeviren, C. *et al.* Transient, biocompatible electronics and energy harvesters based on ZnO. *Small* **9**, 3398–3404 (2013).

363. Guo, J. *et al.* Low-voltage transient/biodegradable transistors based on free-standing sodium alginate membranes. *IEEE Electron Device Lett.* **36**, 576–578 (2015).

364. Cheng, H. & Vepachedu, V. Recent development of transient electronics. *Theor. Appl. Mech. Lett.* 1–11 (2016). doi:10.1016/j.taml.2015.11.012

365. Pullanjiot, N. & Swaminathan, S. Enhanced electrochemical properties of metal oxide interspersed polymer gel electrolyte for QSDSSC application. *Sol. Energy* **186**, 37–45 (2019).

366. Upadhyay, N. K. *et al.* Emerging Memory Devices for Neuromorphic Computing. *Adv. Mater. Technol.* **4**, 1800589 (2019).

367. Cunha, M., Lourenço, A., Barreiros, S., Paiva, A. & Simões, P. Valorization of cork using subcritical water. *Molecules* **25**, (2020).

368. Aroso, I. M., Araújo, A. R., Pires, R. A. & Reis, R. L. Cork: Current Technological Developments and Future Perspectives for this Natural, Renewable, and Sustainable Material. *ACS Sustain. Chem. Eng.* **5**, 11130–11146 (2017).

369. Mislata, A. M., Puxeu, M. & Ferrer-Gallego, R. Aromatic Potential and Bioactivity of Cork Stoppers and Cork By-Products. *Foods* **9**, 133 (2020).

370. Ferreira, R. *et al.* Isolation of suberin from birch outer bark and cork using ionic liquids: A new source of macromonomers. *Ind. Crops Prod.* **44**, 520–527 (2013).

371. Cordeiro, N. *et al.* Cork suberin as an additive in offset lithographic printing inks. *Ind. Crops Prod.* **11**, 63–71 (2000).

372. Fernandes, E. M., Correlo, V. M., Chagas, J. A. M., Mano, J. F. & Reis, R. L. Properties of new cork–polymer composites: Advantages and drawbacks as compared with commercially available fibreboard materials. *Compos. Struct.* **93**, 3120–3129 (2011).

373. Gil, L. New Cork-Based Materials and Applications. *Materials (Basel).* **8**, 625–637 (2015).

374. Pullar, R. C. & Novais, R. M. Ecoceramics. *Mater. Today* **20**, 45–46 (2017).

375. Crouvisier-Urion, K. *et al.* Four hundred years of cork imaging: New advances in the characterization of the cork structure. *Sci. Rep.* **9**, 1–10 (2019).

376. Miranda, I., Gominho, J. & Pereira, H. Cellular structure and chemical composition of cork from the Chinese cork oak (Quercus variabilis). *J. Wood Sci.* **59**, 1–9 (2013).

377. Gil, A. ., Lopes, M., Rocha, J. & Pascoal Neto, C. A 13C solid state nuclear magnetic resonance spectroscopic study of cork cell wall structure: the effect of suberin removal. *Int. J. Biol. Macromol.* **20**, 293–305 (1997).

378. Fernandes, E. M., Correlo, V. M., Mano, J. F. & Reis, R. L. Cork-polymer biocomposites: Mechanical, structural and thermal properties. *Mater. Des.* **82**, 282–289 (2015).

379. Ferreira, R. *et al.* Suberin isolation from cork using ionic liquids: characterisation of ensuing products. *New J. Chem.* **36**, 2014 (2012).

380. Silva, S. P. *et al.* Cork: properties, capabilities and applications. *Int. Mater. Rev.* **53**, 256–256 (2008).

381. Garcia, H. *et al.* Dissolution of cork biopolymers in biocompatible ionic liquids. *Green Chem.* **12**, 367 (2010).

382. De Oliveira, H., Yoon, B., Michaud, V., Nam, J. Do & Suhr, J. All natural cork composites with suberin-based polyester and lignocellulosic residue. *Ind. Crops Prod.* **109**, 843–849 (2017).

383. Vilela, C., Sousa, A. F., Freire, C. S. R., Silvestre, A. J. D. & Pascoal Neto, C. Novel sustainable composites prepared from cork residues and biopolymers. *Biomass and Bioenergy* **55**, 148–155 (2013).

384. Ferreira, R. *et al.* Unveiling the dual role of the cholinium hexanoate ionic liquid as solvent and catalyst in suberin depolymerisation. *RSC Adv.* **4**, 2993–3002 (2014).

385. Gandini, A., Pascoal Neto, C. & Silvestre, A. J. D. Suberin: A promising renewable resource for novel macromolecular materials. *Prog. Polym. Sci.* **31**, 878–892 (2006).

386. Garcia, H. *et al.* Ex situ reconstitution of the plant biopolyester suberin as a film. *Biomacromolecules* **15**, 1806–1813 (2014).

387. Filipe-Ribeiro, L., Cosme, F. & Nunes, F. M. A Simple Method To Improve Cork Powder Waste Adsorption Properties: Valorization as a New Sustainable Wine Fining Agent. *ACS Sustain. Chem. Eng.* **7**, 1105–1112 (2019).

388. Correia, V. G. *et al.* The molecular structure and multifunctionality of the cryptic plant polymer suberin. *Mater. Today Bio* **5**, (2020).

389. Balouiri, M., Sadiki, M. & Ibnsouda, S. K. Methods for in vitro evaluating antimicrobial activity: A review. *J. Pharm. Anal.* **6**, 71–79 (2016).

390. Abebe, B., Zereffa, E. A., Tadesse, A. & Murthy, H. C. A. A Review on Enhancing the Antibacterial Activity of ZnO: Mechanisms and Microscopic Investigation. *Nanoscale Res. Lett.* **15**, 190 (2020).

391. Jiang, S., Lin, K. & Cai, M. ZnO Nanomaterials: Current Advancements in Antibacterial Mechanisms and Applications. *Front. Chem.* **8**, 1–5 (2020).

392. Sirelkhatim, A. *et al.* Review on Zinc Oxide Nanoparticles: Antibacterial Activity and Toxicity Mechanism. *Nano-Micro Lett.* **7**, 219–242 (2015).

393. Zhu, H. *et al.* Transparent nanopaper with tailored optical properties. *Nanoscale* **5**, 3787

(2013).

394. Kleemann, H., Krechan, K., Fischer, A. & Leo, K. A Review of Vertical Organic Transistors. *Adv. Funct. Mater.* **30**, 1907113 (2020).

395. Kleemann, H., Schwartz, G., Zott, S., Baumann, M. & Furno, M. Megahertz operation of vertical organic transistors for ultra-high resolution active-matrix display. *Flex. Print. Electron.* **5**, (2020).

396. Yun, H. *et al.* Stencil Nano Lithography Based on a Nanoscale Polymer Shadow Mask : Towards Organic Nanoelectronics. *Nat. Publ. Gr.* 1–8 (2015). doi:10.1038/srep10220

397. Linghu, C., Zhang, S., Wang, C. & Song, J. Transfer printing techniques for flexible and stretchable inorganic electronics. *npj Flex. Electron.* **2**, (2018).

398. Bai, Z. *et al.* High sensitivity, fast speed and self-powered ultraviolet photodetectors based on ZnO micro/nanowire networks. *Prog. Nat. Sci. Mater. Int.* **24**, 1–5 (2014).

399. Purusothaman, Y., Alluri, N. R., Chandrasekhar, A., Venkateswaran, V. & Kim, S.-J. Piezophototronic gated optofluidic logic computations empowering intrinsic reconfigurable switches. *Nat. Commun.* **10**, 4381 (2019).

Annex A

Supplementary figures

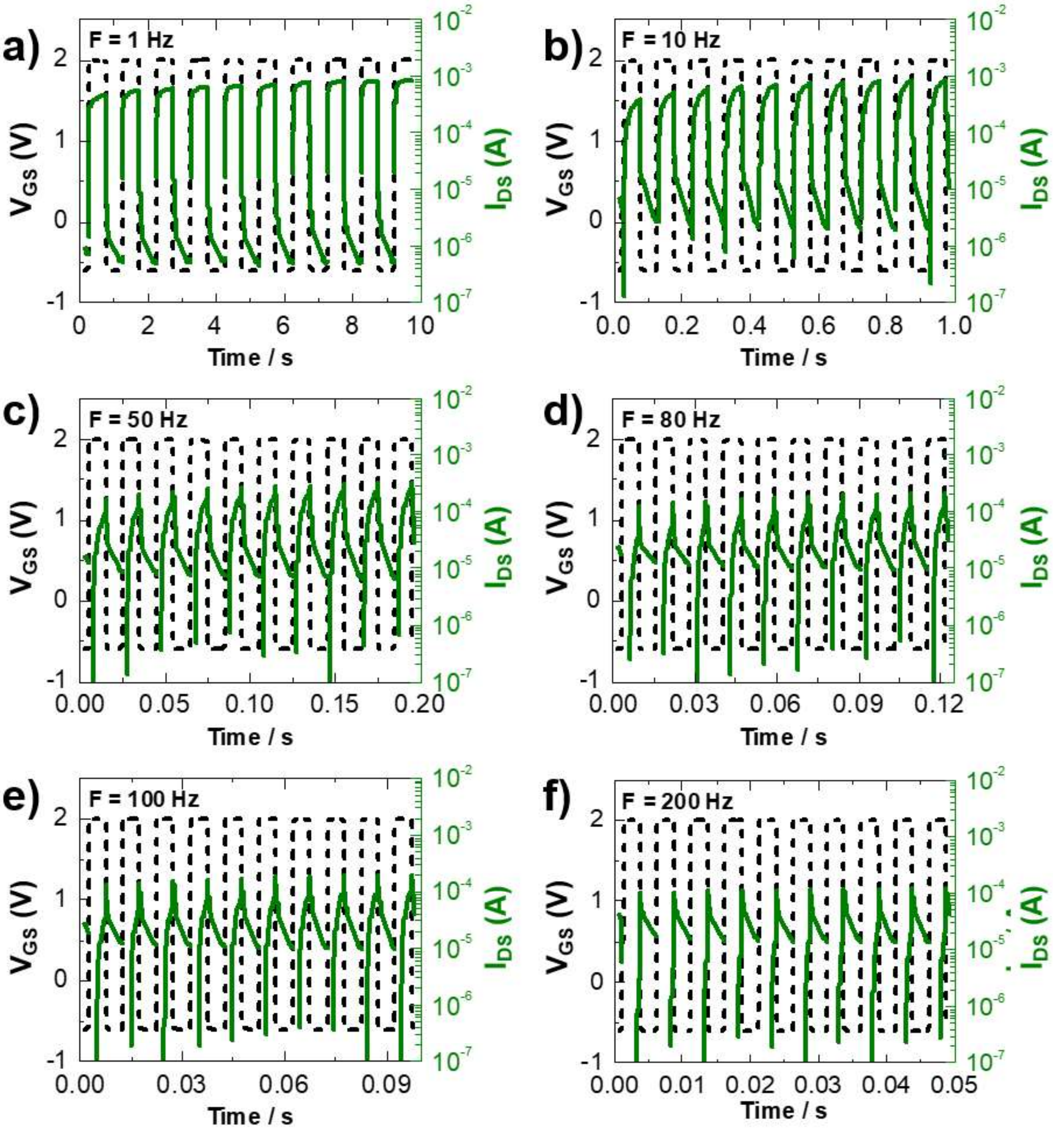

Figure S1. Dynamic electrical characterization of IGZO EGTs on paper gated by M1C1 electrolyte. Variation of drain current with increasing cycles of gate voltage pulses from -0.6 until 2 V for different frequencies: **a)** 1 Hz, **b)** 10 Hz, **c)** 50 Hz, **d)** 80 Hz, **e)** 100 Hz and **f)** 200 Hz.

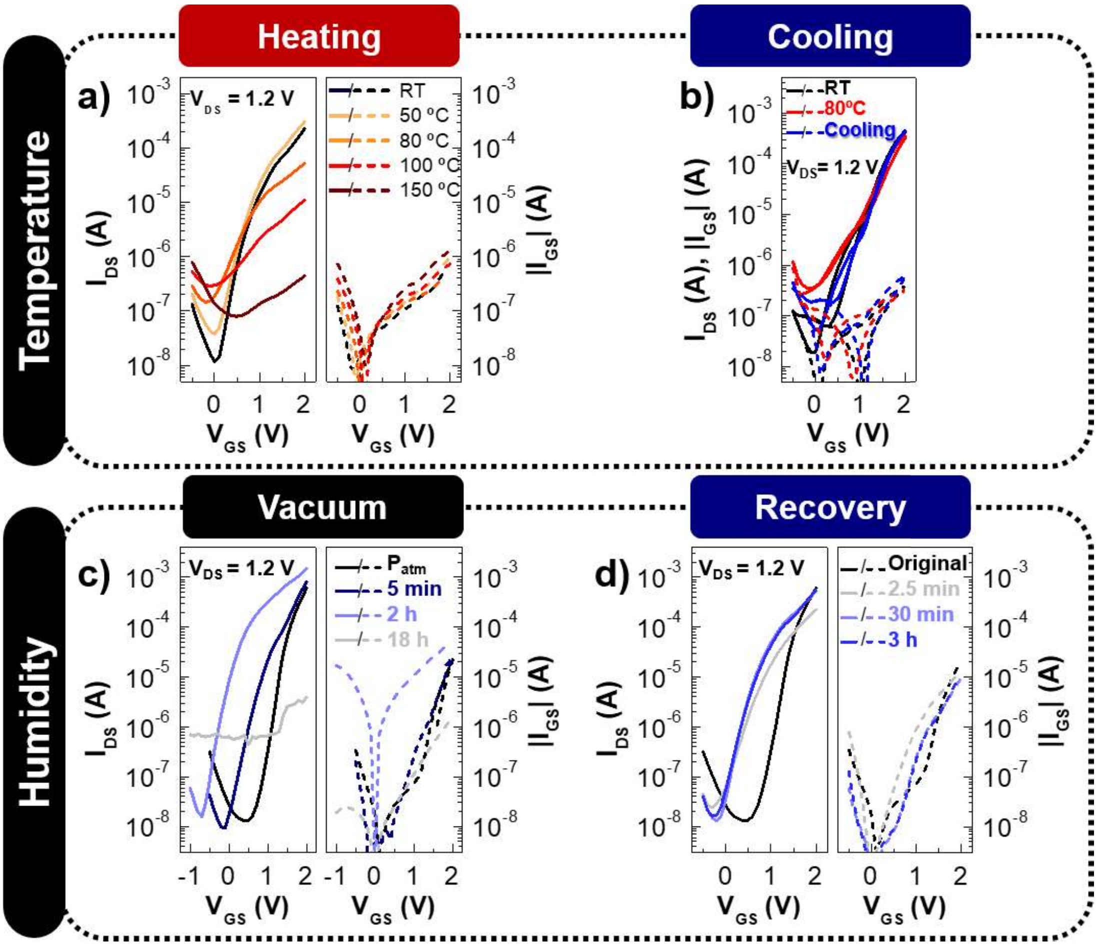

Figure S2. Electrical performance of L1N3 hydrogel-gated IGZO transistors on multilayer-coated paper after exposure to distinct environmental conditions. **a)** I_{DS}–V_{GS} curves obtained at different temperatures during heating (20 min of stabilization at each temperature before measuring). **b)** I_{DS}–V_{GS} curves obtained while cooling a device at ambient conditions, previously heated on a hotplate at 80 ºC for 20 min. I_{DS}–V_{GS} curves obtained **c)** under vacuum conditions, and **d)** during recovery at atmospheric pressure. All curves were acquired with a V_{GS} scan rate of 50 mV s^{-1} for saturation regime (V_{DS} = 1.2 V).

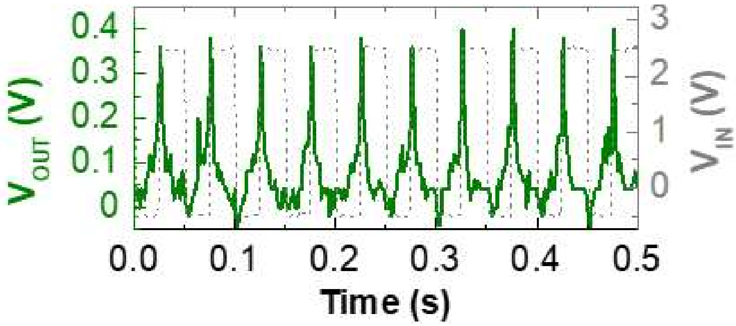

Figure S3. Dynamic response of N100 hydrogel-gated NOT gate with a pencil-drawn resistance of 36 kΩ. V_{OUT} vs. time to an input square-wave pulse from V_{IN} = -0.5 to 2.5 V and V_{DD} = 1 V for 20 Hz.

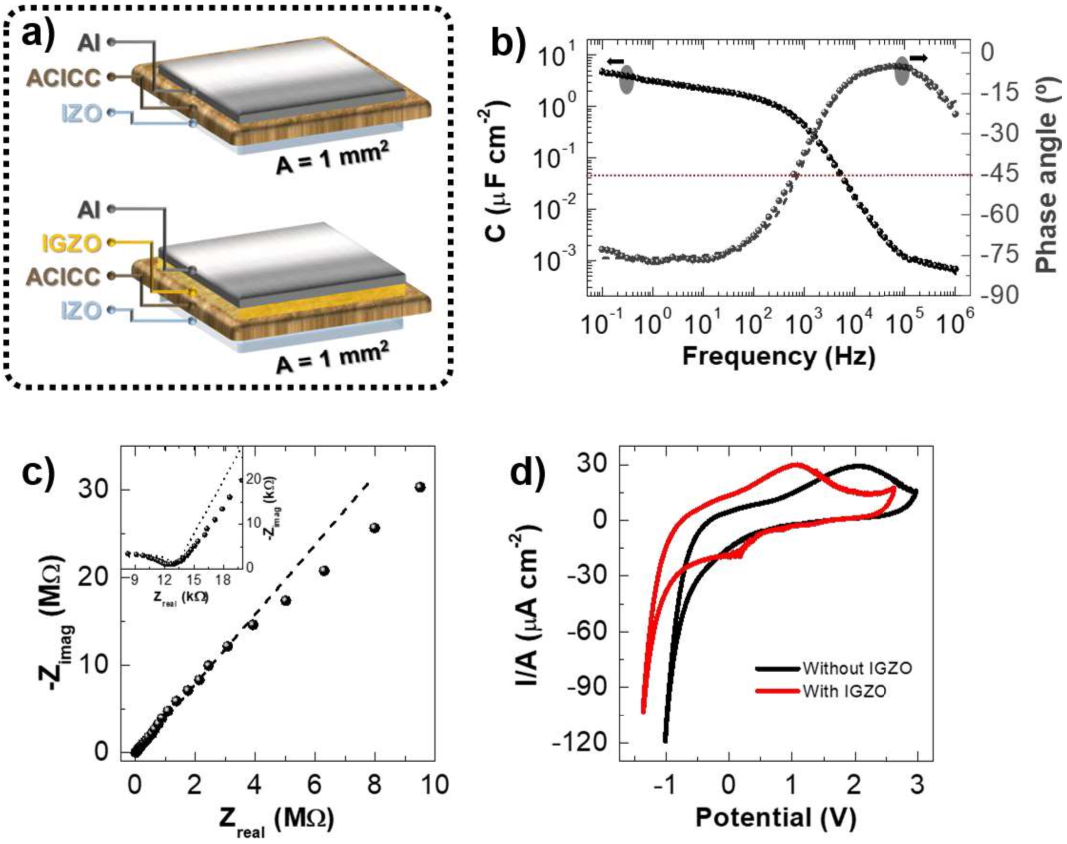

Figure S4. Electrochemical characterization of the ACICC membrane using a capacitor structure similar to the IGZO NCGTs. **a)** Schematics of the electrochemical cells, with or without IGZO layer. **b)** Capacitance and phase angle as a function of frequency for ACICC membrane using IZO/ACICC/Al structures with an area of 1mm^2, and respective **c)** Nyquist plot. **d)** Influence of the semiconducting layer in the CV curves (scan rate: 0.4 V s^{-1}).

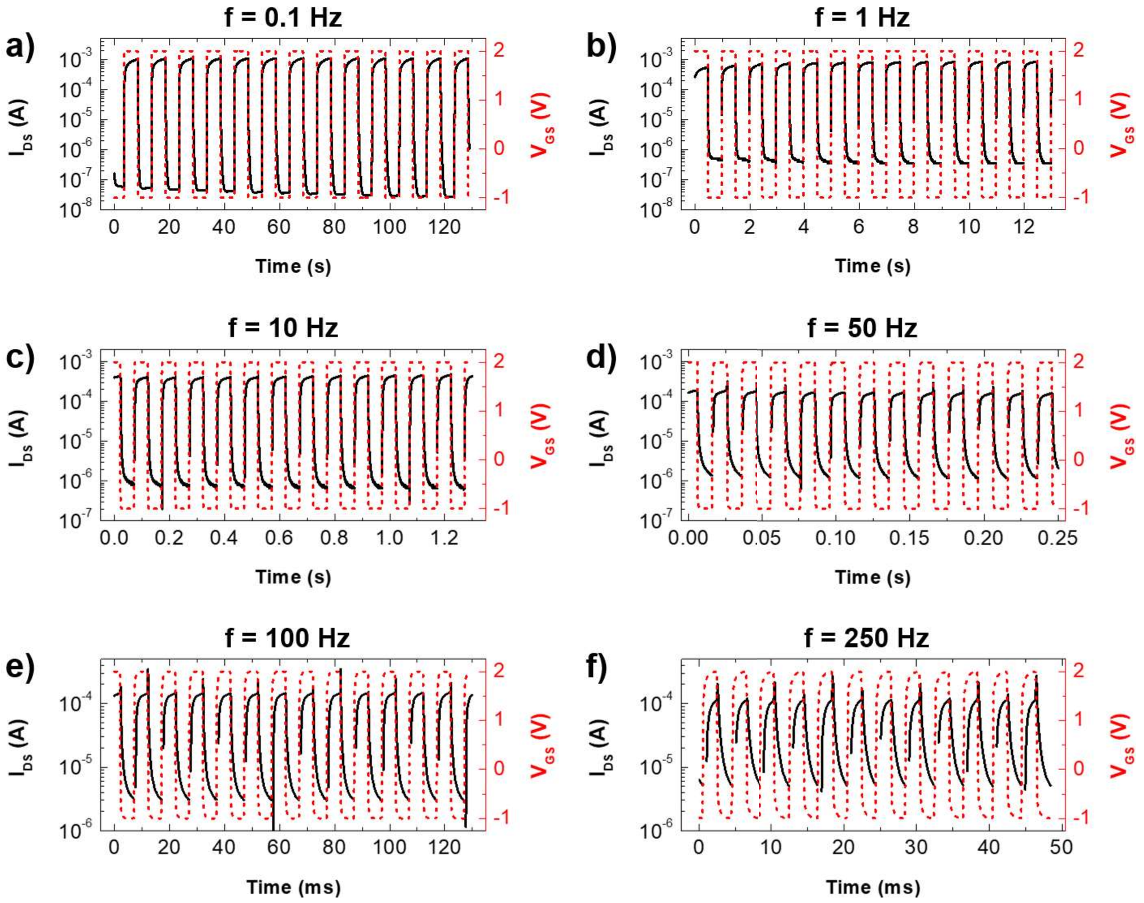

Figure S5. Variation of I_{DS} with increasing cycles of gate voltage pulses from -0.5 until 2 V for different frequencies: **a)** 0.1 Hz, **b)** 1 Hz, **c)** 10 Hz, **d)** 50 Hz, **e)** 100 Hz, and **f)** 250 Hz.

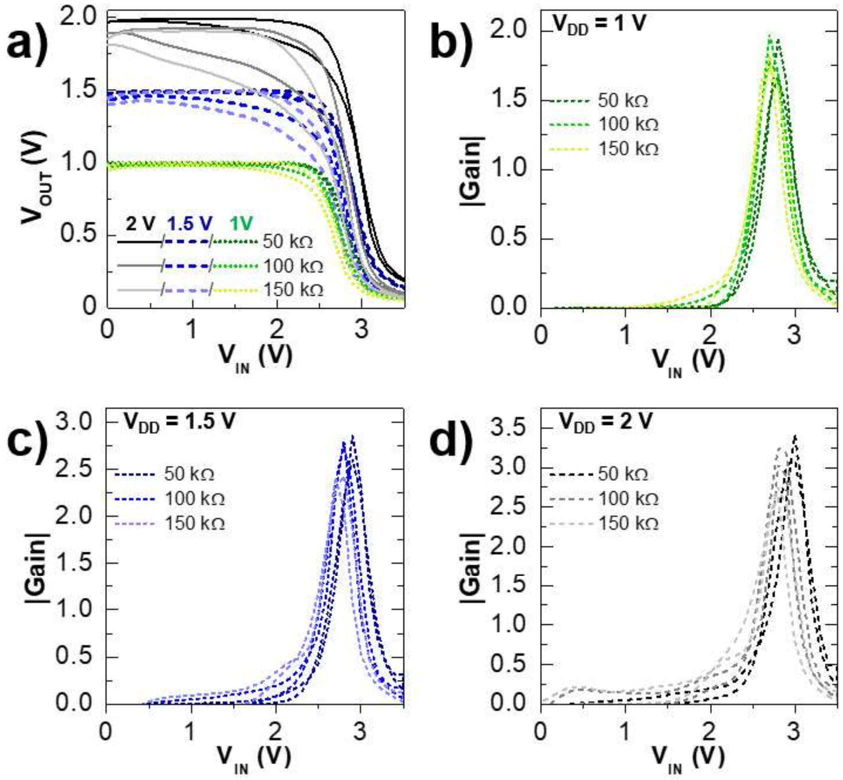

Figure S6. Influence of V_{DD} and R_L on the electrical performance of the fabricated inverter with a pencil-drawn load resistance. Static VTC curves of the NOT gate for different R_L (from 50 kΩ to 150 kΩ) along the pencil-drawn graphite line for different V_{DD} (1, 1.5 and 2 V), and respective static |gain| characteristic curves for a V_{DD} of **b)** 1 V, **c)** 1.5 V and **d)** 2 V (voltage scan rate of 50 mV s^{-1}).

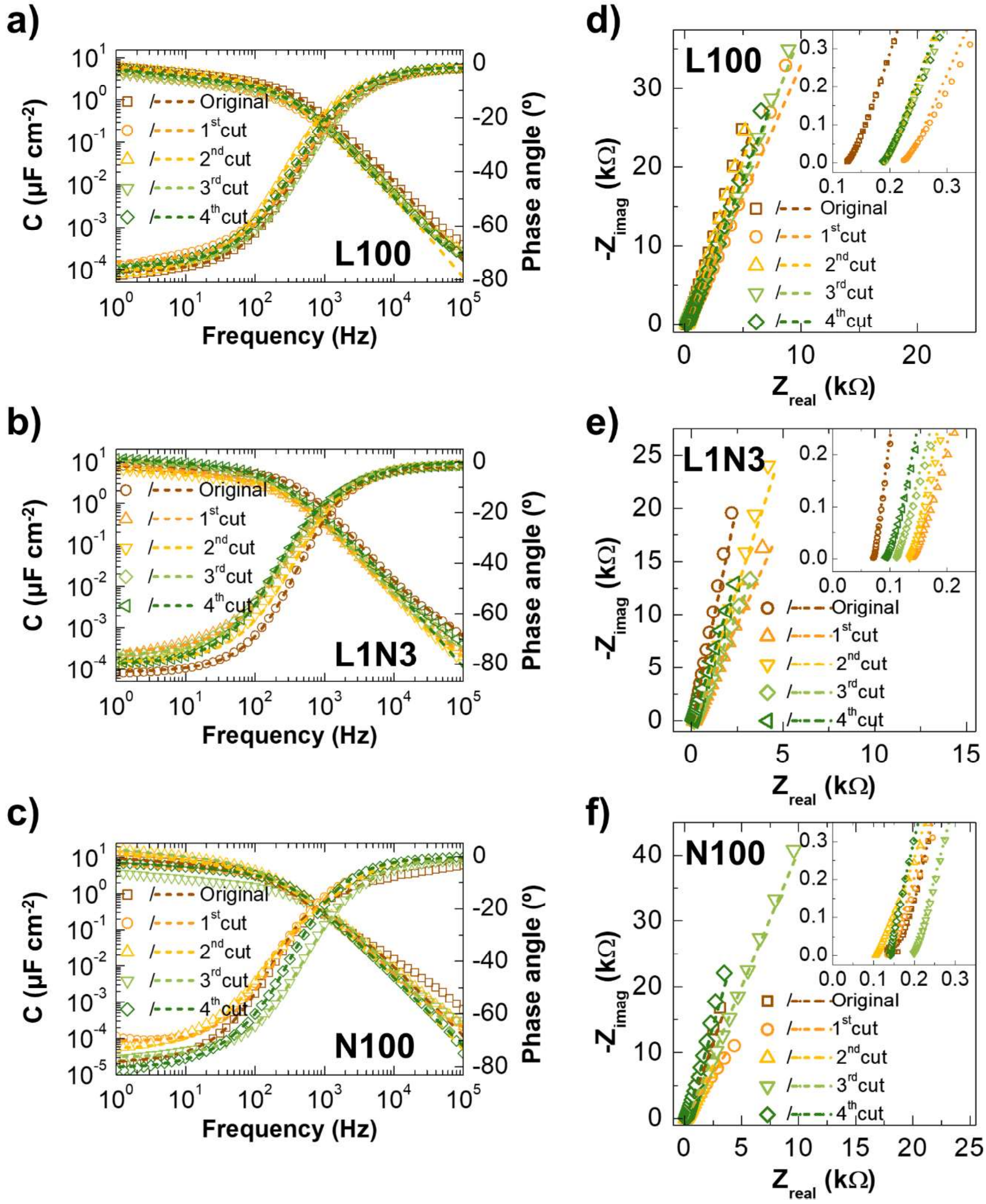

Figure S7. Electrochemical performance of the L100, L1N3 and N100 membranes before and after several cut/healing cycles at room temperature. **a-c)** Capacitance and phase angle versus frequency plots, and corresponding **d–f)** nyquist plots for L100, L1N3 and N100 membranes, respectively. The open symbols and the dashed lines denote the experimental and the fitted data, respectively.

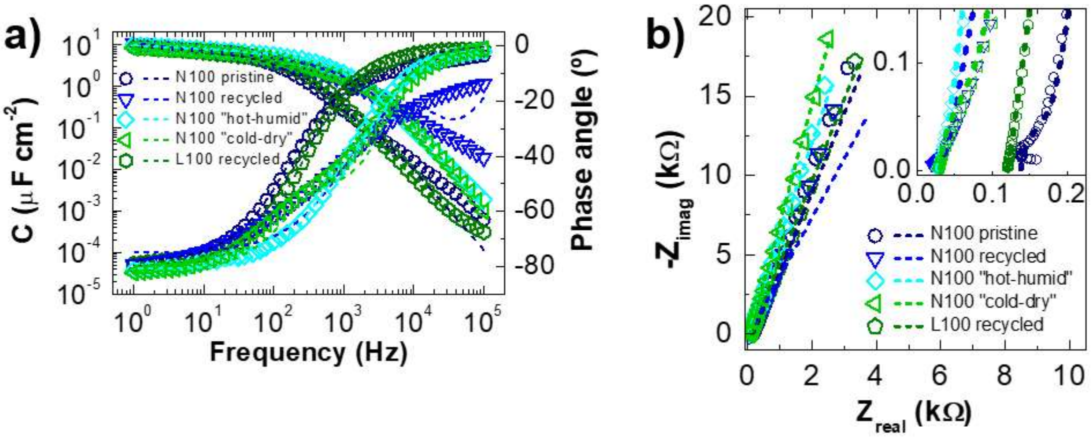

Figure S8. Electrochemical performance of distinct N100 membranes (pristine, healed, and recycled) and comparison with recycled L100 membrane. **a)** Capacitance and phase angle versus frequency plots of the different N100 membranes (pristine, recycled, and healed). **b)** Respective nyquist plots. The open symbols and the dashed lines denote the experimental and the fitted data using Dasgupta's ECM, respectively.

Annex B

Supplementary tables

Table S1. Summary of processing routes (precursor method **–** PM, and/or nanoparticulate method - NM), and processing parameters (printing technique, and temperature of thermal annealing) adopted for printed n- or p-type TMOS materials, and features of the resulting printed TMOS transistors, including their configuration, channel dimensions, materials, and electrical performance.

Processing route	**TMOS material**	**Printing technique**	**Thermal annealing [ºC]**	**Device configuration**	**Substrate**	**Gate dielectric/ electrolyte**	**Dimensions [µm]**	**V_{ON} [V], V_{th} [V]**	**$I_{ON/OFF}$**	**Mobility [$cm^2V^{-1}s^{-1}$]**	**Year**	**Ref.**
NM	ZnO NPs	Screen	350	Planar	Glass	CSPE	W/L ≈120 L = 330	V_{ON} = 1.9	8.74×10^3	5.73	2017	57
NM	ZnO NPs	Screen	150	Planar	Office paper	CSPE	W/L ≈120 L = 330	V_{ON} = 2.1	1.73×10^3	0.01	2017	57
NM	ZnO NPs	Screen	150	Planar	MFC nanopaper	CSPE	W/L ≈120 L = 330	V_{ON} = 1.9	3.72×10^3	0.07	2017	57
NM	ZnO NPs	Inkjet	400	SBGT	Si wafer	SiO_2	W/L = 25 L = 80	-	$\approx 10^4$	0.03	2016	204
NM	ZnO NRs	Inkjet	RT	CBGT	Si wafer	SiO_2	W/L = 10 L = 10	-	$<10^4$	0.17	2014	205
NM	ZnO NRs	Inkjet	150	CBGT	Si wafer	SiO_2	W/L = 10 L = 10	V_{th} = -3.3	$<10^6$	3.03	2014	205
NM	ZnO NWs	Inkjet	200	STGT	Glass	Poly(methyl methacrylate)	L = 0.5	V_{ON} =-2.5	$\approx 10^5$	21.3	2007	203
NM and PM	ZnO NPs + precursor	Pen writing	120	SBGT	Office paper	Office paper	W/L ≈185 L = 200	V_{ON} = 1	8.06×10^1	4.45×10^{-3}	2017	58
PM	ZnO	Aerosol jet	250	STGT	PI	Ion gel	W/L = 20 L = 2	V_{th} = 0.97	2.15×10^5	1.61	2013	132
PM	ZnO	Aerosol jet	300	STGT	Si wafer	Ion gel	W/L = 20 L = 50	V_{th} = 0.9	$\approx 10^4$	1.48	2014	209
PM	ZnO	Aerosol jet	300	STGT	Si wafer	Ion gel	W/L = 4 L = 50	V_{th} = 0.5	$\approx 10^5$	1.9	2014	208
PM	ZnO	Nozzle jet	500	SBGT	Si wafer	SiO_2	W/L = 2 L = 200	-	6×10^3	1.42	2015	207
PM	ZnO	Inkjet	150	SBGT	Si wafer	SiO_2	-	V_{ON} = 12	$\approx 10^6$	0.4	2008	206
PM	ZnO	Inkjet	300	SBGT	Si wafer	SiO_2	-	V_{ON} = 13	$>10^6$	4-6	2008	206
PM	ZTO	Inkjet	500	CBGT	Si wafer	SiO_2	W/L =10 L = 10	V_{th} = 1.9	5×10^6	0.58	2009	211
PM	ZTO	Inkjet	500	SBGT	Glass	SiO_2	W/L =10 L = 10	V_{ON} = -9, V_{th} = 8.6	1.5×10^9	4.98	2010	210
PM	ZTO	Inkjet	300	CBGT	Glass	AlO_x	W/L =25 L = 8	V_{th} = 0.86	$\approx 10^7$	36	2011	213

Table S1. Continuation (I).

Processing route	TMOS material	Printing technique	Thermal annealing [ºC]	Device configuration	Substrate	Gate dielectric/ electrolyte	Dimensions [µm]	V_{ON} [V], V_{th} [V]	$I_{ON/OFF}$	Mobility [$cm^2V^{-1}s^{-1}$]	Year	Ref.
PM	ZTO	EHD	400	SBGT	Si wafer	SiO_2	W/L =15 L = 100	V_{th} = 7.17	≈10^7	4.89	2013	214
PM	ZTO	EHD	500	SBGT	Si wafer	SiO_2	W/L =15 L = 50	V_{th} = 2.16	3.68×10^6	9.82	2014	212
PM	IGZO	Inkjet	450	SBGT	Glass	SiN_x	W/L ≈6.67 L = 150	V_{th} = 6.2	5×10^4	0.03	2009	217
PM	IGZO	Inkjet	400	SBGT	Si wafer	SiO_2	W/L = 9 L = 50	V_{th} = 17.4	5×10^6	1.3	2012	215
PM	IGZO	Inkjet	300	SBGT	Si wafer	SiO_2	W/L = 7:1	V_{th} =14	7×10^6	3	2013	216
PM	IGZO	Inkjet	300	SBGT	Si wafer	SiO_2	L = 250	V_{th} = 7.9	≈10^5	6.42	2016	218
PM	IGZO	Inkjet	400	SBGT	Si wafer	SiO_2	W/L = 5 L = 50	V_{th} = -5	2.16×10^6	1.6	2017	187
PM	IGZO	EHD	400	SBGT	Si wafer	SiO_2	W/L = 10 L = 100	-	4×10^6	1.3	2013	219
PM	IGZO	Gravure	550	SBGT	Glass	SiN_x	W/L ≈6.67 L = 150	V_{th} = 1.35	1.36×10^6	0.81	2010	220
PM	IZTO	Inkjet	600	SBGT	Si wafer	SiO_2	W/L = 7 L = 200	V_{ON} = 2	>10^6	30	2009	221
PM	IZTO	Inkjet	300	CBGT	Glass	AlO_x	W/L = 25 L = 100	V_{th} =-0.16	>10^6	114	2014	222
PM	IZO	EHD	500	SBGT	Si wafer	SiO_2	W/L = 5 L = 20	-	≈10^5	3.7	2012	223
PM	IZO	EHD	500	SBGT	Glass/ITO	HfO_2	W/L = 5 L = 20	V_{th} = 2	≈10^3	32	2012	223
PM	IZO	Gravure	425	CBGT	Si wafer	SiO_2	W/L = 500 L = 20	V_{th} = 2.3	>10^6	9.4	2015	224
PM	IZO	Flexo	450	CBGT	Si wafer	SiO_2	W/L =1000 L = 10	V_{th} = 4	5.2×10^7	2.4	2014	225
PM	IZO	Flexo	425	CBGT	Si wafer	SiO_2	W/L = 500 L = 20	V_{th} = 1.3	<10^6	8.3	2015	224
PM	IZO	Inkjet	600	SBGT	Si wafer	SiO_2	W/L = 7 L = 200	V_{ON} = -26	≈10^4	7.4	2007	226
PM	IGO	Inkjet	320	CBGT	Glass	ZrO_x	W/L = 1.5 L = 40	V_{th} = 0.04	≈10^7	7.5	2017	227

Table S1. Continuation (II).

Processing route	TMOS material	Printing technique	Thermal annealing [ºC]	Device configuration	Substrate	Gate dielectric/ electrolyte	Dimensions [µm]	V_{ON} [V], V_{th} [V]	$I_{ON/OFF}$	Mobility [$cm^2V^{-1}s^{-1}$]	Year	Ref.
NM	ITO NPs	Inkjet	RT	Planar	Glass/ITO	CSPE	W/L = 8 L = 10	V_{th} = -0.22	2×10^4	5	2012	52
PM	In_2O_3	EHD	250	SBGT	Si wafer	SiO_2	W/L = 2 L = 50	V_{th} = -15	$\approx 10^8$	7.7	2016	238
PM	In_2O_3	EHD	250	SBGT	Si wafer r	Zr:AlO_x	W/L = 2 L = 50	V_{th} = -2.6	$\approx 10^3$	230	2016	238
PM	In_2O_3	EHD	250	SBGT	PI	Al_2O_3	W/L = 0.15 L = 40	-	$\approx 10^5$	5	2016	238
PM	In_2O_3	Flexo	300	SBGT	PI	Al_2O_3	W/L = 12.5 L = 80	V_{ON} = -0.6	$>10^6$	8	2013	234
PM	In_2O_3	Aerosol jet	400	STGT	Si wafer	Ion gel	-	V_{ON} = -0.4	$\approx 10^6$	3.4	2017	235
PM	In_2O_3	Inkjet	200	SBGT	Si wafer	SiO_2	15, 100	V_{th} = 1.83	1.66×10^8	3.98	2013	236
PM	In_2O_3	Inkjet	400	Planar	Glass/ITO	CSPE	W/L = 3 L = 50	V_{th} = 0.37	2×10^7	126	2013	239
PM	In_2O_3	Inkjet	400	Planar	Si wafer	CSPE	W/L = 1 L = 100	V_{th} = 0.32	$\approx 10^6$	48	2015	54
PM	In_2O_3	Inkjet	400	Planar	Glass/ITO	CSPE	L = 50	V_{th} = 0.2	10^5–10^6	90	2016	229
PM	In_2O_3	Inkjet	350	CBGT	Si wafer	SiO_2	W/L = 10 L = 10	V_{th} = -1.4	$\approx 10^6$	9.9	2017	228
PM	In_2O_3	Inkjet	225	SBGT	Si wafer	SiO_2	W/L = 2 L = 100	V_{th} = -4	3.5×10^6	13.7	2018	237
NM	In_2O_3 NPs	Inkjet	RT	Planar	PEN/ITO	CSPE	W/L = 12 L = 10	V_{ON} = 0.08, V_{th} = 0.54	2×10^3	0.8	2011	53
NM	In_2O_3 NPs	Inkjet	RT	Planar	Glass	CSPE	W/L = 1.7 L = 80	V_{th} = 0.35	$>10^6$	12.5	2015	230
PM	InO_x	Inkjet	300	CBGT	Glass	AlO_x:Nd	W/L ≈17 L = 3.5	V_{th} = -8.4	2.7×10^9	4.9	2016	231
PM	InO_x	Inkjet	250	SBGT	Si wafer	AlO_x	W/L = 4-6	V_{ON} = -0.5	$\approx 10^7$	10	2017	232
PM	SnO_2	Inkjet	550	Vertical S/D, lateral gate	Si wafer	CSPE	W/L = 500 L = 0.05	V_{th} = 0.6	$\approx 10^8$	3	2016	240
PM	NiO_x	Inkjet	280	SBGT	Si wafer	Al_2O_3	W/L = 10 L = 30	V_{th} = -0.6	5.3×10^4	0.78	2018	241
NM	CuO QDs	Inkjet	RT	CBGT	Si wafer	SiO_2	W/L = 2 L = 40	V_{th} = 0.41	8.3×10^3	16.4	2013	190

Table S1. Continuation (III).

Processing route	TMOS material	Printing technique	Thermal annealing [ºC]	Device configuration	Substrate	Gate dielectric/ electrolyte	Dimensions [µm]	V_{ON} [V], V_{th} [V]	$I_{ON/OFF}$	Mobility [$cm^2V^{-1}s^{-1}$]	Year	Ref.
PM	CuO	Inkjet	400	Planar	Si wafer	CSPE	W/L = 7 L = 10	V_{th} = -0.23	≈10^3	0.22	2015	[54]
NM	Cu_2O NPs	Inkjet	RT	Planar	Glass	CSPE	W/L = 1.6 L = 50	-	≈10^2	-	2015	[230]

Table S2. Summary of processing routes (PM and/or NM), and processing parameters (printing technique, and low-temperature annealing process) adopted for printed n- or p-type TMOS materials, and features of the resulting printed TMOS transistors, including their configuration, channel dimensions, materials, and electrical performance.

Processing route	TMOS material	Printing technique	Annealing process	Device configuration	Substrate	Gate dielectric/ electrolyte	Dimensions [µm]	V_{ON} [V], V_{th} [V]	$I_{ON/OFF}$	Mobility [$cm^2V^{-1}s^{-1}$]	Year	Ref.
PM	IGZO	Inkjet	Thermal (200 ºC) and laser	SBGT	Si wafer	SiO_2	W/L = 5 L = 50	V_{th} = -8.5	1.29×10^6	1.5	2017	[187]
PM	IGZO	Inkjet	Laser annealing	SBGT	PEN	PVP/Al_2O_3	W/L = 1 L = 50	V_{th} ≈3.25	7.2×10^5	4.24	2019	[188]
PM	In_2O_3	Inkjet	Thermal (150 ºC) and FUV	SBGT	Si wafer	SiO_2	W/L = 12.5 L = 80	V_{th} = 2.6	$\approx 10^6$	4.3	2017	[189]
PM	In_2O_3	Inkjet	Temperature (150 ºC) and FUV	SBGT	PEN	Al_2O_3	W/L = 12.5 L = 80	V_{th} = 0	$\approx 10^6$	1	2017	[189]
PM	In_2O_3	Inkjet	High energy UV-visible light pulses	Planar	Glass/ITO	CSPE	W/L = 2 L = 50	V_{th} = 0.01	4.4×10^7	29	2018	[233]
PM	In_2O_3	Inkjet	High energy UV-visible light pulses	Planar	Glass/ITO	CSPE	W/L = 2 L = 50	V_{th} = 0.01	4.4×10^7	29	2018	[233]
PM	In_2O_3	Inkjet	Focused continuous wave UV-laser	Planar	Glass/ITO	CSPE	W/L = 2 L = 50	V_{th} = -0.3	1.2×10^6	10	2018	[233]
PM	In_2O_3	Inkjet	High energy UV-visible light pulses	Planar	Glass/ITO	CSPE	W/L = 2 L = 50	V_{th} = 0.01	4.4×10^7	29	2018	[233]
PM	In_2O_3	Inkjet	Focused continuous wave UV-laser	Planar	Glass/ITO	CSPE	W/L = 2 L = 50	V_{th} = -0.3	1.2×10^6	10	2018	[233]
PM	In_2O_3	Inkjet	Thermal (180 ºC) and FUV	SBGT	Polymide	Al_2O_3	W/L = 12.5 L = 80	V_{ON} = -0.1	2×10^6	2.83	2020	[178]
NM	CuO QDs	Inkjet	Microwave-assisted annealing	CBGT	Si wafer	SiO_2	W/L = 2 L = 40	V_{th} = 0.37	2.5×10^4	28.7	2013	[190]

Table S3. State-of-the-art of cellulose (nano)paper-gated transistors.

Substrate	Semiconductor	S/D contacts	Gate	Device configuration	Dimensions [μm]	V_{GS} range [V]	V_{DS} [V]	V_{ON} [V], V_{th} [V]	$I_{ON/OFF}$	Mobility [$cm^2V^{-1}s^{-1}$]	Year	Ref.
Paper	Sputtered IGZO	Thermally evaporated Al	Sputtered IZO	SBGT	W/L = 10.6	-20 to 20	15	V_{th} = 1.9	2.9×10^4	34	2008	35
Paper with ionic resin	Sputtered IGZO	Thermally evaporated Al	Sputtered IZO	SBGT	W/L = 10 L = 216	-20 to 20	15	V_{ON} = 1.0	$\approx 10^4$	40	2008	36
Paper	Sputtered IGZO	Sputtered Ti/Au	Sputtered IZO	SBGT	W/L = 20 L = 6	-20 to 40	40	V_{th} = 3.8	1.0×10^4	36	2009	275
Paper with ionic resin	Sputtered IGZO	Thermally evaporated Al	Sputtered IZO	SBGT	W/L = 10.5	-10 to 20	15	-	3.0×10^4	29	2009	270
Paper with ionic resin	Sputtered IGZO	Thermally evaporated Al	Sputtered IZO	SBGT	W/L = 10.5	-20 to 20	15	$V_{ON} \approx 0.0$	3.0×10^4	35 – 45	2009	273
Paper	Sputtered IGZO	Thermally evaporated Ni/Au	Sputtered IZO	SBGT	W/L = 3.47 L = 256	-5 to 20	10	V_{th} = 2.1	$\approx 10^4$	23	2012	39
Paper	Sputtered SnOx	Thermally evaporated Ni/Au	Sputtered IZO	SBGT	W/L = 3.47 L = 256	-20 to 20	30	V_{th} = 1.4	$\approx 10^2$	1.3	2012	39
Paper	Pulse electron beam deposition of In_2O_3	Pulse electron beam deposition of In_2O_3	Pulse electron beam deposition of In_2O_3	SBGT	W/L=7.5–10 L = 150–200	-5 to 5	5	V_{th} = -3.6	6.0×10^4	40000	2013	271
NCC	Sputtered IGZO	Thermally evaporated Al	Sputtered IZO	SBGT	W/L = 10.6 L = 210	-30 to 30	15	V_{ON} = -8.0	2.0×10^5	7.3	2014	40
Standard tracing paper	Sputtered IGZO	Thermally evaporated Al	Sputtered IZO	SBGT	W/L = 6.6 L = 210	15 to 16	15	V_{ON} = -2.5	2.5×10^4	2.3	2014	41
MFC/NFC	Sputtered IGZO	Thermally evaporated Al	Sputtered IZO	SBGT	W/L = 6.6 L = 210	15 to 16	15	V_{ON} = -4.7	2.2×10^4	0.94	2014	41
MFC/NFC - HCl	Sputtered IGZO	Thermally evaporated Al	Sputtered IZO	SBGT	W/L = 6.6 L = 210	15 to 16	15	V_{ON} = -4.8	7.5×10^4	16	2014	41

Table S3. Continuation (I).

Substrate	Semiconductor	S/D contacts	Gate	Device configuration	Dimensions [µm]	V_{GS} range [V]	V_{DS} [V]	V_{ON} [V], V_{th} [V]	$I_{ON/OFF}$	Mobility [$cm^2V^{-1}s^{-1}$]	Year	Ref.
Paper	Sputtered IGZO	Thermally evaporated Al	Sputtered IZO	SBGT	W/L = 6.6 L = 210	-15 to 15	15	V_{ON} = -2.5	2.5×10^4	2.3	2015	[34]
MFC/NFC	Sputtered IGZO	Thermally evaporated Al	Sputtered IZO	SBGT	W/L = 6.6 L = 210	-15 to 15	15	V_{ON} = -4.8	7.5×10^4	16	2015	[34]
Bacterial cellulose	Sputtered IGZO	Thermally evaporated Al	Sputtered IZO	SBGT	W/L = 10.5	-20 to 20	15	-	$\approx 10^4$	-	2016	[272]
Office paper	Pen-written ZnO	Screen-printed Ag	Screen-printed Ag	SBGT	W/L = 185 L = 200	-20 to 50	15	V_{ON} = 1	8.1×10^1	0.004	2017	[58]
Standard tracing paper	Sputtered IGZO	Thermally evaporated Al	Floating gate: sputtered IZO Gate 1 and 2: thermally evaporated Al	Planar dual-gate	W/L = 6.1 L = 170	-30 to 30	15	V_{ON} <0	4.0×10^4	3	2018	[4,44]
TEMPO-oxidized NFC	Thermally evaporated C8-BTBT	Thermally evaporated Au	Thermally evaporated Au	Planar	W/L = 30 L = 200	1.5 to -1.5	-1	-	$<10^2$	1.25	2018	[358]
TEMPO-oxidized NFC	Thermally evaporated C8-BTBT	Thermally evaporated Au	Thermally evaporated Au	Planar	W/L = 210 L = 100	3 to -10	-5	V_{th} = -1.26	3.0×10^4	0.07	2018	[51]
TEMPO-oxidized NFC	Thermally evaporated NTCDI-F15	Thermally evaporated Au	Thermally evaporated Au	Planar	W/L = 210 L = 100	-4 to 10	5	V_{th} = 0.16	6.9×10^3	0.01	2018	[51]

Table S4. Results of the electrical characterization of IGZO transistors on glass gated by Li-ClCHs (V_{DS} = 1.2 V).

Li-ClCHs	Scan rate [mV s^{-1}]	$I_{ON/OFF}$	V_{ON} [V]	g_m [mS]	S_S [V dec^{-1}]	μ_{Sat} [cm^2 V^{-1} s^{-1}]a)	μ_{Sat} [cm^2 V^{-1} s^{-1}]b)
MC0	25	1.5×10^{6}	0.0	11.6	0.17	24.8	9.25
	50	1.1×10^{6}	-0.1	12.2	0.16	25.6	9.53
	100	8.8×10^{5}	-0.1	12.0	0.16	25.1	9.35
	200	7.9×10^{5}	-0.1	11.5	0.15	23.6	8.81
	400	6.3×10^{5}	-0.1	10.8	0.14	21.2	7.88
M2C1	25	1.5×10^{6}	-0.5	20.4	0.13	17.3	6.77
	50	1.8×10^{6}	-0.5	17.4	0.12	12.7	4.99
	100	1.9×10^{6}	-0.5	13.2	0.12	12.1	4.72
	200	2.7×10^{6}	-0.4	12.8	0.10	12.1	4.76
	400	5.4×10^{6}	-0.2	11.7	0.09	12.0	4.69
M1C1	25	1.4×10^{6}	-0.3	22.2	0.11	20.8	5.31
	50	2.0×10^{6}	-0.3	22.9	0.11	20.4	5.21
	100	2.7×10^{6}	-0.3	19.7	0.10	15.0	3.83
	200	5.3×10^{6}	-0.2	15.7	0.10	15.3	3.91
	400	8.2×10^{6}	-0.2	12.5	0.09	12.8	3.26

a) Mobility calculated using the C_{DL} values determined from the data fitting of the EIS measurements using Dasgupta's ECM.

b) Mobility calculated using the capacitance values extracted directly from the EIS data at 0.1 Hz.

Table S5. Resume of the electrical performance of ClCH-gated IGZO transistors on multilayer-coated paper. The values show the average and respective standard error of the mean obtained from five samples (V_{DS} = 1.2 V, V_{GS} scan rate: 0.05 V s^{-1}).

ClCHs	V_{ON} [V]	$I_{ON/OFF}$ [$\times10^{4}$]	g_m/width [μS mm^{-1}]	S_S [V dec^{-1}]	μ_{Sat} [cm^2 V^{-1} s^{-1}]a)
L100	0.18 ± 0.04	8.97 ± 3.15	214 ± 78.8	0.22 ± 0.02	5.30 ± 2.00
L1N1	0.14 ± 0.07	7.38 ± 2.31	316 ± 66.9	0.23 ± 0.02	6.92 ± 1.62
L1N3	0.16 ± 0.05	5.56 ± 2.50	169 ± 38.2	0.24 ± 0.03	4.04 ± 0.52
L1N19	0.04 ± 0.07	5.28 ± 2.05	284 ± 104	0.26 ± 0.02	6.74 ± 2.52
N100	0.10 ± 0.05	1.85 ± 0.29	155 ± 11.7	0.26 ± 0.02	3.43 ± 0.23

a) Mobility calculated using the C_{DL} values determined from the data fitting of the EIS measurements using Dasgupta's ECM.

Table S6. Variation of V_{ON} and S_S of the fabricated L1N3 hydrogel-gated IGZO transistor on multilayer-coated paper during heating at different temperatures (V_{DS} = 1.2 V, V_{GS} scan rate: 50 mV s^{-1}).

Temperature [ºC]	V_{ON} [V]	S_S [V dec^{-1}]
RT	0.0	0.22
50	0.0	0.27
60	0.0	0.30
70	-0.1	0.35
80	-0.2	0.49
90	-0.2	0.66
100	-0.1	0.92
120	-0.5	1.69

Table S7. Variation of V_{ON} and S_S of the fabricated L1N3 hydrogel-gated IGZO transistor on multilayer-coated paper during vacuum for various time intervals (V_{DS} = 1.2 V, V_{GS} scan rate: 50 mV s^{-1}).

Pressure	Time [min]	V_{ON} [V]	S_S [V dec^{-1}]
Atmospheric pressure	0	0.1	0.27
4.8×10^{-2} mbar	5	-0.1	0.27
3.1×10^{-2} mbar	10	-0.4	0.27
2.5×10^{-2} mbar	15	-0.8	0.22
1.7×10^{-2} mbar	30	-0.8	0.21
1.0×10^{-2} mbar	60	-0.7	0.21
6.8×10^{-3} mbar	90	-0.7	0.21
6.2×10^{-3} mbar	120	-0.7	0.21
4.2×10^{-3} mbar	150	-0.8	0.22
7.4×10^{-4} mbar	1080	0.5	0.08

Annex C

Supplementary equations

$$CrI = \frac{I_{(002)} - I_{am}}{I_{(002)}}$$

Equation S1. Equation used for calculating the crystallinity index (CrI) from the empiric method proposed by Segal. $I_{(002)}$ is the maximum intensity (in arbitrary units – a.u.) of the (002) lattice diffraction taken at 2θ = 22°, and I_{am} is the intensity of the amorphous phase diffraction in the same units at 2θ = 18°.

$$C_{DL} = \left[Y_0 R_c{}^{-(\alpha-1)}\right]^{1/\alpha}$$

Equation S2. Equation used for calculating the double layer capacitance from the Dasgupta's ECM. Y_0 is the capacitance associated to the CPE, R_c is the contact resistance, and α is a constant between 0 and 1 that determines how non-ideal the capacitor behaves (α = 1 corresponds to the case of an ideal capacitor).

$$\sigma_i = \frac{l}{R_b A}$$

Equation S3. Equation used for calculating the ionic conductivity from the Dasgupta's ECM. R_b is the bulk resistance, l is the thickness of the electrolyte membrane, and A is the surface area.

$$S_S = \left(\frac{\partial \log I_{DS}}{\partial V_{GS}}\bigg|_{max}\right)^{-1}$$

Equation S4. Equation used for calculating the subthreshold swing (S_S). I_{DS} and V_{GS} correspond to drain current and gate voltage, respectively.

$$\mu_{Sat} = \left(\frac{\partial\sqrt{I_{DS}}}{\partial V_{GS}}\right)^2 \frac{2L}{WC_{DL}}$$

Equation S5. Equation used for calculating the saturation mobility (μ_{Sat}). I_{DS}, V_{GS}, C_{DL}, W and L correspond to drain current, gate voltage, double layer capacitance of the CICHs, width and length of the channel, respectively.

$$R_s = 4.532\frac{V}{I}$$

Equation S6. Equation used for calculating the sheet resistance (R_s) from four-point probe measurements. V, and I correspond to the measured voltage between the two inner probes, and the current applied between the outer probes, respectively.

$$\varepsilon \approx \frac{(t_{CMC/ZnO} + t_{office\ paper})}{2r}$$

Equation S7. Equation used for calculating the bending strain (ε). r, $t_{CMC/ZnO}$, and $t_{office\ paper}$ correspond to the bending radius, and thicknesses of the CMC/ZnO film (≈ 8.65 μm) and office paper substrate (≈ 100 μm), respectively.